LOCKHEED MARTIN ENERGY RESEARCH LIBRARIES

3 4456 0449272 4

ORNL-5536

# GAS-COOLED REACTOR PROGRAMS

## HIGH-TEMPERATURE GAS-COOLED REACTOR BASE-TECHNOLOGY PROGRAM ANNUAL PROGRESS REPORT FOR PERIOD ENDING DECEMBER 31, 1978

F. J. Homan

Paul R. Kasten

OAK RIDGE NATIONAL LABORATORY
CENTRAL RESEARCH LIBRARY
CIRCULATION SECTION
4500N ROOM 175
LIBRARY LOAN COPY
DO NOT TRANSFER TO ANOTHER PERSON
If you wish someone else to see this report, send in name with report and the library will arrange a loan.
UCN-7969 (3 9-77)

OAK RIDGE NATIONAL LABORATORY
OPERATED BY UNION CARBIDE CORPORATION · FOR THE DEPARTMENT OF ENERGY

Printed in the United States of America. Available from
National Technical Information Service
U.S. Department of Commerce
5285 Port Royal Road, Springfield, Virginia 22161
Price: Printed Copy $10.75; Microfiche $3.00

This report was prepared as an account of work sponsored by an agency of the United States Government. Neither the United States Government nor any agency thereof, nor any of their employees, contractors, subcontractors, or their employees, makes any warranty, express or implied, nor assumes any legal liability or responsibility for any third party's use or the results of such use of any information, apparatus, product or process disclosed in this report, nor represents that its use by such third party would not infringe privately owned rights.

ORNL-5536
Distribution
Category UC-77

Contract No. W-7405-eng-26

GAS-COOLED REACTOR PROGRAMS

# HIGH-TEMPERATURE GAS-COOLED REACTOR BASE-TECHNOLOGY PROGRAM
# ANNUAL PROGRESS REPORT FOR PERIOD ENDING DECEMBER 31, 1978

F. J. Homan, Program Manager
Paul R. Kasten, Program Director

Date Published: June 1979

OAK RIDGE NATIONAL LABORATORY
Oak Ridge, Tennessee 37830
operated by
UNION CARBIDE CORPORATION
for the
DEPARTMENT OF ENERGY

LOCKHEED MARTIN ENERGY RESEARCH LIBRARIES
3 4456 0449272 4

CONTENTS


Page

SUMMARY . . . . . vii

1. HTGR CHEMISTRY . . . . . 1
   1.1 PEACH BOTTOM SURVEILLANCE PROGRAM . . . . . 1
   1.2 FISSION PRODUCT SORPTION AND DESORPTION FROM PRIMARY CIRCUIT MATERIALS . . . . . 2
      1.2.1 Iodine Sorption and Desorption from Alloy T-22 . . . . . 2
      1.2.2 Iodine Sorption and Desorption from Core Graphite . . . . . 6
   1.3 GRAPHITE STRENGTH LOSS CAUSED BY CORROSION . . . . . 8
      1.3.1 Graphite Corrosion Tests . . . . . 9
      1.3.2 Graphite Preparation and Characterization . . . . . 10
      1.3.3 Fractography . . . . . 14
   1.4 TRITIUM DISTRIBUTION AND INVENTORY IN THE PEACH BOTTOM HTGR . . . . . 14
   1.5 FISSION PRODUCT TRANSPORT IN GRAPHITE . . . . . 16
      1.5.1 Diffusion of Cesium in Graphite . . . . . 16
      1.5.2 Diffusion of Silver in Core Graphite . . . . . 17
      1.5.3 Diffusion of Plutonium, Uranium, and Thorium in Graphite . . . . . 18
   1.6 REFERENCES . . . . . 18

2. FUELED GRAPHITE DEVELOPMENT . . . . . 21
   2.1 INTRODUCTION . . . . . 21
   2.2 IRRADIATION EXPERIMENTS . . . . . 22
      2.2.1 HFIR Target Capsules . . . . . 23
         2.2.1.1 Capsules HT-17 Through -19 . . . . . 23
         2.2.1.2 Capsule HT-31 . . . . . 23
         2.2.1.3 Capsule HT-32 . . . . . 24
         2.2.1.4 Capsule HT-33 . . . . . 28
         2.2.1.5 Capsule HT-34 . . . . . 31
      2.2.2 HRB Capsules . . . . . 38
         2.2.2.1 Capsules HRB-11 and -12 . . . . . 38
         2.2.2.2 Capsule HRB-13 . . . . . 40
         2.2.2.3 Capsule HRB-14 . . . . . 41
         2.2.2.4 Capsule HRB-15b . . . . . 47
      2.2.3 ORR Capsules . . . . . 47
      2.2.4 Fort St. Vrain Test Element Program . . . . . 47
   2.3 DEVELOPMENT WORK . . . . . 51
      2.3.1 Permeability Studies . . . . . 52
         2.3.1.1 Permeability of Production Coatings . . . . . 52
         2.3.1.2 Ne:He Intrusion Measurements on Biso Coatings . . . . . 56
      2.3.2 Pyrocarbon Coating by Use of $CO_2$ Carrier Gas . . . . . 56

Page


2.3.3 Dense UCO Fuel Development . . . . . 57
2.3.4 Silicon Carbide Development, Characterization, and Testing . . . . . 57
2.3.4.1 Experimental Plan . . . . . 58
2.3.4.2 Results and Discussion . . . . . 59
2.3.4.3 Work Plan for the Next Reporting Period . . . . . 60
2.4 IRRADIATION SUPPORT ACTIVITIES . . . . . 63
2.4.1 Nuclear Evaluation and Thermal Analysis . . . . . 63
2.4.1.1 Experiment HRB-15b: Particle Loadings and Thermal and Neutronics Analysis . . . . . 63
2.4.2 Fission Product-SiC Coating Interaction Studies . . . . . 79
2.5 PROJECT WORK STATEMENT ACTIVITIES UNDER U.S.-FRG UMBRELLA AGREEMENT . . . . . 83
2.5.1 PWS FD-1 . . . . . 84
2.5.2 PWS FD-12 . . . . . 87
2.5.3 PWS FD-13 . . . . . 88
2.5.4 PWS FD-18 . . . . . 88
2.6 EQUIPMENT DEVELOPMENT AND SUPPORT ACTIVITIES . . . . . 89
2.6.1 Irradiated Microsphere Gamma Analyzer System . . . . . 89
2.6.1.1 IMGA Operation . . . . . 89
2.6.1.2 Analysis of OF-2 Fuel . . . . . 90
2.6.1.3 Analysis of HT-34 Fuel . . . . . 90
2.6.2 Postirradiation Gas Analyzer System . . . . . 95
2.7 SERVICE WORK FOR GENERAL ATOMIC COMPANY . . . . . 99
2.7.1 Permeability Studies on Unirradiated Biso-Coated Particles Fabricated by GA . . . . . 100
2.7.2 Assay Measurements on FSVR Test Element Fuel Rods . . . . . 105
2.7.3 Hot Gaseous Chlorine Leaching of Irradiated General Atomic Company Fuel Rods . . . . . 113
2.7.4 Miscellaneous Requests from General Atomic Company for Service Work . . . . . 113
2.8 REFERENCES . . . . . 113

3. PRESTRESSED CONCRETE PRESSURE VESSEL DEVELOPMENT . . . . . 121
3.1 INTRODUCTION . . . . . 121
3.2 PCRV OPTIMIZATION PLAN . . . . . 121
3.3 ANALYSIS METHODS DEVELOPMENT . . . . . 122
3.3.1 Concrete Constitutive Models . . . . . 122
3.3.1.1 Description of the ADINA Model . . . . . 122
3.3.1.2 Description of the Endochronic Model . . . . . 123
3.3.1.3 Comparisons with Experimental Data . . . . . 125
3.3.2 Embedded Bar Modeling Technique . . . . . 130

Page

3.4 CONCRETE PROPERTIES IN A NUCLEAR ENVIRONMENT . . . . . 133
3.5 INSTRUMENTATION EVALUATION AND DEVELOPMENT . . . . . 135
3.5.1 Concrete Embedment Strain-Gauge Evaluation . . . . . 136
3.5.2 Acoustic Emission . . . . . 136
3.5.2.1 Acoustic-Emission Laboratory Investigation . . . . . 137
3.5.2.2 Monitoring of Plain Concrete Specimens . . . . . 137
3.5.2.3 Monitoring of Prestressed Concrete Beam Members . . . . . 146
3.5.2.4 Monitoring of Flawed Thick-Walled Steel Pressure Vessel . . . . . 150
3.6 STRUCTURAL MODEL TESTS . . . . . 157
3.6.1 Grouted-Nongrouted Tendon Study . . . . . 157
3.6.2 PCRV Model Program Definition . . . . . 160
3.7 LINER AND PENETRATION STUDIES . . . . . 169
3.8 REFERENCES . . . . . 177

4. STRUCTURAL MATERIALS . . . . . 179
4.1 INTRODUCTION . . . . . 179
4.2 MECHANICAL PROPERTIES . . . . . 180
4.2.1 Creep Testing of Base Metals and Weldments . . . . . 180
4.2.2 Low-Cycle Fatigue and Creep Fatigue . . . . . 182
4.2.3 Fatigue Crack Growth . . . . . 186
4.2.3.1 Hastelloy X and Hastelloy X Weld Metal . . . . . 187
4.2.3.2 2-1/4 Cr-1 Mo Steel . . . . . 191
4.2.3.3 Heat-Affected Zone of 2-1/4 Cr-1 Mo Steel-ERNiCr-3 Weld Metal . . . . . 194
4.2.4 Thermal Stability . . . . . 194
4.2.5 Corrosion . . . . . 197
4.3 WELDING DEVELOPMENT . . . . . 201
4.3.1 Dilution Effects on Weld Creep Properties . . . . . 202
4.3.2 Fusion Line Aging . . . . . 204
4.4 STEAM CORROSION . . . . . 205
4.4.1 Inconel 617 Loop . . . . . 206
4.4.2 Inconel 625 Loop . . . . . 206
4.4.3 Heat-Transfer Corrosion Test Loop . . . . . 207
4.5 REFERENCES . . . . . 207

5. HTGR GRAPHITE STUDIES . . . . . 209
5.1 GRAPHITE CREEP EXPERIMENT . . . . . 209
5.1.1 Graphite Creep Capsules . . . . . 209
5.1.2 Neutronics Analysis for OC-2 Experiment . . . . . 210
5.1.3 Graphite Creep Data . . . . . 210
5.1.4 Creep Bench Test . . . . . 211

Page

5.2 KERNFORSCHUNGSANLAGE GRAPHITE IRRADIATIONS IN HFIR . . . . . 211
5.2.1 Capsule Construction . . . . . 211
5.2.2 Preirradiation Characterization . . . . . 211
5.2.3 Irradiation Results from HTK-1 . . . . . 215
5.3 REFERENCE . . . . . 219

6. EVALUATION OF PEBBLE-BED-TYPE HTR . . . . . 221
6.1 INTRODUCTION . . . . . 221
6.2 ANALYSIS METHODS . . . . . 222
6.2.1 Neutronics and Exposure . . . . . 222
6.2.2 Cross Sections . . . . . 222
6.2.3 Thermal Hydraulics . . . . . 223
6.3 PERFORMANCE CHARACTERISTICS OF SPECIFIC FUEL CYCLES . . . . . 223
6.3.1 Burner Operation . . . . . 223
6.3.2 Converter Operation with Recycle . . . . . 223
6.3.3 Denatured Fuel . . . . . 225
6.3.4 Breeder Operation . . . . . 225
6.3.5 Prebreeder Operation . . . . . 225
6.4 ORE UTILIZATION AND FUEL COSTS . . . . . 226
6.5 REFERENCES . . . . . 226

ORGANIZATION CHART . . . . . 229

# SUMMARY

## 1. HTGR CHEMISTRY

### Peach Bottom Surveillance Program

Work on this task was completed in FY 1978 with the disposal of fuel element remnants and publication of the last two fuel element examination reports. In all, six fuel element examination reports were published, including four end-of-life elements, a primary circuit analysis report, and a study of fuel-particle failure fractions.

### Fission Product Sorption/Desorption from Primary Circuit Materials

An apparatus for the study of iodine sorption/desorption from primary circuit alloy materials has been assembled, and one series of test runs has been completed. These initial runs revealed both a problem with oxygen contamination and a design flaw in the iodine source generator, which are being corrected.

An apparatus for the study of iodine sorption on graphite at 1-atm total pressure is being assembled. Modifications of this apparatus, which would allow sorption tests at 10 atm as well as depressurization tests from this pressure, are currently being designed.

### Graphite Strength Loss Caused by Corrosion

Four corrosion runs have been completed (as of February 1979) on 1/2- and 3/4-in. diam specimens of H-451 graphite. Run durations ranged from 7 to 28 days; total burnoffs ranged from 5 to 10%.

Apparatuses to measure surface area, porosimetry, and apparent density in helium are either completed or in calibration runs. Densitometry profiling by x ray appears to be quite feasible and is being developed. Sonic attenuation has evolved as a means of estimating background flaw size.

Graphite grades H-451 and S-2020 are on hand, and nondestructive testing of H-451 is complete. Similar tests on S-2020 are in progress.

### Tritium Distribution and Inventory in the Peach Bottom HTGR

The final report of this work has been drafted and technically reviewed. Measured inventories of tritium in fuel and graphite components of the core are reported as well as an initial attempt at general descriptions of tritium movements in the core and of releases from the reactor.

Fission Product Transport in Graphite

A write-up is currently in process of the research on cesium diffusion in various graphite, conducted by R. B. Evans III prior to his death. A study of silver diffusion in H-451 graphite has been initiated under subcontract with the Texas A. & M. Research Foundation. Plutonium, uranium, and thorium concentration profiles are being obtained in previously acquired samples of Peach Bottom fuel elements.

## 2. FUELED GRAPHITE DEVELOPMENT

The Fueled Graphite Development Program at ORNL is part of a national HTGR fuel development program being conducted at ORNL and at the General Atomic Company (GA). A "unified" program plan has been written by GA and ORNL personnel, organized around three goals: (1) to develop and qualify low-enriched uranium (LEU)/medium-enriched uranium (MEU) fuel for use in proliferation-resistant fuel cycles in HTGRs; (2) to complete the fuel development work that is generic to LEU, MEU, and highly enriched uranium (HEU) fuel cycles; and (3) to complete the development of HEU fuel to the point of proof testing. This program plan is unified because it deals with all possible fuel cycles for the HTGR, although current emphasis is on the MEU cycle.

The ORNL program is organized around several subtasks. We discuss here the highlights of work done during this reporting period under each subtask.

Irradiation Experiment Subtask

HFIR Target Capsules: Final reports were completed on capsule experiments HT-17 through -19, HT-31, HT-32, and HT-33. Postirradiation examination (PIE) was completed on capsule HT-34. No new HFIR target (HT) capsule experiments were initiated during the reporting period. The next HT capsule is scheduled to begin irradiation in March 1980, but this schedule is dependent on adequate funding for the work, which is very uncertain at present.

HFIR Removable Beryllium Capsules: Postirradiation examination was completed on capsule experiments HRB-11, -12, and -13 [except for irradiated microsphere gamma analyzer (IMGA) examination]. A final report was completed on the HRB-11 and -12 experiments. Two capsules (HRB-14 and -15b) were assembled and irradiated during the reporting period. The next HFIR removable beryllium (HRB) capsule (HRB-15a) is scheduled to begin irradiation in March 1980 but is dependent on the uncertain funding pattern.

ORR Capsules: A final report was completed on the OF-2 experiment. No additional Oak Ridge Reactor (ORR) capsules are scheduled until March 1982.

Peach Bottom Reactor Experiments: A final report was issued on the Peach Bottom Reactor Recycle Test Element (RTE) Program, which was supported by the HTGR Recycle Program.

Fort St. Vrain Reactor Experiments: This work was also supported by the HTGR Recycle Program but is reported here to provide a complete picture of the irradiation program. The Fort St. Vrain Reactor (FSVR) test elements have been at the reactor site awaiting insertion with the first reload since May 1978. Quality inspection showed higher-than-acceptable failure rates in some weak-acid resin (WAR)- derived fuel manufactured at ORNL. It was not known whether the high failure rate was a result of the fabrication process or was caused by the cure-in-place operation and subsequent removal of fuel rods from the test fixtures for activation in the Triga Reactor at GA. Additional quality inspection work was performed during this reporting period to determine the cause of the high failure rate. This work will be completed during the first half of 1979. Other work on the FSVR test element fuel includes impurity as well as heavy metal assay analysis.

Development Subtask

Permeability Studies: During this reporting period the techniques that have been developed to measure permeability in pyrocarbon (PyC) coatings were applied to a large number of batches. Correlations were made between (1) PyC permeability to fission gas and other inert gases and (2) coating properties and deposition conditions. A conclusion was reached that it is possible to make gastight PyC coatings but that it is difficult with current coating technology and probably cannot be done economically on a production basis because the reject rate will be too high.

Pyrocarbon Coating Using Carbon Dioxide Diluent Gas: This work was initiated because of the outstanding irradiation performance of batch OR 2013 in several HT capsule irradiations. This batch was fabricated in the laboratory-scale coaters. The objective of the work was to produce the same quality of coatings in the production-scale coaters. Several runs have been made, but none have reproduced the properties of the coatings in batch OR 2013.

Sintering and Conversion Studies on Dense UCO Fuel: Dense UCO fuel appears to offer superior irradiation performance and has none of the disadvantages of dense $UC_2$ or $UO_2$. The dense kernel also offers better fission-gas retention than the porous WAR UCO fuel. Efforts are under way at ORNL to develop a dense product that has the desired initial chemistry.

Improved Silicon Carbide (SiC) Coating Development: The fission product spectrum for MEU fuel is such that much more silver and palladium are produced than are produced with HEU fuel. Silver is very mobile and has been observed to diffuse through SiC. Palladium is corrosive and attacks SiC. Silicon carbide, which resists silver diffusion

and palladium corrosion, is being developed by characterizing the SiC microstructure and subsequently correlating resistance to silver diffusion and palladium corrosion (measured in out-of-reactor thermal gradient heating tests) with microstructure. After the best-performing SiC microstructure has been identified, the fabrication conditions necessary to produce that microstructure will be established. This work was initiated during the last half of the reporting period.

Irradiation Support Subtask

Two areas of work are reported: (1) the nuclear and thermal analysis of capsule HRB-15b and (2) out-of-reactor studies of fission product/SiC coating interaction.

Capsule HRB-15b was designed somewhat differently from previous HRB capsules. The fuel, in the form of individual coated particles, was loaded into trays that resembled flat graphite washers with holes drilled into one face. The trays were stacked in alternate fissile/fertile arrays. No graphite sleeve was included in the capsule. The objective was to provide particles irradiated at low temperatures for subsequent thermal-gradient, out-of-reactor testing.

The fission product/SiC interaction studies during this reporting period focused on particles with "fission product" concentrations representative of MEU fuel operated to burnups of about 25% FIMA. The simulated fission products of appropriate concentration were added to $UO_2$ or $UC_2$ kernels and then Triso coated and heated in a thermal gradient. The fission products studied include Mo, Ru, Rh, Pd, Ag, and Cd. In Triso-coated $UO_2$ the fission products Ru, Rh, Pd, and Ag can interact with the SiC at temperatures several hundreds of degrees Celsius above the reactor operating temperature. In Triso-coated $UC_2$ the fission products ruthenium, rhodium, and palladium promote the interaction of a uranium-containing second phase throughout the SiC layer at more normal reactor operating temperatures.

Project Work Statement Subtask

Four project work statement subtasks (PWSs) are included under the Fueled Graphite Development Program:

1. Work on PWS FD-1 (Critical Evaluation of LEU Fuel Performance Data) was completed during the reporting period, and a joint ORNL-KFA-GA report was published.

2. Work on PWS FD-12 (Quantification of Irradiation-Induced Permeability in Pyrocarbon Coatings) was delayed from the schedule initially planned because of delays encountered in the shipment of fuel from Germany to the United States. This PWS involved characterization of irradiated coated particles with techniques developed in the United States for measurement of permeability. Data on irradiated German fuel is to be compared with data from HT-34 and HRB-14 fuel irradiated in the United States. Measurements are complete on archive fuel from all experiments to be considered under this PWS.

3. Work on PWS FD-13 [comparison of IMGA and Postirradiation Annealing and Autoradiography (PIAA)] has proceeded approximately on the original schedule, although some shipping delays have been encountered. Descriptions of both IMGA and PIAA are completed, and the IMGA analysis of the U.S. fuel is complete.

4. Work on PWS FD-18 (Fuel Chemical Performance Modeling) was initiated at the end of the reporting period, and there is little to report.

Equipment Development and Support Subtask

The IMGA system was operational for most of the year. A few problems were encountered with the particle-handling system, and work was initiated on the design of a second particle-handling system which will have improved in-cell reliability. Coated particles from OF-2, HT-34, and HRB-11 through -13 were examined with IMGA during the reporting period.

Equipment (time-of-flight mass spectrometer, PDP-8 minicomputer) for the postirradiation gas analyzer (PGA) system was procured during the reporting period. The particle-breaking system was designed and constructed. The system was assembled, but during checkout a number of problems were encountered that were not solved by the end of the reporting period.

Service Work for General Atomic Company

In addition to work on the above five subtasks, considerable work was done for GA in areas in which ORNL has unique capabilities. During this reporting period the following work was accomplished:

1. Permeability studies were conducted on 24 batches of Biso-coated fertile particles fabricated in production-scale coating equipment. An additional ten Biso-coated batches were characterized for comparison with irradiation results on these particles. The purpose of these studies was to correlate coating permeability with coating properties and deposition conditions.

2. Nondestructive assay measurements of fertile and fissile content were accomplished on FSVR test-element fuel that was fabricated by GA. Delayed neutron and prompt neutron techniques were employed. Destructive assay, using wet chemistry techniques, was also used on these rods, and results from the various techniques used were compared.

3. Hot gaseous chlorine leach (1000°C) of eight fuel rods irradiated in the Peach Bottom Reactor (FTE-16) was accomplished and the resulting data forwarded to GA during the reporting period.

4. Metallographic examination of eight GA fuel rods irradiated in Capsule HRB-12 was accomplished and the data forwarded to GA.

5. Microprobe examination of one cross section from a GA fuel rod irradiated in Experiment P13Q was accomplished and the data forwarded to GA.

## 3. PRESTRESSED CONCRETE PRESSURE VESSEL DEVELOPMENT

A plan for the development of an optimized prestressed concrete pressure vessel (PCRV) has been prepared. Although the plan was originally based on optimization of the PCRV for the 900-MW(e) steam-cycle HTGR Reference Plant, it is equally applicable to PCRVs proposed for use with advanced HTGR systems.

Under the analytical methods task area, improved PCRV nonlinear analysis methods and analytical procedures for efficiently modeling steel reinforcing bar layouts in finite-element analyses are being developed. Of the two nonlinear constitutive models that have been evaluated, the endochronic model predicts nonlinear behavior and ultimate load much more accurately than does the concrete model employed in the ADINA finite-element computer code. A procedure is being developed to permit arbitrarily oriented reinforcing bars in isoparametric continuum elements. The development of such a satisfactory procedure will greatly improve capability for modeling rebars because current procedures restrict the location of rebars to the edges of continuum elements.

The best available concrete constitutive models are severely restricted by the lack of complete concrete multiaxial test data. Consequently, work has been initiated on development of a concrete multiaxial testing capability at ORNL. Current activities consist of preparing a compilation of published multiaxial test data and of performing an evaluation of existing facilities in which multiaxial tests have been conducted. Based on our conclusion that there is need for a facility in which to conduct a full spectrum of multiaxial tests for a fairly wide range of temperatures, we have initiated the design of an enclosure for a multiaxial test facility at ORNL.

The experimental evaluation study of a representative sampling of commercially available concrete embedment strain instrumentation has been completed. It was concluded that calibration factors supplied by the manufacturers require verification, that improved sealing and corrosion protection is required, and that improved types of embedment instrumentation should be developed by using different measurement techniques.

The results of studies that were conducted to assess the desirability of using acoustic emission (AE) to monitor PCRV structural performance indicate that the technique has considerable potential. Recent evaluations have included monitoring of plain concrete cylinders, prestressed concrete beams, and thick-walled steel pressure vessels. Results show that, using AE, we can identify, locate, and indicate the severity of flaw propagation in prestressed concrete structures as well as detect the onset of failure.

A PCRV Model Program Definition was prepared under subcontract by GA in support of the 900-MW(e) HTGR Steam Cycle Plant development. This document outlines the objective, scope, modeling philosophy requirements,

review responsibility, and schedule of the required testing program. We anticipate that model tests of PCRVs designed for advanced HTGR systems will have similar model requirements.

Under the ongoing fracture testing program for typical PCRV plates, forgings, and weldments, recent Charpy impact and fracture toughness test results are described. A distinct difference has been found between bulk-weld metal and root-weld toughness; however, we plan further testing to provide confirmation and understanding of this effect.

## 4. STRUCTURAL MATERIALS

The principal objective of the Structural Materials Program is to provide the required data for design and licensing of safe and economic high-temperature components for the HTGR. Mechanical properties of selected materials are being determined in prototypical helium environments. In addition, structural stability, weldability, and steam corrosion are being studied to characterize more fully material behavior. A new task was added to the program during this reporting period: studies on structural ceramics. This task started at the beginning of FY 1979, and work was in progress for only the last three months of the reporting period; consequently, there are no results to report.

Highlights of the work done during the past year are:

### Helium Effects Subtask

Creep tests on Hastelloy X up to 20,000 h in duration have shown that the creep behavior of this alloy in helium is not detectably different from that in air, although carburization occurs in helium. The kinetics of carburization become rapid above 850°C.

The creep strength of 2-1/4 Cr-1 Mo steel is lower in helium than in air because of carburization. Reduction in creep strength is greater at higher temperatures because the kinetics of carburization become quite rapid above 600°C.

Inconel 617 is considerably stronger than Hastelloy X in both helium and air. Modified Hastelloy N was not carburized during creep testing in helium for over 1000 h at 871°C.

Creep tests on weldments of Hastelloy X joined to itself with Hastelloy X and Hastelloy S filler metals showed that test specimens prepared using the gas-tungsten-arc (GTA) welding procedure had longer rupture lives than specimens prepared using the shielded-metal-arc welding (SMAW) procedure. Minimum fracture strains of 3% were noted for the SMAW welds tested at 649°C, whereas minimum values for Hastelloy X filler metal deposited by the GTA process were 6.5%, and those for Hastelloy S deposited by the GTA process were 10%.

Weld failures consistently occurred in the Incoloy 800H base metal or in the heat-affected zone (HAZ) of the Incoloy 800H end of the weld during creep testing of specimens prepared by joining Hastelloy X and Incoloy 800H and by using either the Inco 82 filler metal and the GTA welding procedure or the Inco Weld A filler metal and the SMAW procedure.

Conclusions drawn from fatigue testing of 2-1/4 Cr-1 Mo steel in air are: (1) use of hold periods reduces cyclic life compared with testing with no-hold period, (2) compressive holds are more damaging than tensile holds, and (3) combined tensile and compression holds of equal duration are more damaging than either tensile or compressive holds. Testing in helium showed that compressive holds were less damaging than tensile holds, which indicates that environment influences the conclusion about the most damaging type of hold period. For continuous cycling tests (zero hold time) at 538°C, the cyclic life of 2-1/4 Cr-1 Mo steel tested in impure helium either exceeds or is equivalent to that tested in air.

Fatigue crack-growth rates (CGR) are higher in air and steam than in HTGR helium and vacuum environments for 2-1/4 Cr-1 Mo steel. The exclusion of oxygen from the crack tip in the vacuum and helium environments is thought to be the reason for this behavior. In the HAZ of 2-1/4 Cr-1 Mo steel/ERNiCR-3 welds, the fatigue CGR is between that of 2-1/4 Cr-1 Mo steel base metal and ERNiCr-3 weld metal. Fatigue CGRs in Hastelloy X weld metal were lower than in base metal at 538 and 649°C.

The carburization rate of Hastelloy X does not increase uniformly from 750 to 950°C; the activation energy for carburization appears to change abruptly from 44 kcal/mol below 854°C to 10 kcal/mol above 854°C.

Welding Development Subtask

We examined the effect of weld dilution on short-term creep properties and on fusion line aging characteristics for three nickel-based weld metals used in transition joints involving a ferritic steel. It was found that, for ERNiCr-3 and ENiCrFe-3 tested at 649°C in air, weld dilution reduces the creep-rupture life compared with a pure undiluted sample. No significant differences were apparent in the fusion line aging characteristics of the three weld metals.

Steam Corrosion Subtask

The long-term exposure of a variety of alloys to superheated steam at 482 and 538°C continued throughout the year. After 18,000 h, exfoliation of oxide was noted only on 2-1/4 Cr-1 Mo and about nine chromium steel specimens tested at 538°C; all other materials gained weight at a slow, constant rate. In another test, it was demonstrated that Incoloy alloy 800H, stressed to 90% of its ASME design yield stress, is not subject to stress corrosion cracking in superheated steam containing 20 to 30 ppb sodium (as NaOH) at 538°C.

## 5. HTGR GRAPHITE STUDIES

Creep capsule OC-2 completed its planned 110-d irradiation in the ORR during this reporting period. Design improvements were incorporated into this capsule to overcome the problems associated with the OC-1 capsule, which was operated at 600°C. Work on the OC-3 capsule was completed for a January 1979 insertion, which will operate for two ORR cycles (about 110 d) at 900°C. Samples are recycled from the OC-1 capsule to OC-3 so that the planned peak fluence (total) for these specimens at the end of OC-3 operation will be $3 \times 10^{25}$ neutrons $cm^{-2}$. Bench testing of the 1250°C capsule was completed during the past year. Capsule OC-6 will be the first 1250°C capsule and is scheduled to begin irradiation in April 1981.

Capsule HTK-1 completed irradiation in the HFIR during this reporting period. This capsule, containing a number of grades of German graphite, was irradiated for five cycles. The HTK capsules operate as screening tests to investigate the dimensional stability of German graphites at high neutron exposures.

This work is part of the United States/Federal Republic of Germany (FRG) cooperation in fuel and graphite development. The second capsule in this series, HTK-2, began irradiation during the reporting period and is scheduled to complete irradiation early in 1979. Additional work during the reporting period included the preirradiation characterization of the German graphites and examination of specimens irradiated in capsule HTK-1.

## 6. EVALUATION OF PEBBLE-BED HTR

The design and mode of operation of the high-temperature, gas-cooled, graphite-moderated, pebble-bed reactor are under study to project its performance. Calculations are being done with enhanced local analysis methods to predict ore use and fuel cost in various modes of operation under design constraints. Aspects of importance and key results are presented. The concept shows potential for electrical energy and process heat applications. This work is under a technical information exchange umbrella agreement with the Federal Republic of Germany.

# 1. HTGR CHEMISTRY

R. P. Wichner

## 1.1 PEACH BOTTOM SURVEILLANCE PROGRAM — F. F. Dyer, L. L. Fairchild, and R. P. Wichner

Activities this year included completion of the final two postirradiation examination (PIE) reports on Peach Bottom fuel elements as well as disposal of the remains of the fuel elements into retrievable storage in the ORNL burial ground. These activities conclude the Peach Bottom Surveillance Program, which has been active since about 1972.

The main purpose of this task was to provide data for design code verification efforts conducted at General Atomic Company (GA) within the larger effort termed the Peach Bottom End-of-Life Program. Fission product diffusion (FIPER) and plateout (PAD) codes were compared with fission product distribution data, provided in a series of examination reports on six fuel elements[1-6] and the primary circuit.[7] We assisted in the verification of thermal codes by providing the necessary dimensional change information for the fuel element examination reports. We also conducted a fuel-particle failure fraction estimate[8] by a modified chlorine leach procedure, which was initially in sharp disagreement with the results obtained by GA by measuring noble gas release. We concluded that the chlorine leach results were correct (which indicated failure rates of less than 1%) and that the GA fuel samples were probably humidity-damaged in storage or in transit.

In addition to completing these specific task objectives, we obtained much potentially valuable data in the examination reports on the behavior of fission products ($^{3}H$, $^{90}Sr$, $^{95}Zr$, $^{103}Ru$, $^{106}Ru$, $^{110m}Ag$, $^{125}Sb$, $^{134}Cs$, $^{137}Cs$, $^{144}Ce$, and $^{154}Eu$) and activation products ($^{3}H$, $^{14}C$, $^{54}Mn$, and $^{60}Co$) in the HTGR primary system, which has not yet been fully used.

## 1.2 FISSION PRODUCT SORPTION AND DESORPTION FROM PRIMARY CIRCUIT MATERIALS

### 1.2.1 Iodine Sorption and Desorption from Alloy T-22 — M. F. Osborne and R. B. Briggs*

The objectives of this experimental task are (1) to determine the amount of iodine that may be deposited on metal surfaces in the coolant circuit under normal operating conditions and (2) to establish rates of iodine desorption from these surfaces under conditions that may be related to accident situations. Such data are needed to evaluate the potential radiological hazards associated with the equilibrium plateout of fission product iodine in the coolant circuit.[9]

The materials of primary interest are the alloys T-22 (2-1/4 Cr-1 Mo steel) and Alloy 800 (21 Cr-32 Ni-45 Fe), which comprise a large fraction of the coolant circuit. The 200-1000°C range of test temperatures spans the range of metal temperatures that corresponds to normal operating conditions and extends partly into temperatures that may be experienced under accident conditions. All tests are limited to helium pressures of about 1 atm. Because the partial pressure of iodine expected to exist in the reactor ($\lesssim 10^{-12}$ atm) are difficult to attain experimentally, these tests are being conducted in the range $P_I = 10^{-12}$ to $10^{-8}$ atm. The effects of low-level impurities, such as $H_2$, $O_2$, CO, $CO_2$, and $H_2O$, that influence the conditions of the metal surfaces will be investigated; the concrete degradation gases, largely $CO_2$ and $H_2O$, are of particular interest. Most of the earlier investigations of iodine sorption on metal oxides and graphite in vacuum[10,11] and on various metal surfaces in helium[12-14] were conducted at higher partial pressures of iodine, some under poorly defined atmospheric conditions that would result in unknown surface characteristics.

The transpiration, or flow, method is being used in these tests; the main components of the apparatus are shown in Fig. 1.1. The metal adsorber specimens are composed of a series of thin plates mounted in rectangular holders in a quartz furnace tube. A helium stream is passed

---

*Consultant.

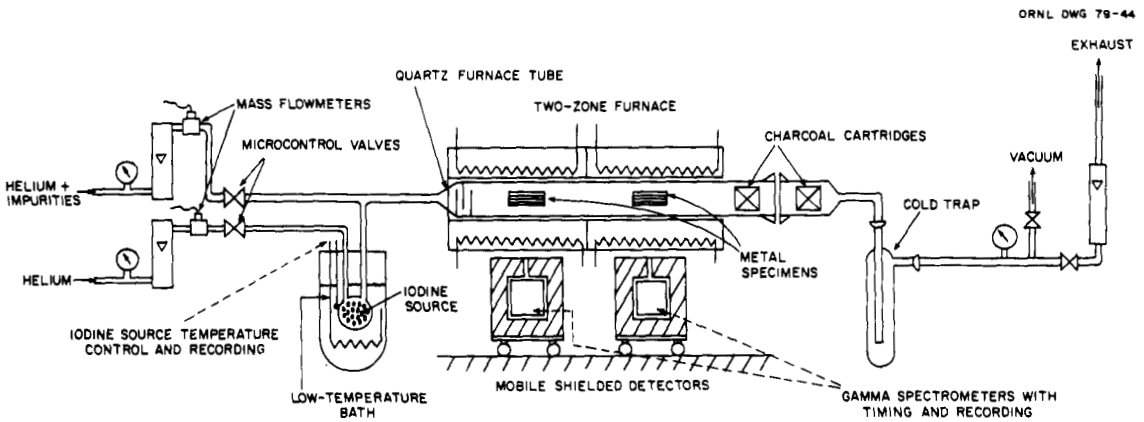


Fig. 1.1. Experimental Apparatus for Iodine Adsorption/Desorption Studies.

over a $^{131}I$-traced $I_2$ source that is maintained at low temperature (typically -75 to 90°C) to provide the desired $P_I$. This stream may be diluted with a parallel helium stream and subsequently passed over the adsorption specimens. The amount and distribution of iodine on the adsorbers is monitored by mobile NaI detectors. Desorption is investigated in situ by stopping the flow of $I_2$, followed by a change in test conditions such as temperature increase or sweep gas variation.

Two experiments have been conducted, in which the experimental procedures were developed and some useful data were obtained. Concentration profiles of iodine deposited on T-22 specimens at 400 and 200°C at about 1-d intervals are shown in Fig. 1.2. The maximum concentration corresponds to about $3.3 \times 10^{16}$ atoms I/cm$^2$ (7.0 μg I/cm$^2$). This loading could not be related to a specific partial pressure of iodine because a brief loss of control at the start of the test allowed a relatively large, unmeasured quantity of iodine to escape from the source. As indicated, the leading edge of the specimen reached an equilibrium loading relatively quickly, and deposition on the downstream part of the specimen increased with time. Very little $^{131}I$ reached the second, lower temperature specimen until the third day. After about 10 d, the iodine concentration on the second specimen approached that on the first specimen.

Desorption from the first specimen is illustrated in Fig. 1.3. Reduction of $P_I$ to about $2 \times 10^{-12}$ atm resulted in no desorption, but a

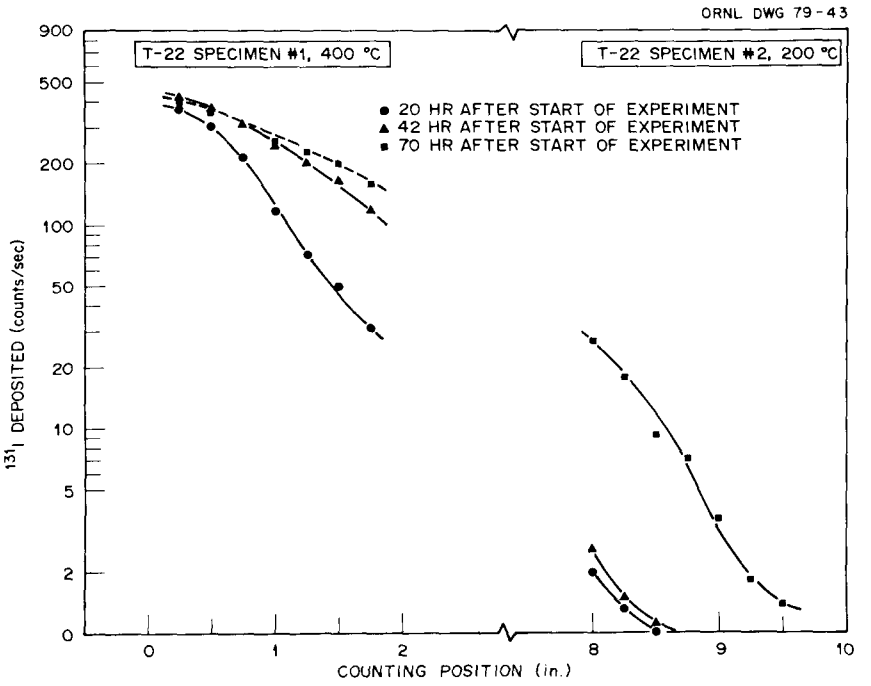


Fig. 1.2. Iodine Deposition Profiles on T-22 Adsorption Specimens.

temperature increase of 600°C caused a desorption rate of about $3.2 \times 10^{-6}$ $s^{-1}$. A subsequent increase in helium flow rate resulted in a small increase in the desorption rate, to about $4.2 \times 10^{-6}$ $s^{-1}$. This desorption behavior is much slower than would be expected for iodine (or $FeI_2$) deposited on a clean steel surface. Although the helium had been passed through a hot zirconium trap, which should remove essentially all impurities, the formation of an oxide film concurrent with the iodine sorption was suspected. (Posttest examination verified the existence of an oxide film.) Thus the stream of purified helium was replaced by a mixture of He + 1.12% $H_2$ at the same flow rate and temperature; as a result, the desorption rate increased quickly to about $1.4 \times 10^{-5}$ $s^{-1}$. This behavior implies that the desorption of iodine deposited on the T-22 surface was stimulated by a chemical reaction such as

$$H_2 + I_2 \rightarrow 2HI$$

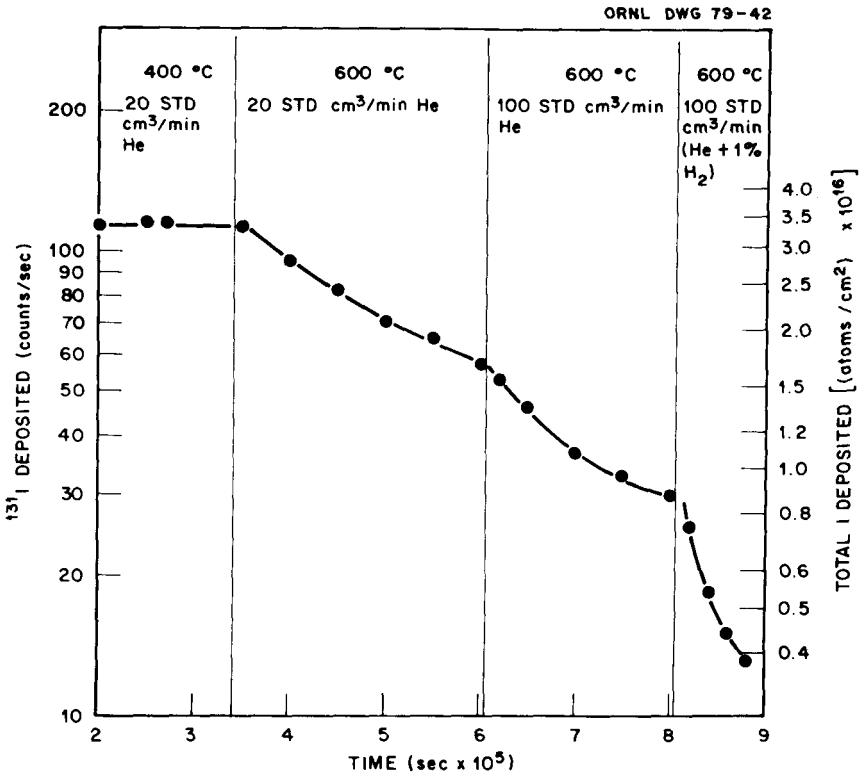


Fig. 1.3. Desorption of Iodine from T-22 under Different Test Conditions.

or

$$Fe_3O_4 + 4H_2 \rightarrow 3Fe + 4H_2O \ .$$

In addition to the experimental studies, methods are being investigated for calculating the rate of iodine deposition from the gas stream onto the specimen and the distribution along the length of the specimen. Preliminary calculations give high values for the coefficient for transfer of iodine from the gas to the surface. If the rate of deposition is controlled by the low resistance to transfer through the gas, one would expect an adsorption front with a steep gradient in iodine concentration to progress along an initially clean specimen. This picture is not entirely consistent with our first observations, but additional calibration of the counting apparatus and calculations are required to compart better the observed with the anticipated adsorption behavior.

### 1.2.2 Iodine Sorption and Desorption from Core Graphite — F. F. Dyer and S. K. Whatley

The objective of this task is to develop knowledge that will aid in understanding the uptake and release of iodine on H-451 graphite under normal operation and depressurization conditions in an HTGR. Although several investigators[11,15,16] have studied the sorption of iodine on graphite and its subsequent desorption, many gaps in knowledge of the subject still exist. In a study of the sorption of iodine on several reactor materials, Osborne, Compere, and de Nordwall[11] found that the loading capacity of graphite (atoms of iodine sorbed per unit surface area) is about 100 times less than that of oxidized steel surfaces. Simple analysis shows that, because the specific surface area of the internal porous structure of H-451 is about 5 $m^2/g$ (ref. 17) and the mass of graphite to be used in a large HTGR would be about $10^9$ g, the resulting surface area of the graphite would be about $10^5$ times larger than the area of the metal surfaces in the primary system. It therefore seems clear that this large surface area is potentially one of the largest sinks for iodine that is released from the fuel. The extent to which the absorbed iodine would be released in a depressurization accident cannot currently be adequately estimated.

Experiments are in progress in which the absorption of iodine on H-451 graphite under a broad range of temperatures, iodine partial pressures, and helium pressure conditions will be studied. Initial experiments will consist of the determination of iodine absorption isotherms in helium with pressures of helium of about 1 atm. An apparatus in which these studies will be made is shown in Fig. 1.4. The apparatus consists of a quartz furnace tube with an inner removable quartz sample holder in which the graphite sample will be placed. The tube is heated with a well-insulated furnace, whose temperature can be preset and accurately controlled. High-purity helium is allowed to flow into and around the graphite sample from both a direct path indicated by flow element 1 (FE-1) and an indirect path indicated by FE-2. Additional purification of the helium is provided by routing the flow through a heated tube containing zirconium chips as shown in Fig. 1.4 near the

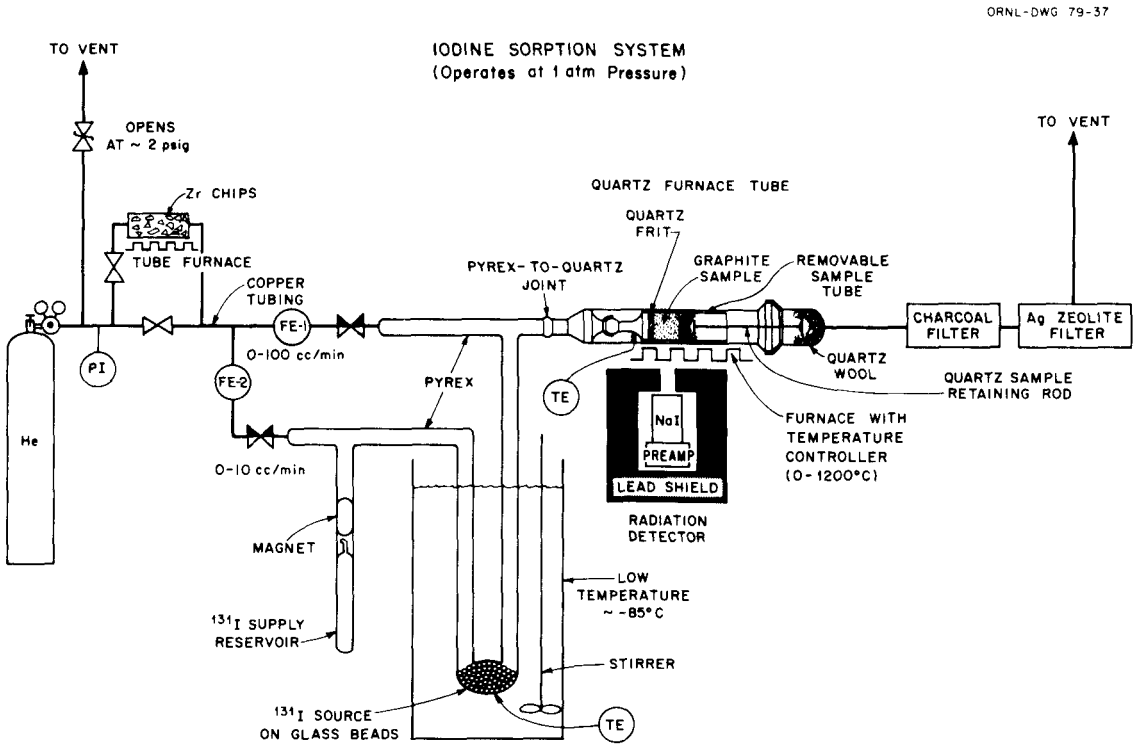


Fig. 1.4. Apparatus for Absorption and Desorption of Iodine on Core Graphite.

helium tank. The indirect flow of helium is passed through a bed of glass beads onto which high-purity elemental iodine containing $^{131}$I tracer has been deposited at low temperature. Prior to deposition on the beads, the iodine is contained in a supply reservoir provided with a break seal that can be opened with a magnet. By controlling the temperature of the low-temperature bath in which the iodine source is immersed and the relative flow rates of helium through the two paths, the partial pressure of iodine to which the graphite is exposed can be accurately regulated. Charcoal and silver zeolite filters are provided downstream of the furnace tube to capture iodine not sorbed on the graphite. The quantity of iodine deposited on the graphite will be monitored by a shielded NaI gamma-ray detector as shown in Fig. 1.4.

In addition to the studies outlined above, experiments are planned in which iodine will be sorbed on graphite from helium at 10 atm pressure. In these experiments, provision will be made to lower rapidly

the helium pressure to 1 atm and to measure the quantity of iodine released by the depressurization. Using this technique, we expect to gain knowledge that may be extrapolated to the iodine desorption effects of HTGR depressurization accidents.

Preliminary design studies of the 10-atm pressure system, which are currently in progress, indicate that the basic apparatus will be very similar to the 1-atm pressure system, including the added feature of a pressure vessel that will enclose the furnace tube, its furnace, and the iodine supply. The furnace tube will be constructed of quartz, and small pinholes will be provided to equalize the pressure within the tube and regions outside the tube but inside the pressure vessel. Construction of the pressure vessel for this apparatus is expected to be completed in FY 1979.

## 1.3 GRAPHITE STRENGTH LOSS CAUSED BY CORROSION — R. P. Wichner and W. P. Eatherly

The principal objective of this task is to determine experimentally the loss of graphite strength as a function of degree of corrosion, the corrosion profile, the graphite type, and the specimen size. Two graphites are currently included in the test series: H-451, the core graphite, which is an extruded, pure, isotropic graphite, and Stackpole 2020, the selected core post material, which is an isostatically molded anisotropic graphite.

Activities in this task include the following:

1. Precorrosion characterization. Prepared graphite specimens are extensively examined to determine statistically significant baseline information. Density, orientation, compressive and tensile strength versus density, BET surface area, and pore-size distribution are determined.
2. Specimens are corroded under accelerated conditions in a circulating flow apparatus.
3. Postcorrosion characterization. Changes in compressive and tensile strength are determined. The burnoff profile is determined by x-ray profiling. On selected specimens changes in the microstructure, BET area, and pore-size distribution are observed.

Two types of specimens are being fabricated: cylindrical specimens from about 1/2 to 1-in. diam and ring-type specimens of about 1-in. diam and 1/4-in.-square cross section. The cylindrical specimens provide a geometrically simple and direct measure of compressive and tensile strength loss; however, the number of specimens that can be tested is severely limited because of size. The brittle-ring specimens, for which the interpretation of load versus deflection data is less direct, provide a means for testing large numbers of specimens, principally because of their smaller mass.

### 1.3.1 Graphite Corrosion Tests — R. P. Wichner, L. L. Fairchild, and J. D. Kintigh

A schematic of the corrosion apparatus is illustrated in Fig. 1.5. Purified helium from a cylinder, which is humidified in a thermostatically controlled vessel, enters the circulating flow system indicated by the bold line. Operation of the saturator has been tested in the flow rate range of 0 to 50 $cm^3$/min and from 9 to 20°C. Under these conditions, the tests indicate that the helium flow through the saturator is fully equilibrated with the water.

The circulating system consists of 1/2-in. nickel tubing for the low-temperature section and quartz for the section passing through the furnace. Flows of up to 1.6 scfm may be induced by the metal bellows pump. A temperature gradient exists around the circuit because the bellows temperature cannot exceed 200°C, whereas specimen temperatures range from 800 to 1000°C. It has been determined that flow rates in the range of about 1 cfm will cause the specimen, occupying an approximate 1-1/2-ft region in the furnace, to be uniformly corroded in the axial direction.

A flow from the circulating system is drawn to the vent or through a gas chromotograph at a rate equal to the inflow rate. Thus far, the gas analysis system is not functioning properly, and the corroding atmosphere composition may only be estimated.

The corrosion runs that have been completed or are currently in process (February 1979) are listed in Table 1.1.

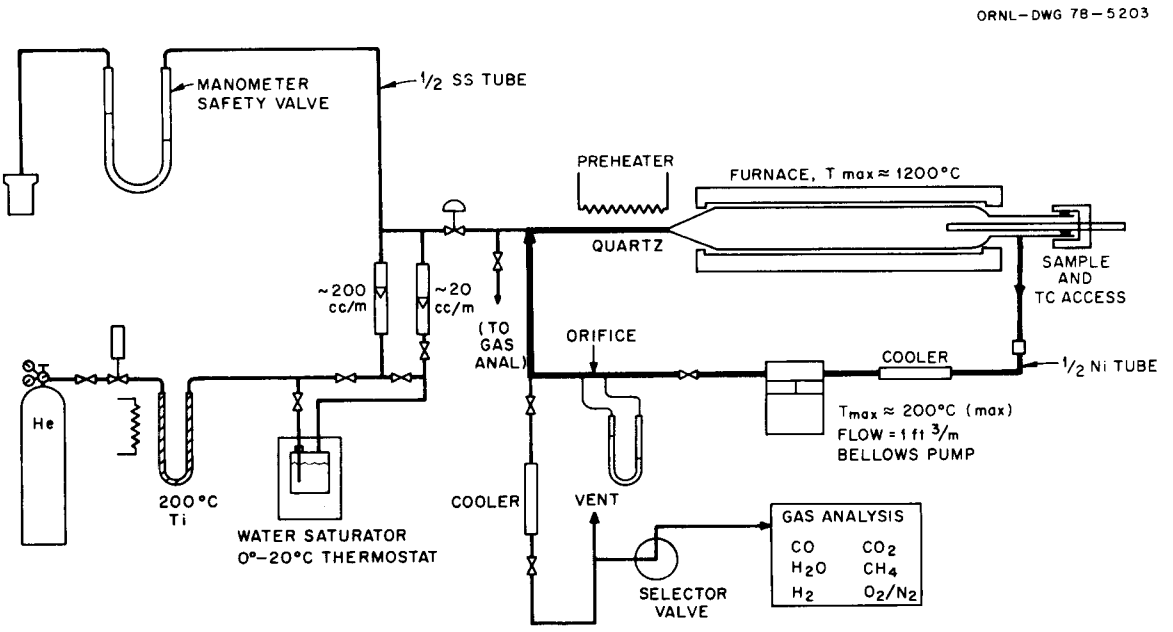


Fig. 1.5. Graphite Oxidation Schematic.

### 1.3.2 Graphite Preparation and Characterization — W. P. Eatherly, C. R. Kennedy, and J. D. Kintigh

The early part of this reporting period was spent on planning the experiment, determining the number and geometry of the samples, and defining the measurements to be made. Three graphites were considered as potential types to be studied: H-451 (fuel elements), 2020 (core support posts), and PGX (floor blocks). The first two graphites are relatively pure, and catalyzed oxidation is minor or nonexistent. The last, PGX, has high iron concentrations and is dominantly a catalyzed oxidation. We decided to proceed with the first two graphites and defer a decision on the PGX until requirements for future reactor materials are better defined.

Accordingly, two half billets of H-451 were obtained from GA, and five partial billets of 2020 were purchased from Stackpole Graphite in conjunction with GA. The nondestructive evaluation of H-451 graphite is complete, and the graphite is being sampled accordingly. Similar work on the 2020 material has just been initiated.

Table 1.1. Graphite Corrosion Runs, February 1979

| Graphite material | Specimen geometry | Temperature (°C) | Saturator | | Run duration (d) | Burnoff (%) |
|---|---|---|---|---|---|---|
| | | | Flow ($cm^3$/min) | Temperature (°C) | | |
| H-451 | 1/2-in. cylinder | 1000 | 50 | 20 | 7 | 5 |
| H-451 | 1/2-in. cylinder | 1000 | 50 | 20 | 14 | 10 |
| H-451 | 3/4-in. cylinder | 1000 | 50 | 20 | 28 | 10 |
| H-451 | 1/2-in. cylinder | 900 | 50 | 20 | 14 | 6.7 |

The H-451 billets were slabbed into 2-1/2-in.-thick sections for the nondestructive testing. Each slab was gridded into 1-in. squares and mapped accordingly. Eddy current tests (electrical resistivity), x-ray densitometry, and sonic velocities (Young's modulus) mappings were made, and contour maps were constructed. A representative 10-in.-long cylinder of the 2020 graphite was similarly mapped to provide preliminary samples. The density scans on H-451 indicate a generally higher density skin (about 1.75 $g/cm^3$ at the surface), decreasing to about 1.70 $g/cm^3$ about 1 to 2 in. into the interior of the cylindrical billet. Some low-density regions (as low as 1.67 $g/cm^3$) were found on the centerline. Density variations in the molded 2020 were much less: 1.79 $g/cm^3$ average with a standard deviation of 0.007.

Eddy current response paralleled the density measurements, the H-451 indicating a much lower average resistivity.

Sonic velocity measurements proved to be quite informative. For the longitudinal wave, radial velocity was almost constant from center to edge, but the circumferential velocity increased significantly. The same was true for the shear wave, confirming increased preferential orientation toward the surface of the cylinder; but one billet, containing a large open flaw, also indicated regions of upset geometry that was confirmed by radiography. Apparently this billet was held in the die during recharging of the extrusion press chamber, allowing the mix to cool and preventing the complete knitting of the material. This billet will be largely rejected for sampling because it is atypical.

A brief study was performed to establish sample cleaning and storage techniques. Dedusting after machining can be fully accomplished by three 1-min sonic cleaning operations, the first two in acetone and the third in ether. Degassing can be accomplished to "constant" weight by heat-treating to 750°C for 30 min. Degassed samples rapidly picked up water in a saturated environment but showed negligible weight gains when exposed to 70% humidity for up to several days. Samples stored in sealed bottles but exposed about 1 h per day for several weeks showed a negligible water pickup. Hence, storage in sealed containers with normal occasional handling appears sufficient to protect the samples.

Apparatuses to measure a number of properties of direct interest to quantifying the oxidation behavior have been or are being put into operation. These include:

1. Helium density. The apparatus had to be redesigned and recalibrated to accept the sample geometries required. The apparatus is now operable, and helium densities of about 0.2% precision can be obtained.
2. BET surface area. A new apparatus has been constructed to cover the range of 1 to 100 $m^2/g$ for both powder and solid samples of the required geometry. The system uses an MKS Baratron solid-state electronic manometer and is fully automated for both control and data acquisition around a Hewlett Packard 9825A calculator. The system has been assembled and programmed and is undergoing shakedown tests.
3. Mercury porosimetry. The existing apparatus is unsatisfactory because of the poor accuracy of the existing pressure gauges. New precision Heise gauges have been obtained but are not yet installed. However, some preliminary, more qualitative measurements have been made to establish the maximum pressure that H-451 graphite will tolerate before structural damage occurs. For H-451, this is 2000 psia, equivalent to a hydraulic "diameter" of 0.1 μm. That the mercury can be vaporized out of the specimen to a few ppm by heating to 900°C in flowing argon has also been established, which permits the use of porosimetry as a nondestructive measurement.
4. X-ray densitometry. X-ray equipment exists at ORNL for both radiographic and counting techniques to determine the density of graphite. Step wedges of a nominal 0.250-in. thickness but with 0.001- and 0.0005-mil steps have been machined from a highly uniform aerospace graphite; the steps were easily picked up by the counter and were visible on the photographic plate. The counter system is of currently limited availability, however, because of other programs. In the immediate future the radiographic technique seems to be feasible, but proof awaits rebuilding of a precision optical densitometer. Results should be available in March 1979.

5. Flexural and ring strengths. A number of graphites, including H-451, have been sampled and tested to establish Weibull statistical parameters. These parameters are required to establish strengths as a function of sample geometry. The H-451 graphite appears to belong to the class of extruded graphites with a Weibull exponent of seven. As data on the unoxidized samples accumulate, this exponent will become better defined, and comparisons will be made for the oxidized materials.

### 1.3.3 Fractography — D. G. Swanson*

A contract was initiated in June 1978 with the Aerospace Corporation to study crack initiation and propagation for oxidized graphite. This study required modification of their equipment to handle brittle-ring specimens and to measure deflection as well as load. At this time both unoxidized H-451 and 2020 graphites have been examined. In both cases fracture is intergranular and through voids. No difficulty has been encountered in following fracture propagation in the relatively coarse-grained H-451. Conversely the 2020 graphites resist fracture initiation but fail completely once fracture initiates, which has been circumvented by employing brittle rings with a trapezoidal cross section. This solution can be used on oxidized materials only if machining is performed after oxidation.

## 1.4 TRITIUM DISTRIBUTION AND INVENTORY IN THE PEACH BOTTOM HTGR — R. P. Wichner and F. F. Dyer

The first phase of a two-phase effort to understand and to describe tritium production and movement in an operating HTGR system has been completed.[18] The principal objective of this first phase of the effort is to report the findings about tritium concentrations in the core components that were acquired in the course of the Peach Bottom Surveillance Program, which dealt with fission product migration in general and subsequently with tritium specifically. Administrative procedures are

---

*Aerospace Corporation, Los Angeles, Calif.

currently in process for the second phase of the work to be performed in the Federal Republic of Germany (FRG) under the auspices of the international umbrella agreement on gas-cooled reactor (GCR) development. In the FRG effort, computer model predictions of tritium transport in the reactor system will be compared with the observed concentration levels.

The types of tritium concentration data in the acquired core components were: (1) radial distribution of tritium in the graphite parts of six fuel elements, (2) axial concentration profiles in five fuel elements, (3) concentration levels in the fuel, (4) concentration profiles in the fission product traps of four fuel elements, and (5) concentration measurements in a graphite reflector element. As reported[8] fuel particle failure fractions, graphite BET surface areas, and lithium impurity level determinations in graphite are needed to assist data interpretation. To augment the data from our measurements, we have summarized pertinent information from the operations reports of the Philadelphia Electric Company (which describe the onsite tritium measurements on the coolant and effluent streams) and from the results of a special tritium survey conducted by GA in 1971.

We have gone beyond the principal objective of describing the concentration level observations in an attempt to obtain a preliminary understanding of the sources and ultimate fate of tritium born in the Peach Bottom core. We estimate that the approximately 2200 Ci born during core-2 operation resulted from: ternary fission, 55%; neutron reactions with lithium impurity in the graphite, 3.3%; neutron reactions with $^{3}He$ in the coolant, 1.9%; and $^{10}B$, 40% (an unexpectedly large share), primarily in the control rods and, to a lesser extent, in the burnable poison elements.

Concentration profile data indicate that the tritium caused by $^{10}B$ in the poisoned fuel elements remained in place; we therefore feel (with no direct evidence) that tritium born in the control rods was also immobile. However, tritium from the other sources migrated to a significant degree. About 60% of the tritium resulting from fission migrated from the fuel to deposit in nearby graphite or to pass with the fuel element purge flow to the fission product trapping system. Although

there is insufficient data to fix firmly the fate of the tritium carried with the purge flow, the major portion (∿90%) probably passed freely through the trapping system to rejoin the primary coolant.

Our estimate for the amount of tritium that permeated through the steam generator tubing (1.1 Ci) is about a factor of 4 less than a previous estimate by GA. Discharges via the liquid-waste and off-gas systems were estimated from concentrations given in the operations reports. It is slightly surprising that tritium discharge as solid waste (tritiated water adsorbed on clay) exceeded liquid and gaseous discharges. The amount of tritium in the solid wastes was determined from the estimated transport to the chemical purification system via the steam generator purge flow. Leakage estimates through the containment vessel were found to be insignificant compared with gaseous discharge through the stack.

In general, a fairly good tritium mass balance was achieved. Of the portion of the tritium believed to have been mobile (1325 Ci), about 83% is accounted for as measured inventory in core components and estimated discharge flows. The remainder probably resided as unmeasured inventory in unsampled reactor components, principally in the permanent radial reflector and ex-core fission product traps.

## 1.5 FISSION PRODUCT TRANSPORT IN GRAPHITE

### 1.5.1 Diffusion of Cesium in Graphite — W. Davis, Jr.

Prior to his death in January 1977, R. B. Evans, III, was writing a report on studies performed on the transport of cesium through several types of graphites. The experiments involved placing $^{137}Cs$-traced $CsNO_3$ solution on a flat end of a graphite cylinder, typically 1/2 in. long by 1/2 in. diam, butting this treated end against the end of a second cylinder of the same dimensions, placing this pair of cylinders in a tightly fitting quartz tube in a furnace, and rapidly heating the system to a specified temperature. After heating to this temperature, the system was rapidly cooled. Subsequently, the two cylinders were analyzed for $^{137}Cs$ activity remaining on the initially contacting surfaces. The degree of penetration of cesium was determined by

successively removing small (∿0.01-mm) layers of graphite and counting the remaining $^{137}Cs$ activity.

Evans and Sutton presented a few of the early cesium transport data and the development of a theoretical treatment.[19] Their treatment involved the coupling of diffusional transport and the trapping of part of the cesium by an irreversible first-order chemical reaction with graphite. The differential equation describing this model was integrated and shown to be compatible with experimental data for Hawker-Siddeley graphite at 800°C and for Great Lakes graphite H-327 at 609°C.

A large number of cesium-transport experiments performed during 1975 and 1976 were to be included in the report Evans was writing. Much data from these experiments are in notebooks and have not been analyzed. We are now recovering these data and typing them on computer cards for use in testing mathematical models of cesium transport and for making the data available to others. To date we have recovered the following: (1) seven experiments involving cesium transport in ATJ graphite at temperatures of 500 to 830°C; (2) nine experiments with H-327 graphite at 500 to 720°C; and (3) two experiments with H-451 graphite at 638°C. At least another dozen experiments are yet to be documented, including some with Hawker-Siddeley graphite and some with sleeve graphite such as that used in the Peach Bottom Reactor.

While recovering the experimental data, we have written computer programs to plot and to analyze the data according to Evans's model. The few plots drawn and the few data analyzed suggest that Evans's model may be too simplistic to be compatible with all of this experimental data.

### 1.5.2 Diffusion of Silver in Core Graphite — R. Causey*

This task will determine silver diffusion rates in core graphite and will attempt to interpret the observed rates in terms of a physical model. Data taken in the course of the Peach Bottom Surveillance work has indicated that silver has the highest mobility in graphite of all the fission products. This fact together with the higher yields that

---

*Consultant, Texas A. & M. Research Foundation, College Station, Tex.

go with medium-enriched uranium (MEU) fuel and the near optimal half-life of $^{110m}Ag$ (from the standpoint of radiation hazard) makes silver and cesium the two most critical fission products in the estimation of hazards associated with equipment maintenance. This experiment is currently in the early stages of design and equipment procurement.

### 1.5.3 Diffusion of Plutonium, Uranium, and Thorium in Graphite — R. P. Wichner

Measurements are currently in process in the Radiochemistry Group of the Analytical Chemistry Division for determining concentration levels of plutonium, uranium, and thorium in samples of core graphite acquired in the course of the Peach Bottom Surveillance Program. The graphite specimens were selected from the radially sectioned portions of the graphite sleeve and spine of the fuel element. Successful concentration determinations would allow formulation of radial concentration profiles and estimation of diffusion coefficients for these heavy metals in graphite. The principal motivation for these measurements is the estimation of plutonium leakage rates from MEU to the coolant.

## 1.6 REFERENCES


1. F. F. Dyer, R. P. Wichner, W. J. Martin, L. L. Fairchild, R. J. Kedl, and H. J. de Nordwall, *Postirradiation Examination of Peach Bottom HTGR Fuel Element E06-01,* ORNL-5126 (March 1976).
2. R. P. Wichner, F. F. Dyer, W. J. Martin, and L. C. Bate, *Distribution of Fission Products in Peach Bottom HTGR Fuel Element E11-07,* ORNL-5214 (April 1977).
3. R. P. Wichner, F. F. Dyer, and W. J. Martin, *Distribution of Fission Products in Peach Bottom HTGR Fuel Element E14-01,* ORNL/TM-5730 (August 1977).
4. F. F. Dyer, R. P. Wichner, W. J. Martin, and L. L. Fairchild, *Distribution of Fission Products in Peach Bottom HTGR Fuel Element F03-01,* ORNL/TM-5996 (June 1978).

5. R. P. Wichner, F. F. Dyer, W. J. Martin, and L. L. Fairchild, *Distribution of Fission Products in Peach Bottom HTGR Fuel Element E01-01*, ORNL/TM-6353 (August 1978).

6. R. P. Wichner, F. F. Dyer, W. J. Martin, and L. L. Fairchild, *Distribution of Fission Products in Peach Bottom HTGR Fuel Element F05-05*, ORNL/TM-6455, to be published.

7. F. F. Dyer et al., *Distribution of Radionuclides in the Peach Bottom HTGR Primary Circuit During Core 2 Operation*, ORNL-5188 (March 1977).

8. R. P. Wichner and J. L. Botts, "Fuel Particle Failure Fractions in Peach Bottom HTGR Fuel Elements," *Trans. Am. Nucl. Soc.* 28: 689-91 (1978).

9. General Atomic Company, *HTGR Accident Initiation and Progression Analysis Status Report*, vol. 1, GA-A13617, UC-77, San Diego, Calif. (January 1976).

10. E. Hoinkis, "Surface Interactions of Iodine with $Fe_3O_4$," *Vacuum* 22(11): 525-30 (1972).

11. M. F. Osborne, E. L. Compere, and H. J. de Nordwall, *Studies of Iodine Adsorption and Desorption on HTGR Coolant Circuit Materials*, ORNL/TM-5094 (April 1976).

12. F. H. Neill, D. L. Gray, and T. S. Kress, *Iodine Transport and Deposition in a High Temperature Helium Loop*, ORNL/TM-1386 (1966).

13. C. E. Milstead, W. E. Bell, and J. H. Norman, "Deposition of Iodine on Low Chromium-Alloy Steel," *Nucl. Appl. Technol.* 7: 361-66 (1968).

14. F. H. Neill, *Adsorption and Desorption of Iodine on Mild Steel*, ORNL/TM-2763 (1970).

15. F. J. Salzano, "The Behavior of Iodine in Graphite," *Carbon* 2: 73-84 (1964).

16. K. Iwanoto and J. Oishi, "The Behavior of Iodine in Adsorption and Desorption by Graphite," *J. Nucl. Sci. Technol.* 5(9): 437-46 (1968).

17. F. F. Dyer, personal communication to W. P. Eatherly, January 17, 1979.

18. R. P. Wichner and F. F. Dyer, *Distribution and Transport of Tritium in the Peach Bottom HTGR*, ORNL-5497 (June 1979).

19. R. B. Evans, III, and A. L. Sutton, Jr., "Transport of Strongly Adsorbed Species in Porous Media," pp. 154-81 in *HTGR Base-Technology Program Prog. Rep. Jan. 1, 1974–June 30, 1975*, ORNL-5108 (1975).

# 2. FUELED GRAPHITE DEVELOPMENT

F. J. Homan

## 2.1 INTRODUCTION

In the introduction to the Fueled Graphite Development chapter in last year's annual report,[1] the period of time covered was described as a transition period. The main transition was from a fuel cycle based on highly enriched uranium (HEU) to lower enrichments. But the transition also included dovetailing of the fresh-fuel and recycle-fuel development efforts and of the General Atomic Company (GA) and ORNL fuel development programs. During the current reporting period, work was continued according to the trends detailed in the introduction to the fuels chapter in last year's annual. The first two irradiation capsules, containing medium-enriched uranium (MEU) fuel, were built and irradiated. New emphasis was given to examination of driver fuel from previous High Flux Isotope Reactor (HFIR) target (HT) capsules because this fuel contained low-enriched uranium (LEU) kernels. Emphasis has continued on development of sophisticated procedures for postirradiation examination (PIE), analysis, and assessment of fuel performance. The irradiated microsphere gamma analyzer (IMGA) system was used extensively during the reporting period, and a new postirradiation gas analyzer (PGA) system was developed. We describe the work on both of these systems in this chapter.

Work on coating development and MEU fuel fabrication yielded important results this year. Extensive studies on pyrocarbon (PyC) permeability resulted in characterization techniques that can be used with confidence. The major conclusion from the permeability studies is that, although impermeable PyC coatings can be produced, the range of acceptable coating properties that must be achieved is quite small and will be difficult to achieve economically on a production scale.

The transition mentioned last year has continued. A new direction was identified for the HTGR Program, away from the steam-cycle HTGR toward advanced applications, in particular toward the direct-cycle HTGR. This new direction will place even more severe requirements on the fuel.

Operating temperatures will ultimately be higher than for the steam-cycle HTGR, and the requirements for low-failure fraction will be even more severe than before. The ability to measure accurately the failure fraction for large quantities of coated particles under irradiation will be absolutely essential for fuel qualification. The switch in emphasis from steam cycle to direct cycle brings the U.S. fuel development program into better alignment with the German program, which has consistently emphasized advanced concepts. Work under the U.S.-Federal Republic of Germany (FRG) umbrella agreement progressed well during this past year, and the size and scope of this cooperative effort are expected to grow in 1979.

## 2.2 IRRADIATION EXPERIMENTS — F. J. Homan

Irradiation testing during this reporting period has been confined to the HFIR. Only two capsules were irradiated (HRB-14 and HRB-15b). Postirradiation examination continued on fuel from a number of other capsules, including some that were irradiated several years ago. Additional PIE was conducted on fuel from these old capsules because of the interest in using new PIE procedures to supplement the data gathered from previous examinations and because of the recent emphasis on fuels of lower enrichment.

The most recent HT capsule was HT-34. Postirradiation examination of this capsule was completed during the reporting period. No additional HT capsules are planned in the immediate future. The most recent HFIR removable beryllium (HRB) capsule was HRB-15b. This capsule was still in the reactor at the end of the reporting period but was removed from the reactor in early January 1979. The next HRB capsule (HRB-15a) is scheduled to begin irradiation in the second or third quarter of FY 1980. The most recent Oak Ridge Reactor (ORR) capsule was OF-2; a final report on that experiment was completed during the reporting period. A final report was also issued during the reporting period on the Peach Bottom Reactor recycle test elements. A small amount of quality assurance work was done during this year on the Fort St. Vrain Reactor (FSVR) test elements. These elements are waiting at the FSVR site for insertion with the first reload of that reactor.

### 2.2.1 HFIR Target Capsules — F. J. Homan

Postirradiation examination was completed during the past year on the HT-34 capsule. Final reports were completed on capsule experiments HT-17 through -19, HT-31, HT-33, and HT-32, which will be published in 1979. Reports completed during the last reporting period, for which abstracts were included in last year's annual (HT-20 through -23 and HT-28 through -30) were published this year. Reporting is now up to date on all HT capsules. Postirradiation examination results for capsules HT-31 through -34 are included here.

#### 2.2.1.1 Capsules HT-17 Through -19 — E. L. Long, Jr.

The results of the PIE of capsules HT-17 through -19 have been discussed previously.[2,3] A final topical report[4] on this experiment was completed during this reporting period, the abstract of which follows:

> A series of Biso-coated fertile particles was irradiated in the target facility of the HFIR. The primary objectives of this experiment were to relate the fast-neutron stability of dense propylene-derived PyCs to preferred orientation and to relate irradiation performance to preirradiation characterization values. Coating characterization included x-ray Bacon anisotropy factor (BAF), optical anisotropy, gaseous permeability, small-angle x-ray scattering, and thickness and density determinations. Other objectives were to test Biso-coated large-diameter $ThO_2$ kernels and coatings derived from propylene diluted with $CO_2$ rather than argon.
>
> Visual examination of the irradiated particles showed that the majority had failed as a result of fast-neutron damage. Some correlation could be made of particle failures with preirradiation optical anisotropy values, but the most consistent correlation was with small-angle x-ray scattering data. The performance of the coating prepared from $CO_2$-diluted propylene was outstanding; no failures were observed after the HTGR-design fast fluence was exceeded by 75% at a maximum particle surface temperature of 1575°C.

#### 2.2.1.2 Capsule HT-31 — T. N. Tiegs

A final report[5] was completed during this reporting period, which documented the results from HFIR capsule HT-31. The abstract of the report follows:

Irradiation capsule HT-31 was a cooperative effort between GA, Los Alamos Scientific Laboratory (LASL), and ORNL. This report describes the ORNL portion of the experiment only.

The capsule was irradiated in the HFIR at ORNL to peak particle temperatures up to 1600°C, fast neutron fluences ($E$ >0.18 MeV) up to $9 \times 10^{25}$ neutrons/m$^2$, and burnups up to 8.9% FIMA for $ThO_2$ particles.

The oxygen release from plutonium fissions was less than calculated, possibly because of the solid solution of SrO and rare earth oxides in $UO_2$.

Tentative results show that pyrocarbon permeability decreases with increasing fast neutron fluence.

Fission products in sol-gel $UO_2$ particles containing natural uranium behaved similarly to those in particles containing HEU. Thus, much of the data base collected on HEU fuel can be applied to low-enriched fuel. Fission product palladium penetrated into the silicon carbide (SiC) on Triso-coated particles. The SiC coating also provided some retention of $^{110m}$Ag.

The SiC coatings on Triso-coated particles irradiated above about 1200°C without an outer PyC coating were degraded.

### 2.2.1.3 Capsule HT-32 — E. L. Long, Jr.

The design, objectives, operating history, and postirradiation results of capsule HT-32 have been reported.[6,7] Additional PIEs have been performed during this reporting period.

Visual examination of the fuel rods from the high- and low-temperature magazines showed that they were in good condition, as shown in Fig. 2.1. Fuel rods from the low-temperature magazine were electrolytically deconsolidated to recover the fuel particles for metallography, electron microprobe analysis, and gamma spectrometry.

The metallographic results for the particles from the fuel rods were identical to the loose particles from the low-temperature magazine. The particles with HOBEG coatings had dense, anisotropic buffer coatings, which resulted in radial cracks through coating layers. Typical failed and intact particles from rod 42 that had been heat treated at 1500°C are shown in Fig. 2.2; the time-averaged surface and centerline temperatures of this rod were 1155 and 1190°C, respectively. Failed and intact particles from rod 40 that had been heat treated at 1800°C are shown in Fig. 2.3. The time-averaged surface and centerline temperatures of this rod were 1115 and 1150°C, respectively, and the fast-fluence exposure

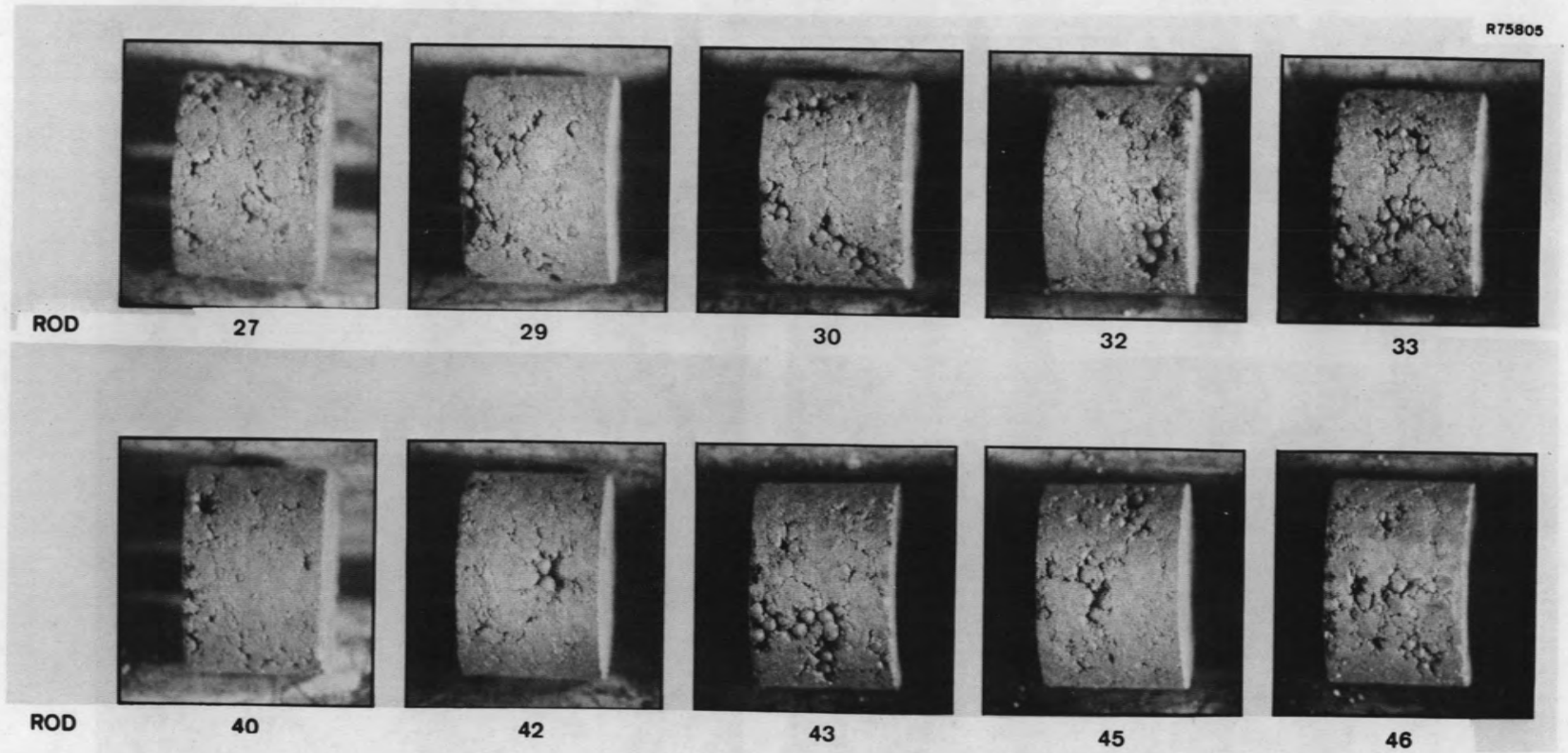


Fig. 2.1. Appearance of Fuel Rods in (*a*) High- and (*b*) Low-Temperature Magazines of Capsule HT-32 (3.5 ×).

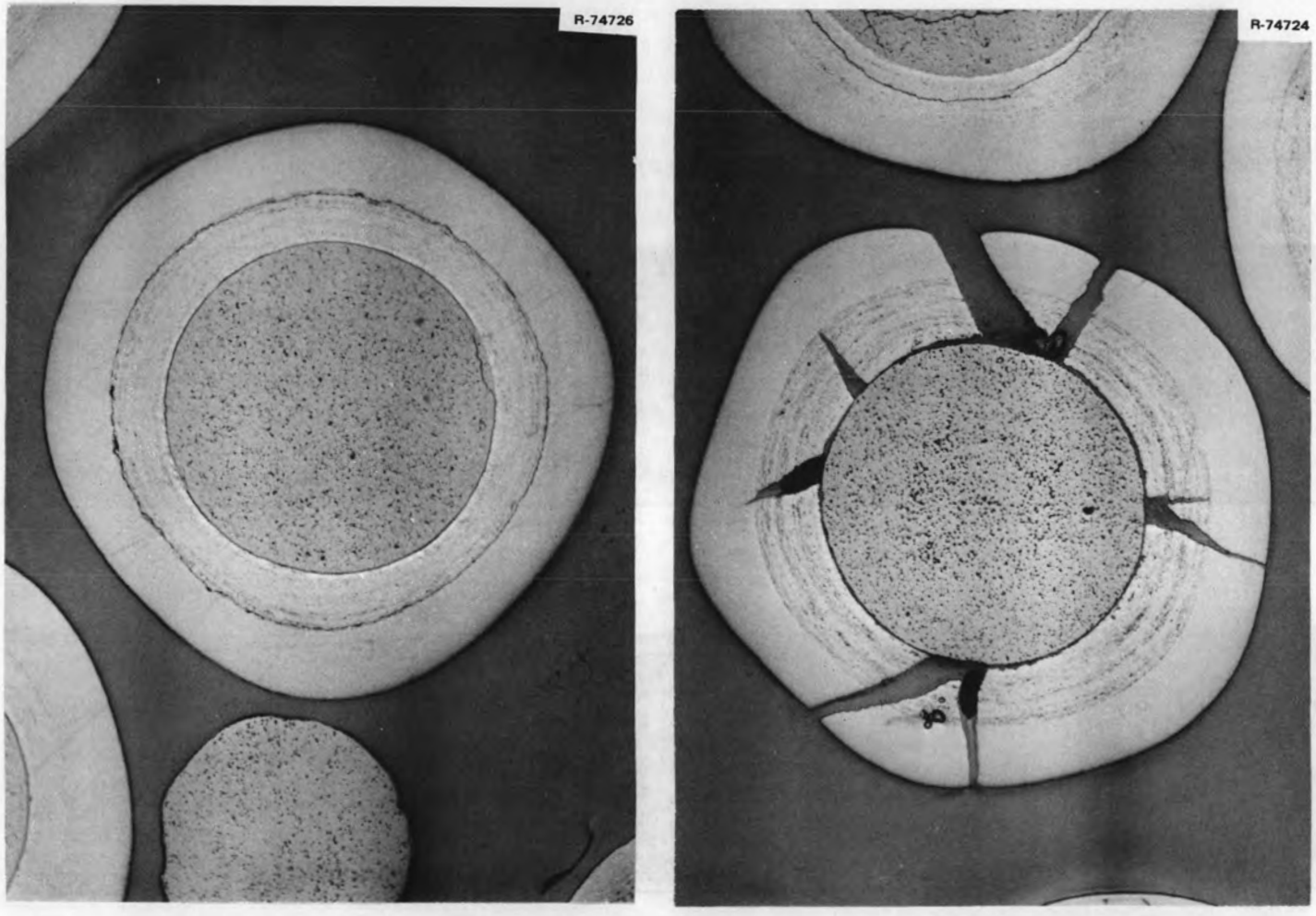


Fig. 2.2. Failed and Intact Particles from Fuel Rod 42, Coated by HOBEG, Heat Treated at 1500°C. The time-averaged surface and centerline temperatures of this rod were 1155 and 1190°C, respectively; the fast-fluence ($E$ >0.18 MeV) exposure was $7.3 \times 10^{25}$ neutrons/m$^2$ (125 ×).

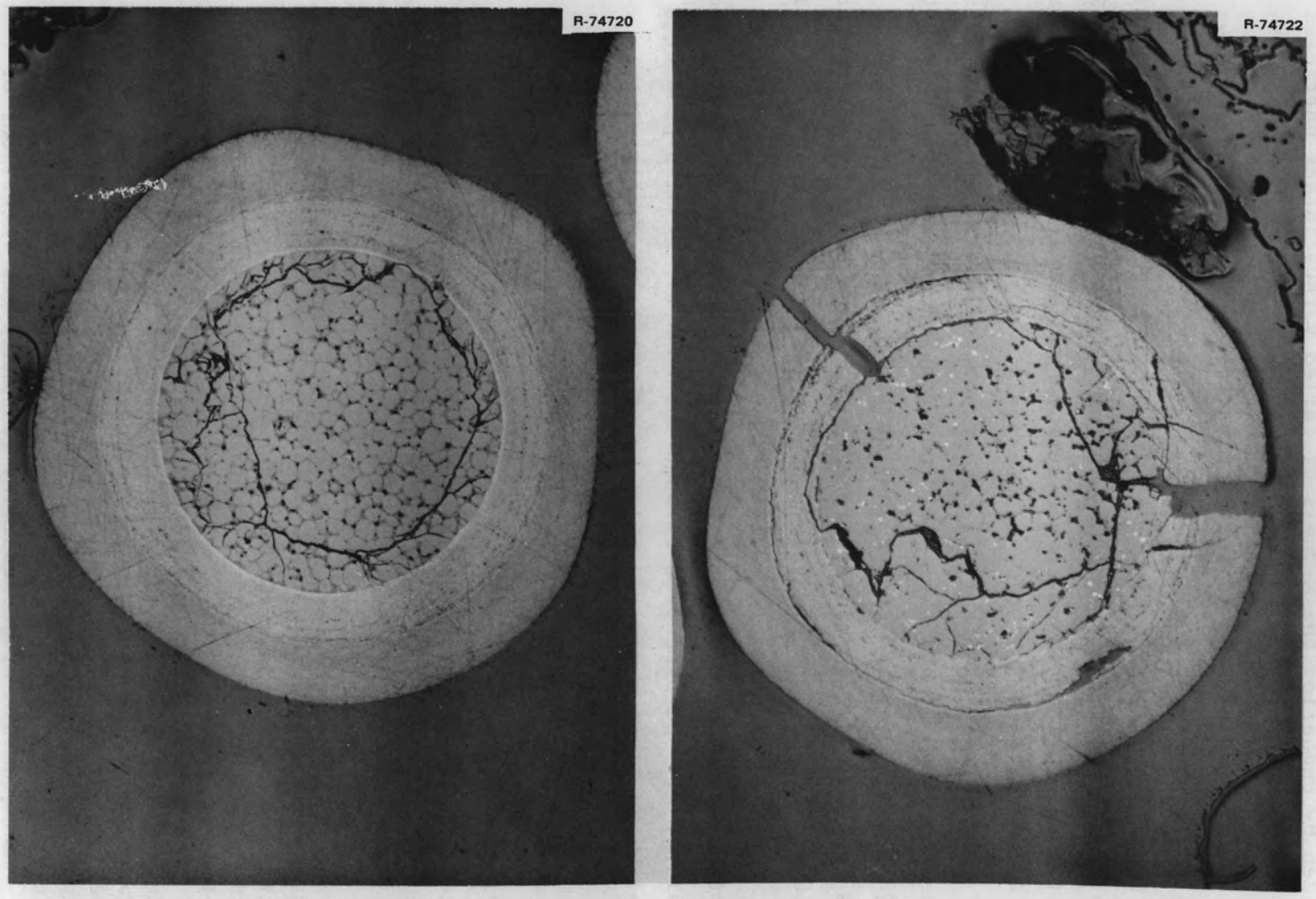


Fig. 2.3. Failed and Intact Particles from Fuel Rod 40, Coated by HOBEG, Heat Treated at 1800°C. The time-averaged surface and centerline temperatures of this rod were 1115 and 1150°C, respectively; fast-fluence ($E$ >0.18 MeV) exposure was $7.7 \times 10^{25}$ neutrons/m$^2$ (125 ×).

level was $7.7 \times 10^{25}$ neutrons/$m^2$. Apparently the bulk of the Si-Al oxide phase escaped from the kernel when coating failure occurred, as can be seen by comparing the kernels of failed versus intact particles in Fig. 2.3.

No failures were noted in the examination of particles with ORNL coatings incorporated in fuel rods from the low-temperature magazine. Typical particles from rods 43 and 45 are shown in Fig. 2.4. The particles in rod 43 were heat treated at 1800°C prior to irradiation, and those in rod 45 at 1500°C. The time-averaged surface and centerline temperatures for rod 43 were 1155 and 1190°C, respectively; for rod 45, 1140 and 1170°C. The fast-fluence ($E$ >0.18 MeV) exposure levels were $7.1 \times 10^{25}$ neutrons/$m^2$ for rod 43 and $6.6 \times 10^{25}$ neutrons/$m^2$ for rod 45. Examination of the ORNL reference Biso-coated $ThO_2$ particles in rod 46 revealed no failures (Fig. 2.5). The time-averaged surface and centerline temperatures were 1130 and 1160°C, respectively, and the fast-fluence exposure level was $6.3 \times 10^{25}$ neutrons/$m^2$ ($E$ >0.18 MeV).

Particles have been selected for electron microprobe analysis, and the remainder will be processed through the IMGA for fission product inventories. A final report on this experiment is in preparation.

### 2.2.1.4 Capsule HT-33 — T. N. Tiegs

A final report[8] was completed during this reporting period, which documented the results from HFIR capsule HT-33. The abstract of the report follows.

> Irradiation capsule HT-33 was a cooperative effort between GA and ORNL. Tested were $ThO_2$ particles (fabricated by GA), LEU particles, inert carbon particles, and various fuel rod matrices (fabricated at ORNL) under accelerated irradiation conditions in the HFIR. This report covers only the ORNL portion of the experiment.
>
> The visual PIE showed good irradiation behavior for fuel rods having slug-injected matrices (using a pitch binder) and warm molded matrices (using a thermosetting resin binder). Some improvement in rod debonding was observed with fuel rods using Great Lakes Carbon Company (GLCC) H-451 ground-graphite shim particles rather than Speer fluid coke shim particles.
>
> Measurements of permeability (by inert gas intrusion) of the pyrocarbon coatings on the inert kernel showed that the disorder created by the neutron flux did not cause the inert gas permeability to increase.

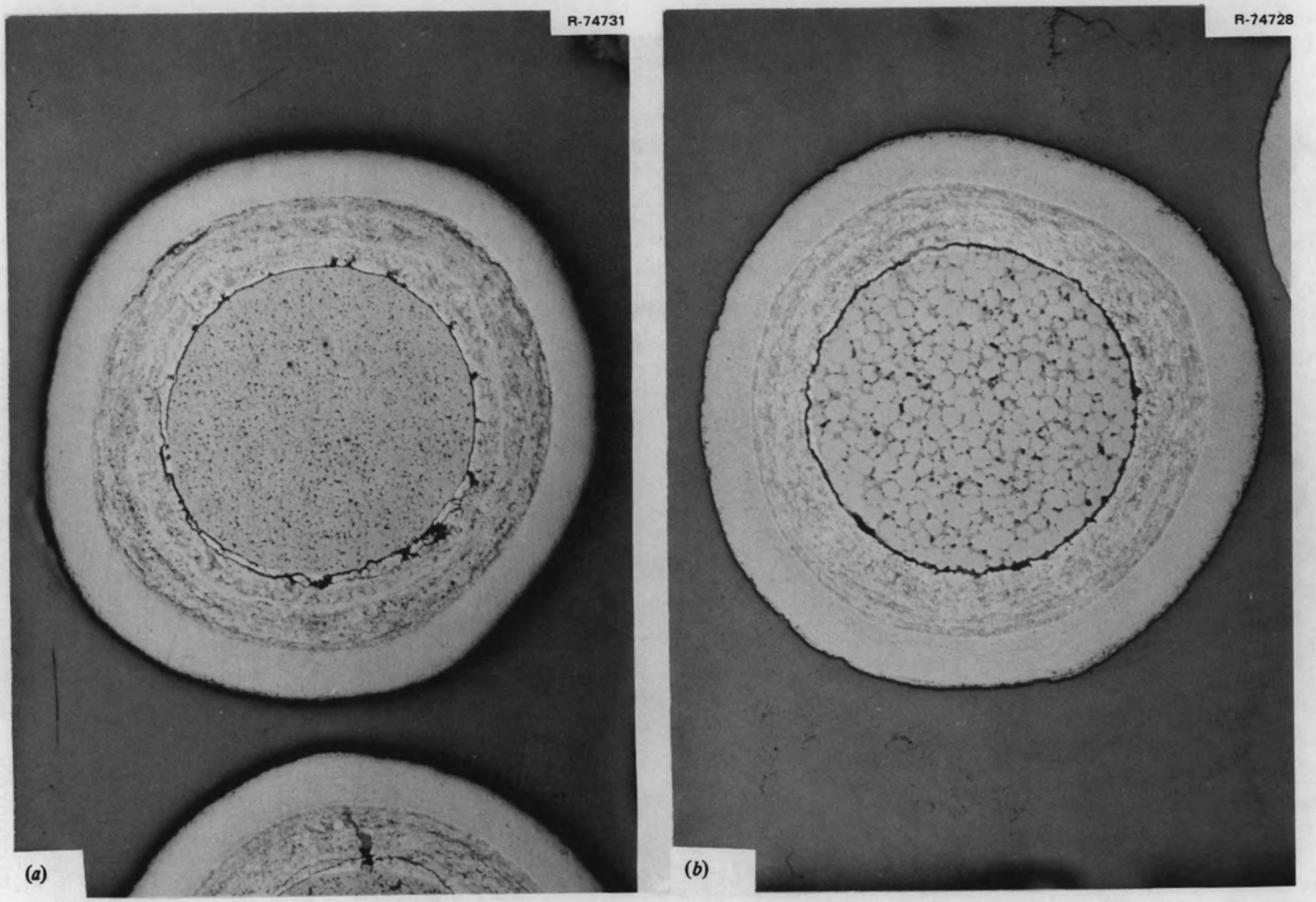


Fig. 2.4. Particles Coated by ORNL and Irradiated in Rods (*a*) 43 and (*b*) 45. Particles in rod 43 heat treated at 1800°C and in rod 45 at 1500°C. Time-averaged rod surface and centerline temperatures for rod 43 were 1155 and 1190°C, respectively; for rod 45, 1140 and 1170°C. Fast-fluence ($E$ >0.18 MeV) for rod 43 was $7.1 \times 10^{25}$ neutrons/m$^2$ and $6.6 \times 10^{25}$ neutrons/m$^2$ for rod 45 (125 ×).

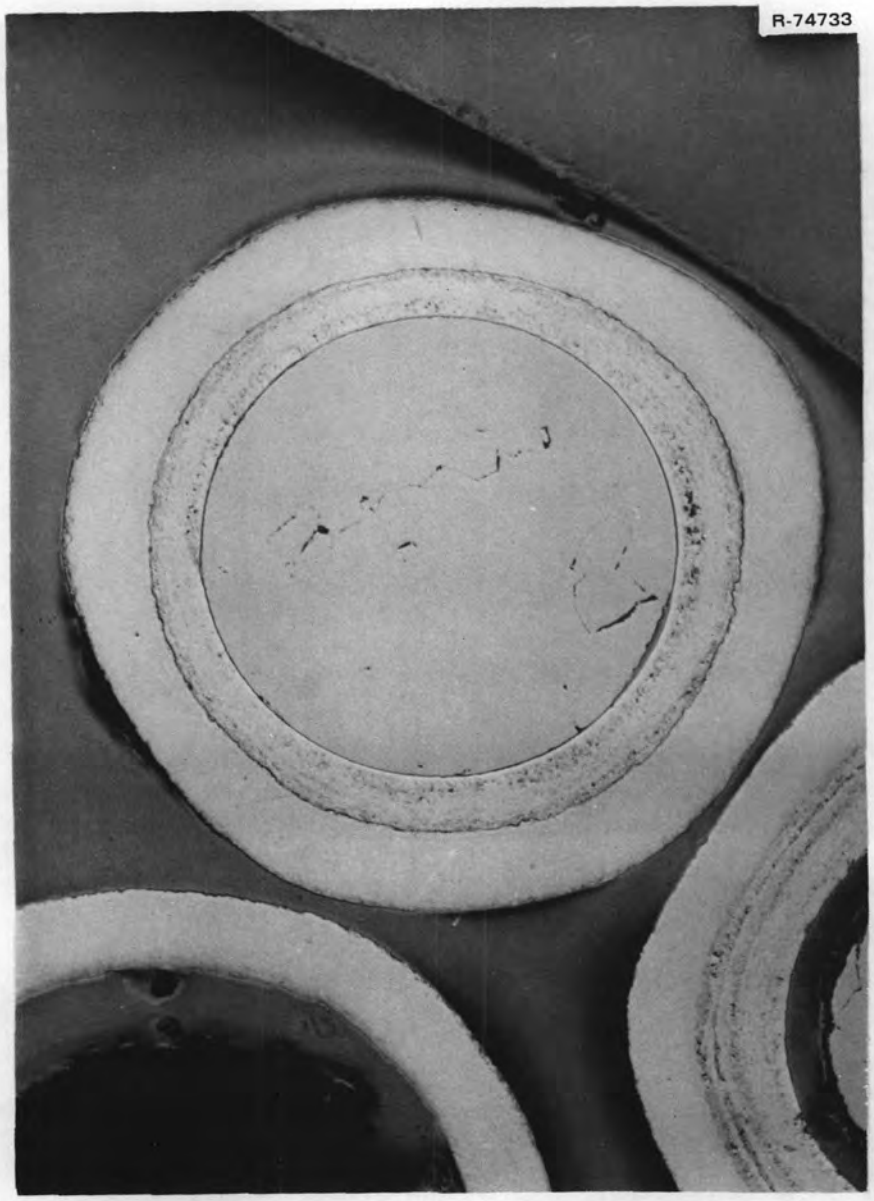


Fig. 2.5. ORNL Reference Biso-Coated $ThO_2$ Particle Irradiated in Rod 46. Time-averaged rod surface and centerline temperatures were 1130 and 1160°C, respectively. Fast-fluence ($E$ >0.18 MeV) was $6.3 \times 10^{25}$ neutrons/$m^2$ (125 ×).

Metallographic examination of Triso-coated particles irradiated with and without an outer PyC coating revealed that the outer PyC coating is necessary to supress SiC degradation at temperatures above about 1375°C.

The fission product behavior, as determined by the electron microprobe, was similar in LEU and HEU particles made from weak-acid resins (WARs). Fission product palladium caused severe SiC corrosion at time-averaged temperatures above 1400°C.

2.2.1.5 Capsule HT-34 — E. L. Long, Jr.

The objectives, capsule design, and operating history of capsule HT-34 were described previously.[9] At that time the capsule had been removed from the reactor, but the PIE had not begun.

2.2.1.5.1 Thermal Analysis — A. M. Howard* and M. J. Kania. Time-temperature relationships for the ORNL specimens irradiated in capsule HT-34 were calculated with the thermal modeling code HTCAP1 (modified version of HTCAP).[10] The ORNL specimens were in the form of loose particles in special holders and bonded fuel rods. Figures 2.6 and 2.7 are representative of the temperatures calculated for each specimen type irradiated in the high-temperature region. Peak irradiation temperatures were near 1500°C, with average-life temperatures near 1350°C.

*Co-op student, Purdue University, Lafayette, Ind.

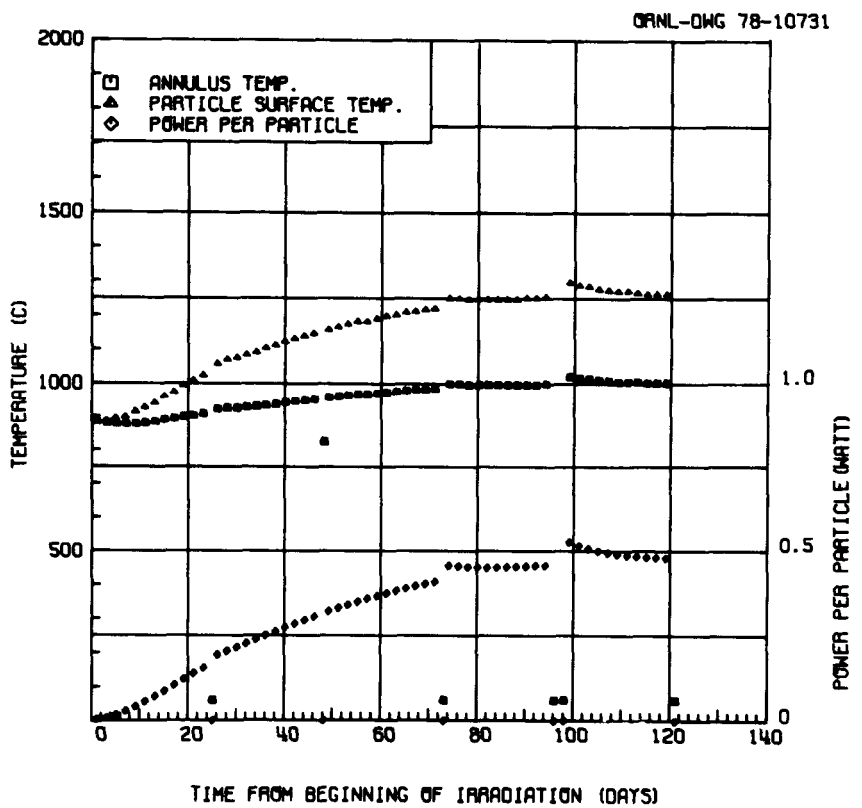


Fig. 2.6. HT-34 Particle Holder 43, Batch A-785, 816.5-μm Particle Diameter.

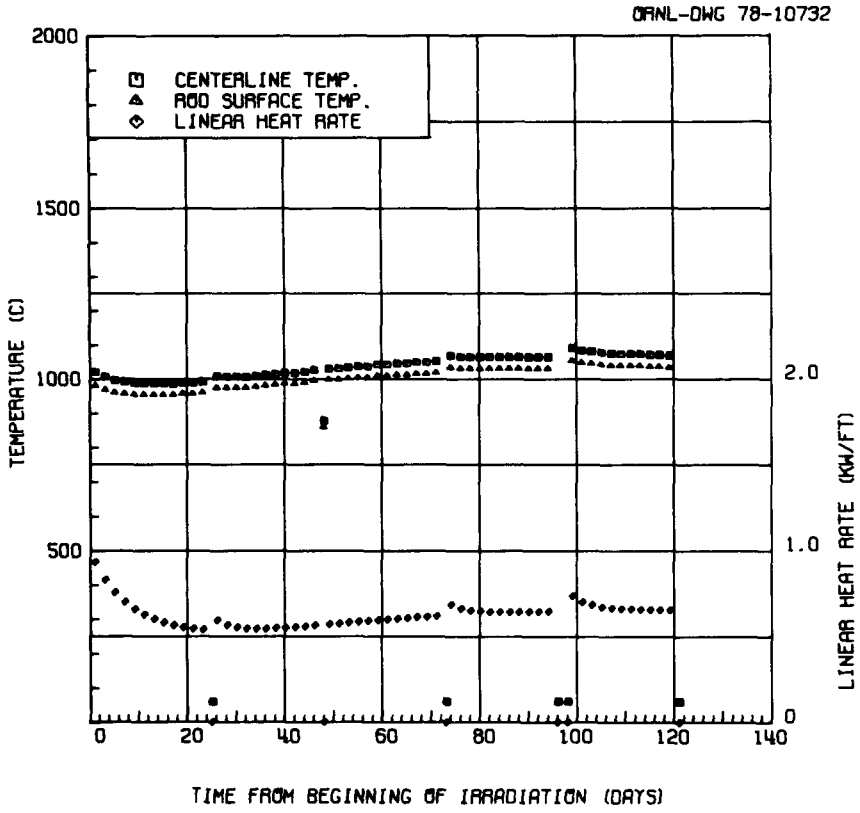


Fig. 2.7. HT-34 Fuel Rod 44, Batch A835 + OR-2576H, 743.1-μm Average Particle Diameter.

The peak temperature for the rods occurred at beginning of life because of the fissile $^{235}U$ present in the rod, whereas for the loose particles, the peak temperatures occurred at end of life. Figures 2.8 and 2.9 are representative of temperatures calculated for specimens irradiated in the low-temperature region of HT-34. Peak temperatures were near 1250°C for the loose particles and near 1100°C for the rods. Average-life temperatures were near 1175°C for the loose particles and 1050°C for the rods. Temperatures presented for the fuel rods represent peak and average centerline temperatures, not particle-surface temperatures as is the case for loose particles.

The temperatures quoted above are 100-200°C higher than design temperatures of 1250 and 900°C for the two temperature regions. Calculations were also made on the ORNL section with the fissile and fertile metal removed. In these cases, the only source of heat generation was that caused by gamma heating [peak value of about 35 W/g at the

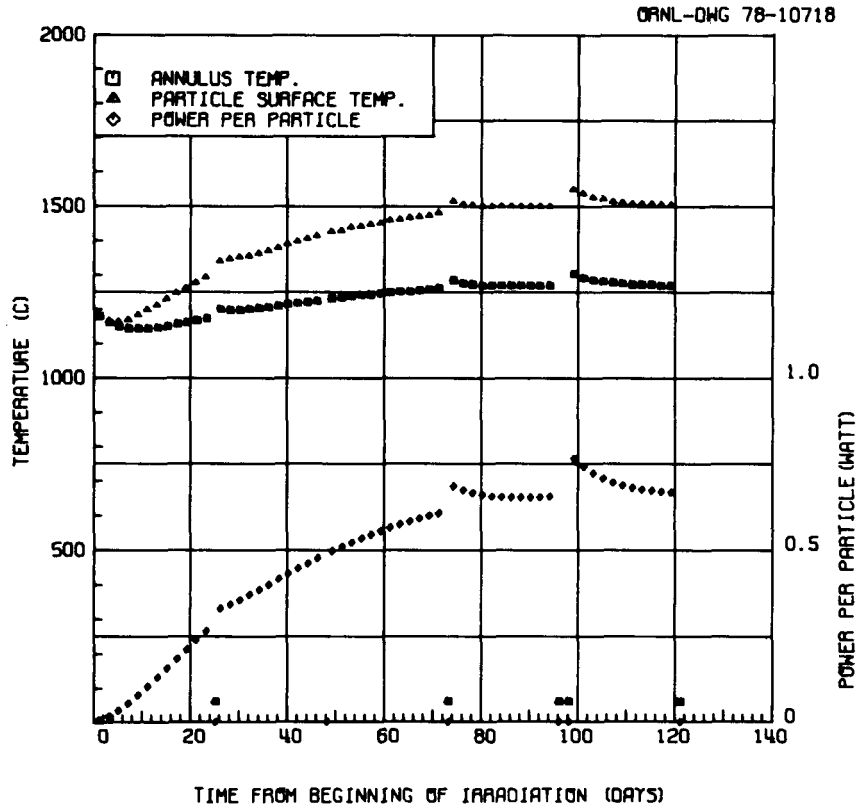


Fig. 2.8. HT-34 Particle Holder 30, Batch A-785, 816.5-μm Particle Diameter.

horizontal midplane of the reactor (HMP)]. For the high-temperature region, the peak temperature was about 1025°C; for the low-temperature region, it was about 825°C (these values are for the particle holders; fuel rod temperatures were about 25°C higher). These temperatures appear to be the minimum temperatures for target capsules without fissile or fertile fuel.

For the high-temperature region, a third case was run wherein only the uranium driver fuel was considered. Here the peak holder temperatures increased to about 1270°C at the HMP and decreased to about 1130°C at about 13 cm from the HMP. These temperatures occurred at beginning of life only; temperatures at end of life had reduced to 1140°C at the HMP and 1075°C at 13 cm from HMP. Similar temperature changes would also occur in the low-temperature region of the capsule. In each of the above cases, end of life was after five full HFIR cycles.

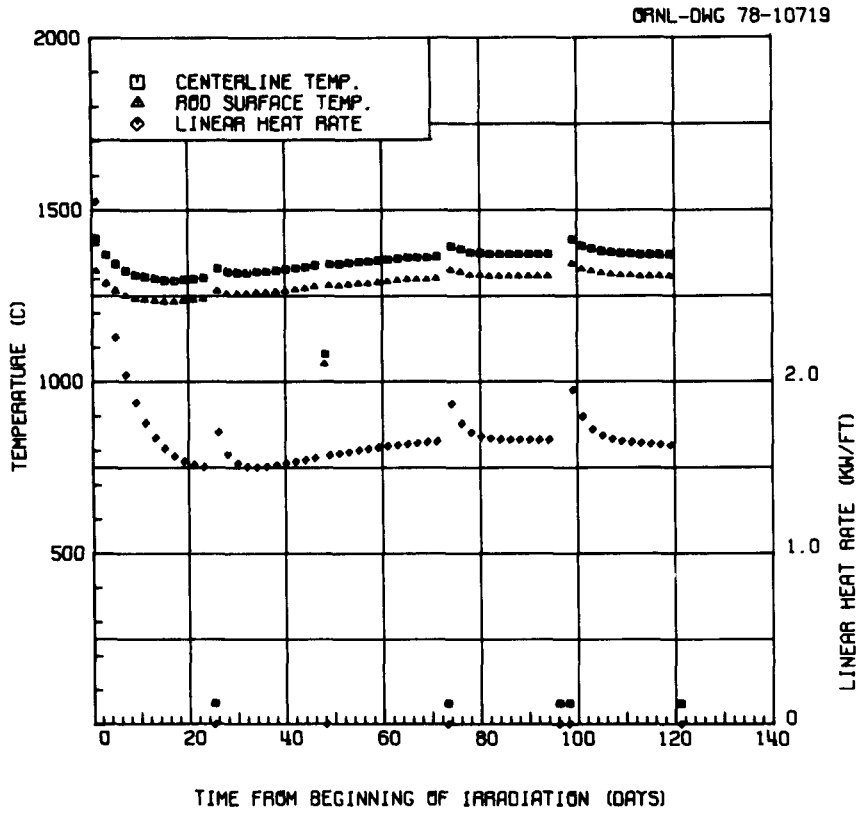


Fig. 2.9. HT-34 Fuel Rod 31, Batch A835 + OR-2576H, 743.1-μm Average Particle Diameter.

2.2.1.5.2 Postirradiation Examination of Capsule HT-34 — T. N. Tiegs, E. L. Long, Jr., and E. L. Ryan. Capsule HT-34 was received at the High-Radiation-Level Examination Laboratory (HRLEL) in mid-December 1977 for PIE. Prior to disassembly, gross-gamma scans of the capsule were recorded, and a sample of the internal gas was analyzed. The gamma scans showed no unusual effects, and the results from the gas sample showed that the cladding remained gastight throughout the irradiation test.

After containment removal, visual and dimensional inspections of the four graphite magazines were made. The exterior of the magazines appeared to be in good condition, but an excessive amount of soot was present in the capsule. A representative from GA was present to oversee the disassembly, retrieval, and visual examination of the upper magazines from the capsule.

The two low-temperature magazines were unloaded without difficulty. However, the end plugs in the high-temperature magazines were stuck, and

in their removal, the ends of the magazines were broken. Particle holders and fuel rods could not be removed until the magazines were slit and split open. No particles were lost from the end plugs because the graph-foil plugs were still in place.

The appearance of the bonded fuel rods from both the low- and high-temperature regions was good, with no debonding noted. Five of the loose particle holders in the high-temperature regions were broken during removal; most of the particles in those holders were recovered. Some difficulty was encountered in retrieving the loose particles from the low-temperature holders. Scanning electron microscopy examination indicated a buildup of an unidentified granular material in the annulus, where particles are held, as the cause of the problem (Fig. 2.10). Attempts to identify this material through electron microprobe analysis were unsuccessful.

The loose coated particles from the ORNL portion of the experiment were visually examined, and the results are given in Table 2.1. As shown, numerous pressure-vessel failures were observed, with most occurring in the low-temperature region. It is believed that the failures are a

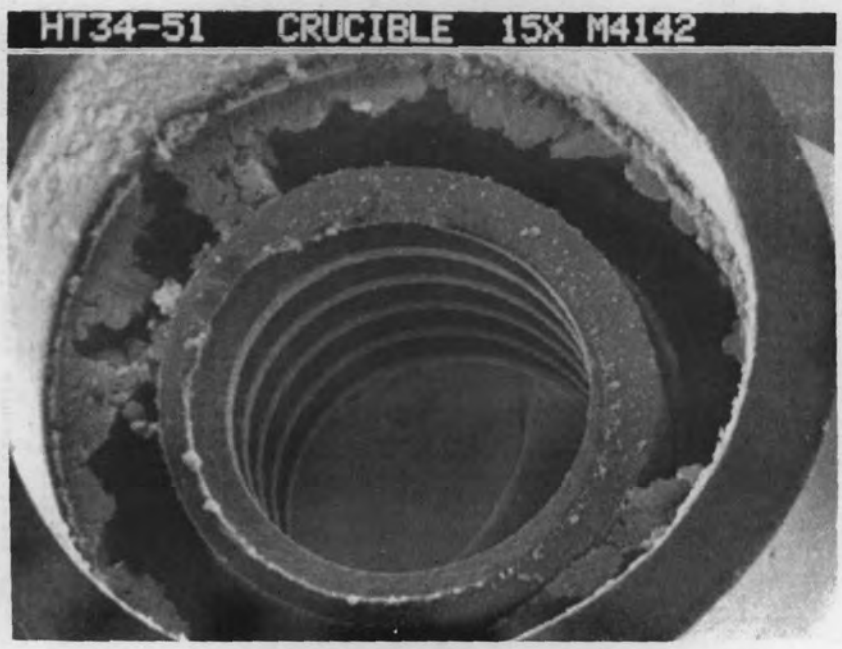


Fig. 2.10. Scanning Electron Micrograph of Loose-Particle Holder 51 from Capsule HT-34 (15 ×).

Table 2.1. Summary of Results from Visual Examination of ORNL Biso-Coated Fertile Particles in HT-34

| Capsule position | Batch | Number of coated particles: Loaded | Recovered: Intact | Recovered: Failed[a] | Unaccounted for[a] | Failure mode[b] | Failed[c] (%) |
|---|---|---|---|---|---|---|---|
| | | | High-temperature magazine | | | | |
| 27 | A-765 | 42 | 31 | 6 | 5 | PV | 14–26 |
| 29 | A-780 | 41 | 39 | 1 | 1 | PV | 2–5 |
| 30 | A-785 | 42 | 37 | 1 | 4 | PV | 2–12 |
| 32 | A-806 | 43 | 41 | 2 | 0 | PV | 5 |
| 33 | A-762 | 42 | 34 | 4 | 4 | PV | 10–19 |
| 35 | A-782 | 41 | 41 | 0 | 0 | None | 0 |
| 36 | A-786 | 43 | 43 | 0 | 0 | None | 0 |
| 38 | A-787 | 42 | 42 | 0 | 0 | None | 0 |
| 39-1 | OR-1975-T | 21 | 16 | 3 | 2 | FND | 14–24 |
| 39-2 | OR-2013-T | 21 | 21 | 0 | 0 | None | 0 |
| | | | Low-temperature magazine | | | | |
| 40 | A-765 | 35 | 25 | 10 | 0 | PV | 29 |
| 42 | A-780 | 35 | 28 | 7 | 0 | PV | 20 |
| 43 | A-785 | 37 | 29 | 6 | 0 | PV | 16 |
| 45 | A-806 | 37 | 34 | 3 | 0 | PV | 8 |
| 46 | A-762 | 36 | 23 | 10 | 3 | PV | 28–36 |
| 48 | A-782 | 36 | 31 | 5 | 0 | PV | 14 |
| 49 | A-786 | 37 | 35 | 1 | 1 | PV | 3–5 |
| 51 | A-787 | 37 | 22 | 0 | 15 | | 0–(30)[d] |
| 52 | OR-1975-T | 37 | 19 | 1 | 18 | PV | 3–(38)[d] |

[a]Estimated from coating fragments.

[b]PV, pressure vessel; FND, fast neutron damage.

[c]First numbers are based on coating fragments; second numbers are based on fragments + unaccounted-for particles.

[d]Thirty-three intact particles found in common container used to store holders from low-temperature magazines.

result of the particles not being annealed prior to irradiation. (In the past all loose particles were annealed at 1800°C for a minimum of 10 min.) Evidently the annealing is necessary to relieve stresses in the PyC coatings that are introduced during the coating process, which would also explain why the particles in high-temperature regions had higher survival rates (i.e., the PyC coating stresses were partially relieved in the reactor). The particles that did survive appeared to be in good condition.

The issue of whether or not particles need to be annealed after coating has been actively discussed with GA on numerous occasions. Experience at ORNL has shown that particles coated by using a conical gas distributor in the coating furnace frequently experience large numbers of broken or cracked particles during postfabrication characterization (chlorine leach, etc.) unless the particles are annealed at 1800°C prior to cooling the coating furnace.[11] It was therefore ORNL's position that the annealing was a necessary step, and annealing was routinely done on all batches fabricated, as indicated earlier. Studies at ORNL have shown that annealing the coated particles that were deposited using a conical distributor increases the crushing strength. However, ORNL has since switched to the fritted gas distributor. The HT-34 particles were coated using the frit. Studies on coated particles prepared by using frit distributors showed essentially no difference in particle breakage or crushing strength for annealed versus unannealed particles.[11] Because the particles are effectively annealed during fuel rod fabrication, it was decided that annealing after particle coating was no longer necessary. The HT-34 experience has caused us to question the validity of this assumption. We have speculated that the cause of the pressure vessel failures in the HT-34 specimens is the lack of an annealing step. Further PIE may show another cause. Another experiment would be required to make a definitive statement about the need for the annealing of loose particles prior to irradiation. That experiment would be to irradiate annealed and unannealed particles from the same batch under identical irradiation conditions. However, because of funding limitations, it is unlikely that such an experiment will be conducted in the near future.

The samples of particles from the two OR batches, which were annealed after coating, were tested in an earlier HT series[12] and showed results similar to those from HT-34. Coatings for Batch OR-2013-T were deposited by using propylene and $CO_2$ as a diluent rather than 100% argon, as for OR-1975-T. The deposition rates, temperatures, gas concentrations, and gas fluxes were equivalent. The range in failure rate shown for particles irradiated in low-temperature magazine positions 51 and 52 is believed to be too high; 37 particles were unaccounted for in this magazine, but 33 were found in the storage container used for the "empty" particle holders.

All of the intact particles are scheduled for IMGA classification, and an inventory of the fission-gas content will be determined with the aid of the PGA system. The IMGA will provide solid fission product inventories of the particles, and the PGA will determine which, if any, of the Biso coatings became permeable because of fast-neutron damage.

### 2.2.2 HRB Capsules — F. J. Homan

Postirradiation examination was completed on fuel from capsules HRB-11 through -13. The IMGA analysis of these capsules has not been completed because of the large backlog of fuel particles wating for IMGA classification. This portion of the PIE will be completed in 1979. A topical report on HRB-11 and -12 was completed during the reporting period, covering all details of the experiment except IMGA analysis of the fuel, which will be reported separately. Capsules HRB-14 and -15b were assembled and irradiated; both capsules were removed from the reactor in January and will be examined during 1979.

#### 2.2.2.1 Capsules HRB-11 and -12 — F. J. Homan

A topical report on this irradiation experiment was completed during the reporting period; the abstract is given below.

> The HRB-11 and -12 experiment had seven objectives, each of which was accomplished. The first objective was to supplement the data from previous experiments regarding the influence of initial oxygen-to-uranium ratio (O:U) on the irradiation performance of WAR-derived fissile fuel particles. The HRB-11 and

-12 results confirmed the conclusions reached in the earlier experiments; that is, fuel particles with initial O:U values between 1.0 and 1.7 give acceptable performance to full burnup for HEU fuel. Fuels with initial O:U below 1.0 show excessive chemical interaction between rare-earth fission products and the SiC layer in the Triso fissile particle design.

The second objective was to obtain performance data on a second resin material. All experience prior to HRB-11 and -12 was with Amberlite IRC-72 resin. Duolite C-464 resin was tested in HRB-11 and -12, and performance was acceptable. Use of the Duolite resin resulted in both a lower initial kernel density and a greater kernel shrinkage under irradiation than occurs with the Amberlite resin, but there was no evidence of a deleterious effect on irradiation performance. However, the higher initial density possible with the Amberlite resin caused it to be favored.

The third objective was to determine the minimum buffer-layer thickness necessary with WAR-derived fissile fuels. Because of the large amount of porosity available in the kernel, especially the Duolite resin, the buffer layer is needed only to protect the inner low-temperature isotropic (ILTI) coating from fission-recoil damage. Buffers of full nominal thickness (∿40 μm), half thickness (∿25 μm), and zero thickness were tested. All performed well, although there appeared to be a slight thinning of the ILTI layer in the particles with no buffer.

The fourth objective was to test the influence of SiC layer-deposition rate on fission product retention capabilities in Triso-coated fissile particles. Particles were tested with SiC layers deposited at rates between 0.2 and 0.9 μm/min. The results of this experiment showed greater fission product attack of the SiC with increasing coating rate. These results are not conclusive, however, because other experiments have shown significant attack on the SiC coatings of particles wherever the coating rate was as low as the lowest rate used in the HRB-11 and -12 experiment. This problem will require additional study.

The fifth objective was to compare the performance of coatings deposited in the 13-cm coating furnace that uses a fritted-plate gas distribution system with coatings deposited in the same furnace that uses a conical gas distribution system. This comparison will supplement data from other experiments in which these same batches of particles have been tested. The HRB-11 and -12 portion of this comparison is only partially completed; the real comparison will be made on the basis of analysis using the IMGA system. The HRB-11 and -12 fuel is yet to be examined with IMGA.

The sixth objective was to test GA fuel, fabricated with thermosetting matrices. The GA rods were irradiated and shipped to San Diego for examination, and the results of this portion of the experiment will be reported separately by GA.

The final objective of the experiment was to test fuel fabricated at LASL using ZrC coatings and graded ZrC-PyC coatings in place of SiC in the Triso fissile design. The results of gamma scanning, metallographic analysis, and microprobe analysis indicate that the fuel with ZrC coatings did not perform well. Further analysis using the IMGA system is planned.

2.2.2.2 Capsule HRB-13 — T. N. Tiegs

The objectives, design, and fabrication details of HRB-13 have been reported.[13] A summary of the capsule operation was also reported.[14]

The capsule was disassembled and the fuel rods removed without difficulty. Postirradiation dimensional measurements of the fuel rods and graphite sleeve were made and compared to preirradiation measurements. The dimensional changes as a function of fast neutron fluence ($E$ >0.18 MeV) are summarized in Figs. 2.11 and 2.12.

Visual examination of the fuel rod surfaces revealed numerous coated particle failures. The visual results are summarized in Table 2.2 for all ORNL rods. Particle types 1 and 5, which were the reference particle designs with regard to shape, had surface failures at the peak HRB-13 fluences. All other particle types exhibited surface

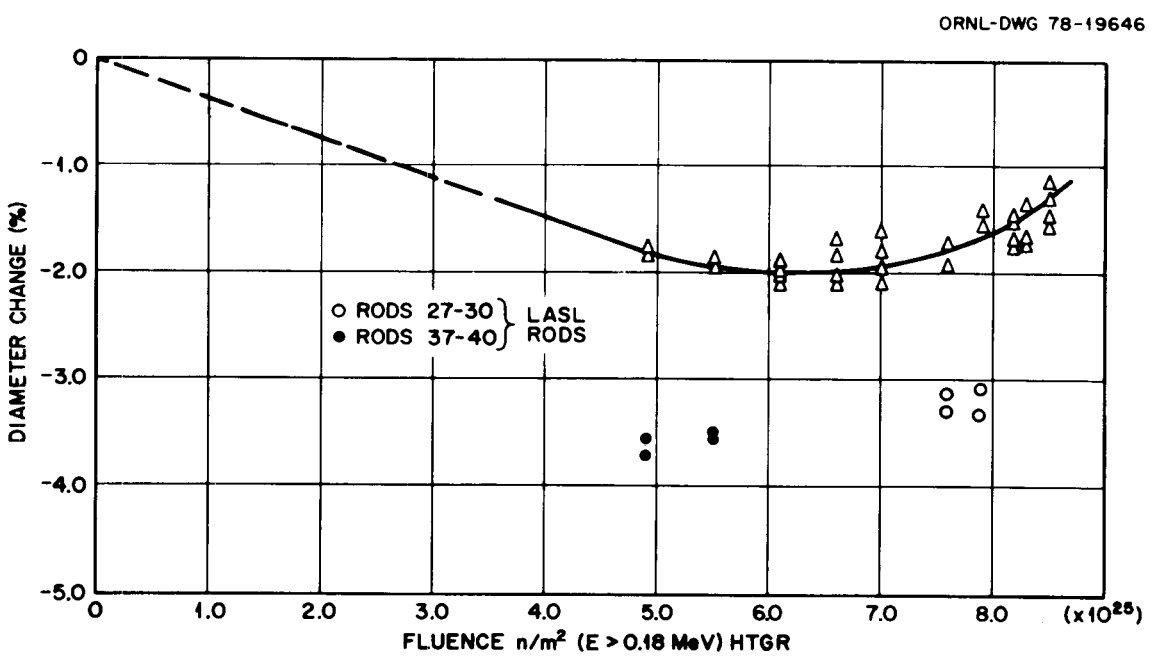


Fig. 2.11. HRB-13 Fuel Rods Diameter Change % Versus Fluence.

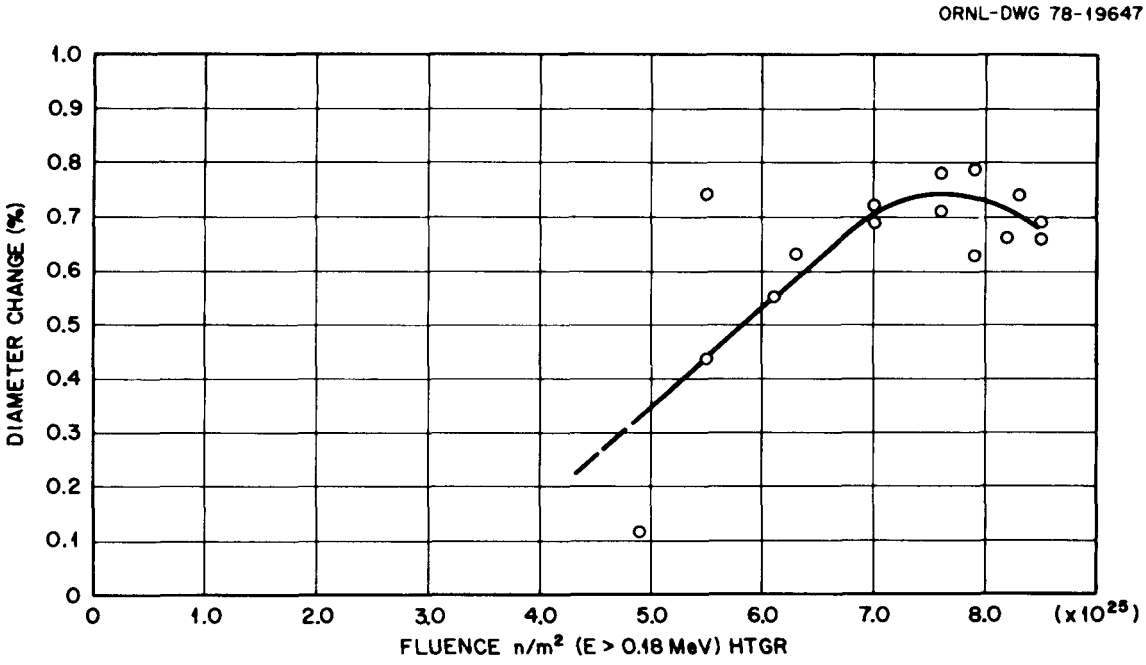


Fig. 2.12. HRB-13 Sleeve Diameter Change % Versus Fluence.

failures, with type 4-C having the most (total of 70 for four rods). No explanation of the failure mechanism has been established.

Selected fuel rods have been electrolytically deconsolidated[15] and will be analyzed by the IMGA system in early 1979. Results from those analyses and subsequent metallography will give a better understanding of the influence of particle shape on fuel performance.

2.2.2.3 Capsule HRB-14 — K. R. Thoms

The objectives and description of capsule HRB-14 have been reported.[16] Capsule HRB-14 was inserted in the removable beryllium (RB) facility of HFIR and brought to full power of 100 MW at 3:11 AM on May 20, 1978. The capsule was swept with 100% helium during the first cycle to lower fuel temperatures while a portion of the $^{235}U$ burned out. For the remaining nine irradiation cycles, the fuel temperature was adjusted by varying the Ne/He sweep-gas mixture. During the third cycle the ENCTRK[17] computer code was used to determine fuel centerline temperatures, and it was discovered that the capsule had been operating about 200°C below design conditions. This was corrected, and the capsule was controlled

Table 2.2. Results of Visual Examination of Fuel Rod Surfaces from HRB-13

| Type/ objective | Position | Number of surface failures | Total failures | Fast fluence (neutrons/$m^2$ $E$ >0.18 MeV) HTGR |
|---|---|---|---|---|
| | | Amberlite | | |
| 1[a] | 15 | 2 | 5 | $8.2 \times 10^{25}$ |
| | 16 | 3 | | |
| 2-A | 1 | 0 | 2 | 4.9 |
| | 2 | 2 | | |
| | 11 | 7 | 10 | 7.6 |
| | 12 | 3 | | |
| | 19 | 2 | 5 | 8.5 |
| | 20[b] | 3 | | |
| 3-B | 5 | 3 | 6 | 6.1 |
| | 6 | 3 | | |
| | 9 | 8 | 13 | 7.0 |
| | 10 | 5 | | |
| 4-C | 7 | 16 | 42 | 6.6 |
| | 8 | 26 | | |
| | 17 | 11 | 28 | 8.3 |
| | 18 | 17 | | |
| | | Duolite | | |
| 5[a] | 25 | 0 | 2 | 8.2 |
| | 26 | 2 | | |
| 6-D | 3 | 4 | 8 | 5.5 |
| | 4 | 4 | | |
| | 13 | 6 | 10 | 7.9 |
| | 14 | 4 | | |
| | 21 | 6 | 10 | 8.5 |
| | 22 | 4 | | |
| 7-E | 31 | 0 | 1 | 7.0 |
| | 32 | 1 | | |
| | 35 | 2 | 3 | 6.6 |
| | 36 | 1 | | |
| 8-F | 23 | 14 | 18 | 8.3 |
| | 24 | 4 | | |
| | 33 | 6 | 9 | 6.1 |
| | 34 | 3 | | |

[a]Quality assurance document MET-CER-EP-24.

[b]Peak fluence (horizontal midplane of the reactor).

in an effort to operate with the maximum fuel centerline temperature at 1250°C. One fission-gas sample was taken each week from the beginning of the irradiation test period. The CACA-2 code[18] was used to calculate the fission product birth rates, which was required to determine the release-to-birth (R/B) data for HRB-14. A summary of the fission-gas R/B data collected as of November 7, 1978, is presented in Table 2.3; a significant increase in R/B was noted during the sixth cycle of irradiation. The temperature history of fuel specimens located at the same elevation as the thermocouples is shown in Figs. 2.13, 2.14, and 2.15. Capsule HRB-14 is scheduled to complete its tenth and final irradiation cycle in early January 1979.

Table 2.3. Capsule HRB-14 Release-to-Birth Data

| Sample number | Date | Accumulated irradiation time (h) | Fission gas release-to-birth ($\times 10^{-5}$) | | | | |
|---|---|---|---|---|---|---|---|
| | | | $^{85m}Kr$ | $^{87}Kr$ | $^{88}Kr$ | $^{135}Xe$ | $^{133}Xe$ |
| 1 | 5/26/78 | 154 | 0.22 | 0.13 | 0.13 | 0.05 | 0.18 |
| 2 | 6/2/78 | 320 | 0.35 | 0.19 | 0.16 | 0.09 | 0.43 |
| 3 | 6/8/78 | 467 | 0.50 | 0.27 | 0.28 | 0.13 | 0.68 |
| 4 | 6/15/78 | 598 | 0.69 | 0.39 | 0.38 | 0.25 | 0.89 |
| 5 | 6/23/78 | 785 | 1.04 | 0.49 | 0.56 | 0.37 | 1.41 |
| 6 | 6/30/78 | 955 | 1.25 | 0.76 | 0.84 | 0.38 | 1.54 |
| 7 | 7/13/78 | 1225 | 1.41 | 0.74 | 0.79 | 0.49 | 1.69 |
| 8 | 7/21/78 | 1416 | 2.49 | 1.14 | 1.38 | 0.91 | 3.29 |
| 9 | 8/4/78 | 1668 | 2.84 | 1.31 | 1.60 | 1.60 | 6.56 |
| 10 | 8/15/78 | 1932 | 2.48 | 1.13 | 1.69 | 1.24 | 5.94 |
| 11 | 9/12/78 | 2583 | 4.04 | 2.85 | 2.75 | 2.09 | 18.4 |
| 12 | 9/20/78 | 2715 | 58.1 | 72.1 | 63.0 | | 261. |
| 13 | 9/26/78 | 2860 | 77.8 | 114. | 111. | 0.50 | 278. |
| 14 | 10/4/78 | 3048 | 90.4 | 172. | 133. | 59.8 | 335. |
| 15 | 10/11/78 | 3195 | 53.8 | 47.7 | 67.8 | 34.8 | 222. |
| 16 | 10/17/78 | 3337 | 57.7 | 47.0 | 65.6 | 36.2 | 209. |
| 17 | 10/26/78 | 3550 | 72.4 | 72.0 | 77.8 | 46.8 | 313. |
| 18 | 11/1/78 | 3676 | 70.2 | 64.1 | 66.1 | 40.4 | 257. |
| 19 | 11/7/78 | 3820 | 78.5 | 74.9 | 78.7 | 43.6 | 234. |

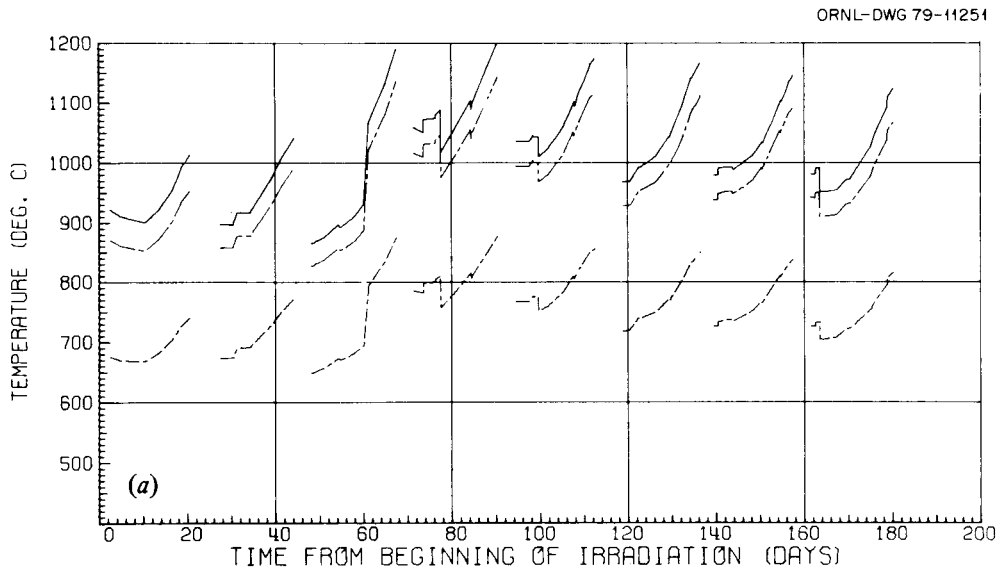


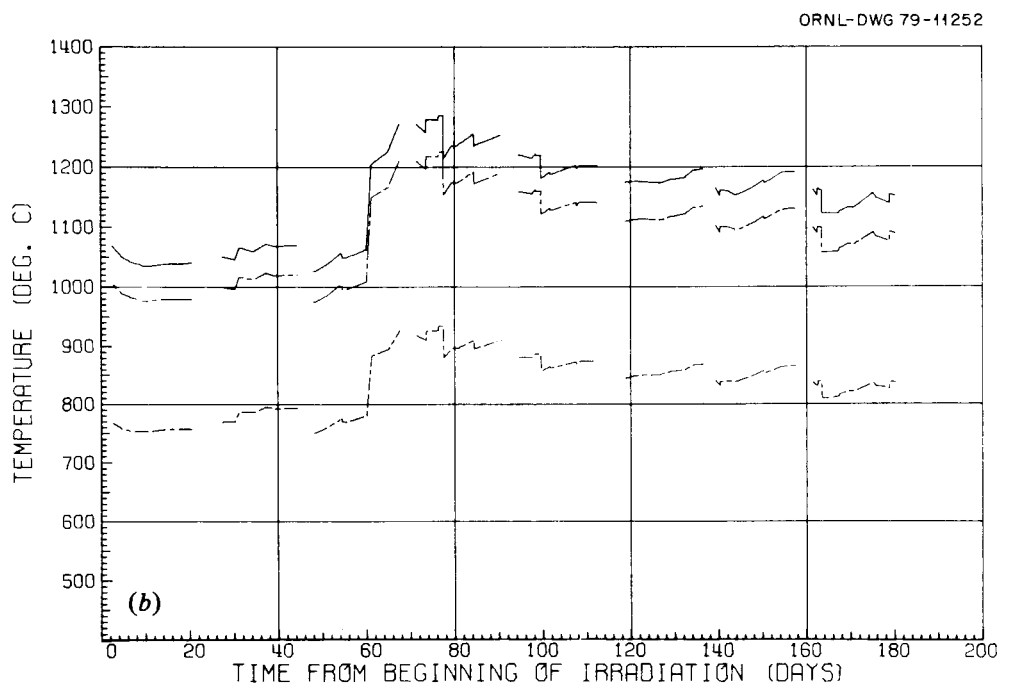


Fig. 2.13. Time Temperature Histories for ORNL Planchets: (*a*) Planchet 2-14G and (*b*) Planchet 6-14D in HRB-14. Top, middle, and bottom lines represent maximum fuel, minimum fuel, and midwall graphite sleeve temperatures, respectively.

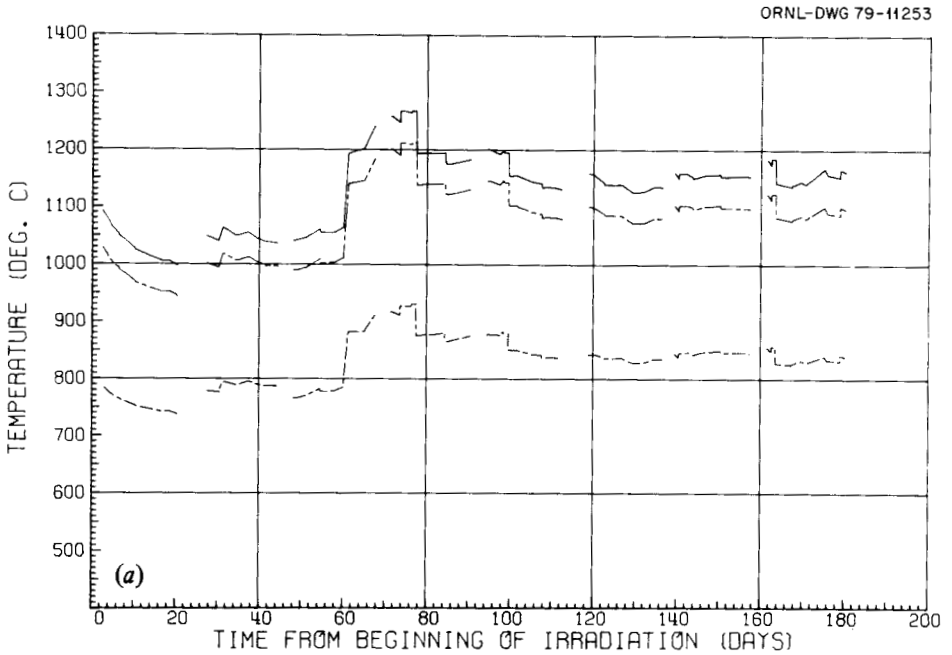


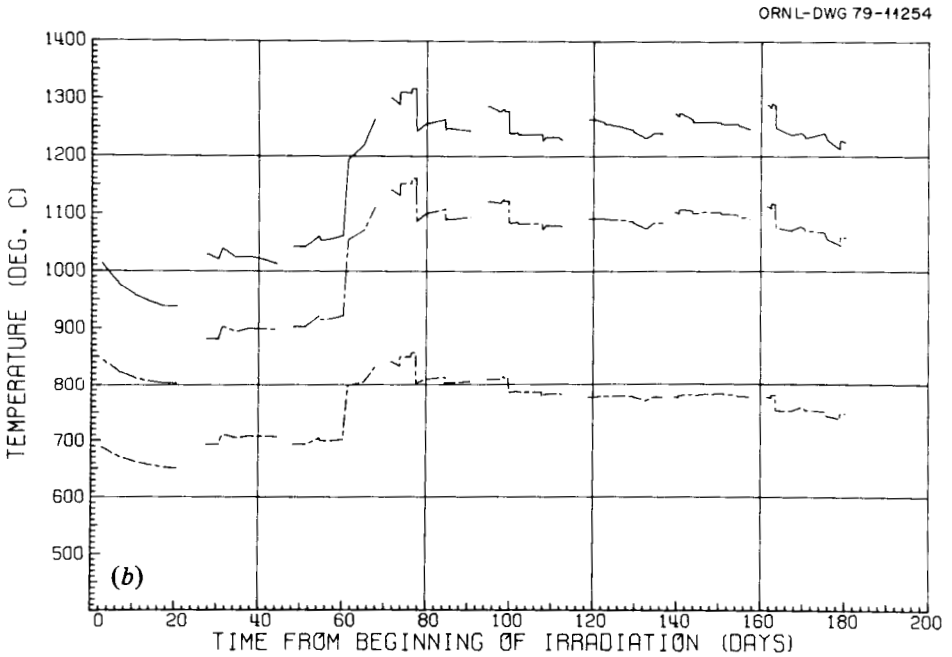


Fig. 2.14. Time Temperature Histories for (*a*) ORNL Planchet 9-5D and (*b*) GA Fuel Rod 2 in HRB-14. Top, middle, and bottom lines represent maximum fuel, minimum fuel, and midwall graphite sleeve temperatures, respectively.

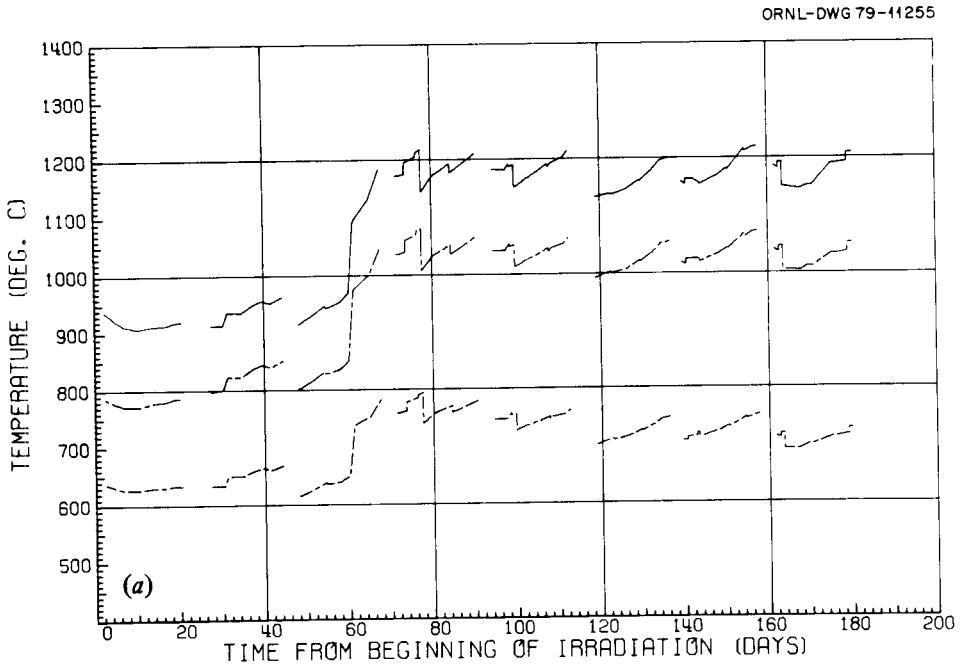


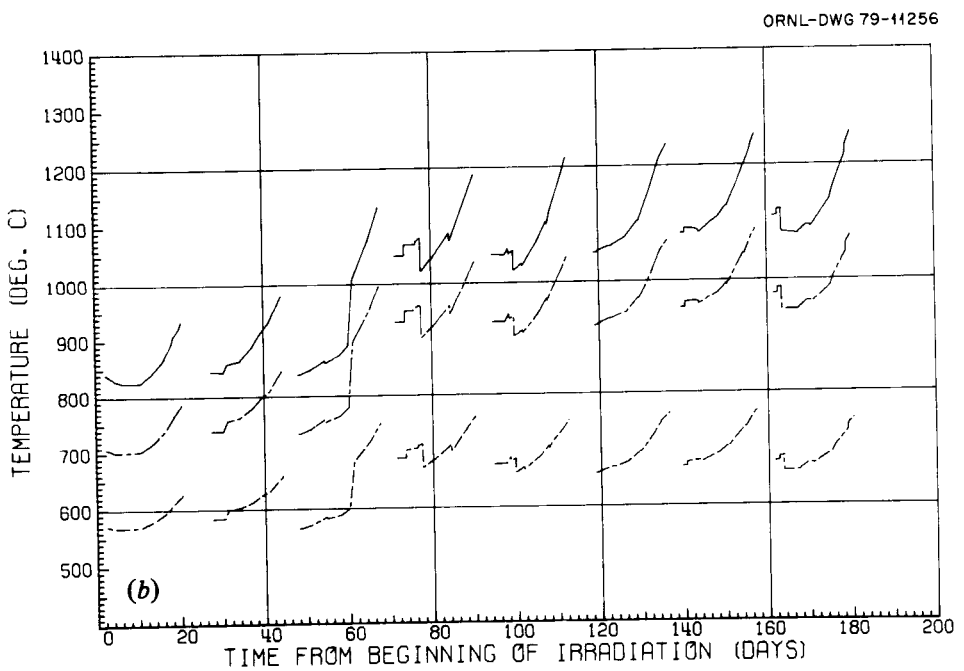


Fig. 2.15. Time Temperature Histories for GA Fuel Rods in HRB-14 for (*a*) Rod 10 and (*b*) Rod 17. Top, middle, and bottom lines represent maximum fuel, minimum fuel, and midwall graphite sleeve temperatures, respectively.

2.2.2.4 Capsule HRB-15b — W. E. Thomas, Jr.

The description and objectives of capsule HRB-15b have been reported.[19] Capsule HRB-15b was installed in HFIR on July 5, 1978. The reactor went to power on July 6, and the initial temperature data agreed with the thermal analysis within 10°C at the horizontal-midplane position of the capsule. For the first cycle the capsule was swept with 100% helium, which resulted in a maximum particle-surface temperature of about 850°C. Neon was added to the sweep gas during the second cycle to bring the maximum particle-surface temperature to no more than 1000°C. During the third cycle of operation it became apparent from the thermocouple data that the midlength of the fuel column was slightly above the HFIR horizontal midplane. At the end of the third cycle the capsule was lowered 0.02 m. This slight adjustment of the capsule corrected the problem, as was evidenced by a symmetrical temperature profile about the horizontal midplane. The capsule continued to operate without incidence through seven cycles of irradiation and is scheduled to end its eighth and final cycle in early January 1979. For more details concerning the nuclear evaluation and thermal analysis of capsule HRB-15b, see Sect. 2.4.1 of this report.

2.2.3 ORR Capsules — T. N. Tiegs

At the end of the reporting period, no OF-type capsules were in the ORR, and none are planned for 1979. A topical report covering the operation and PIE of capsule OF-2 has been published.[20] Gamma analysis of the particles from OF-2 are reported in Sect. 2.6.1 of this report.

2.2.4 Fort St. Vrain Test Element Program — P. Angelini

During this report period, work has been concentrated in three areas. First, impurity analyses were obtained on the ORNL Triso-coated fissile particles used in this experiment. Results showed that the particles met impurity and boron equivalent product specifications. Second, ORNL and GA have been cooperating in a "round robin" to determine the agreement between heavy metal assay determinations using GA-produced driver fuel rods for the Fort St. Vrain Test Element Program

(see Sect. 2.7.2). Results have shown excellent agreement between intra- and inter-laboratory assay determinations. And third, GA TRIGA R/B data for $^{85m}Kr$ determinations of failed-particle fractions in the unirradiated rods that had been fabricated at ORNL and subsequently carbonized in-block at GA were higher than allowed by either FSVR or Large High-Temperature Gas-Cooled Reactor product specifications. This result indicates that damage to the particles may have occurred in fuel rod manufacture, in shipment to GA, during assembly and in-block carbonization at GA, or during removal of rods from the test fixture at GA. An experimental plan has been designed and is being carried out that should indicate the reasons for the increase in failed fractions. Archive fuel rods are being used and are being analyzed both in the green state and after carbonization. Carbonization runs have been performed at both ORNL and GA, using archive rods. Analyses will include $Cl_2$ gas leach, TRIGA R/B, and mercury intrusion determinations.

Impurity analyses were obtained by spark-source mass spectrometry for Triso-coated particle batches A-601 and A-611. The A-611 particles were used in campaigns 1 and 3, and the A-601 particles were used in campaigns 2 and 4 on fuel rods produced at ORNL for the irradiation experiment. The impurity data and the calculated boron equivalents were transmitted to GA. The boron equivalents are presented in Table 2.4 as burnable (Li, B, Cd, Sm, Eu, and Gd) and nonburnable (remainder of elements) for each particle type. The boron equivalents were calculated from the mass spectrometric data by using conversion coefficients for boron equivalents present in the interim II specification. The impurity and boron equivalent results show that the particles met the required product specifications.

ORNL and GA have been cooperating in a round robin on the uranium and thorium assay of 36 green fuel rods produced by GA for the Fort St. Vrain Test Element Program. The driver rods were randomly selected from blends 12, 13, and 14 and were assayed by the following techniques:

1. GA — TRIGA nondestructive delayed-neutron assay,
2. ORNL — nondestructive delayed-neutron assay,
3. ORNL — nondestructive prompt-neutron assay, and
4. ORNL — wet chemistry.

Table 2.4. Weight and Boron Equivalents for Trisco-Coated Weak-Acid Resin Coated Particles A-611 and A-601

| | | Weight (ppm) | Boron equivalent (ppm) |
|---|---|---|---|
| A-611 | Lithium | 0.25 | 0.04 |
| | Burnable | | 2.21 |
| | Nonburnable | | 0.20 |
| A-601 | Lithium | 0.25 | 0.04 |
| | Burnable | | 2.21 |
| | Nonburnable | | 0.30 |

The GA assay of each rod was performed prior to shipment of the rods to ORNL. Once at ORNL, each of the 36 rods was measured twice in the delayed-neutron assay device and twice in the prompt neutron assay device. Separate calibration standards were fabricated. Except that the same calibration standards were used, the measurements on the separate devices were independent. They were performed by separate operators, and analysis of the data was performed by separate individuals. No comparison of the results was made until the final figures were obtained, and no adjustments have been made in the results.

The same fuel rods analyzed by nondestructive assay were later analyzed by wet chemistry techniques (modified Davies Gray potentiometric titration for uranium; EDTA volumetric titration method for thorium). The assay results from all four methods are presented in Table 2.5.

Review of the data shows that agreement of the assay as determined by each method for each of the 36 rods is good. The following statistic was used to evaluate the data for each fuel rod, with the TRIGA measurement taken as a reference:

$$X = (\text{TRIGA measurement} - \text{other method result}/\text{TRIGA measurement}) \times 100 \ .$$

The averages of the above relative percentage differences for fuel rods from each blend are presented in Table 2.6 and show excellent agreement between methods.

Table 2.5. Assay Results of GA-Produced Driver Fuel Rods for the Fort St. Vrain Early Validation Irradiation Experiment

| Fuel rod identification number | Estimated total $^{235}U$ content (g) with corresponding 95% confidence | | | | Analytical chemistry results | | TRIGA delayed-neutron assay GA $^{235}U$ content (g) |
|---|---|---|---|---|---|---|---|
| | ORNL delayed-neutron assay device | | ORNL prompt-neutron assay device | | ORNL $^{235}U$ content (g) | ORNL thorium content (g) | |
| | | | | Blend 12 | | | |
| 10-12-6-12B | 0.1645 | 0.0011 | 0.1647 | 0.0024 | 0.1623 | 3.494 | 0.1653 |
| 10-12-17-12 | 0.1622 | 0.0011 | 0.1615 | 0.0024 | 0.1631 | 3.540 | 0.1620 |
| 10-34-39-12B | 0.1644 | 0.0011 | 0.1628 | 0.0024 | 0.1651 | 3.535 | 0.1649 |
| 10-82-8-12B | 0.1619 | 0.0011 | 0.1645 | 0.0024 | 0.1621 | 3.532 | 0.1626 |
| 10-82-31-12B | 0.1621 | 0.0011 | 0.1606 | 0.0024 | 0.1628 | 3.500 | 0.1633 |
| 10-95-3-12 | 0.1627 | 0.0011 | 0.1644 | 0.0024 | 0.1646 | 3.528 | 0.1604 |
| 10-130-10-12B | 0.1665 | 0.0011 | 0.1632 | 0.0024 | 0.1645 | 3.535 | 0.1648 |
| 10-160-12-12B | 0.1627 | 0.0011 | 0.1620 | 0.0024 | 0.1617 | 3.553 | 0.1642 |
| 10-184-11-12B | 0.1644 | 0.0011 | 0.1632 | 0.0024 | 0.1638 | 3.546 | 0.1626 |
| 10-235-5-12B | 0.1607 | 0.0011 | 0.1592 | 0.0022 | 0.1597 | 3.532 | 0.1614 |
| 10-262-1-12B | 0.1658 | 0.0011 | 0.1649 | 0.0022 | 0.1666 | 3.541 | 0.1664 |
| 10-298-32-12B | 0.1596 | 0.0011 | 0.1589 | 0.0022 | 0.1589 | 3.525 | 0.1611 |
| | | | | Blend 13 | | | |
| 10-7-14 | 0.1197 | 0.0009 | 0.1172 | 0.0022 | 0.1195 | 4.744 | 0.1208 |
| 10-7-35 | 0.1288 | 0.0009 | 0.1299 | 0.0022 | 0.1280 | 4.641 | 0.1295 |
| 10-12-20 | 0.1215 | 0.0009 | 0.1208 | 0.0022 | 0.1221 | 4.735 | 0.1221 |
| 10-12-28 | 0.1221 | 0.0009 | 0.1209 | 0.0022 | 0.1206 | 4.665 | 0.1227 |
| 10-16-8 | 0.1262 | 0.0009 | 0.1252 | 0.0022 | 0.1272 | 4.730 | 0.1266 |
| 10-16-26 | 0.1217 | 0.0009 | 0.1238 | 0.0022 | 0.1210 | 4.746 | 0.1226 |
| 10-21-9 | 0.1278 | 0.0009 | 0.1292 | 0.0022 | 0.1283 | 4.754 | 0.1281 |
| 10-21-32 | 0.1224 | 0.0009 | 0.1216 | 0.0022 | 0.1223 | 4.710 | 0.1230 |
| 10-26-18 | 0.1289 | 0.0009 | 0.1291 | 0.0022 | 0.1289 | 4.730 | 0.1300 |
| 10-26-38 | 0.1245 | 0.0009 | 0.1252 | 0.0022 | 0.1251 | 4.740 | 0.1260 |
| 10-30-14 | 0.1295 | 0.0009 | 0.1303 | 0.0022 | 0.1231 | 4.745 | 0.1303 |
| 10-30-37 | 0.1233 | 0.0009 | 0.1227 | 0.0022 | 0.1258 | 4.721 | 0.1252 |
| | | | | Blend 14 | | | |
| 10-9-14 | 0.2840 | 0.0015 | 0.2871 | 0.0032 | 0.2850 | 3.599 | 0.2848 |
| 10-9-35 | 0.2939 | 0.0015 | 0.2960 | 0.0032 | 0.2931 | 3.590 | 0.2910 |
| 10-19-20 | 0.2859 | 0.0015 | 0.2884 | 0.0032 | 0.2899 | 3.619 | 0.2882 |
| 10-19-28 | 0.2852 | 0.0015 | 0.2873 | 0.0032 | 0.2867 | 3.575 | 0.2848 |
| 10-45-8 | 0.2937 | 0.0015 | 0.2961 | 0.0032 | 0.2954 | 3.586 | 0.2925 |
| 10-45-26 | 0.2858 | 0.0015 | 0.2878 | 0.0032 | 0.2870 | 3.583 | 0.2885 |
| 10-54-9 | 0.2871 | 0.0015 | 0.2857 | 0.0032 | 0.2879 | 3.587 | 0.2889 |
| 10-54-32 | 0.2813 | 0.0015 | 0.2830 | 0.0032 | 0.2873 | 3.602 | 0.2835 |
| 10-69-18 | 0.2849 | 0.0015 | 0.2865 | 0.0032 | 0.2855 | 3.612 | 0.2841 |
| 10-69-38 | 0.2852 | 0.0015 | 0.2864 | 0.0032 | 0.2871 | 3.587 | 0.2885 |
| 10-85-37 | 0.2904 | 0.0015 | 0.2916 | 0.0032 | 0.2907 | 3.603 | 0.2912 |
| 10-81-14 | 0.2866 | 0.0015 | 0.2910 | 0.0032 | 0.2900 | 3.595 | 0.2880 |

Tests are being performed to determine the possible reasons for the higher-than-specification failed fractions of ORNL fuel rods as determined by TRIGA R/B and gas leach measurements. The fuel particles may have been damaged during rod manufacture, during shipment to GA, during assembly and in-block carbonization at GA, or during removal from the test fixture after carbonization. An experimental plan was developed to determine where in the sequence of fabrication steps the fuel may have been damaged as well as to indicate the state of fuel rods in the

Table 2.6. Average Percentage Differences of Methods with TRIGA Measurements Used as Reference

| Rods of blend | Method | Average percentage differences ($\bar{x}$) |
|---|---|---|
| 12 | ORNL delayed-neutron | 0.07 |
| 12 | ORNL chemistry | 0.19 |
| 12 | ORNL prompt-neutron | 0.46 |
| 13 | ORNL delayed-neutron | 0.70 |
| 13 | ORNL chemistry | 0.57 |
| 13 | ORNL prompt-neutron | 0.74 |
| 14 | ORNL delayed-neutron | 0.29 |
| 14 | ORNL chemistry | -0.34 |
| 14 | ORNL prompt-neutron | -0.37 |

heat-treated fuel element. Analytical tests on fuel particles and on archive green rods have been performed. Archive rods have also been carbonized in different test fixtures at both ORNL and in the GA cure-in-place furnace. Analytical tests to be performed on the carbonized fuel rods include $Cl_2$ gas leach, TRIGA R/B, and mercury intrusion determinations.

## 2.3 DEVELOPMENT WORK — F. J. Homan

The work described in this section is aimed at product improvement, preirradiation and postirradiation characterization of fuels, and techniques for performance assessment of particle coatings. Four areas are included here as follows:

1. pyrocarbon permeability studies centering around both the techniques for measurement of permeability and the correlations of measured permeability with PyC properties,
2. coating studies using $CO_2$ as a diluent gas in attempting to produce PyC coatings in the large coater having the same outstanding

properties as batch OR 2013-T, which was produced in the laboratory scale coater,

3. sintering and conversion studies on dense UCO fuel for use with the MEU fuel cycle, and
4. developing an improved SiC coating that can resist both attack by the fission product palladium and diffusion of the fission product silver.

### 2.3.1 Permeability Studies

#### 2.3.1.1 Permeability of Production Coatings — D. P. Stinton and B. A. Thiele

All recent process development used the porous plate gas distributor[21,22] and centered on improving the properties of the low-temperature isotropic (LTI) layer of the Biso particle. This year we examined the permeability of high-density PyC coatings. A report was written which describes a technique developed to determine the permeability of the LTI layer.[23] The abstract and conclusions of this report are as follows:

> Fuel for HTGRs consists of uranium oxide/carbide and thoria microspheres coated with layers of PyC and SiC. The PyC layer of thoria particles is the barrier to fission gases. Therefore, thoria particles must be carefully characterized to determine the number of defective particles (i.e., bare kernels and cracked or permeable coatings). Techniques are available to determine the number of bare kernels or cracked coatings; however, no reliable technique is known to measure coating permeability. This work describes a technique recently developed to determine whether coatings for a batch of thoria particles are gastight or are permeable.
>
> About 150 randomly selected Biso-particle batches were studied in this work. These batches were first subjected to an 18-h chlorination at 1500°C, and the volatile thorium tetrachloride released was measured versus chlorination time. Chlorinated batches were also radiographed to detect any thorium that had migrated from the kernel into the coatings.
>
> From this work a technique was developed to determine coating permeability, which consists of an 18-h chlorination of multiple samples without measurement of the thorium released. Each batch is radiographed, and the thorium migration within each particle is examined. From this examination it is possible to determine if a particle batch is permeable, slightly permeable, or gastight.

The technique of an 18-h chlorination and microradiography has proven very successful in determining the gas permeability of Biso-coated particles. Particles can be classified very easily into categories of permeable, impermeable, or only slightly permeable. Several modifications have allowed numerous batches to be chlorinated simultaneously with no need for an analytical determination of the heavy metal released.

Long-term chlorination can also be applied to Triso particles. However, because the permeability of the inner LTI is of interest, chlorination must be performed after the inner LTI is applied and before the silicon carbide is applied.

All 45 particle batches from two statistically designed experiments performed in the 13- and 24-cm coaters by using a porous plate-type gas distributor were thoroughly examined. Every particle batch was characterized for as-produced gas permeability of the PyC coating by both the Ne:He intrusion technique[24] and long-term chlorine leach and radiograph.[23] Excellent agreement was found between these two techniques. Particles with gas-permeable PyC coatings had Ne:He ratios of greater than or equal to 0.4, whereas the gastight ones had values of less than or equal to 0.3. Pyrocarbon coatings with Ne:He values of 0.3 to 0.4 could be gastight or gas permeable. Particles with $Cl_2$ gas-permeable coatings could be easily identified because of heavy-metal migration into the buffer layer. Thorium migrated into the buffer of gas-permeable coatings because chlorine diffused through the PyC coating and reacted with the actinide kernel. The migration could be seen in x-ray microradiographs of these defective particles. Some particle batches had extremely gas-permeable LTI coatings. Heavy metal diffused through these coatings and was collected and analyzed in the reaction chamber of the chlorine leach apparatus. The Ne:He ratios of these batches were greater than 0.5. The correlations between the following LTI PyC-coating properties and gas permeability were carefully examined: thickness, optical anisotropy, open porosity, and density. Evaluation of the permeability data of these 45 Biso $ThO_2$ batches showed that gas permeability is independent of LTI coating thickness when the current product specifications are met (Fig. 2.16). Batches in the following figures were determined to be permeable or gastight by using the long-term chlorine leach and radiograph technique. Optical anisotropy was also shown to be independent of permeability in the range of interest ($BAF_0$ <1.05) (Fig. 2.17). The important properties that did influence

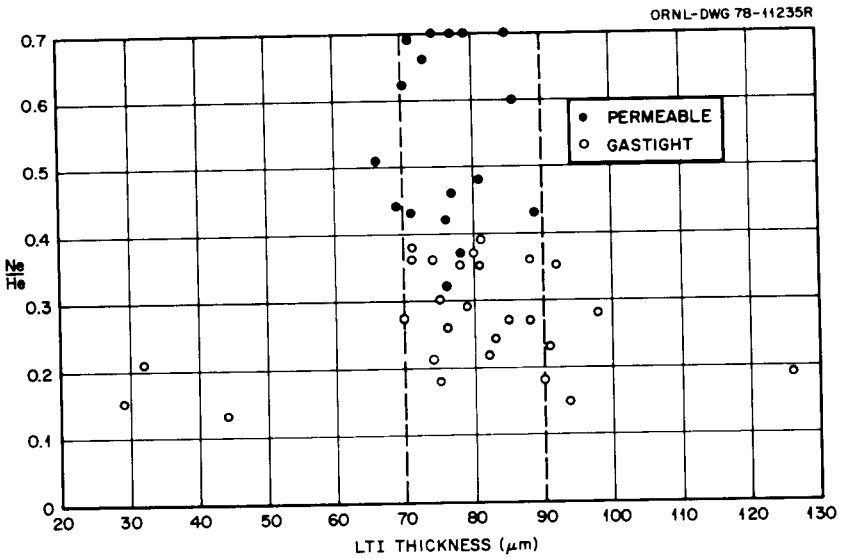


Fig. 2.16. Coating Thickness Has Little Effect on Gas Permeability.

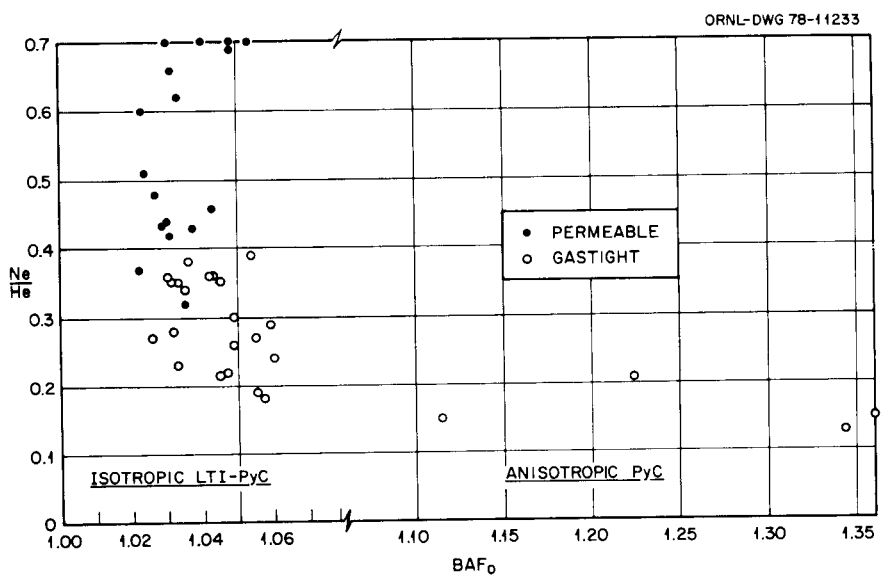


Fig. 2.17. Isotropic LTI PyC Coatings Show Large Variations in Gas Permeability.

LTI coating permeability were open porosity and corrected gradient density (bulk density).[25,26] As the percentage of open porosity increases, the Ne:He values increase until the coating becomes permeable (Fig. 2.18). High corrected-gradient densities were found to produce gastight coatings (Fig. 2.19). As the density decreased the Ne:He values increased until the coatings became permeable.

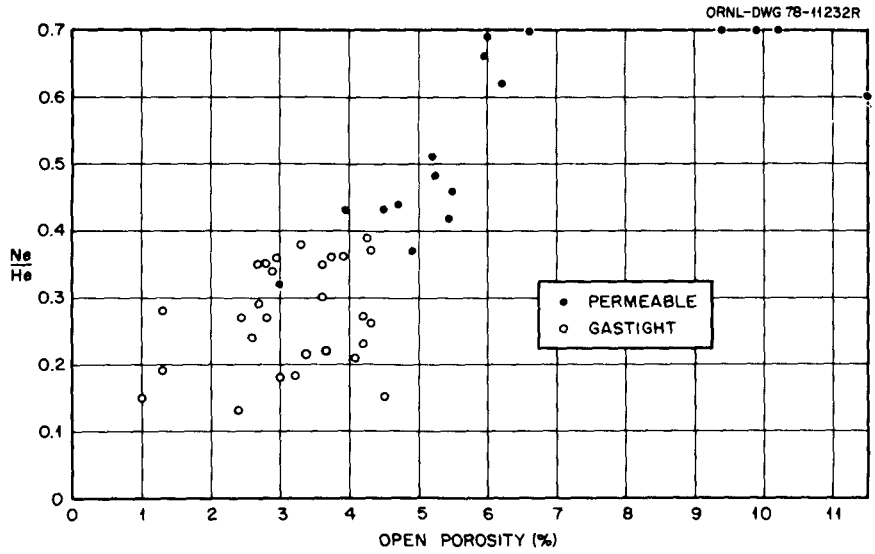


Fig. 2.18. Large Percentages of Open Porosity Cause Permeable Coatings.

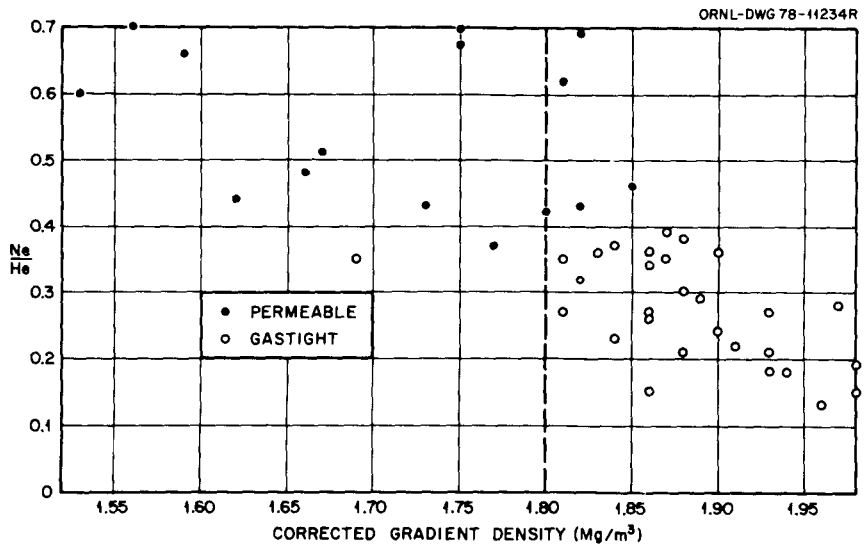


Fig. 2.19. Low Corrected-Gradient Densities Cause Permeable Coatings.

### 2.3.1.2 Ne:He Intrusion Measurements on Biso Coatings — C. S. Morgan and G. L. Powell

A topical report covering the use of Ne:He ratio measurements in evaluating permeability of the PyC coatings for HTGR Biso-fuel particles has been completed,[27] which discusses the progress made in 1978. The abstract of this report follows.

> The permeability of the PyC coatings of Biso-fuel particles has been measured by intrusion of inert gases, particularly helium and neon. The experimental procedures and mass-spectrometer measurements for evaluating inert-gas permeability of coatings are reported. The mole quantity ratio of Ne:He entering the particles in 1 hr at 1375°C constitutes a useful measure of the coating permeability. Activation energy results are given for intrusion of helium, neon, and argon. Pyrocarbon coatings have a measurable permeability for krypton only at very high temperatures and in the more permeable coatings. The permeability of Biso-coated fuel particles with inert kernels is reduced by neutron irradiation. Ne:He ratios measured on hundreds of fuel-particle batches range from 0.03 to greater than 1.0, and it is estimated that a fuel-particle batch with a ratio below 0.3 to 0.35 will be gastight under HTGR operating conditions.

### 2.3.2 Pyrocarbon Coating by Use of $CO_2$ Carrier Gas — D. P. Stinton

Work was initiated this year to produce PyC coatings by using $CO_2$ as the diluent. Evidence from several irradiation tests[28*] indicated that $CO_2$ dilution[†] improved the irradiation performance by making the coatings less permeable. The first few runs[‡] used 50% $CO_2$ and 50% coating gas. These conditions produced gastight coatings, but the fraction of cracked or otherwise defective particles was quite high. The use of 50% $CO_2$ also oxidized the graphite components of the furnace quite severely. Coatings were then deposited by using 25% $CO_2$ and 75% coating gas. The fluidization of the particle bed was found to be only marginal, with

---

*HT-34 experiment; see Sect. 2.2.1.5 of this report.

†Coating deposited in laboratory-scale coaters.

‡Coating deposited in production-scale coaters.

25% dilution at the desired coating rates. These conditions reduced the initial fraction of defective particles. Future work will be concentrated on producing coatings from a mixture of argon and $CO_2$ that will be sufficient to fluidize the particles and produce gastight coatings.

### 2.3.3 Dense UCO Fuel Development — D. P. Stinton and J. E. Seele

The fissile kernels for MEU-fueled HTGRs will be microspheres about 360 μm in diameter produced by the sol-gel process. Carbon is added to the $UO_3$ broth, and the microspheres are produced. After drying the $UO_3$ + C, microspheres are calcined to remove such volatiles as $H_2O$, $NH_3$, $NO_3^-$, and other organics. The microspheres are then converted to $UO_2$ + $UC_2$ and sintered at high temperatures to near-theoretical density. Work was initiated to determine the amount of carbon and a sintering schedule that would produce high-density spheres of the desired composition.

Numerous batches of sol-gel-derived microspheres with a composition of $UO_2$ plus various amounts of carbon were heat treated. The heat treatment consisted of heating at 100°C to 450°C/h in argon, then heating at 300°C/h to the desired temperature, and holding for 4 h. These microspheres were characterized by x-ray diffraction, and the results are shown in Table 2.7. From these results, it became clear that large amounts of carbon were lost from the microspheres and that small amounts of UC were being formed instead of $UC_2$. Loss of carbon is undesirable because careful composition control of the kernel is necessary. The formation of UC is also undesirable because carbon from the buffer coating will react with the UC and alter the kernel composition. Various atmospheres during calcining and sintering are being tested to reduce the loss of carbon during calcining and the formation of UC during sintering.

### 2.3.4 Silicon Carbide Development, Characterization, and Testing — R. J. Lauf and V. J. Tennery

A need exists for improved understanding of SiC interactions with silver and palladium in HTGR fuel particles for the following reasons:

Table 2.7. Characterization of $UO_2$ + C Microspheres

| Run number | C:U ratio before sintering | C:U ratio after sintering | Kernel density[a] ($Mg/m^3$) | Composition (%) | | |
|---|---|---|---|---|---|---|
| | | | | $UO_2$ | $UC_2$ | UC |
| S-167[b] | 3.0 | 1.94 | 5.76 | 0 | 70-90 | 10-30 |
| V-125B[c] | 1.5 | 0.51 | 8.80 | 75-90 | 5-15 | 5-10 |
| S-168 | 1.0 | 0.06 | 9.24 | 80-95 | 0 | 5-20 |
| S-169 | 0.65 | 0.04 | 8.96 | 85-95 | 0 | 5-15 |
| S-170 | 0.3 | 0.02 | 6.30 | 100 | 0 | 0 |

[a]As measured by mercury porosimetry.

[b]All S-runs were sintered at 1550°C for 4 h in a static bed.

[c]Sintered at 1650°C for 2 h in a fluidized bed.

1. Release of silver from the fuel particles is undesirable because it results in high gamma activity in the primary coolant circuit as a result of its rapid diffusion through the graphite in the core.
2. Both in-reactor studies and out-of-reactor annealing experiments have shown that silver and palladium can attack the SiC coatings of HTGR fuel particles.
3. The fission of LEU fuel produces about 50 times more silver and 10 times more palladium than does the fission of HEU fuel. Silver and palladium inventories in MEU fissile particles at 27% FIMA are 10 and 2.5 times higher, respectively, than the inventories in HEU fuel at 80% FIMA.

### 2.3.4.1 Experimental Plan

Previous work[29,30] identified deposition parameters that affect SiC coating density and microstructure. These parameters are deposition temperature, coating rate, and hydrogen-to-methyltrichlorosilane ratio ($H_2$:MTS). The goal of the present work is to optimize the SiC deposition conditions with respect to maximizing retention of silver and palladium in HTGR fuel particles.

To determine the optimum SiC deposition parameters, SiC coatings will be applied to $UO_2$ microspheres containing small amounts of silver

and palladium (to simulate fission products). A wide range of deposition parameters will be used to produce a range of SiC microstructures; the experimental coating matrix selected on the basis of previous work is given in Table 2.8. Annealing studies of SiC-coated simulated high-burnup fuel particles conducted subsequent to coating will make possible the determination and optimization of those SiC deposition parameters that are critical to the retention of silver and palladium.

Table 2.8. Silicon Carbide Coating Parameters to Be Investigated

| Coating rate (μm/min) | $H_2$:MTS[a] ratios for temperatures (°C) of — | | | |
|---|---|---|---|---|
| | 1500 | 1550 | 1650 | 1700 |
| 0.2-0.4 | 50:1 | 50:1 | 75:1 | 90:1 |
| 0.5-0.7 | 50:1 | 50:1 | 75:1 | 90:1 |
| 1.0-1.5 | 50:1 | 50:1 | 75:1 | 90:1 |

[a]Hydrogen-to-methyltrichlorosilane.

Silicon carbide-coating microstructures must be characterized on a finer scale than previously thought because of the complex nature of the SiC microstructure and the scale of its major features. All phases must be identified, including SiC polytypes and the size and distribution of microporosity. This identification will be made by using transmission and scanning-transmission electron microscopy (TEM and STEM) techniques on ion-thinned foils of coating specimens of known orientation.

The diffusivity of silver in SiC single crystals will be studied in parallel with our other work and will provide baseline data on the lowest possible value for silver transport in SiC coatings.

### 2.3.4.2 Results and Discussion

To provide highly reproducible SiC coating rates, a Tylan source II MTS generator* was purchased, installed, and calibrated. This

*Tylan Corporation, 19220 S. Normandie Avenue, Torrance, Calif. 90502.

instrument accurately maintains a preset flow of MTS into the coating furnace.

Simulated high-burnup fuel kernels consisting of $UO_2$ microspheres containing silver or palladium have been produced by infiltration of the microspheres with aqueous $AgNO_3$ or $PdCl_2$, followed by thermal decomposition at 600°C in hydrogen. These simulated spent fuel particles can be Triso coated and annealed in a thermal gradient to evaluate silver and palladium attack or retention under thermal conditions similar to those in an HTGR.

Samples of coating fragments are being examined in a JEM 100CX electron microscope. A typical coating microstructure and a typical diffraction pattern are shown in Figs. 2.20 and 2.21, respectively.

The microstructure of a specimen from coating run SC207 is shown in Fig. 2.20. The grains are heavily faulted and contain numerous microtwins. X-ray diffraction showed that the microstructure is nearly all fcc beta-SiC, but a diffraction line that was possibly from the hcp or alpha-SiC phase was also observed. Selected-area electron diffraction patterns also showed traces of another phase that could be HCP in this particular coating.

An example of an electron diffraction pattern taken from a beta-SiC grain is given in Fig. 2.21. Splitting of the low-index reflections indicates that the structure is twinned, whereas the streaks joining these reflections are caused by the large number of stacking faults present. [The upward electron beam normal $\bar{B}$ for this pattern is $(\bar{1}\bar{1}0)$.]

Work is under way to identify the morphology of the few alpha micrograins detected so that micrographs of the SiC coatings can be interpreted quantitatively.

### 2.3.4.3 Work Plan for the Next Reporting Period

Batches of $UO_2$ microspheres containing silver and palladium will be Triso coated according to the parameters given in Table 2.8. These batches will then be annealed at typical HTGR operating temperatures and with typical HTGR thermal gradients,[31] and their behavior with respect to fission product retention will be evaluated.

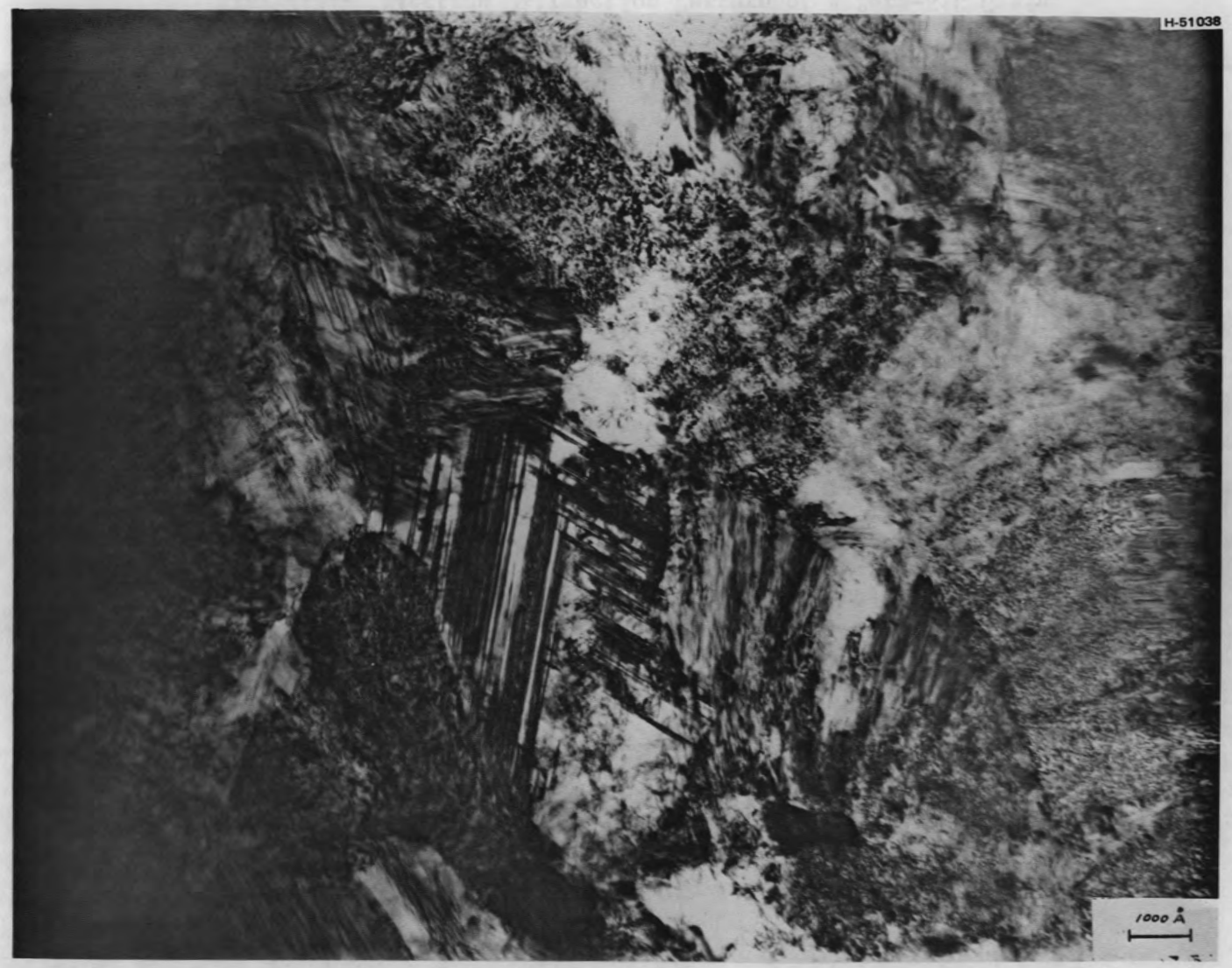


Fig. 2.20. Typical SiC Coating Microstructure at 65000 × showing Heavily Faulted Beta-SiC grains.

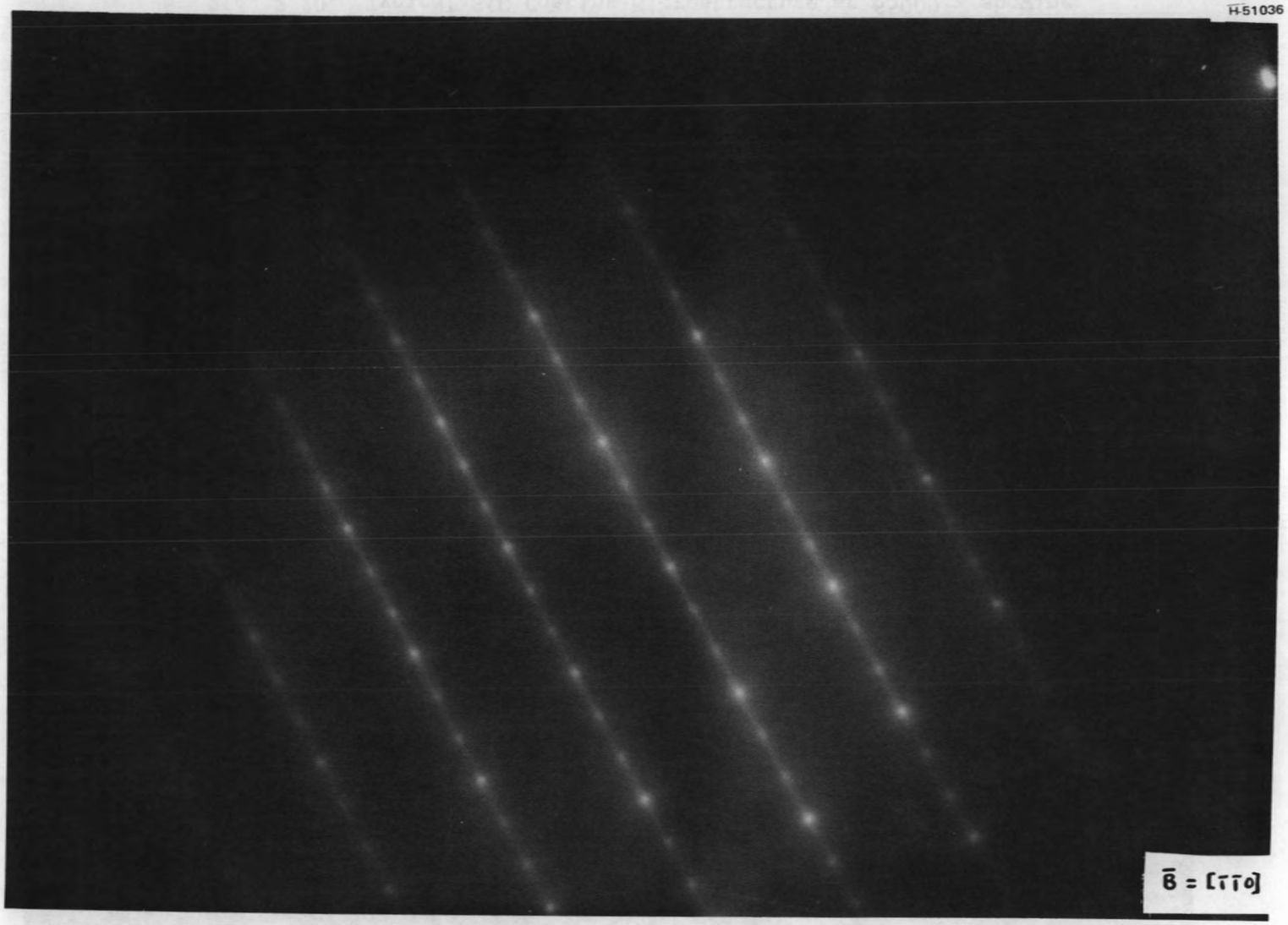


Fig. 2.21. Electron Diffraction Pattern of a Beta-SiC Grain, Showing the Effect of Twins and Faulting.

Microstructures of SiC coatings will be analyzed by transmission electron microscopy and other techniques. A preliminary report on SiC microstructure characterization is scheduled for June 1979.

A preliminary report on the relation between SiC microstructure and deposition parameters is scheduled for December 1979. A preliminary report on fission product attack/retention correlations with SiC microstructure is scheduled for March 1980.

## 2.4 IRRADIATION SUPPORT ACTIVITIES — F. J. Homan

This work is associated with both supplementing and improving the quality of information developed through irradiation testing. In the past, work associated with characterizing the irradiation facilities (temperatures, flux distributions, etc.) was included. No work has been done during the current reporting period on capsule thermometry, flux mapping, or gamma-heating characterization. Both nuclear and thermal analyses of the HRB-15b capsule are included. The out-of-reactor, thermal-gradient heating experiments to measure fission product/SiC coating interaction rates are also reported.

### 2.4.1 Nuclear Evaluation and Thermal Analysis — W. E. Thomas

#### 2.4.1.1 Experiment HRB-15b: Particle Loadings and Thermal and Neutronics Analysis

Experiment HRB-15b was irradiated in the HFIR removable beryllium reflector facility RB-5. The experiment was in the reactor for eight cycles; the first cycle began at 4:15 PM (EDT) on July 6, 1978.

The purpose of the experiment was to test a variety of HTGR particles: fissile, fertile, Triso, and Biso. The loose particles were loaded into trays that resembled flat graphite washers, each having 116 holes drilled in one face. The trays were stacked in an alternate fertile-particle, fissile-particle sequence — 46 trays per unit or subassembly. A column of four units was sealed in a stainless steel primary vessel. The primary vessel was contained in a secondary stainless steel vessel to provide double-wall containment for the experiment.

When in the reactor, heat is removed from the experiment by the flow of reactor coolant (water) through an annulus external to the secondary vessel.

The experiment tested 18 different types of HTGR fissile particles and 5 types of HTGR fertile particles. The types of particles to be loaded into each of the 184 trays had been predetermined and were not subject to change. Our obligation was limited to specifying the number of particles of each type to be loaded into each of the 184 trays. The approach taken for specifying particle loading for the experiment can be broken down into four major steps: (1) fuel depletion per particle type, (2) power matching, (3) temperature matching, and (4) final thermal analysis to confirm the design. Each of the steps is discussed briefly below; a topical report is being prepared to document details of the design.

For calculating fuel depletion, fissile particles were reclassified into seven types according to initial amounts of fissile material contained in the kernel. Data for each particle type are shown in Table 2.9. All uranium was 20% enriched in $^{235}U$. The fuel depletion computation provides power (watts) per particle for each particle type during the irradiation history at 24 discrete axial positions, that is, average power per particle as a function of axial position and irradiation time for each particle classification. We used the CACA-2 code[32] (with some revisions) for performing these calculations. A value of 180 MeV per fission was used for useful energy release per fission locally within the specimen region. For thermal analysis, nuclear heating in the graphite trays would augment the heat source in that region. The magnitude of the time-averaged total neutron flux was determined by the results from a previous experiment.[33] Time-averaged total neutron flux varies from about $2.4 \times 10^{19}$ neutrons $m^{-2}$ $s^{-1}$ near the HMP to about $1.0 \times 10^{19}$ neutrons $m^{-2}$ $s^{-1}$ at the extremities of the experiment. The cylindrical reactor control plates ("rods") are located between the experiment and the reactor core. During each reactor cycle, motion of the control plates introduces considerable variation in the neutron flux in the experiment. To account for these perturbations, the

Table 2.9. Particle Classification for Fuel Depletion Study Experiment HRB-15b

| Type | Kernel material | Kernel loading (Mg U/Th) |
|---|---|---|
| | Fissile particles | |
| I | $(Th\text{-}U)O_2$ | 0.111/0.109 |
| II | UCO (o/u = 0.5) | 0.258/ |
| III | UCO (o/u = 1.5) | 0.237/ |
| IV | UCO (o/u = 1.0) | 0.207/ |
| V | $UC_2$ | 0.216/ |
| VI | $UO_2$ | 0.130/ |
| VII | $UO_2$ | 0.150/ |
| | Fertile particles | |
| I | $ThO_2$ | /0.412 |
| II | $ThO_2$ | /0.430 |
| III | $ThO_2$ | /0.590 |
| IV | $ThO_2$ | /0.600 |
| V | $ThO_2$ | /0.575 |

experimentally determined time-averaged total neutron flux was multiplied by normalized time distribution functions; that is:

$$\bar{\phi}(z, t) = \psi(z, t)\bar{\phi}(z) ,$$

where:

$$\int_{\text{time}} \psi(z, t)dt = 1.0 .$$

One-group microscopic cross sections[33] used to calculate fuel depletion are shown in Table 2.10; the values shown in parentheses are results from sensitivity studies with previous rod-type HRB experiments. We found that the cross sections not in parentheses were more realistic for the dilute HRB-15b experiment.

A one-dimensional cylindrical heat-transfer model was chosen for computing temperatures in the various regions of the experiment. Early in the irradiation history, trays containing fissile particles produced

Table 2.10. One-Group Microscopic Cross Section (barn) for Experiment HRB-15b

| Nuclide | Capture | Fission |
|---|---|---|
| $^{232}Th$ | 3.96 (2.77) | 0.008 (0.006) |
| $^{233}Pa$ | 32.2 | |
| $^{234}Pa$ | 150.0 | 1500.0 |
| $^{233}U$ | 16.1 | 151.0 |
| $^{234}U$ | 40.1 | |
| $^{235}U$ | 27.9 | 144.0 |
| $^{236}U$ | 10.2 | |
| $^{237}U$ | 110.0 | |
| $^{238}U$ | 8.44 (5.908) | 0.033 (0.023) |
| $^{237}Np$ | 65.6 | |
| $^{238}Np$ | 13.0 | 570.0 |
| $^{239}Np$ | 8.3 | |
| $^{238}Pu$ | 130.0 | |
| $^{239}Pu$ | 142.0 | 281.0 |
| $^{240}Pu$ | 287.0 | |
| $^{241}Pu$ | 109.0 | 239.0 |
| $^{242}Pu$ | 36.5 | |

most of the fission heat, whereas later, as bred uranium built up in the adjacent trays of fertile particles, fission heat in those trays also became significant. The particle-stacking pattern suggests that it is reasonable to model the specimen region with a uniformly dispersed heat source contributed by one tray of fertile particles plus one tray of fissile particles. Once the experiment is in the reactor, the only way that particle temperatures can be controlled is by varying the composition of sweep gas, that is, by varying thermal conductivity in the gap between the stack of trays and the capsule primary vessel. Ideally, we would load each tray such that the power per each tray pair would change the same amount with time. If the ideal condition were possible, we could load the trays and vary gap thickness to obtain a flat axial temperature profile continuously throughout the irradiation history.

Because of the HFIR control rod management, we cannot achieve the above ideal condition, but we can power-match at two points in time. That is, we can load the trays to obtain a common value for the constant c in the following equation:

$$c = (N_1P_{12} + N_2P_{22}/N_1P_{11} + N_2P_{21}) \ , \tag{1}$$

where $N_1$ is the number of fissile particles in a tray, and $N_2$ is the number of fertile particles in the adjacent tray; $P_{11}$ is the power per fissile particle at, say, the beginning of life (BOL), and $P_{12}$ is the power per fissile particle at some other time, such as at the middle of cycle seven. Likewise, $P_{21}$ and $P_{22}$ are power per fertile particle at BOL and mid-cycle-seven, respectively. Power per particle depends on the type of particle to be loaded into each tray and the axial position of that tray in the experiment. It is also advantageous to maximize the value for c in Eq. (1) above. The highest value for c reduces the likelihood of using argon gas and having to cope with $^{41}Ar$ activities in the sweep gas. Helium and mixtures of helium and neon were preferred. We obtained c = 0.5, which was adequate. A more useful form of Eq. (1) is expressed in terms of the ratio of the number of fertile particles to the number of fissile particles $R$ for each tray pair.

$$R = (cP_{11} - P_{12})/(P_{22} - cP_{21}) \ . \tag{2}$$

A maximum of 116 particles can be loaded into a tray. The minimum number of particles per tray $M$ was specified to be not less than about 60. Hence, for a loading to be acceptable, the implication is that the value for $R$ must lie within the following range:

$$(M/116) \leqslant R \leqslant (116/M) \tag{3}$$

In the discussion that follows, assume that $R$ is within acceptable range. If $R = 1.0$, then 116 fertile particles and 116 fissile particles could be loaded in the tray pair. If $R < 1.0$, only the tray containing

fissile particles could be filled; $R > 1.0$ implies that only the tray containing fertile particles can be filled. An acceptable minimum number of particles will also be in each tray. The minimum number of particles per tray also depends on the value of $R$. For example, if $R > 1.0$, there will be $M$ ($\sim$60) fissile particles per tray but somewhat more (the product $RM$) fertile particles in the adjacent tray. Hence, the fission power per each tray pair can range from some maximum power to some minimum power. The trays should be loaded such that a plot of the fission power per each tray pair versus the mean axial position of that tray pair will form a smooth curve and will always lie between maximum and minimum.

The axial temperature profile should be as flat (constant) as possible. The only remaining variable for "temperature matching" is the gap between each tray and the capsule primary vessel. The gap can be varied by varying the tray diameter. In deciding on tray diameters, we try to avoid the conditions of a small gap, then of a larger gap, then back to the conditions of a smaller gap over each half-length of the experiment; that is, we strive for a step-wise increasing gap from the middle of the experiment to each extremity. The temperature rise across the gap varies directly with gap thickness. Both the fission rate per unit volume of fuel and the nuclear heating in graphite[34] decrease from the middle to each end of the experiment. If the temperature at the inside radius of each tray pair is to be constant, the sum of the nuclear heating in graphite plus the fission power from the particles in the trays must also be a constant over the length of each stack of trays having the same diameter. This situation implies that there will be a "best compromise" fission power per tray pair $P^*$. Once $P^*$ is known, the number of particles to be loaded into each tray can be computed; $P^*$ should range between the maximum and the minimum power per tray pair and should also be as large as possible in order to load the most particles in the experiment. A summary of the expressions applicable to particle loading is given in Table 2.11.

Before the experiment was placed in the reactor, several additional thermal cases were run. The purpose of these calculations was to (1) check the computed temperatures at various times during a cycle and

Table 2.11. Experiment HRB-15b: Summary of Expressions for Particle Loading

| | $R > 1.0$ | $R < 1.0$ |
|---|---|---|
| Range of particles per tray | | |
| Maximum number of fertile particles | 116 | $116R$ |
| Maximum number of fissile particles | $116/R$ | 116 |
| Minimum number of fertile particles | $MR$ | $M$ |
| Minimum number of fissile particles | $M$ | $M/R$ |
| Range of fission power per tray pair | | |
| Maximum power | $(P_{11}/R + P_{21})116$ | $(P_{11} + P_{21}/R)116$ |
| Minimum power | $(P_{11} + RP_{21})M$ | $(P_{11}/R + P_{21})M$ |
| Number of particles loaded per tray | | |
| Fertile particles | $RP^*/(P_{11} + RP_{21})$ | $RP^*/(P_{11} + P_{21}/R)$ |
| Fissile particles | $P^*/(P_{11} + RP_{21})$ | $P^*/(P_{11} + P_{21}/R)$ |

over the expected irradiation history (many cycles); (2) check the sensitivity of the computed temperatures to uncertainties in basic thermal data, for example, thermal conductivity, surface emissivity, coefficient of linear expansion, etc.; and (3) include graphite growth[35] in the model and test its effect on temperature control. The maximum tray diameter (23.57 mm) was established from consideration of anticipated graphite growth. Tray size and final loadings are shown in Tables 2.12 through 2.15 for each unit in the experiment. Particles in each tray are identified by test plan designation.

Our preirradiation results indicated that, with helium sweep gas, temperatures at the inside surface of those trays located around the HMP should stabilize at about 800°C early in the first cycle. After about 1 d of power operation, the thermocouples in the bottom of unit 15b-2 and those in the top and bottom of unit 15b-3 peaked at 775°C, 795°C, and 810°C, respectively. Agreement between computed temperatures

Table 2.12. Experiment HRB-15b, Tray Size and Particle Loadings for Subassembly 15b-1

| Tray | | Fertile particles | | Tray | | Fissile particles | |
|---|---|---|---|---|---|---|---|
| Identification | Radius (in.) | Identification | Number | Identification | Radius (in.) | Identification | Number |
| 1 | 0.439 | ORNL | 58 | 2 | 0.439 | 8 | 116 |
| 3 | 0.439 | ORNL | 85 | 4 | 0.439 | 12 | 106 |
| 5 | 0.439 | 17-B | 116 | 6 | 0.439 | 10 | 65 |
| 7 | 0.439 | ORNL | 58 | 8 | 0.439 | 1 | 116 |
| 9 | 0.439 | ORNL | 58 | 10 | 0.439 | 1 | 116 |
| 11 | 0.448 | ORNL | 106 | 12 | 0.448 | 3 | 83 |
| 13 | 0.448 | ORNL | 106 | 14 | 0.448 | 3 | 83 |
| 15 | 0.448 | 15 | 116 | 16 | 0.448 | 5 | 114 |
| 17 | 0.454 | ORNL | 111 | 18 | 0.454 | 2 | 65 |
| 19 | 0.454 | ORNL | 111 | 20 | 0.454 | 14 | 77 |
| 21 | 0.454 | 17-B | 116 | 22 | 0.454 | 4 | 73 |
| 23 | 0.454 | 15 | 116 | 24 | 0.454 | 13-A | 97 |
| 25 | 0.458 | ORNL | 112 | 26 | 0.458 | 4 | 69 |
| 27 | 0.458 | ORNL | 112 | 28 | 0.458 | 13-B | 108 |
| 29 | 0.458 | ORNL | 112 | 30 | 0.458 | 2 | 63 |
| 31 | 0.458 | 16 | 102 | 32 | 0.458 | 5 | 116 |
| 33 | 0.458 | 17-B | 116 | 34 | 0.458 | 7 | 68 |
| 35 | 0.458 | ORNL | 103 | 36 | 0.458 | 5 | 113 |
| 37 | 0.461 | ORNL | 116 | 38 | 0.461 | 7 | 76 |
| 39 | 0.461 | ORNL | 105 | 40 | 0.461 | 6-B | 99 |
| 41 | 0.461 | ORNL | 105 | 42 | 0.461 | 6-B | 99 |
| 43 | 0.461 | 15 | 116 | 44 | 0.461 | 4 | 66 |
| 45 | 0.461 | ORNL | 105 | 46 | 0.461 | 7 | 68 |

Table 2.13. Experiment HRB-15b, Tray Size and Particle Loadings for Subassembly 15b-2

| Tray | | Fertile particles | | Tray | | Fissile particles | |
|---|---|---|---|---|---|---|---|
| Identification | Radius (in.) | Identification | Number | Identification | Radius (in.) | Identification | Number |
| 47 | 0.461 | 16 | 69 | 48 | 0.461 | 1 | 116 |
| 49 | 0.461 | ORNL | 72 | 50 | 0.461 | 1 | 116 |
| 51 | 0.461 | 17-B | 104 | 52 | 0.461 | 1 | 116 |
| 53 | 0.461 | ORNL | 75 | 54 | 0.461 | 1 | 116 |
| 55 | 0.461 | ORNL | 75 | 56 | 0.461 | 1 | 116 |
| 57 | 0.461 | 16 | 72 | 58 | 0.461 | 1 | 116 |
| 59 | 0.461 | ORNL | 78 | 60 | 0.461 | 1 | 116 |
| 61 | 0.461 | ORNL | 78 | 62 | 0.461 | 1 | 116 |
| 63 | 0.461 | ORNL | 78 | 64 | 0.461 | 1 | 116 |
| 65 | 0.461 | ORNL | 78 | 66 | 0.461 | 1 | 116 |
| 67 | 0.464 | 17-B | 116 | 68 | 0.464 | 9 | 55 |
| 69 | 0.464 | ORNL | 109 | 70 | 0.464 | 13-C | 91 |
| 71 | 0.464 | 15 | 116 | 72 | 0.464 | 11 | 57 |
| 73 | 0.464 | ORNL | 108 | 74 | 0.464 | 3 | 65 |
| 75 | 0.464 | ORNL | 108 | 76 | 0.464 | 3 | 62 |
| 77 | 0.464 | 16 | 103 | 78 | 0.464 | 3 | 62 |
| 79 | 0.464 | ORNL | 107 | 80 | 0.464 | 3 | 62 |
| 81 | 0.464 | 17-B | 116 | 82 | 0.464 | 3 | 62 |
| 83 | 0.464 | ORNL | 107 | 84 | 0.464 | 4 | 54 |
| 85 | 0.464 | ORNL | 107 | 86 | 0.464 | 3 | 62 |
| 87 | 0.464 | 15 | 116 | 88 | 0.464 | 6-B | 85 |
| 89 | 0.464 | ORNL | 107 | 90 | 0.464 | 7 | 59 |
| 91 | 0.464 | ORNL | 86 | 92 | 0.464 | 1 | 114 |

Table 2.14. Experiment HRB-15b, Tray Size and Particle Loadings for Subassembly 15b-3

| Tray | | Fertile particles | | Tray | | Fissile particles | |
|---|---|---|---|---|---|---|---|
| Identification | Radius (in.) | Identification | Number | Identification | Radius (in.) | Identification | Number |
| 93 | 0.464 | 15 | 114 | 94 | 0.464 | 1 | 114 |
| 95 | 0.464 | ORNL | 107 | 96 | 0.464 | 7 | 59 |
| 97 | 0.464 | 16 | 103 | 98 | 0.464 | 6-B | 85 |
| 99 | 0.464 | ORNL | 107 | 100 | 0.464 | 3 | 61 |
| 101 | 0.464 | ORNL | 107 | 102 | 0.464 | 5 | 98 |
| 103 | 0.464 | 17-A | 105 | 104 | 0.464 | 3 | 62 |
| 105 | 0.464 | 15 | 116 | 106 | 0.464 | 3 | 62 |
| 107 | 0.464 | 17-A | 105 | 108 | 0.464 | 3 | 62 |
| 109 | 0.464 | ORNL | 107 | 110 | 0.464 | 3 | 62 |
| 111 | 0.464 | ORNL | 109 | 112 | 0.464 | 3 | 66 |
| 113 | 0.464 | ORNL | 87 | 114 | 0.464 | 8 | 116 |
| 115 | 0.464 | ORNL | 110 | 116 | 0.464 | 10 | 66 |
| 117 | 0.464 | 16 | 105 | 118 | 0.464 | 12 | 105 |
| 119 | 0.464 | ORNL | 114 | 120 | 0.464 | 6-A | 98 |
| 121 | 0.464 | 16 | 109 | 122 | 0.464 | 6-A | 98 |
| 123 | 0.464 | ORNL | 114 | 124 | 0.464 | 6-A | 98 |
| 125 | 0.464 | ORNL | 114 | 126 | 0.464 | 6-A | 98 |
| 127 | 0.464 | 17-A | 115 | 128 | 0.464 | 6-A | 105 |
| 129 | 0.464 | ORNL | 116 | 130 | 0.464 | 6-A | 105 |
| 131 | 0.464 | 15 | 116 | 132 | 0.464 | 6-A | 105 |
| 133 | 0.464 | ORNL | 116 | 134 | 0.464 | 6-A | 105 |
| 135 | 0.464 | ORNL | 116 | 136 | 0.464 | 6-A | 112 |
| 137 | 0.464 | 16 | 116 | 138 | 0.464 | 6-A | 112 |

Table 2.15. Experiment HRB-15b, Tray Size and Particle Loadings for Subassembly 15b-4

| Tray | | Fertile particles | | Tray | | Fissile particles | |
|---|---|---|---|---|---|---|---|
| Identification | Radius (in.) | Identification | Number | Identification | Radius (in.) | Identification | Number |
| 139 | 0.458 | ORNL | 70 | 140 | 0.458 | 1 | 116 |
| 141 | 0.458 | 17-A | 90 | 142 | 0.458 | 3 | 62 |
| 143 | 0.458 | ORNL | 70 | 144 | 0.458 | 1 | 116 |
| 145 | 0.458 | 15 | 116 | 146 | 0.458 | 3 | 62 |
| 147 | 0.458 | ORNL | 99 | 148 | 0.458 | 5 | 108 |
| 149 | 0.458 | ORNL | 99 | 150 | 0.458 | 2 | 55 |
| 151 | 0.458 | ORNL | 99 | 152 | 0.458 | 4 | 60 |
| 153 | 0.458 | 16 | 95 | 154 | 0.458 | 13-C | 94 |
| 155 | 0.454 | ORNL | 107 | 156 | 0.454 | 13-A | 103 |
| 157 | 0.454 | ORNL | 107 | 158 | 0.454 | 14 | 72 |
| 159 | 0.454 | ORNL | 107 | 160 | 0.454 | 4 | 66 |
| 161 | 0.454 | 17-A | 105 | 162 | 0.454 | 6-C | 104 |
| 163 | 0.448 | 15 | 116 | 164 | 0.448 | 6-C | 103 |
| 165 | 0.448 | ORNL | 99 | 166 | 0.448 | 7 | 69 |
| 167 | 0.448 | 16 | 95 | 168 | 0.448 | 4 | 63 |
| 169 | 0.448 | ORNL | 99 | 170 | 0.448 | 6-B | 99 |
| 171 | 0.448 | ORNL | 100 | 172 | 0.448 | 7 | 75 |
| 173 | 0.448 | ORNL | 93 | 174 | 0.448 | 5 | 116 |
| 175 | 0.448 | 17-A | 91 | 176 | 0.448 | 6-B | 101 |
| 177 | 0.448 | ORNL | 93 | 178 | 0.448 | 7 | 70 |
| 179 | 0.448 | ORNL | 93 | 180 | 0.448 | 9 | 59 |
| 181 | 0.448 | 15 | 116 | 182 | 0.448 | 13-B | 100 |
| 183 | 0.448 | ORNL | 93 | 184 | 0.448 | 11 | 64 |

and measured temperatures appeared to be quite good. The axial temperature profile, Fig. 2.22, was expected to be more symmetrical about the HMP than the early results had indicated. We discovered that the middle of the experiment was positioned about 0.02 m above the HMP, which is probably the reason for the asymmetric axial temperature distribution. Temperatures shown in all figures are results from

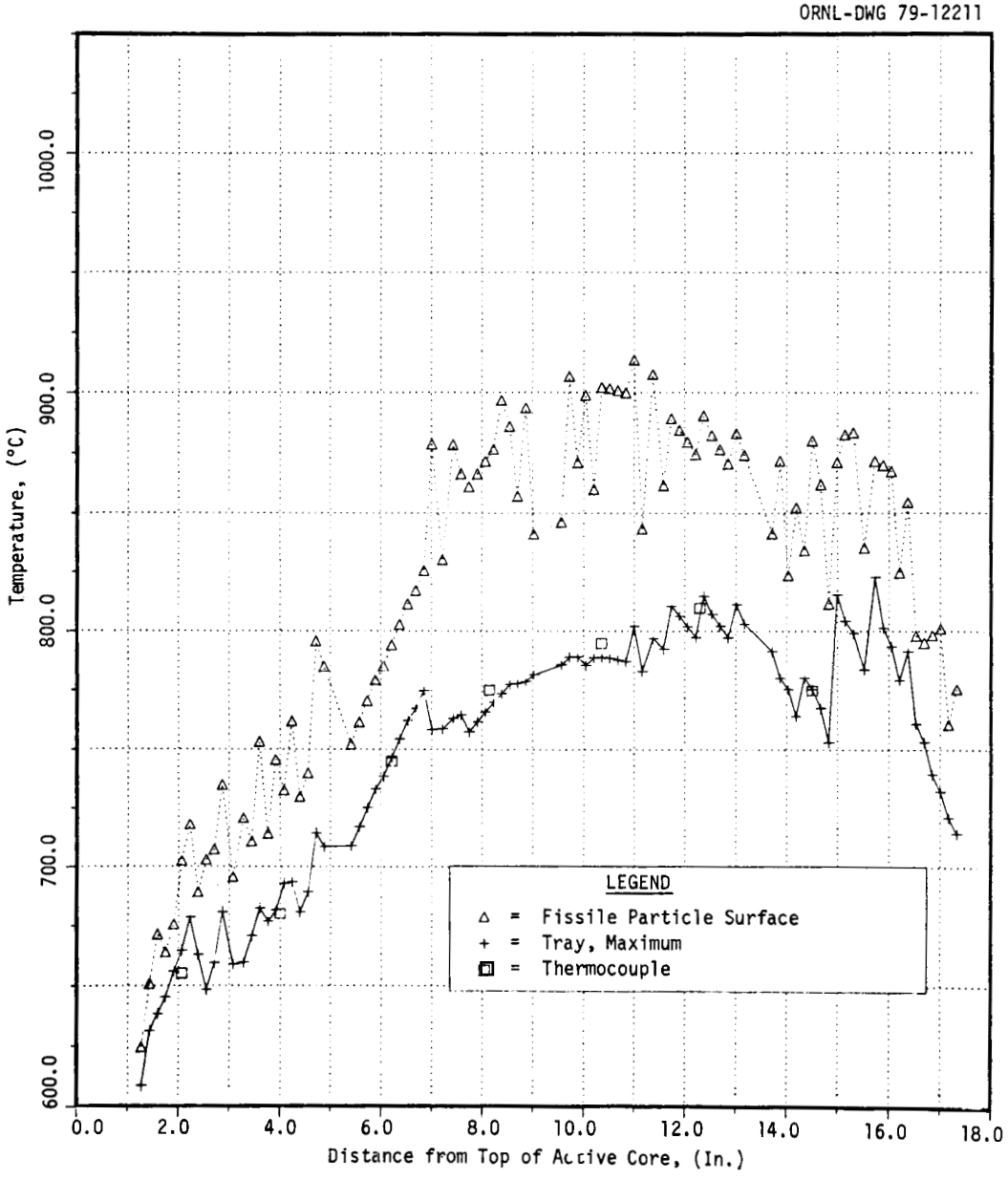


Fig. 2.22. Experiment HRB-15b, Temperature Versus Axial Position at 1 d into Cycle 1.

separate one-dimensional heat-transfer calculations. The temperatures are connected by straight lines to form the axial profiles shown in each graph. Temperatures labeled "tray maximum" are computed at the tray inside radius, which is approximately the location of each thermocouple. During cycle one, helium was used as sweep gas; beginning with the second cycle (7-31-78), fuel had burned out enough so that mixtures of helium and neon could be used to control temperatures. Temperatures in Fig. 2.23 illustrate the distribution early in cycle two, and the temperatures in Fig. 2.24 show how the distribution has changed toward the end of the cycle; that is, these two graphs illustrate the effect that HFIR control rod management has on the axial temperature profile during a cycle. By the end of cycle three (9-13-78), a procedure and the necessary parts were available for centering the experiment with respect to reactor HMP. As illustrated in Fig. 2.25, axial temperature distribution was more symmetrical about the reactor HMP thereafter.

Another temperature requirement was that the maximum particle-surface temperature should not exceed 1000°C for any particle in the experiment. To represent a particle resting in the drilled holes, we considered both an equivalent 1-D spherical model and multidimensional models. The multidimensional models required considerable setup time to prepare input for the heating code;[36] results were not complete until after startup. The 1-D spherical model overestimated $\Delta t$ (tray to particle surface). It was used only until better results became available. Convection was ignored with all models. For the 800-μm particle, results from the heating code for maximum $\Delta t$ could be expressed as functions of sweep gas composition, particle power $p$, and tray mean temperature $T$. With helium sweep gas, the expression is as follows:

$$\Delta t_{(\max)} = P(2915.7387 - T)/19.1415 \ . \qquad (4)$$

If $P$ = 1.32 W per particle and $T$ = 800°C, $\Delta t$ from Eq. (4) is 146°C. For the same problem, the 1-D spherical model estimates average $\Delta t$ = 183°C. Equations similar to Eq. (4) for various mixtures of helium and neon were programmed in our thermal code for use in computing maximum paticle-surface temperature during the irradiation history of the experiment.

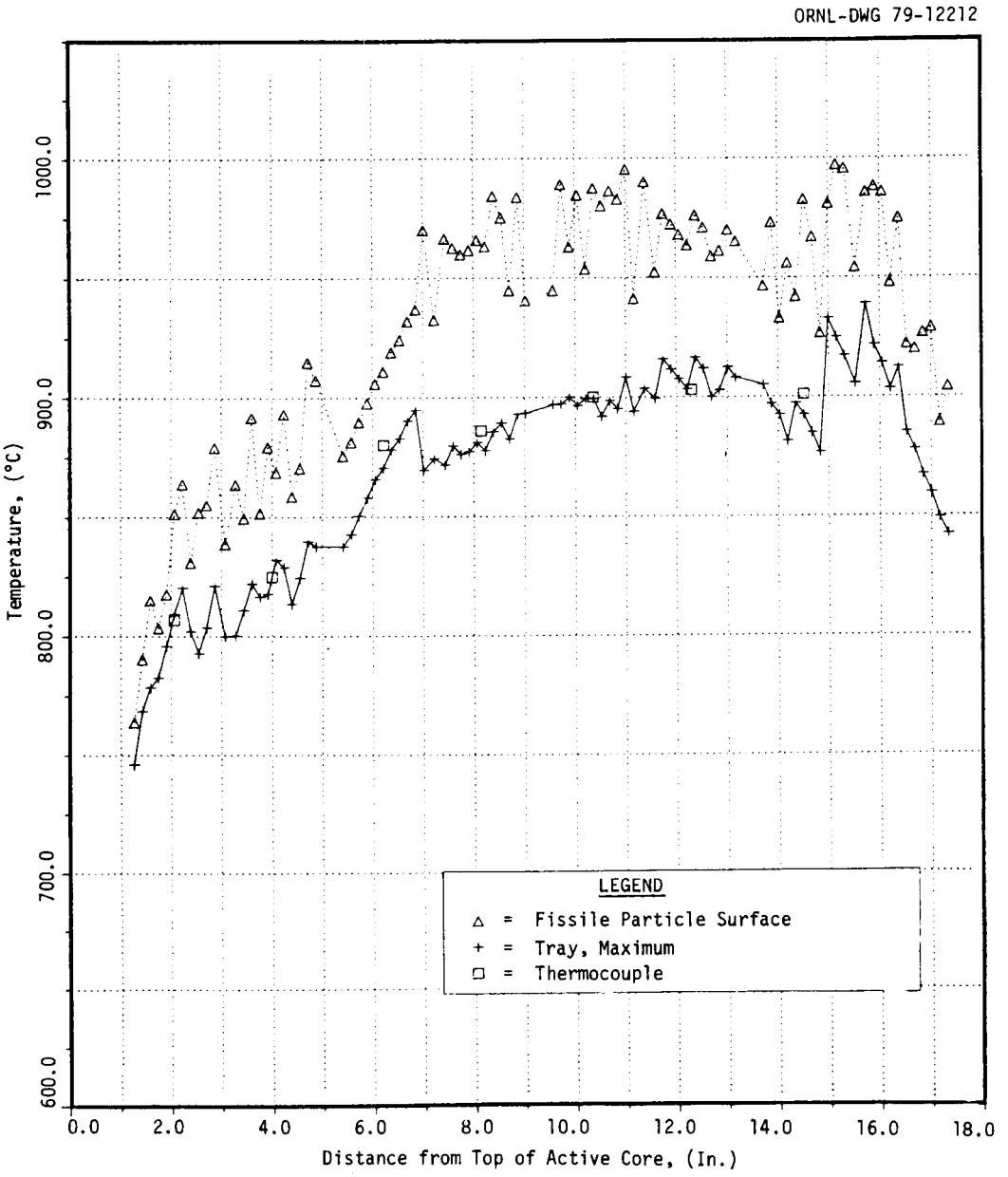


Fig. 2.23. Experiment HRB-15b, Temperature Versus Axial Position at 2 d into Cycle 2.

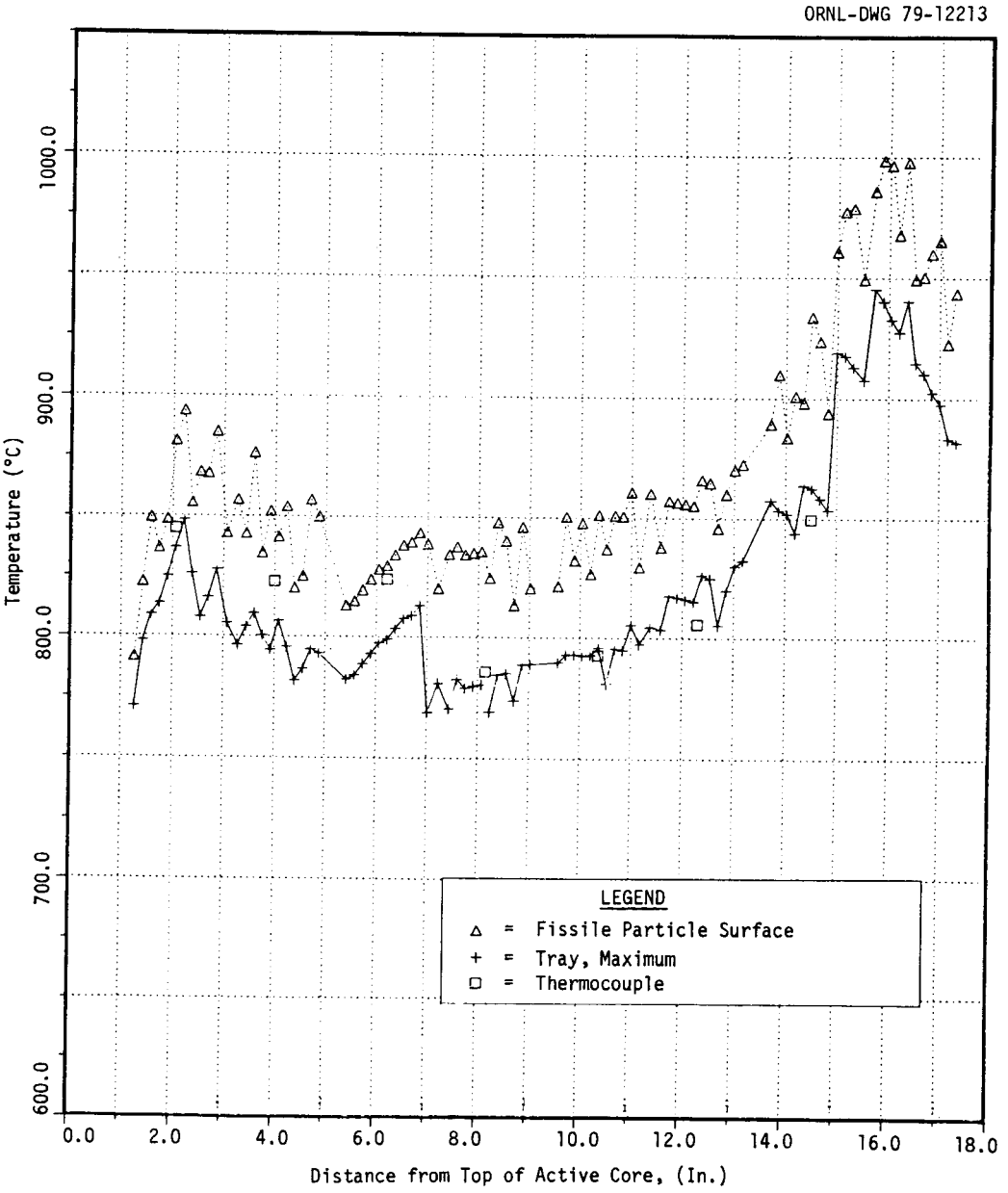


Fig. 2.24. Experiment HRB-15b, Temperature Versus Axial Position at 21 d into Cycle 2.

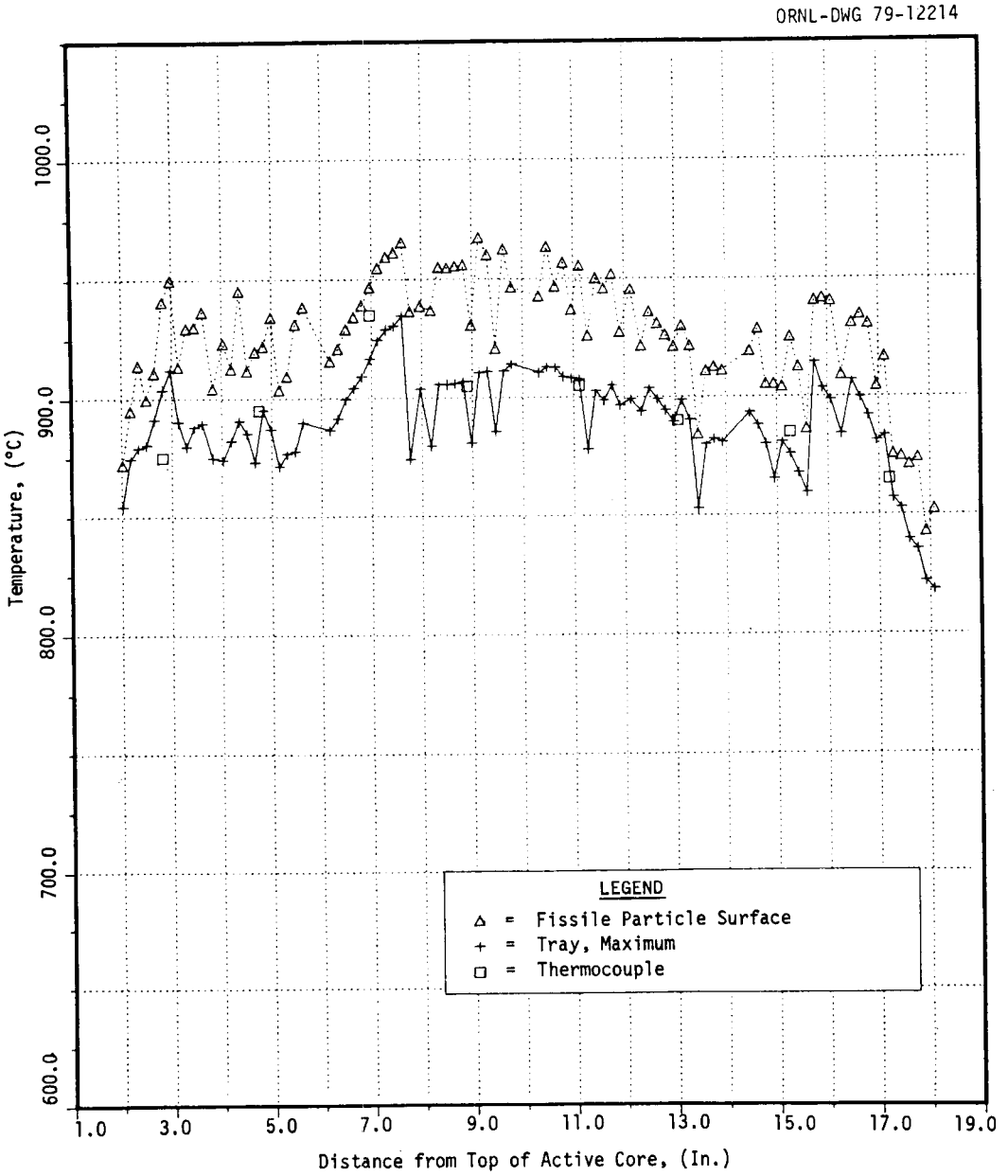


Fig. 2.25. Experiment HRB-15b, Temperature Versus Axial Position at 5 d into Cycle 4.

At the end of this report period (12-31-78), experiment HRB-15b had been in the reactor for 178.4 calendar days or for 165.7 full power days, that is, equivalent calendar days of operation at HFIR-rated power [100 MW(t)]. Average fuel burnup in units of fissions per initial (heavy) metal atom (FIMA) for fissile particles and fertile particles are shown in Figs. 2.26 and 2.27, respectively. The abscissa of these graphs are graduated in lengths equal to the length of a subassembly. Burnup was evaluated at 24 discrete axial positions, and a cubic spline interpolation was used to fit each curve through the data points. Fast neutron fluence ($E$ > 183 KeV), shown in Fig. 2.28, is based on HFIR fast neutron flux distribution in the experiment. Another parameter,[37] the "equivalent HTGR fluence for damage in graphite," can be obtained from Fig. 2.28 by multiplying the fast fluence by the factor 0.940. Reasons why the burnup curves and the fast neutron fluence curve do not peak at the middle of the experiment are: (1) the calculations reflect the first three-cycle operation with the experiment midlength displaced 0.02 m above the HMP and (2) asymmetric axial flux distributions appear to be characteristic of the RB-5 facility.[38]

### 2.4.2 Fission Product–SiC Coating Interaction Studies — R. L. Pearson and T. B. Lindemer

The main objective of this program is to acquire an understanding of the fuel, fission product, and coating kinetic processes and thermodynamics of the system to the degree that permits identification and quantitative descriptions of failure mechanisms and improved fuel performance by means of kernel chemical modification.

In these studies in-reactor interactions between fission products and SiC are chemically duplicated by Triso-coated simulated fission product systems. The Triso-coated particles are heat treated either isothermally or in a temperature gradient, and the reaction products and other phases are studied by metallographic, radiographic, crystallographic, and microprobe techniques. The experimental results are used to obtain data on the rate of attack and to evaluate possible failure mechanisms.

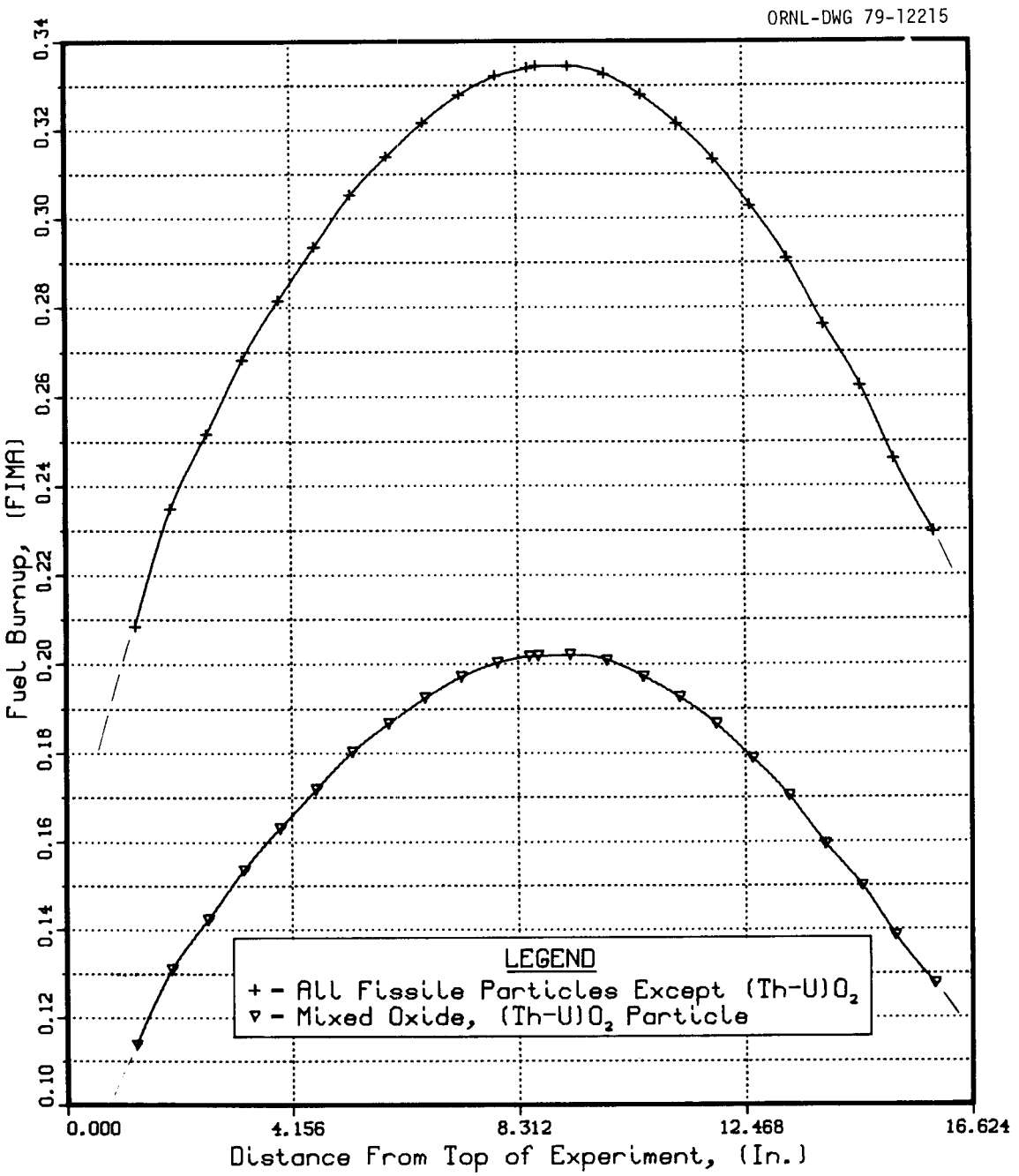


Fig. 2.26. Experiment HRB-15b, Particle Average Burnup for Fissile Particles.

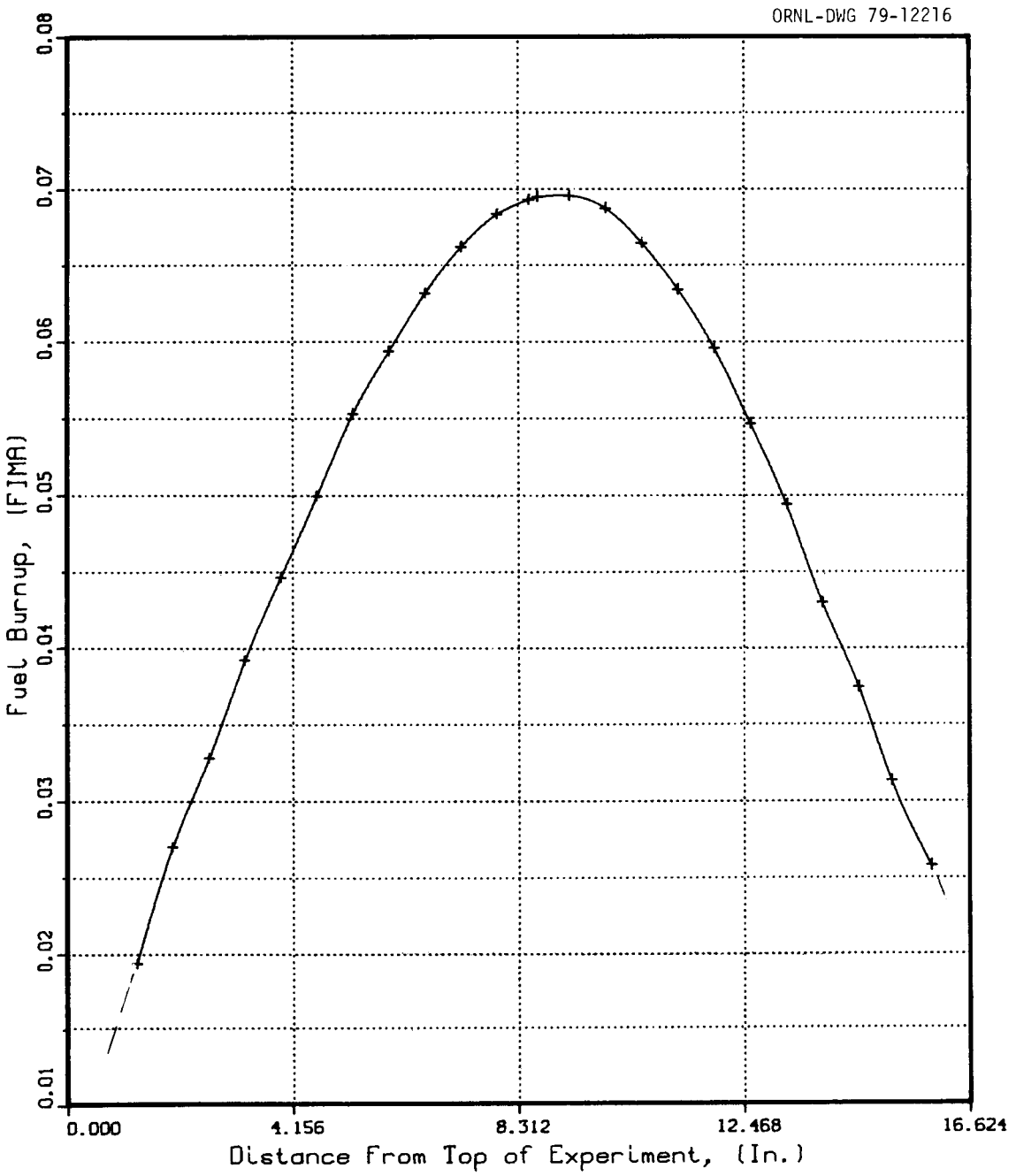


Fig. 2.27. Experiment HRB-15b, Particle Average Burnup for Fertile Particles.

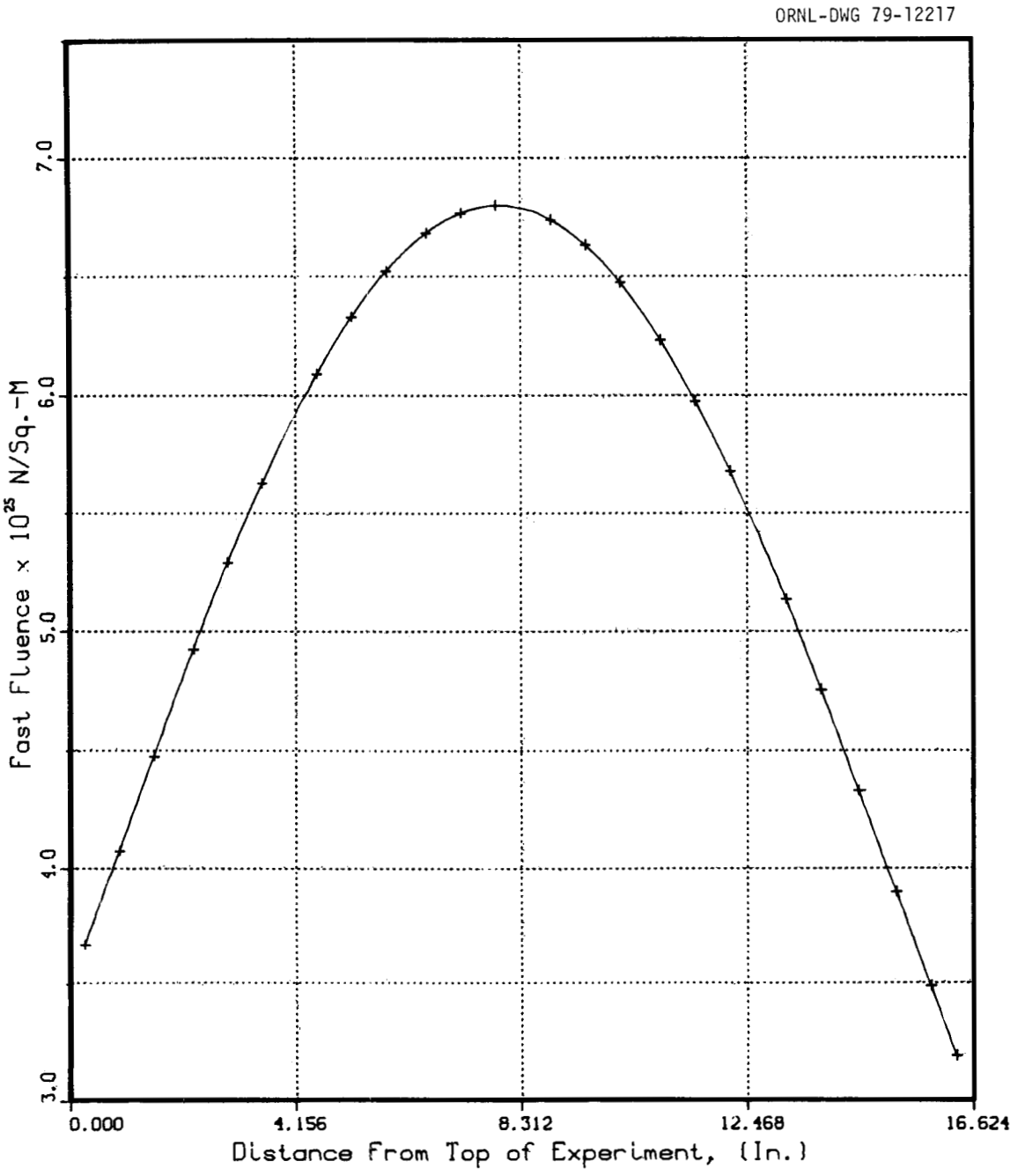


Fig. 2.28. Experiment HRB-15b, Fast Neutron Fluence.

A final report on the behavior of simulated fission product oxides in Triso-coated HTGR fuel was completed;[39] an abstract follows.

> Several combinations of Triso-coated $UO_2$ particles and simulated fission product oxides were investigated. The combinations were heat treated in the laboratory and their behavior examined by metallography, radiography, scanning electron microscopy, and electron microprobe x-ray analysis. Pressures of the various gaseous species within the particles were calculated and displayed as Ellingham diagrams. It appears to be essential that Triso-coated fuel have impermeable ILTI layers because the gaseous form of fission product strontium will interact with SiC. As oxides, the rare-earth fission products redistributed slightly within the buffer layer but did not interact with the SiC layers.

During the last several years, interest has developed in evaluating an LEU or MEU fuel to alleviate the proliferation issues related to the use of fully enriched fissile fuel. In LEU or MEU fuel, plutonium will also be fissioning, which results in a shift of the fission product yield spectrum. Two sets of Triso-coated particles were prepared simulating MEU-$UO_2$ or MEU-$UC_2$ fuel at 25% FIMA. The simulated fission products added included Mo, Ru, Rh, Pd, Ag, and Cd, whose yield ratios for $^{239}Pu$:$^{235}U$ are 0.94, 1.61, 2.29, 9.89, 50.12, and 8.58, respectively. It was learned that, in Triso-coated $UO_2$, the Ru, Rh, Pd, and Ag can interact with SiC several hundred degrees above operating reactor temperatures. In Triso-coated $UC_2$, the ruthenium, rhodium, and palladium promote the interaction of a uranium-containing second phase throughout the SiC layer under more normal reactor operating temperatures.

## 2.5 PROJECT WORK STATEMENT ACTIVITIES UNDER U.S.-FRG UMBRELLA AGREEMENT — F. J. Homan

Work was performed under the auspices of the Fueled Graphite Development Program on four project work statements (PWS) during the reporting period, which are: (1) PWS FD-1, Critical Evaluation of LEU Fuel Performance Data; (2) PWS FD-12, Quantification of Irradiation Induced Permeability in Pyrocarbon Coatings; (3) PWS FD-13, Comparison of IMGA

and Postirradiation Annealing and Autoradiography (PIAA);* and (4) PWS FD-18, Fuel Chemical Performance Modeling.

### 2.5.1 PWS FD-1 — F. J. Homan

Work on this task was completed during the reporting period, and a final report was issued. This report[40] reviews the data from the United Kingdom, United States, the Federal Republic of Germany, and Belgium. A subsequent report covering the French data was provided after the publication of the above report. An abstract of the LEU performance review is given below.

> The available data on low-enriched (LEU) fuel particles were reviewed under the United States-Federal Republic of Germany Agreement. The most influential factors controlling the irradiation performance of LEU fuel particles were found to be plutonium transport, fission product transport, fuel particle mechanical performance, and fuel particle chemical performance.
>
> PLUTONIUM TRANSPORT
>
> Pu-238, which is derived from U-235, represents the dominant radiological hazard. Since the U-235 inventory in an LEU core is approximately the same as that in an HEU core, plutonium transport is therefore of importance to both LEU and HEU systems.
>
> The diffusion coefficient of plutonium in high-temperature-isotropic pyrocarbon is about an order of magnitude higher than that of uranium and two orders of magnitude higher than that of thorium. A BISO coating is not a good barrier for plutonium release, but a TRISO coating retains plutonium. Graphite appears to be an effective trap for plutonium.
>
> The phase compositions and plutonium vapor pressures over irradiated uranium oxycarbide kernels have been deduced from thermodynamic data. It is concluded that plutonium is present in solid solution in the corresponding uranium-containing phases, and that the vapor pressure is lower than that of plutonium carbide. Experimental confirmation of these conclusions is desirable.

---

*IMGA and PIAA are postirradiation examination techniques for measurement of the failed particle fraction.

## FISSION PRODUCT TRANSPORT

The reduced diffusion coefficients D' of cesium diffusion in oxide kernels of different compositions, enrichments, and densities have been compared. Good agreement exists in some cases. More work is needed to establish how the structures (porosity, grain size) and burnup affect the D' values.

Silver release is higher from BISO particles than TRISO particles. Silver release is also higher from carbide fuel than oxide fuel. The retention of silver in intact TRISO particles is not as complete as the other fission products, at least at temperatures above 1450 K. High density SiC with minimum free silicon content (<0.3 weight %) is required for minimum release. A breakthrough mechanism that is activated when a certain critical silver concentration is reached at the inner SiC surface is proposed for silver transport through SiC. Silver is trapped in irradiated nuclear graphite at temperatures around 1300 K. The same is true for unirradiated graphite and matrix materials at some temperatures below 1100 K, but there is no retention in compacts, fuel rods, or spherical fuel elements at typical operating temperatures.

Strontium is retained virtually completely in $UO_2$ kernels surrounded by an intact coating layer, but above 1750 K strontium and barium are lost from the TRISO particles although Kr, Xe, and Cs are still retained. It appears that strontium and barium diffuse through the pyrocarbon coating at these high temperatures and attack the SiC coating. When the SiC layer is penetrated, it is no longer a barrier for the diffusion of these nuclides. The D' values for strontium and barium have been determined for $(Th,U)O_2$ in the temperature range $1760 < T < 1920$ K and in $UO_2$. The D' for barium is slightly higher than that of strontium.

D' values for the diffusion of short-lived gaseous fission products in $UO_2$ and $(Th,U)O_2$ are deduced from release data. The release of short-lived gaseous fission products from porous kernels does not seem to depend on burnup, but for the dense kernels there is a large increase with burnup. Empirical equations have been given to relate the release from failed particles with the burnup. No information, however, is available on the effect of conversion to carbide and hydrolysis on the release from failed particles. A model to be used for reactor safety analysis has been proposed; its purpose is to make conservative estimates of fission product release from failed particles during temperature transients.

## FUEL PARTICLE MECHANICAL PERFORMANCE

The present stress-strain models have been successful in describing TRISO particle failure and BISO particle dimensional changes for existing particles. For neutronic and fuel cycle cost reasons, the LEU/MEU particles are larger in diameter. There are indications that, in agreement with Weibull statistics of strength of brittle materials, coatings of larger diameter

have lower strength and higher failure probability. This is, however, not substantiated by some of the experimental results available. Nevertheless, it appears that the larger LEU/MEU particles might require development work to improve their coating strength in order to survive the required service limits. Otherwise, these particles have to be designed within the range of existing technology (i.e., $\leqslant$800 μm diameter).

Models, diffusion equations, and empirical formulas have been given to describe the release of stable fission gases from oxide kernels. For the burnup planned for the LEU/MEU fuel systems, the release appears to be relatively high. More carefully planned experiments are needed to relate the structures of the kernels, the temperature, and the burnup with the release.

Because of the high free oxygen yield for plutonium fissioning, the CO pressure in irradiated LEU fuel particles is expected to be much higher than that in irradiated HEU fuel particles. Higher CO pressure can lead to pressure vessel failure and "amoeba" failure. The theoretical maximum and minimum values of excess oxygen per fission are calculated from the fission yields of different fissile nuclides and their oxidation state. Most of the experimentally observed values for porous $UO_2$, dense $(Th, U)O_2$, and dense $ThO_2$ fall below the theoretical minimum value.

The use of oxygen getters or buffers (SiC, UC, ZrC, and $Ce_2O_3$) for lowering the CO pressure has shown promise in a number of irradiation experiments, although a small increase in the release of barium and rare earths has been observed.

## FUEL PARTICLE CHEMICAL PERFORMANCE

The existing results obtained by studying kernel migration coefficients have been compared. It appears that the HEU oxide fuel particle results can be used to establish the LEU/MEU oxide fuel particle design. However, some discrepancies exist among the available kernel migration coefficients of $UO_2$, and an understanding of the oxide kernel migration mechanism is still lacking.

Oxygen getters and buffers (SiC, UC, ZrC, and $Ce_2O_3$) have been tested for reduction of amoeba migration in oxide particles. The results are encouraging.

Localized attack of the SiC coating by the noble metal fission product Pd has been observed in a number of irradiation experiments involving LEU and plutonium fuels. Controlled experiments are needed to define the temperature and burnup for the Pd-SiC reaction to occur. Development of improved coatings that can resist Pd attack is necessary in order to prevent the Pd-SiC reaction from limiting LEU/MEU fuel particle performance.

Available LEU fuel particle performance information has provided a broad data base for the development of LEU/MEU fuel systems. With confirmation and refinement of these data, and a

carefully planned program for improving the LEU/MEU fuel particle performance, it should not be difficult to develop a licensable fuel system to meet the demand of LEU/MEU high-temperature gas-cooled reactor systems.

### 2.5.2 PWS FD-12 — E. L. Long, Jr., and B. A. Thiele

Under the auspices of the umbrella agreement between the U.S. and the FRG governments for high-temperature reactor (HTR) technology development, a number of cooperative tasks have been approved for implementation, which will require an exchange of information, materials for testing, and results.

The quantification of irradiation-induced permeability in PyC coating is called for in PWS FD-12, which will require the testing of Biso-coated particles from several sources. Both archive and irradiated particles from a Kernforschungsanlage (KFA) irradiation experiment (BR2-P12) have been received. The results of Ne/He and hot gaseous chlorine leaching characterization showed that the coatings of the three batches of archive particles are impermeable (Table 2.16). Testing of the irradiated particles from BR2-P12 and HT-34 is awaiting completion of the installation of the PGA in the HRLEL. Other particles that will be included in this PWS are currently being irradiated in HRB-14, which is scheduled to be discharged from the HFIR in early January 1979.

Table 2.16. Results of Permeability Characterizations on Archive Particles for Capsule BR2-P12

| Batch | He[a] (pmol) | Ne[a] (pmol) | Ne/He | Cl leach[b] |
|---|---|---|---|---|
| DO-760t | 208 | 39 | 0.19 | 3 |
| DO-761t | 267 | 39 | 0.15 | 3 |
| DO-787t | 195 | 49 | 0.25 | 3 |

[a]Gas contents of particles determined by mass spectrometry after soaking in 1:1 mixture on Ne:He at 1375°C at $11.01 \times 10^5$ Pa.

[b]Four hours at 1500°C; 3 = impermeable as determined by microradiography after leaching.

### 2.5.3 PWS FD-13 — E. L. Long, Jr.

The objective of PWS FD-13 is to compare postirradiation examination techniques used in the United States and in the Federal Republic of Germany for the measurement of statistically significant failure fractions of irradiated coated particles. The IMGA system is used at ORNL; a description of this system and the statistical basis for failure-fraction determinations have been reported.[41,42] Another technique, PIAA, has been developed and is in use at KFA.[43]

Irradiated coated particles from a KFA capsule (BR2-P21) and an ORNL capsule (OF-2) have been agreed on, and arrangements have been made to exchange the particles. About 1300 Triso-coated fissile particles from OF-2 have been classified with the IMGA system[42] and are ready for shipment to KFA for PIAA analysis. About 2000 Triso-coated fertile particles from BR2-P21 have been selected by KFA for shipment to ORNL. The particles will be returned to KFA for PIAA analysis after the failure fraction has been determined with the IMGA system. After failure fractions have been determined, a report will be prepared comparing the results of the two techniques.

### 2.5.4 PWS-FD 18 — T. B. Lindemer

This PWS is entitled "Fuel Chemical Performance Modeling." The long-term objective is to predict the chemical behavior of fuel, fission products, and containment systems (including Fe-Cr-Ni) under normal and hypothetical accident conditions. The first task is a review of and thermodynamic calculations for all relevant chemical systems with cesium, rubidium, and the other alkali metals (A); this effort is being coauthored by T. M. Besmann of ORNL and C. E. Johnson and D. C. Fee of Argonne National Laboratory (ANL) and was started while T. B. Lindemer was on assignment at KFA-Jülich. The available and calculated information has been compiled for many binary and ternary systems, and the Na-Fe-O system is being evaluated at ORNL and the A-actinide-O and A-V-O systems at ANL. An open-literature report is being prepared.

## 2.6 EQUIPMENT DEVELOPMENT AND SUPPORT ACTIVITIES — F. J. Homan

Two major items of PIE equipment are under development at ORNL. They are the IMGA and the PGA systems. The IMGA system has been operational most of the year, but problems have been encountered with the particle handling system which will require modifications to get the system reliability that is needed. The system is working as anticipated overall, giving good measurements of fission product retention. During the reporting period, fuel from OF-2, HT-34, and HT-12 through -15 was analyzed. Data from the OF-2 and HT-34 examinations are reported here. The HT-12 through -15 examinations were done for use with the PGA system, which is not yet operational.

All the hardware for the PGA system was assembled about halfway through the year, but a variety of problems have been encountered in making the system work. A factory representative has been consulted about these problems and has been unable to solve them. Alternate methods of operating the system will be pursued during 1979.

### 2.6.1 Irradiated Microsphere Gamma Analyzer System — T. N. Tiegs, M. J. Kania, A. M. Howard, and G. A. Moore

The IMGA system is a fully automated device to examine the gamma spectrum of individual irradiated HTGR fuel particles. Based on the gamma spectra, the fission retention behavior and the failure fraction of the fuel particles can be determined. The description of the system and the statistical considerations used in analyzing the data have been reported.[44,45]

#### 2.6.1.1 IMGA Operation

The system was fully operational for most of the year, handling about 8000 fueled particles from experiments OF-2, HT-34, and HT-12 through -15. Operation ceased for about two months in June and July and for about one month in December because of failure of the right-angle drive that rotates the sample changer.

A new particle handler is now being fabricated, which will: (1) simplify the handling operation and eliminate the right-angle drive problems; (2) provide four-point symmetry and thereby add the capability for an additional detector to examine low-energy gamma and characteristic florescent x-ray emissions; and (3) have provisions for remote maintenance, which will lower down time in the event of a failure and reduce personnel exposure. Installation of the new particle handler is expected in mid-1979.

2.6.1.2 Analysis of OF-2 Fuel

Results from the IMGA analysis of OF-2 rods C-4-1, C-3-1, and C-1-2 have been reported previously.[44] Results on the analysis of rods C-1-1 and C-2-2 are summarized in Table 2.17. Both rods contained fissile particle batch A-601 (75% converted WAR), whereas rod C-1-1 contained fertile particle batch J-483 and rod C-2-2 contained J-488. See ref. 46 for details about the characteristics of the particles.

Results show low failure fractions ($\leqslant$0.30%) for all the particles examined. This work plus earlier measurements on batch A-601,[44] confirm that A-601 meets the fuel performance requirements for the FSVR (that the fuel have a failure fraction of less than 1% with a 95% confidence level). Batch A-601 is included in the FSVR early validation tests to be irradiated in the first reload of FSVR.

The particles from fuel rod C-2-2 will be used in the work included under PWS-FD-13 described in Sect. 2.5.3 of this report.

2.6.1.3 Analysis of HT-34 Fuel

By the end of December 1978, the IMGA system had completed the analysis of the GA loose Triso-coated $ThO_2$ particles and the ORNL loose Biso-coated $ThO_2$ particles. The ORNL Triso-coated $ThO_2$ and WAR driver particles containing 7% enriched uranium will be analyzed in early 1979. IMGA analysis of HT-34 capsule will then be complete.

Calculations were made using the CACA-II computer code[47] to determine the theoretical yields in HT-34 of the following fission products: $^{95}Zr$, $^{137}Cs$, $^{144}Ce$, and $^{106}Ru$. Ratios of the volatile fission products

Table 2.17. Summary of IMGA Results from Rods C-1-1 and C-2-2

| Sample | $^{137}Cs:^{95}Zr$[a] (DPS/DPS)[b] | | | $^{134}Cs:^{95}Zr$[a] DPS/DPS) | | | $^{134}CS:^{137}Cs$[a] (DPS/DPS) | | | $^{144}Ce:^{95}Zr$[a] (DPS/DPS) | | |
|---|---|---|---|---|---|---|---|---|---|---|---|---|
| | Mean | S.D.[c] (%) | Failure fraction[d] (%) | Mean | S.D.[c] (%) | Failure fraction[d] (%) | Mean | S.D.[c] (%) | Failure fraction[d] (%) | Mean | S.D.[c] (%) | Failure fraction[d] (%) |
| C-1-1 fissile (A-601) | 1.564 | 2.77 | 0 (0/330) | 2.504 | 4.34 | 0.30 (1/330) | 1.600 | 2.14 | 0.30 (1/330) | 11.744 | 2.38 | 0 (0/330) |
| C-2-2 fissile (A-601) | 1.657 | 6.55 | 0.16 (2/1281) | 2.541 | 7.52 | 0.16 (2/1281) | 1.532 | 2.45 | 0.08 (1/1281) | 12.462 | 5.81 | 0.08 (2/1281) |
| C-1-1 fertile (J-483) | 0.5994 | 1.51 | 0.24 (4/1675) | 0.4775 | 2.49 | 0.12 (2/1675) | 0.7964 | 2.44 | 0.06 (1/1675) | 4.883 | 1.36 | 0 (0/1675) |
| C-2-2 fertile (J-488) | 0.6466 | 3.71 | 0.08 (2/2652) | 0.5050 | 4.62 | 0.04 (1/2652) | 0.7808 | 2.85 | 0 (0/2652) | 5.285 | 3.75 | 0.04 (1/2652) |

[a] Data have been corrected for decay time; all OF-2 data is corrected to 6/20/77 at 4:00 pm.

[b] DPS = disintegrations per second.

[c] S.D. = standard deviation.

[d] Failure fraction = [(number of particles 3 S.D. away from mean)/total number of particles] × 100.

(e.g., $^{137}Cs$) to the stable fission products (e.g., $^{95}Zr$) were then calculated and compared with the observed ratios from the Biso-coated $ThO_2$ particles. Results show that $^{95}Zr$, $^{144}Ce$, and $^{106}Ru$ are stable and remain in the kernel, whereas $^{134}Cs$ and $^{137}Cs$ are volatile and migrate out of the kernel (and in some cases out of the particle). Therefore, the cesium-to-zirconium ratios were used as the measure of fission product retention behavior when comparing the particles.

The results of IMGA analysis of the GA Triso-coated $ThO_2$ have been assembled and forwarded to GA. General Atomic Company will use these results in analyzing the performance of their fuel. The results showed good retention of cesium at low temperatures (<1250°C), whereas poor retention was observed at high temperatures (>1430°C). These results will be combined with the results from the ORNL Biso- and Triso-coated $ThO_2$ in a consolidated report.

The ORNL Biso-coated $ThO_2$ particles were visually inspected and all kernels and coating fragments removed prior to IMGA analysis. The summary of the $^{137}Cs$:$^{95}Zr$ ratios for the intact Biso-coated $ThO_2$ particles is given in Table 2.18. The particles from the low-temperature region (positions 40 through 52) performed very well, as evidenced by the complete retention of $^{137}Cs$. (Discrepancies between the theoretical versus the observed ratios are believed to be the result of small uncertainties in the flux spectrum of the HFIR target region, which heavily influence the fission product yields and hence the ratios.) The particles from the high-temperature region (positions 27 through 39) showed mean $^{137}Cs$ losses ranging from 54.9 to 84.6%.

The relationship between the $^{137}Cs$:$^{95}Zr$ ratio and temperature is shown in Fig. 2.29 (also included are the GA particles). Temperatures greater than 1250°C appear to cause severe cesium loss from Biso-coated $ThO_2$ particles. However, previous results[48] have shown that Biso-coated $ThO_2$ irradiated with time-averaged temperatures of 1450°C and 1370°C had less than 2% cesium loss and no cesium loss, respectively. Thus, temperature is not considered to be the sole factor influencing the cesium loss. The relationship between fast neutron fluence ($E$ >0.18 MeV) and the $^{137}Cs$:$^{95}Zr$ ratio (Fig. 2.30) shows that, above $9.5 \times 10^{25}$ neutrons/m$^2$, cesium loss is high. This finding agrees with the other previous data.[48] It is

Table 2.18. Summary of $^{137}Cs:^{95}Zr$ Ratio Measurements from HT-34

| Capsule position | Batch no. | $^{137}Cs:^{95}Zr$ Ratio | | |
|---|---|---|---|---|
| | | Mean | Standard deviation (%) | Fraction of theoretical remaining in particle (%) |
| 27 | A-765 | $3.34 \times 10^{-3}$ | 43.70 | 35.2 |
| 29 | A-780 | $2.64 \times 10^{-3}$ | 37.28 | 27.8 |
| 30 | A-785 | $4.27 \times 10^{-3}$ | 31.72 | 45.1 |
| 32 | A-806 | $2.65 \times 10^{-3}$ | 35.36 | 28.0 |
| 33 | A-762 | $2.61 \times 10^{-3}$ | 47.47 | 27.5 |
| 35 | A-782 | $2.57 \times 10^{-3}$ | 29.72 | 27.2 |
| 36 | A-786 | $2.86 \times 10^{-3}$ | 34.15 | 30.2 |
| 38 | A-787 | $1.46 \times 10^{-3}$ | 21.84 | 15.4 |
| 39-1 | OR-1975 | $4.02 \times 10^{-3}$ | 25.95 | 42.4 |
| 39-2 | OR-2013 | $3.46 \times 10^{-3}$ | 47.94 | 36.5 |
| 40 | A-765 | $9.76 \times 10^{-3}$ | 2.17 | 102.9 |
| 42 | A-780 | $9.81 \times 10^{-3}$ | 1.09 | 103.3 |
| 43 | A-785 | $9.76 \times 10^{-3}$ | 0.97 | 102.8 |
| 45 | A-806 | $9.82 \times 10^{-3}$ | 0.62 | 103.3 |
| 46 | A-762 | $1.02 \times 10^{-2}$ | 1.68 | 106.8 |
| 48 | A-782 | $9.69 \times 10^{-3}$ | 0.56 | 101.7 |
| 49 | A-786 | $9.83 \times 10^{-3}$ | 0.56 | 103.2 |
| 51 | A-787 | $9.71 \times 10^{-3}$ | 0.70 | 101.8 |
| 52 | OR-1975 | $9.87 \times 10^{-3}$ | 0.81 | 103.5 |

concluded that both temperature and fast neutron damage are the main factors affecting cesium loss in Biso-coated $ThO_2$ particles. However, the cesium loss observed in the HT-34 particles was higher than the previous results and is thought to be a result of the particles' not being annealed prior to irradiation. The structure of the PyC coating is changed during annealing, and it has been shown that PyC permeability to inert gases is decreased during annealing.[49] Analysis of the HRB-14 experiment, in which the same HT-34 particles were included but were annealed prior to irradiation, should confirm whether or not the greater cesium loss in the HT-34 particles was a result of the particles' not being annealed.

Figure 2.31 shows the relationship between the standard deviation of the $^{137}Cs:^{95}Zr$ ratio and the fast-neutron fluence ($E$ >0.18 MeV). As the fast-neutron damage to the PyC increases, the cesium retention

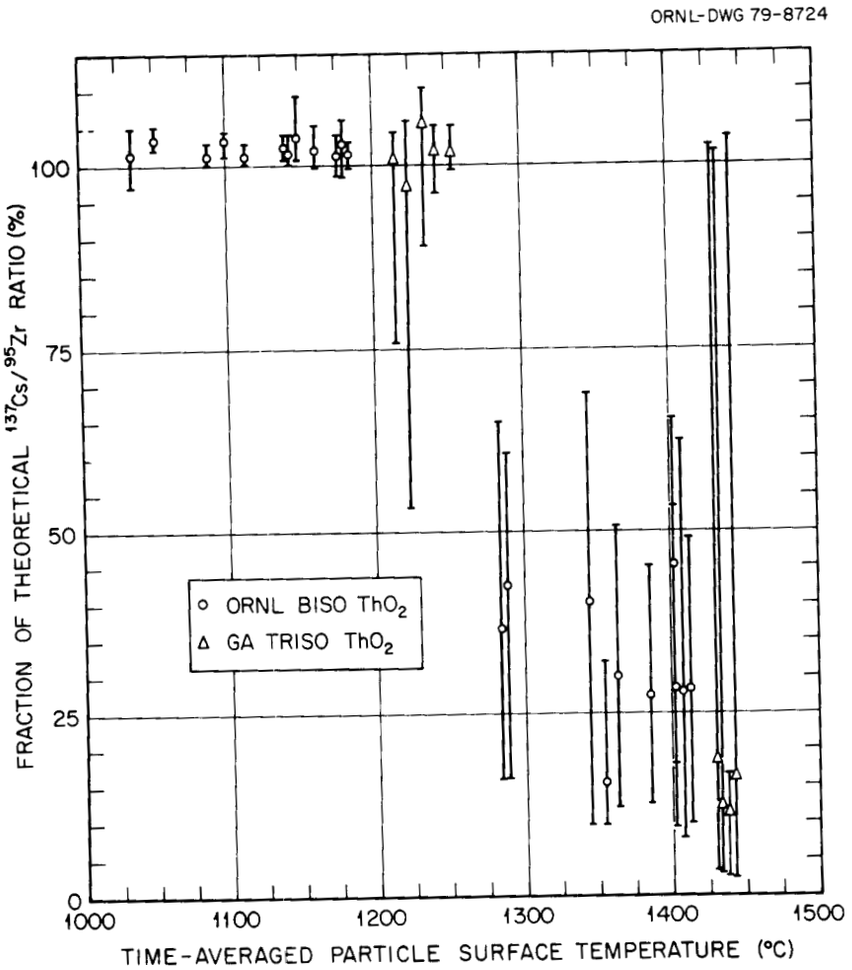


Fig. 2.29. Fraction of Theoretical $^{137}Cs$:$^{95}Zr$ Ratio as a Function of Temperature.

behavior begins to vary widely from particle to particle. These particles all appeared to be intact when examined visually. Also included are results from other examinations of Biso-coated $ThO_2$ (viz., HT-32 and OF-2 irradiation tests). The increase in the standard deviation at low fluences is believed to be an effect of uncertainties associated with low burnup in the particles rather than an effect of the behavior of the pyrocarbon.

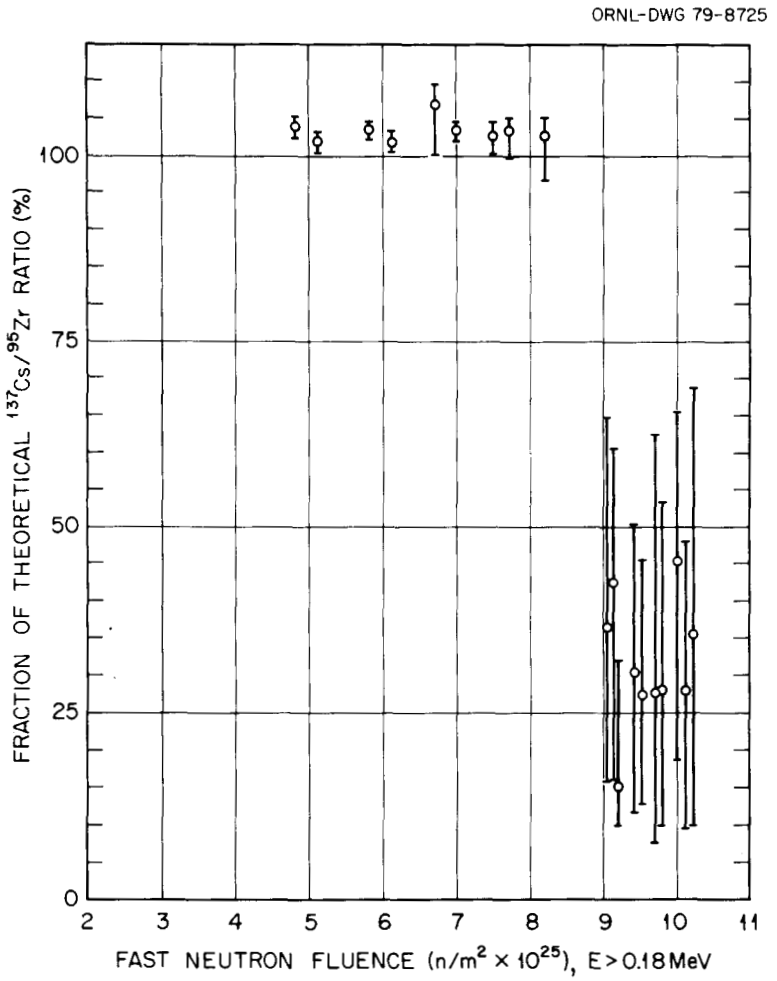


Fig. 2.30. Fraction of Theoretical $^{137}Cs:^{95}Zr$ Ratio as a Function of Fast-Neutron Fluence.

### 2.6.2 Postirradiation Gas Analyzer System — J. M. Robbins, M. J. Kania, and E. L. Ryan

The capability for measuring the gas content of irradiated coated fuel particles has been recognized as being of utmost importance in predicting and evaluating the irradiation performance of coated particles in the oxycarbide fuel system. The gases are primarily carbon monoxide, krypton, and xenon and are released from the kernel into the particle void space during irradiation. A knowledge of the burnup dependence of the in-particle krypton + xenon gas pressure is extremely useful in particle pressure vessel design and for accurate estimates of fission

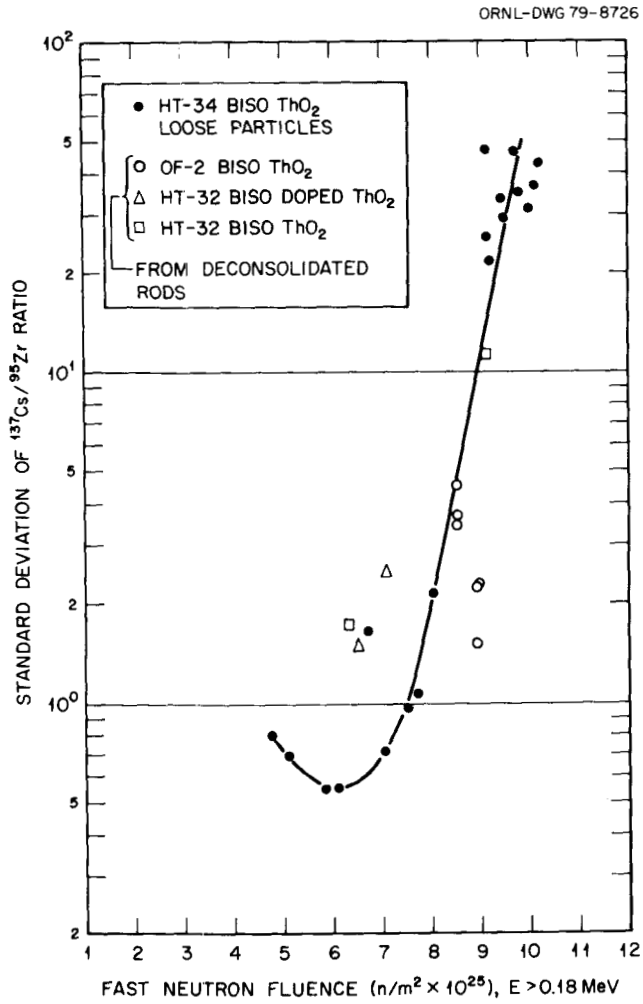


Fig. 2.31. Standard Deviation of $^{137}Cs$:$^{95}Zr$ Ratio as a Function of Fast Fluence.

gas release to the coolant circuit from in-reactor particle failures. Carbon monoxide has been shown to be the only significant reaction gas present in the system.[50] The CO pressures can be equivalent to those for krypton + xenon, thus also affecting the particle pressure vessel design. More significantly, knowledge of the CO pressure can be used to infer the oxidation state of the fuel and fission products during burnup.[51]

The method that has previously been used at ORNL for measuring internal fission gases in coated fuel particles has been described

elsewhere.[52] This system measures the reactive and nonreactive gases by difference and does not identify individual gases. In an effort to overcome these limitations, a system called the PGA has been designed and built and is currently being evaluated for making the required quantitative measurements of fission gases produced by irradiating fuel particles. The PGA system consists of a particle-breaking section, a time-of-flight mass spectrometer (TOFMS), and a PDP-8A minicomputer. The system is shown schematically in Fig. 2.32. The PGA particle-breaking section and the TOFMS flight tube are interconnected and operate at pressures of $1.3 \times 10^{-3}$ Pa or lower. Each of these units is discussed separately.

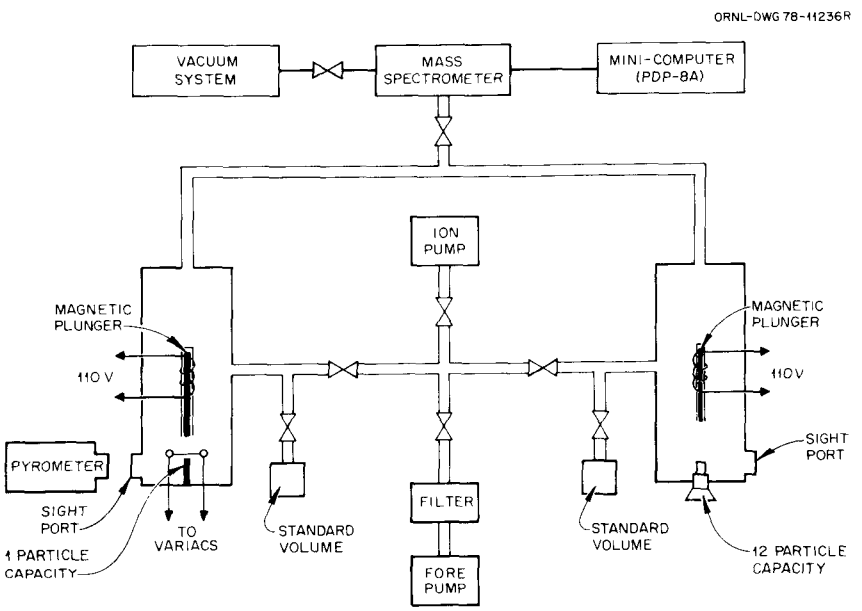


Fig. 2.32. The Postirradiation Analyzer System is Used for Measuring Fission Gases in Coated-Particle Fuels.

The particle-breaking section consists of two particle-breaking stations together with the necessary vacuum and valving systems to transfer the fission gases from the broken particles to the TOFMS flight tube. One particle-breaking station, which operates at ambient temperature, is designed to hold twelve coated particles without reloading.

The second particle-breaking station holds only one coated particle without reloading; however, the particle is contained in a resistance-heated graphite holder, which can be broken at temperatures up to 2000°C.

When released from the broken particles, the fission gases are swept into the TOFMS analyzer assembly. The analyzer assembly consists of an ion source, a drift region, and a magnetic electron multiplier. As the fission gases enter the analyzer assembly, they are ionized by the ion source, and gases of various mass-to-charge ($m/e$) ratios are accelerated to a high level of kinetic energy and directed through the field-free drift region toward the magnetic electron multiplier. Because all of the fission-gas ions leave the starting position simultaneously and drift the same distance to reach the electron multiplier, those of equal mass separate into sheets displaced from sheets of other masses. Each sheet of ions strikes a detector cathode, where secondary ions are dislodged and directed into the multiplying region. The electron current is amplified and directed to the electrometer or collected on an oscilloscope for display. The currents measured by the electrometric amplifier and the peak heights on the oscilloscope or plotter are linearly related to ion abundance, making quantitative measurements possible.

The PGA system designed and built at ORNL has a PDP-8A minicomputer interfaced with the TOFMS for data acquisition, manipulation, output, and storage. The electrical currents measured by the electrometer are amplified, and through the use of an A/D converter, the signal is detected and output digitally on a typewriter interfaced with the PDP-8A.

After initial checkout at the Y-12 Plant by Analytical Chemistry Division personnel, the TOFMS and PDP-8 were moved to ORNL, where they have been installed in their permanent location in Building 3525. Several problem areas have been recognized and are in various states of remedy. Problems were encountered early with the TOFMS vacuum system. It was very difficult to evacuate the system to pressures lower than about $1 \times 10^{-1}$ Pa without the addition of liquid nitrogen to the system's cold trap. Even with liquid nitrogen it was possible to reach pressures of only about $1.3 \times 10^{-3}$ Pa, and this pressure exhibited a cyclic variation because of inconsistent pump speed. By adjusting the expansion

value in the freon line, it has been possible to reach pressures of $1.3 \times 10^{-5}$ Pa or lower, and the cyclic variation in pump speed has been minimized. However, this solution is only temporary and is unsatisfactory because the expansion value requires frequent periodic adjustment to obtain satisfactory results. Changing to water cooling of the diffusion pump is being considered as the permanent solution to the vacuum problems. Many problems have been encountered in the acquisition and output of acceptable data during efforts to calibrate the system by using a known gas composition. The most important of these problems are:

1. Inconsistent results are obtained from identical analyses.
2. Unacceptable shifts occur in the location of mass numbers in the mass selector channels of the data output systems.
3. The electrical signal from the range multiplier to the data output systems should be directly proportional to the multiplier setting. However, when the range multiplier setting is changed, the output systems do not react in a directly proportional manner.
4. A significant background noise exists that influences the data output signal in a nonlinear way relative to the sensitivity range being used.

Corrections to these problems are currently being investigated.

The first evaluation of the PGA system was made, using unirradiated coated particles containing a known ratio of Ne/He. The magnetically operated particle-breaking device successfully broke 25 of the particles either one, two, or three at a time. The TOFMS detected the proper mass numbers for the known gases that were present and the minicomputer assembled and output the data as programmed. Because calibration of the system is incomplete, quantitative evaluation of the amounts of gases was not possible.

## 2.7 SERVICE WORK FOR GENERAL ATOMIC COMPANY — E. L. Long, Jr.

Service work was performed for GA by ORNL in several areas during this reporting period. This work was supportative in nature and was

performed either because the GA hot cells were closed for modification or because ORNL had unique capabilities that would compliment GA's research activities.

### 2.7.1 Permeability Studies on Unirradiated Biso-Coated Particles Fabricated by GA — B. A. Thiele

This section is a summary of the work done at ORNL to characterize 24 batches of GA coated particles for PyC permeability. Both the Ne/He permeation and the long-term chlorination techniques coupled with x-radiography were used. The data are summarized in Table 2.19.

As can be seen in Table 2.19, there is good agreement between the Ne/He numbers and the chlorine-leach results. We have found PyC coatings with Ne/He values below 0.3 to be gastight, values above 0.4 to be gas permeable, and values between 0.3 and 0.4 to be marginally gastight as determined from long-term chlorination and x-radiography.[53] As shown in Table 2.19, particles with Ne/He values of $\geqslant 0.4$ showed heavy-metal migration into the buffer layer after an 18-h chlorination at 1500°C and were declared to be "gas permeable." Only two batches had Ne:He ratios below 0.3, whereas several batches had values between 0.3 and 0.4 that were gastight. However, these batches had seal coats that may have influenced the chlorine-leach results. One batch had an Ne/He value of 0.41 and was gastight, but this was also probably caused by the seal coat.

Several parameters were considered for possible correlation with gas-permeable PyC coatings:

1. the presence of a seal coat between the buffer and LTI coating,
2. bulk density of the LTI,
3. open porosity of the LTI,
4. coater size,
5. coating rate,
6. diluent gas, and
7. hydrocarbon gas.

Table 2.19. Summary of Coating Properties and Results of Gas-Permeability Characterization Work (Done at ORNL) for 24 Biso-Coated Particle Batches Fabricated at GA

| | | | Buffer | | OPyC | | | | | | | | | Total coated particle | | |
|---|---|---|---|---|---|---|---|---|---|---|---|---|---|---|---|---|
| | | | | | | | Density ($Mg/m^3$) | | | | | | | | | |
| | | | | | | | Liquid gradient | | | | | Coater gases | | | | |
| Batch No. | Kernel diameter (μm) | Coater size (mm) | Thickness (μm) | Density ($Mg/m^3$) | Thickness (μm) | Seal coat | Mean | Standard deviation | Bulk | Coating rate (μm/min) | Hg intrusion[a] (mℓ/kg OPyC coating) | Deposition | Diluent | Fission gas release[b] (R/B) | Ne:He ratio[c] | $Cl_2$ leach x-ray[c,d] |
| 4252-06-010 | 516 | 127 | 85 | 1.10 | 76 | Yes | 1.82 | $1.12 \times 10^{-2}$ | 1.73 | 5.75 | 27.1 | $C_3H_6$ | $N_2$ | (e) | 0.37 | 3 |
| 6542-01-010 | 500 | | 79 | 1.08 | 85 | | 1.80 | $6.0 \times 10^{-3}$ | 1.71 | 10.00 | 26.6 | | Ar | | 0.37 | 3 |
| -01-020 | 504 | | 81 | 1.17 | 74 | | 1.82 | $7.0 \times 10^{-3}$ | 1.77 | 2.72 | 17.9 | | | | 0.31 | 3 |
| -02-020 | 481 | | 87 | 1.08 | 72 | | 1.91 | $7.0 \times 10^{-3}$ | 1.82 | 8.47 | 26.0 | | | | 0.30 | 3 |
| -02-030 | 481 | | 79 | 1.18 | 74 | | 1.89 | $0.001 \times 10^{-1}$ | 1.84 | 2.16 | 13.4 | | | | 0.28 | 3 |
| -09-010 | 511 | | 84 | 1.06 | 75 | | 1.93 | $0.001 \times 10^{-1}$ | 1.83 | 4.97 | 26.3 | | $N_2$ | | 0.29 | 3 |
| -11-015 | 497 | | 87 | 1.12 | 74 | No | 1.83 | $0.0 \times 10^{-1}$ | (e) | 2.62 | (e) | | Ar | $2.61 \times 10^{-7}$ | .32 | 3 |
| -18-015 | 476 | | 84 | 1.11 | 70 | | 1.84 | $9.49 \times 10^{-3}$ | 1.73 | 6.48 | 31.5 | | | $5.54 \times 10^{-7}$ | .46 | 1 |
| -19-015 | 486 | | 81 | 1.15 | 77 | Yes | 1.78 | $0.005 \times 10^{-1}$ | (e) | 7.55 | (e) | | | (e) | 0.39 | 3 |
| -21-015 | 492 | | 79 | 1.13 | 82 | | 1.73 | $0.005 \times 10^{-1}$ | 1.59 | 7.81 | 45.2 | M-G[f] | | | .48 | 1 |
| -22-015 | 503 | | 85 | 1.12 | 81 | | 1.80 | $0.0 \times 10^{-1}$ | 1.70 | 4.05 | 32.8 | | | | 0.42 | 3 |
| -24-015 | 511 | | 86 | 1.13 | 83 | | 1.94 | $0.007 \times 10^{-1}$ | 1.83 | 6.59 | 30.4 | | | $1.18 \times 10^{-6}$ | .32 | 3-2 |
| -27-015 | 512 | | 84 | 1.09 | 81 | No | 1.86 | $5.87 \times 10^{-3}$ | 1.78 | 4.59 | 23.3 | | | $1.2 \times 10^{-5}$ | .37 | 1 |
| -29-015 | 499 | | 81 | 1.18 | 76 | | 1.96 | $7.61 \times 10^{-3}$ | 1.87 | 4.31 | 25.2 | | | $8.5 \times 10^{-6}$ | .34 | 3 |
| -29-020 | 505 | 240 | 96 | 1.13 | 74 | | 1.96 | $0.02 \times 10^{-1}$ | 1.89 | 4.30 | 18.5 | | $N_2$ | $2.65 \times 10^{-5}$ | 0.41 | 1 |
| -31-015 | 501 | 127 | 83 | 1.10 | 75 | | 1.92 | $9.23 \times 10^{-3}$ | (e) | 6.00 | (e) | | Ar | $6.4 \times 10^{-6}$ | .42 | 2 |
| -32-015 | 515 | | 82 | 1.12 | 82 | Yes | 1.84 | $5.87 \times 10^{-3}$ | 1.75 | 4.65 | 28.5 | | | $6.1 \times 10^{-6}$ | .35 | 3-2 |
| -33-015 | 515 | | 73 | 0.99 | 83 | No | 1.84 | $4.95 \times 10^{-6}$ | (e) | 4.72 | (e) | | | $7.6 \times 10^{-5}$ | .56 | 1 |
| -34-015 | 505 | | 84 | 1.09 | 80 | | 1.86 | $4.44 \times 10^{-3}$ | 1.73 | 6.40 | 40.1 | | | $4.6 \times 10^{-5}$ | .60 | 1 |
| -35-015 | 505 | | 86 | 1.09 | 70 | | 1.94 | $1.04 \times 10^{-2}$ | 1.81 | 5.60 | 36.8 | | | $4.6 \times 10^{-5}$ | .53 | 1 |
| -39-010 | 505 | 240 | 89 | 1.13 | 73 | | 1.94 | $0.026 \times 10^{-1}$ | 1.88 | 4.06 | 17.3 | | $N_2$ | $1.86 \times 10^{-5}$ | .38 | 3 |
| -40-010 | 508 | | 95 | 1.10 | 73 | | 1.73 | $0.01 \times 10^{-1}$ | 1.67 | 5.84 | 22.7 | | $H_2$ | $4.09 \times 10^{-6}$ | .45 | 1 |
| -40-020 | 502 | | 89 | 1.10 | 79 | | 1.76 | $9.0 \times 10^{-3}$ | 1.69 | 5.85 | 23.5 | | | $3.63 \times 10^{-6}$ | .49 | 1 |
| -41-010 | 506 | | 95 | 1.13 | 72 | | 2.00 | $1.37 \times 10^{-2}$ | 1.93 | 5.76 | 19.0 | | $N_2$ | $4.17 \times 10^{-5}$ | 0.55 | 1 |

[a] Amount of Hg intruding into the coating from 250 to 10,000 psi.

[b] Photofission measurement of Kr-85m at 1100°C.

[c] Measured at ORNL.

[d] ORNL designation of amount of heavy metal in buffer: 1-high, 2-light, 3-none.

[e] Not determined.

[f] M-G · $C_2H_2/C_3H_6$.

The results of these studies are:

1. Nine out of eleven particle batches without a seal coat had permeable LTI coatings. Three out of thirteen batches with seal coats were permeable. Based on the Ne/He numbers for these batches, it is concluded that the presence of the seal coat may have slowed the removal of heavy metal from the kernels in batches that had gas-permeable LTI coatings.
2. Bulk density did not influence gastightness of the PyC coatings in this study for those particles with no seal coating. Gas-permeable coatings from these particles had densities in the range of 1.67 to 1.93 $Mg/m^3$. Particles with seal coatings were gastight when the PyC densities were higher than 1.70 $Mg/m^3$ (Fig. 2.33). Perhaps the presence of the sealing layer "helps" the gastightness of as-fabricated coatings so that coatings with bulk densities as low as 1.70 $Mg/m^3$ remain gastight. The gas permeability of coatings having high bulk densities and no seal coat from the GA-fabricated batches remains unexplained.
3. Open porosity of the PyC coatings did not influence gas permeability. Gas-permeable batches had open porosity values in the range of 18.5 to 45.2 ml/kg PyC.
4. Four out of the five batches from the large (240-mm-diam) coater studied were gas permeable, which may be indicative of an influence of batch size.
5. No influence of coating rate on gastightness of the PyC coatings was observed.
6. No influence was apparent of the diluent gas on gastightness. Permeable coatings were produced with Ar, $N_2$, and $H_2$ as the diluent gases.
7. Ten of the fifteen batches produced with mixed gas were permeable. Only one of nine batches produced using propylene was permeable. This result is not conclusive in that the deposition temperatures used in the mixed-gas-coating runs may have been too low; coating temperatures for these batches were not included with the data supplied by GA.

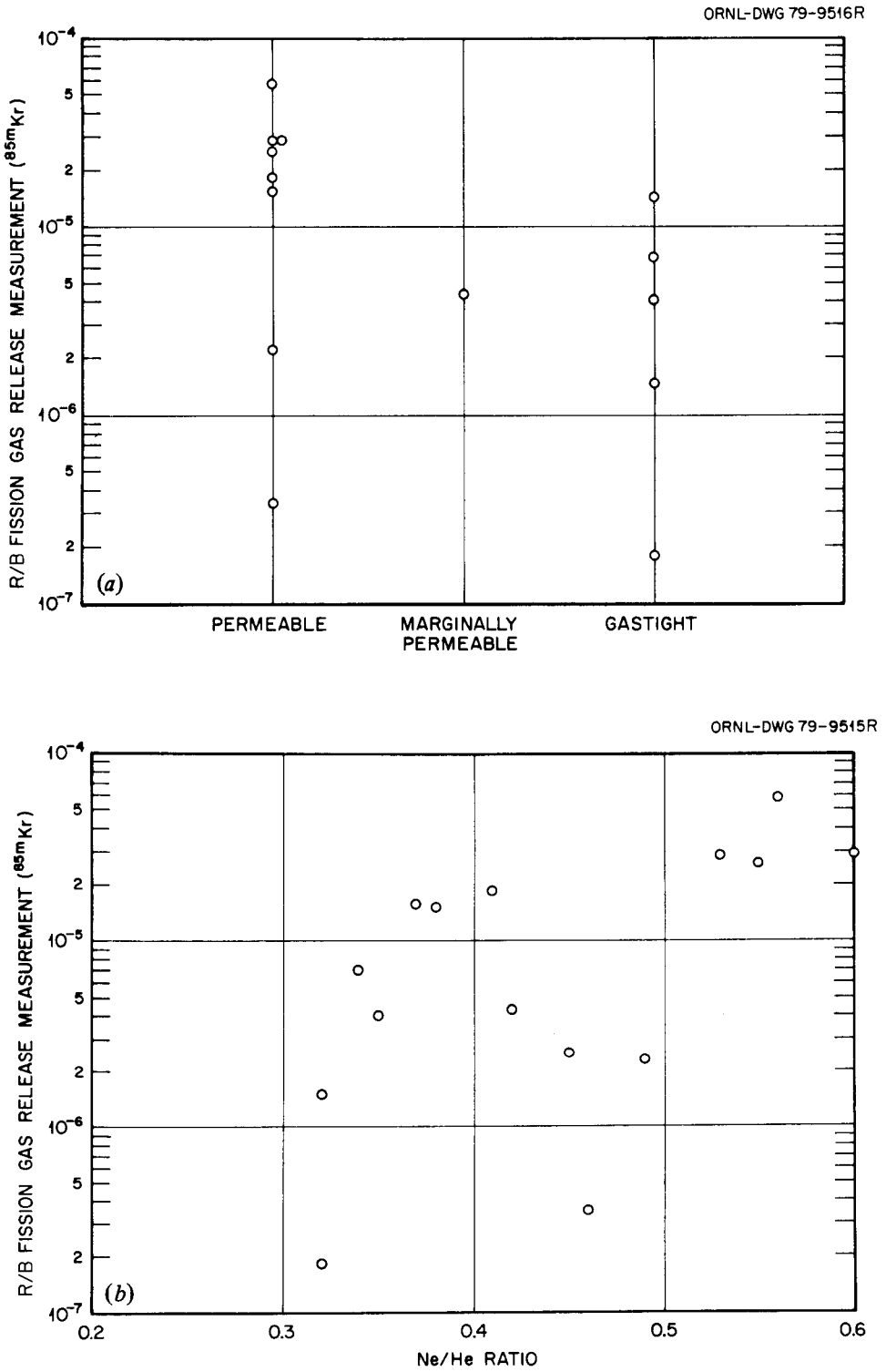


Fig. 2.33. LINAC Fission-Gas-Release Measurements Compared with (*a*) 18-h Chlorine Leach Results and (*b*) with Ne/He Intrusion Measurements.

As shown in Fig. 2.34, no correlation exists between the release-to-birth (R/B) measurements and the permeability of the pyrocarbon coatings, at least with the current R/B procedures. The General Atomic Company has plans to investigate the possibility of increasing the sensitivity of the R/B measurement by longer irradiation and heating times.

Capsules HRB-7 through -9 provided evidence[54,55] that the chlorine leach and Ne/He procedures can characterize the ability of PyC coating to contain fission gas. These capsules contained Biso-coated driver particles from two batches that were later determined, from chlorine-leach and Ne/He measurements, to have permeable LTI coatings. The chlorine-leach results ranked the two batches of driver particles to be very permeable and the Ne/He values were 0.48 and 0.53. The fission-gas release was so high in these capsules that $^{85m}Kr$ R/B values could not be measured.

In addition to the 24 batches of particles described above, an additional 10 batches of Biso-coated $ThC_2$ or $ThO_2$ particles were

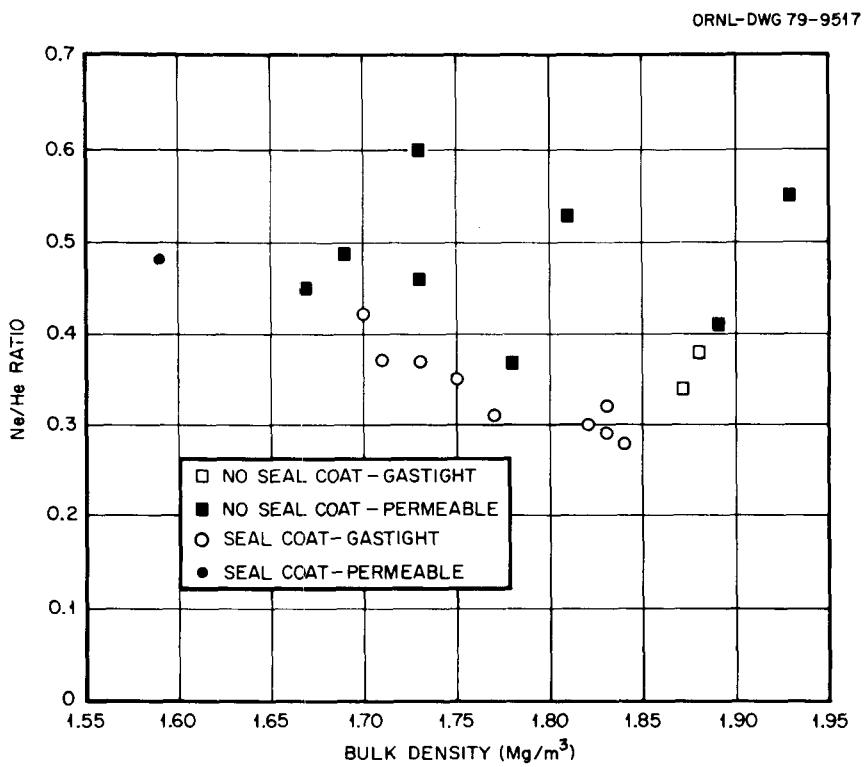


Fig. 2.34. Ne:He Ratios Plotted Against PyC Bulk Density for 24 Batches of Biso-Coated Particles Fabricated at GA.

characterized for gas permeability of their outer PyC coating (LTI layer) and will be compared with irradiation performance later. Two techniques were applied on the unirradiated specimens: Ne-He intrusion and long-term chlorine leach plus x-ray microradiography. Chlorine leach was applied at 1500°C for 18 h. The heavy metal release was analyzed after 3, 6, 12, and 18 h. After the 18 h of chlorination, the particles were radiographed. Table 2.20 shows the batch numbers of the particles supplied by GA and the LTI deposition conditions, coating characteristics, and permeability characterization data.

None of the particles from the ten batches had such severe gas-permeable LTI coatings that large amounts of heavy-metal chlorides were released during chlorination. Thus, only low thorium values were analyzed for 3, 6, 12, and 18 h of chlorination time (Table 2.21), but the x-ray microradiographs showed five of the ten batches to be permeable for chlorine, which is indicated by the large amount of heavy metal trapped in the buffer layer and at the buffer-LTI interface. The batches determined as being permeable to chlorine were: 6542-18-015, 6542-27-015, 6542-35-015, 6542-40-010, and 6542-40-020.

Four of the above batches permeable to chlorine had Ne/He values above 0.4, the fifth batch 0.37. Studies at ORNL show that LTI coatings are permeable to $Cl_2$ if the Ne:He ratio is greater than 0.4 and that batches with Ne:He ratios greater than 0.3 are marginally gastight to chlorine. Although there is no clear correlation between permeable coatings and deposition conditions, the batches with chlorine-permeable coatings have LTI bulk densities of less than 1.83 $Mg/m^3$.

The two batches that contained $ThC_2$ kernels showed heavy-metal migration into the buffer. In these cases the LTI layers were gastight, as indicated by the low Ne:He ratios.

### 2.7.2 Assay Measurements on FSVR Test Element Fuel Rods — P. Angelini

Nondestructive assay measurements have been performed for the fissile and fertile content of 36 fuel rods produced by GA during the production runs for the FSVR early validation tests. The ORNL assay measurements included uranium determination by nondestructive techniques (delayed and prompt neutron devices), using neutron interrogation and

Table 2.20. Pertinent Fabrication and Characterization Data for GA Fertile-Particle Batches Studied at ORNL

| Batch no. | Deposition temperature (C°) | Deposition rate (μm/min) | Size bed (mm) | Coating characteristics: Thickness (μm) | Density ($Mg/m^3$) | Bulk density ($Mg/m^3$) | Hg intrusion (μl/g OLTI) | Characterization: Long-term $Cl_2$ leach | X-ray microradiograph[a] | Ne:He |
|---|---|---|---|---|---|---|---|---|---|---|
| 6542-18-015 | 1395 | 6.48 | 127 | 70 | 1.84 | 1.73 | 31.5 | No Release | 1 | 0.46 |
| 6542-24-015 | 1260 | 6.59 | 127 | 80 | 1.94 | 1.83 | 30.4 | No Release | 3-2 | 0.32 |
| 6542-27-015 | 1300 | 4.59 | 127 | 81 | 1.86 | 1.78 | 23.3 | No Release | 1 | 0.37 |
| 6542-32-015 | 1300 | 4.65 | 127 | 82 | 1.84 | 1.75 | 28.49 | No Release | 3-2 | 0.35 |
| 6542-35-015 | 1265 | 5.6 | 127 | 70 | 1.94 | 1.81 | 36.8 | No Release | 1 | 0.53 |
| 6542-39-010 | 1375 | 4.06 | 240 | 73 | 1.94 | 1.88 | 17.3 | No Release | 3 | 0.38 |
| 6542-40-010 | 1540 | 5.84 | 240 | 73 | 1.73 | 1.67 | 22.7 | No Release | 1 | 0.45 |
| 6542-40-020 | 1525 | 5.85 | 240 | 79 | 1.76 | 1.69 | 23.5 | No Release | 1 | 0.49 |
| 4251-00-031 | 1330 | 2.49 | 127 | 93 | 2.00 | | | No Release | 1 | 0.21 |
| 4251-01-021 | 1340 | 3.20 | 127 | 64 | 1.96 | | | No Release | 1-2 | 0.33 |

[a]1, high heavy-metal migration into buffer layer; 2, light heavy-metal migration into buffer layer; and 3, no heavy-metal migration into buffer layer.

Table 2.21. Analytical Results of Long-Term Chlorine Leach of Biso-Coated $ThO_2$ and $ThC_2$ Batches from General Atomic Company

| Batch no. | Batch weight (g) | Chlorination time (h) | Thorium analyzed (mg) |
|---|---|---|---|
| 6542-18-015 | 1.5742 | 3 | 0.6 |
| | | 6 | 19 |
| | | 12 | 18 |
| | | 18 | 29 |
| 6542-24-015 | 1.6458 | 3 | 16 |
| | | 6 | 9 |
| | | 12 | 12 |
| | | 18 | 13 |
| 6542-27-015 | 1.5953 | 3 | 8 |
| | | 6 | 10 |
| | | 12 | 12 |
| | | 18 | 12 |
| 6542-32-015 | 1.5793 | 3 | 18 |
| | | 6 | 23 |
| | | 12 | 19 |
| | | 18 | 21 |
| 6542-35-015 | 1.5438 | 3 | 12 |
| | | 6 | 18 |
| | | 12 | 22 |
| | | 18 | 56 |
| 6542-39-010 | 1.5751 | 3 | 18 |
| | | 6 | 33 |
| | | 12 | 50 |
| | | 18 | 36 |
| 6542-40-010 | 1.5551 | 3 | 61 |
| | | 6 | 64 |
| | | 12 | 25 |
| | | 18 | 28 |
| 6542-40-020 | 1.7030 | 3 | 27 |
| | | 6 | 34 |
| | | 12 | 28 |
| | | 18 | 710 |
| 4251-00-031 | 1.7157 | 3 | 293 |
| | | 6 | 10 |
| | | 12 | 11 |
| | | 18 | 20 |
| 4251-01-021 | 2.0444 | 3 | 92 |
| | | 6 | 17 |
| | | 12 | 17 |
| | | 18 | 19 |

chemical assay of the same rods by the modified Davies-Gray potentiometric method for uranium and the EDTA volumetric titration method for thorium.

Each of the 36 rods was measured twice in the delayed neutron assay device and twice in the prompt neutron assay device. Separate calibration standards were fabricated. Except for the fact that the same calibration standards were used, the measurements on the separate nondestructive assay devices were independent. The measurements were performed by separate operators, and analysis of the data was performed by separate individuals. No comparison of the results was made until the final figures were obtained, and no adjustments have been made in the results. Tables 2.22, 2.23, and 2.24 list the average results of the two measurements by each device in terms of the estimated total $^{235}U$ content and its corresponding 95% confidence interval.

Table 2.22 Nondestructive Fissile Assay Results on Blend 12 of General Atomic Company Fuel Rods

| Fuel rod identification no. | Estimated total $^{235}U$ content (g) with corresponding 95% confidence | |
|---|---|---|
| | Delayed neutron assay device | Prompt neutron assay device |
| 10-12-6-12B | 0.1645 ± 0.0011 | 0.1647 ± 0.0024 |
| 10-12-17-12 | 0.1622 ± 0.0011 | 0.1615 ± 0.0024 |
| 10-34-39-12B | 0.1644 ± 0.0011 | 0.1628 ± 0.0024 |
| 10-82-8-12B | 0.1619 ± 0.0011 | 0.1645 ± 0.0024 |
| 10-82-31-12B | 0.1621 ± 0.0011 | 0.1606 ± 0.0024 |
| 10-95-3-12 | 0.1621 ± 0.0011 | 0.1644 ± 0.0024 |
| 10-130-10-12B | 0.1665 ± 0.0011 | 0.1632 ± 0.0024 |
| 10-160-12-12B | 0.1627 ± 0.0011 | 0.1620 ± 0.0024 |
| 10-184-11-12B | 0.1644 ± 0.0011 | 0.1632 ± 0.0024 |
| 10-235-5-12B | 0.1607 ± 0.0011 | 0.1592 ± 0.0022 |
| 10-262-1-12B | 0.1658 ± 0.0011 | 0.1649 ± 0.0022 |
| 10-298-32-12B | 0.1596 ± 0.0011 | 0.1589 ± 0.0022 |

The same fuel rods that were analyzed by nondestructive assay were later analyzed by wet chemistry techniques (modified Davies-Gray potentiometric titration for uranium, EDTA volumetric titration method for thorium), and these data are presented in Tables 2.25, 2.26, and

Table 2.23. Nondestructive Fissile Assay Results on Blend 13 of General Atomic Company Fuel Rods

| Fuel rod identification no. | Estimated total $^{235}U$ content (g) with corresponding 95% confidence | |
|---|---|---|
| | Delayed neutron assay device | Prompt neutron assay device |
| 10-7-14 | 0.1197 ± 0.0009 | 0.1172 ± 0.0022 |
| 10-7-35 | 0.1288 ± 0.0009 | 0.1299 ± 0.0022 |
| 10-12-20 | 0.1215 ± 0.0009 | 0.1208 ± 0.0022 |
| 10-12-28 | 0.1221 ± 0.0009 | 0.1209 ± 0.0022 |
| 10-16-8 | 0.1262 ± 0.0009 | 0.1252 ± 0.0022 |
| 10-16-26 | 0.1217 ± 0.0009 | 0.1238 ± 0.0022 |
| 10-21-9 | 0.1278 ± 0.0009 | 0.1292 ± 0.0022 |
| 10-21-32 | 0.1224 ± 0.0009 | 0.1216 ± 0.0022 |
| 10-26-18 | 0.1289 ± 0.0009 | 0.1291 ± 0.0022 |
| 10-26-38 | 0.1245 ± 0.0009 | 0.1252 ± 0.0022 |
| 10-30-14 | 0.1295 ± 0.0009 | 0.1303 ± 0.0022 |
| 10-30-37 | 0.1233 ± 0.0009 | 0.1227 ± 0.0022 |

Table 2.24. Nondestructive Fissile Assay Results on Blend 14 of General Atomic Company Fuel Rods

| Fuel rod identification no. | Estimated total $^{235}U$ content (g) with corresponding 95% confidence | |
|---|---|---|
| | Delayed neutron assay device | Prompt neutron assay device |
| 10-9-14 | 0.2840 ± 0.0015 | 0.2871 ± 0.0032 |
| 10-9-35 | 0.2939 ± 0.0015 | 0.2960 ± 0.0032 |
| 10-19-20 | 0.2859 ± 0.0015 | 0.2884 ± 0.0032 |
| 10-19-28 | 0.2852 ± 0.0015 | 0.2873 ± 0.0032 |
| 10-45-8 | 0.2937 ± 0.0015 | 0.2961 ± 0.0032 |
| 10-45-26 | 0.2858 ± 0.0015 | 0.2878 ± 0.0032 |
| 10-54-9 | 0.2871 ± 0.0015 | 0.2857 ± 0.0032 |
| 10-54-32 | 0.2813 ± 0.0015 | 0.2830 ± 0.0032 |
| 10-69-18 | 0.2849 ± 0.0015 | 0.2865 ± 0.0032 |
| 10-69-38 | 0.2852 ± 0.0015 | 0.2864 ± 0.0032 |
| 10-85-37 | 0.2904 ± 0.0015 | 0.2916 ± 0.0032 |
| 10-81-14 | 0.2866 ± 0.0015 | 0.2910 ± 0.0032 |

Table 2.25. Analytical Chemistry Assay Results on Blend 12 of General Atomic Company Fuel Rods

| Fuel rod identification no. | Analytical chemistry results | |
|---|---|---|
| | $^{235}U$ content (g) | Thorium content (g) |
| 10-12-6-12B | 0.1623 | 3.484 |
| 10-12-17-12 | 0.1631 | 3.540 |
| 10-34-39-12B | 0.1651 | 3.535 |
| 10-82-8-12B | 0.1621 | 3.532 |
| 10-82-31-12B | 0.1628 | 3.500 |
| 10-95-3-12 | 0.1646 | 3.528 |
| 10-130-10-12B | 0.1645 | 3.535 |
| 10-160-12-12B | 0.1617 | 3.553 |
| 10-184-11-12B | 0.1638 | 3.546 |
| 10-235-5-12B | 0.1597 | 3.532 |
| 10-262-1-12B | 0.1666 | 3.541 |
| 10-298-32-12B | 0.1589 | 3.525 |

Table 2.26. Analytical Chemistry Results on Blend 13 of General Atomic Company Fuel Rods

| Fuel rod identification no. | Analytical chemistry results | |
|---|---|---|
| | $^{235}U$ content (g) | Thorium content (g) |
| 10-7-14 | 0.1195 | 4.744 |
| 10-7-35 | 0.1280 | 4.641 |
| 10-12-20 | 0.1221 | 4.735 |
| 10-12-28 | 0.1206 | 4.665 |
| 10-16-8 | 0.1272 | 4.730 |
| 10-16-26 | 0.1210 | 4.746 |
| 10-21-9 | 0.1283 | 4.754 |
| 10-21-32 | 0.1223 | 4.710 |
| 10-26-18 | 0.1289 | 4.730 |
| 10-26-38 | 0.1251 | 4.740 |
| 10-30-14 | 0.1231 | 4.745 |
| 10-30-37 | 0.1258 | 4.721 |

2.27. The assay data include $^{235}U$ as well as thorium content per fuel rod. Agreement between the nondestructive assay and the chemistry results is rather good. Data on the isotopics for the GA as-received fissile and fertile particles are presented in Table 2.28. Data on the uranium and thorium weight percentage and data on the particle and coating thicknesses of the as-received fissile and fertile particles are presented in Tables 2.29 and 2.30, respectively.

Table 2.27. Analytical Chemistry Results on Blend 14 of General Atomic Company Fuel Rods

| Fuel rod identification no. | Analytical chemistry results | |
|---|---|---|
| | $^{235}U$ content (g) | Thorium content (g) |
| 10-9-14 | 0.2850 | 3.599 |
| 10-9-35 | 0.2931 | 3.590 |
| 10-19-20 | 0.2899 | 3.619 |
| 10-19-28 | 0.2867 | 3.575 |
| 10-45-8 | 0.2954 | 3.586 |
| 10-45-26 | 0.2870 | 3.583 |
| 10-54-9 | 0.2879 | 3.587 |
| 10-54-32 | 0.2873 | 3.602 |
| 10-69-18 | 0.2855 | 3.612 |
| 10-69-38 | 0.2871 | 3.587 |
| 10-85-37 | 0.2907 | 3.603 |
| 10-81-14 | 0.2900 | 3.595 |

Table 2.28. Isotopics for General Atomic Company Fuel Particles Batch FSV-D-Fiss Snm 6526

| Isotope | Weight (%) | Standard deviation | Number of samples |
|---|---|---|---|
| 234 | 0.949 | 0.005 | 4 |
| 235 | 93.057 | 0.023 | 4 |
| 236 | 0.344 | 0.003 | 4 |
| 238 | 5.649 | 0.023 | 4 |

Table 2.29. Weight Percentage of Heavy Metal in General Atomic Company Fissile and Fertile Particles

| Particle sample | Uranium | | Thorium | |
|---|---|---|---|---|
| | Original sample mass (g) | Uranium content (wt %) | Original sample mass (g) | Thorium content (wt %) |
| Fissile | 10.0996 | 13.746 | | |
| | 10.3058 | 13.842 | | |
| | 9.9546 | 13.813 | | |
| Mean | | 13.80 | | |
| Standard deviation | | 0.05 | | |
| Fertile | | | 10.553 | 47.83 |
| | | | 10.3313 | 47.58 |
| | | | 10.4058 | 47.43 |
| Mean | | | | 47.61 |
| Standard deviation | | | | 0.20 |

Table 2.30. Particle Characteristics of General Atomic Company Fissile and Fertile Particles

| | Fissile particles | Fertile particles |
|---|---|---|
| Kernel[a] | | |
| Diameter, μm | 202.9 | 444.9 |
| 95% Confidence interval, μm | 4.74 | 2.55 |
| Number of samples | 50 | 50 |
| Buffer and ILTI[a] | | |
| Thickness, μm | 130.05 | 83.15 |
| 95% Confidence interval, μm | 3.21 | 2.83 |
| Number of samples | 50 | 50 |
| SiC[a] | | |
| Thickness, μm | 38.51 | 38.65 |
| 95% Confidence interval, μm | 0.61 | 0.71 |
| Number of samples | 50 | 50 |
| Particle[b] | | |
| Diameter, μm | 604.20 | 761.10 |
| Standard deviation, μm | 26.89 | 21.66 |
| Number of samples | 34,467 | 11,430 |

[a]Based on radiograph.

[b]Based on particle-size analyzer.

### 2.7.3 Hot Gaseous Chlorine Leaching of Irradiated General Atomic Company Fuel Rods — E. L. Long, Jr.

At the request of GA, eight fuel rods from irradiation experiment FTE-16 were shipped to ORNL for hot gaseous chlorine leaching. The rods were leached at 1000°C for various intervals, shown in Table 2.31. In addition, isotopic uranium analyses were run on the leach solutions for each rod; these data are listed in Table 2.32. Results from these experiments were forwarded to GA for review.

### 2.7.4 Miscellaneous Requests from General Atomic Company for Service Work — E. L. Long, Jr.

The metallographic preparation and examination of eight GA fuel rods irradiated in HRB-12 was performed at ORNL. This work was done at GA's request because their hot cells were undergoing modifications.

A metallographic mount was shipped to ORNL for shielded electron microprobe analysis. The mount contained a cross section through a fuel rod from irradiation experiment P13Q. A phase, subsequently identified at palladium, had reacted with the SiC coatings. The results were forwarded to GA and have been incorporated into one of their reports.[56]

## 2.8 REFERENCES


1. F. J. Homan, *HTGR Base-Technology Program Annu. Prog. Rep. Dec. 31, 1977* (ORNL-5412), p. 19.
2. W. P. Eatherly, "Postirradiation Examination of HT-17, -18, -19," *HTGR Base-Technology Program Prog. Rep. July 1, 1975–Dec. 31, 1976,* ORNL-5274, pp. 216-21.
3. R. L. Beatty, "Irradiation Test Capsules HT-17, -18, and -19," *HTGR Base-Technology Program Prog. Rep. Jan. 1, 1974–June 30, 1975,* ORNL-5108, pp. 269-76.
4. E. L. Long, Jr., et al., *Irradiation Performance of HTGR Biso Fertile Particles in HFIR Experiments HT-17, -18, and -19,* ORNL/TM-6414 (November 1978).

Table 2.31. Chlorine Leach Data

| Specimen | Position | Accumulated leach time (h) | Accumulated Th (Σ mg) | Total Th[a] (%) | Heavy metal content (%) | Accumulated U (Σ mg) | Total U[a] (%) | Heavy metal content (%) |
|---|---|---|---|---|---|---|---|---|
| H-663 | 2-5-5 | 3[b] | 49.7 | 24.1 | 1.16 | 0.600 | 16.7 | 0.21 |
| | | 6 | 135.2 | 41.5 | 3.16 | 2.284 | 46.8 | 0.82 |
| | | 12[b] | 174.7 | 19.2 | 4.08 | 2.982 | 19.4 | 1.07 |
| | | 30[b] | 206.0 | 15.2 | 4.81 | 3.600 | 17.2 | 1.29 |
| H-658 | 2-5-10 | 3[c] | 0.007 | <0.002 | <0.001 | 0.009 | 0.14 | 0.003 |
| | | 3[b] | 229.7 | 54.7 | 5.35 | 3.316 | 51.9 | 1.18 |
| | | 6 | 301.8 | 17.2 | 7.03 | 4.202 | 13.9 | 1.50 |
| | | 12 | 370.1 | 16.3 | 8.63 | 5.588 | 21.8 | 2.00 |
| | | 30 | 419.7 | 11.8 | 9.78 | 6.371 | 12.3 | 2.28 |
| H-686 | 2-3-10 | 3[c] | 0.054 | 0.02 | 0.002 | 0.003 | 0.06 | 0.001 |
| | | 3[b] | 178.2 | 90.2 | 7.71 | 4.523 | 90.6 | 1.92 |
| | | 8 | 191.7 | 6.8 | 8.30 | 4.798 | 5.5 | 2.04 |
| | | 14 | 194.1 | 1.2 | 8.40 | 4.894 | 1.9 | 2.08 |
| | | 32 | 197.6 | 1.8 | 8.55 | 4.990 | 1.9 | 2.12 |
| H-633 | 3-5-7 | 3[c] | 0.008 | 0.007 | <.001 | 0.007 | 0.43 | 0.002 |
| | | 3[b] | 68.2 | 57.9 | 2.30 | 0.915 | 55.6 | 0.23 |
| | | 6 | 86.8 | 15.8 | 2.92 | 1.117 | 12.4 | 0.28 |
| | | 12 | 105.1 | 15.5 | 3.54 | 1.420 | 18.5 | 0.36 |
| | | 30 | 117.8 | 10.8 | 3.97 | 1.634 | 13.1 | 0.42 |
| H-732 | 2-8-9 | 3[c] | 0.008 | 0.04 | <.001 | 0.0030 | 0.50 | 0.001 |
| | | 3[b] | 9.27 | 51.9 | 0.40 | 0.2267 | 44.1 | 0.097 |
| | | 6 | 12.54 | 18.3 | 0.54 | 0.3207 | 18.5 | 0.14 |
| | | 12 | 15.66 | 17.5 | 0.68 | 0.4290 | 21.3 | 0.18 |
| | | 30 | 17.83 | 12.2 | 0.77 | 0.5073 | 15.4 | 0.22 |
| H-671 | 2-1-11 | 3[c] | 0.012 | 0.008 | <.001 | 0.0133 | 0.38 | 0.005 |
| | | 3[b] | 96.6 | 61.7 | 4.15 | 1.7233 | 57.8 | 0.73 |

Table 2.31. (continued)

| Specimen | Position | Accumulated leach time (h) | Accumulated Th (Σ mg) | Total Th[a] (%) | Heavy metal content (%) | Accumulated U (Σ mg) | Total U[a] (%) | Heavy metal content (%) |
|---|---|---|---|---|---|---|---|---|
| | | 6 | 116.5 | 12.7 | 5.00 | 2.1033 | 12.8 | 0.89 |
| | | 12 | 136.2 | 12.6 | 5.85 | 2.4533 | 11.8 | 1.04 |
| | | 30 | 156.6 | 13.0 | 6.72 | 2.9643 | 17.2 | 1.26 |
| H-635 | 3-5-5 | 3[c] | 0.019 | 0.014 | <.001 | 0.0087 | 0.51 | 0.002 |
| | | 3[b] | 89.7 | 66.3 | 3.03 | 1.2527 | 73.2 | 0.33 |
| | | 6 | 111.6 | 16.2 | 3.77 | 1.4317 | 10.5 | 0.37 |
| | | 12 | 128.6 | 12.6 | 4.34 | 1.5987 | 9.8 | 0.42 |
| | | 30 | 135.2 | 4.9 | 4.57 | 1.6997 | 5.9 | 0.44 |
| H-731 | 2-8-8 | 3[b] | 16.52 | 66.8 | 0.72 | 0.558 | 64.9 | 0.24 |
| | | 6 | 21.46 | 20.0 | 0.93 | 0.708 | 17.4 | 0.30 |
| | | 12 | 23.12 | 6.7 | 1.00 | 0.778 | 8.1 | 0.33 |
| | | 30 | 24.74 | 6.5 | 1.07 | 0.860 | 9.5 | 0.37 |

[a]Percentage of heavy metal leached during each time interval.

[b]Isotopic analysis performed (refer to Table 2.32).

[c]Treated for 3 h at 1000°C in flowing stream of argon.

Table 2.32. Isotopic Analysis Data

| Specimen | Position | Accumulated leach time (h) | Uranium (at. %) | | | | |
|---|---|---|---|---|---|---|---|
| | | | 233 | 234 | 235 | 236 | 238 |
| H-633 | 2-5-5 | 3 | 79.67 | 6.79 | 4.88 | 1.07 | 7.59 |
| | | 12 | 87.77 | 7.47 | 3.49 | 0.699 | 0.565 |
| | | 30 | 85.36 | 7.24 | 5.36 | 1.19 | 0.847 |
| H-658 | 2-5-10 | 3 | 88.35 | 7.64 | 1.43 | 0.186 | 2.39 |
| H-686 | 2-3-10 | 3 | 75.39 | 6.70 | 12.97 | 3.17 | 1.77 |
| H-633 | 3-5-7 | 3 | 90.60 | 5.74 | 2.46 | 0.379 | 0.821 |
| H-732 | 2-8-9 | 3 | 47.52 | 4.50 | 33.34 | 8.35 | 6.29 |
| H-671 | 2-1-11 | 3 | 83.13 | 7.22 | 6.53 | 1.48 | 1.64 |
| H-635 | 3-5-5 | 3 | 88.53 | 6.15 | 2.29 | 0.345 | 2.69 |
| H-731 | 2-8-8 | 3 | 49.48 | 4.71 | 32.10 | 7.98 | 5.73 |

5. T. N. Tiegs et al., *Irradiation Performance of HTGR Fuel in HFIR Capsule HT-31,* ORNL-5510, to be published.
6. J M Robbins, "Irradiation Experiment HT-32," *HTGR Base-Technology Prog. Rep. July 1, 1975–Dec. 31, 1976,* ORNL-5274, pp. 221-26.
7. T. N. Tiegs et al., "Capsule HT-32," *HTGR Base-Technology Program Annu. Prog. Rep. Dec. 31, 1977,* ORNL-5412, pp. 60-71.
8. T. N. Tiegs and J M Robbins, *Irradiation Performance of HTGR Fuel in HFIR Capsule HT-33,* ORNL report, to be published.
9. M. J. Kania, "Capsule HT-34," *HTGR Base-Technology Program Annu. Prog. Rep. Dec. 31, 1977,* ORNL-5412, pp. 71-85.
10. M. J. Kania, *HTCAP — A FORTRAN IV PROGRAM for Calculating Coated Particle Operating Temperatures in HFIR Target Irradiation Experiments,* ORNL/TM-5332 (May 1976).
11. W. J. Lackey, D. P. Stinton, and J. D. Sease, "Improved Gas Distributor for Coating High-Temperature Gas-Cooled Reactor Fuel Particles," *Nucl. Tech* 35: 227 (September 1977).
12. R. L. Beatty, "Irradiation Capsules HT-17, -18, and -19," *HTGR Base Technology Program Prog. Rep. Jan. 1, 1974–June 30, 1975,* ORNL-5108, pp. 269-76.
13. M. J. Kania, R. L. Hamner, E. L. Long, Jr., and J M Robbins, "Capsule HRB-13," *HTGR Base Technology Program Prog. Rep. July 1, 1975–Dec. 31, 1976,* ORNL-5274, pp. 289-99.
14. E. L. Long, Jr., and K. R. Thoms, "Capsule HRB-13," *HTGR Base Technology Program Annu. Prog. Rep. Dec. 31, 1977,* ORNL-5412, pp. 98-102.
15. T. N. Tiegs et al., *HTGR Fuel Rod Deconsolidation,* ORNL/TM-6426 (December 1978).
16. M. J. Kania and E. L. Long, Jr., "Capsule HRB-14," *HTGR Base-Technology Program Annual Prog. Rep. Dec. 31, 1977,* ORNL-5412, pp. 98-105.
17. K. H. Valentine, *ENCTRK, A Computer Program to Model Heat Transfer Across Asymmetric Gap in Cylindrical Fuel Rods,* ORNL/TM report, to be published.

18. E. J. Allen, *CACA-2: Revised Version of CACA-1 — A Heavy Isotope and Fission-Product Concentration Calculation Code for Experimental Irradiation Capsules,* ORNL/TM-5266 (February 1976).

19. E. L. Long, Jr., and D. P. Stinton, "Capsule HRB-15b," *HTGR Base-Technology Program Annu. Prog. Rep. Dec. 31, 1977,* ORNL-5412, pp. 105-109.

20. T. N. Tiegs and K. R. Thoms, *Operation and Postirradiation Examination of ORR Capsule OF-2,* ORNL-5428 (February 1979).

21. W. J. Lackey, D. P. Stinton, and J. D. Sease, "Improved Gas Distributor for Coating High-Temperature Gas-Cooled Reactor Fuel Particles," *Nucl. Technol.* 35: 227-37 (September 1977).

22. W. J. Lackey and J. D. Sease, "Means for Effecting Fluidization in Pyrolytic Carbon Coating Processes," U.S. Patent 3,889,631, June 17, 1975.

23. B. A. Thiele, D. P. Stinton, and D. A. Costanzo, "Detection of Gas Permeable Biso-Coated Fuel Particles for High-Temperature Gas-Cooled Reactors," ORNL/TM report, to be published.

24. C. S. Morgan, G. L. Powell, W. P. Eatherly, M. Reeves, and J. S. Tolliver, "Inert Gas Permeability of Pyrocarbon Coatings," *Gas-Cooled Reactor Programs HTGR Fuel Recycle Development Annu. Prog. Rep. Sept. 30, 1977,* ORNL-5423, pp. 124-27.

25. D. P. Stinton, "Microsphere Coating," *Gas-Cooled Reactor Programs HTGR Fuel Recycle Development Annu. Prog. Rep. Sept. 30, 1977,* ORNL-5423, pp. 115-18.

26. D. P. Stinton and W. J. Lackey, "Effect of Deposition Conditions on the Properties of Pyrolytic Silicon Carbide Coatings for HTGR Fuel Particles," *Am. Ceram. Soc. Bull.,* to be published.

27. C. S. Morgan, *Characterization of Pyrocarbon Coatings of HTGR Fuel Particles by Inert Gas Intrusion,* ORNL/TM report, to be published.

28. E. L. Long, Jr., et al., *Irradiation Performance of HTGR Biso Fertile Particles in HFIR Experiment HT-17, -18, and -19,* ORNL/TM-6414 (November 1978).

29. J. I. Federer, *Fluidized Bed Deposition and Evaluation of Silicon Carbide Coatings on Microspheres,* ORNL/TM-5152 (January 1977).

30. D. P. Stinton and W. J. Lackey, *Effect of Deposition Conditions on the Properties of Pyrolytic Silicon Carbide Coatings for High-Temperature Gas-Cooled Reactor Fuel Particles,* ORNL/TM-5743 (October 1977).

31. T. B. Lindemer and R. L. Pearson, *J. Am. Ceram. Soc.* 60(1-2): 5 (1977).

32. E. J. Allen, *CACA-2: Revised Version of CACA — A Heavy Isotope and Fission-Product Concentration Calculational Code for Experimental Irradiation Capsules,* ORNL/TM-5266 (February 1976).

33. J. F. Mincey, ORNL, personal communication to W. E. Thomas, February 1978.

34. R. L. Senn and W. R. Mixon, "Experimental Measurement of Gamma Heat in the High-Flux Isotope Reactor," *Nucl. Technol.* 12: 239 (1971).

35. M. J. Kania, ORNL, personal communication to W. E. Thomas, June 1978.

36. W. D. Turner, D. C. Elrod, and I. I. Simon-Tov, *Heating 5 — An IBM 360 Heat Conduction Program,* ORNL/CDS/TM-15 (October 1977).

37. H. T. Kerr, C. J. Allen, and D. L. Reed, *Lattice Displacement Calculations and Comparisons for Different Irradiation Facilities,* ORNL/TM-5269 (March 1976).

38. R. D. Cheverton and T. M. Sims, *HFIR Core Nuclear Design,* ORNL-4621 (July 1971).

39. R. L. Pearson and T. B. Lindemer, *Simulated Fission Product Oxide Behavior in Triso-Coated HTGR Fuel,* ORNL/TM-6741, to be published.

40. F. Homan, ORNL; H. Nabielek, KFA; and L. Yank, GA, *Low-Enriched Fuel Particle Performance Review,* JÜL-1502 and GA-A14579, General Atomic Company, San Diego, Calif. (August 1978).

41. K. H. Valentine, "Irradiated Microsphere Gamma Analyzer System" *HTGR Base-Technology Prog. Rep. Jan. 1–June 30, 1975,* ORNL-5108, pp. 446-56.

42. M. J. Kania and K. H. Valentine, "Irradiated Microsphere Gamma Analyzer System," *HTGR Base-Technology Annu. Prog. Rep. for Period Ending Dec. 31, 1977,* ORNL-5412, pp. 136-52.

43. B. A. Thiele and M. Herren, *Determination of End-of-Life Failure Fractions of HTGR-Fuel Particles by Postirradiation Annealing and Beta Autoradiography,* ORNL/TM-6619 (November 1978).

44. M. J. Kania and K. H. Valentine, "Irradiated Microsphere Gamma Analyzer System," *HTGR Base Technology Program Annu. Prog. Rep. Dec. 31, 1977,* ORNL-5412 (July 1978), pp. 136-52.

45. K. H. Valentine and M. J. Kania, *IMGA Operating Manual,* ORNL/TM report, to be published.

46. T. N. Tiegs and K. R. Thoms, *Operation and Postirradiation Examination of ORR Capsule OF-2,* ORNL-5428 (February 1979).

47. E. J. Allen, *CACA-2,* ORNL/TM-5266 (February 1976).

48. M. J. Kania et al., *Performance of HTGR Fuel in HFIR Capsules HT-12 Through -15,* ORNL/TM-5305 (February 1977).

49. C. S. Morgan, *Characterization of Pyrocarbon Coatings by Inert Gas Intrusion,* ORNL/TM report, to be published.

50. H. Bildstein and H. Strigl, "Determination of Free Volumes and Gas Content of Coated Fuel Particles for Gas-Cooled Reactors," *Proc. Conf. Post-Irradiation Examination Techniques, University of Reading, 1972,* British Nuclear Energy Society–Institute of Civil Engineers, London, 1972.

51. M. J. Kania et al., *Irradiation Performance of HTGR Fertile Fuel in HFIR Target Capsules HT-12 through HT-15: Part I — Experimental Description and Fission Product Behavior,* ORNL/TM-5305 (February 1977).

52. T. B. Lindemer and R. L. Pearson, "Apparatus for Measuring Gases from Irradiated Fuel Particles," *J. Nucl. Mater.* 55: 359-61 (1975).

53. C. S. Morgan, *Characterization of Pyrocarbon Coatings of HTGR Fuel Particles by Inert Gas Intrusion,* ORNL/TM-6819, to be published.

54. K. H. Valentine et al., *Irradiation Performance of HTGR Fuel Rods in HFIR Experiments HRB-7, and -8,* ORNL-5228 (May 1977).

55. F. J. Homan et al., *Irradiation Performance of HTGR Fuel Rods in HFIR Experiments HRB-9 and -10,* ORNL-5254 (April 1978).

56. General Atomic Company, *HTGR Generic Technology Program — Fuels and Core Development Program Quarterly Prog. Rep. May 31, 1978,* GA-A14953, pp. 2-10.

# 3. PRESTRESSED CONCRETE PRESSURE VESSEL DEVELOPMENT

## 3.1 INTRODUCTION

The activities described under the Prestressed Concrete Reactor Vessel (PCRV) Program for the reporting period reflect transitions from the original generic program to one designed to provide design verification and support for the reference 900 MW(e) steam-cycle High-Temperature Gas-Cooled Reactor (HTGR) and back to a generic program oriented to support the development of PCRVs for advanced HTGRs. The activities remain divided into the following six task areas:

1. analysis methods,
2. concrete properties in nuclear environments,
3. prestressing systems,
4. instrumentation,
5. structural models, and
6. liners and penetrations.

Sections 3.3 through 3.7 discuss progress in these task areas. Section 3.2 describes a plan for the development of an optimized PCRV, which if implemented, would involve design support activities in several of the basic task areas. The PCRV Model Program Definition presented in Sect. 3.6.2 was originally undertaken as the first step in planning the test of a PCRV model to support design of the 900 MW(e) HTGR reference plant. No further development of this specific model will be undertaken in light of the recent decision to bypass the development of a steam-cycle HTGR; however, the proposed optimization study could make important contributions to the development of a PCRV for a gas-turbine or process-heat HTGR, and significant cost reductions could be realized.

## 3.2 PCRV OPTIMIZATION PLAN

A plan for the development of an optimized PCRV[1] has been prepared by technical representatives of an architectural engineer, Stone and Webster Engineering Corporation; the HTGR designer and potential vendor,

General Atomic Company (GA); and a national laboratory (ORNL). Although the plan originally focused on the steam-cycle HTGR, it is equally applicable to the PCRVs for the gas-turbine HTGR and process heat HTGRs. The abstract of the report follows.

> A plan is presented for the development of an optimized PCRV for the steam-cycle HTGR 900 MW(e) reference plant. The purpose of the proposed program is to identify desirable construction innovations and cost-effective changes in configuration, materials, and design criteria to provide the basis for the evolution of more economical plants. Such a study is proposed, to be conducted by the potential gas-cooled reactor vendor, an architectural engineering firm, and a national laboratory — all having experience in the various aspects of PCRV design and development. The scope of the proposed program is outlined, and the tasks to be undertaken during the intial year are discussed together with the estimated first-year costs.

## 3.3 ANALYSIS METHODS DEVELOPMENT

The major objective of the PCRV analytical effort is to develop techniques that can be incorporated into existing modern finite-element computer programs to improve the accuracy and efficiency of these codes. Two techniques that were studied are an improved inelastic concrete constitutive model and a method for efficiently modeling the enormous quantity of reinforcing steel in multicavity PCRVs.

### 3.3.1 Concrete Constitutive Models

Many analytical representations have been proposed that attempt to describe the response of concrete under complex loading conditions such as those existing in multicavity PCRVs. Two constitutive models investigated at ORNL are the model contained in the ADINA finite-element code[2] and the endochronic model proposed by Z. P. Bazant.[3]

#### 3.3.1.1 Description of the ADINA Model

The concrete constitutive model that is contained in the ADINA finite-element code utilizes an isotropic nonlinear stress-strain relation based on a uniaxial stress-strain representation. To obtain the

stress-strain relation for triaxial loading conditions, a tangent Young's modulus $t_{E_i}$ is obtained for each principal stress direction using the equation

$$t_{E_i} = E_0\left(1 - t_{e_i}/e_c\right)^2 \Big/ \left[1 + \left(E_0/E_s - 2\right)\left(t_{e_i}/e_c\right) + \left(t_{e_i}/e_c\right)^2\right]^2 , \qquad (1)$$

where $E_0$ is the initial uniaxial tangent modulus, $E_s$ is the uniaxial secant modulus corresponding to the maximum uniaxial compressive stress, $e_c$ is the strain corresponding to the maximum uniaxial compressive stress, and $t_{e_i}$ is the principal strain. An equivalent multiaxial Young's modulus is calculated using the equation

$$t_E = \left(t_{E_1}\left|t_{\sigma_1}\right| + t_{E_2}\left|t_{\sigma_2}\right| + t_{E_3}\left|t_{\sigma_3}\right|\right) \Big/ \left(\left|t_{\sigma_1}\right| + \left|t_{\sigma_2}\right| + \left|t_{\sigma_3}\right|\right) , \qquad (2)$$

where $t_{\sigma_1}$, $t_{\sigma_2}$, and $t_{\sigma_3}$ are principal stresses and $t_{E_1}$, $t_{E_2}$, and $t_{E_3}$ are the corresponding uniaxial Young's moduli. For unloading, the initial Young's modulus $E_0$ is used to form the incremental stress-strain matrix. The material is defined to be unloading if the effective deviatoric stress is less than the maximum that has occurred during previous solution increments.

The failure envelope proposed by Khan and Saugy[4] is used to determine tensile and compressive failure under triaxial states of stress. The principal stresses are determined whenever stresses are calculated. If tensile stress in a principal direction exceeds the tensile failure criteria, the normal and shear stiffnesses across the plane perpendicular to the principal direction are reduced and the corresponding stresses are released. On the other hand, if the stress state exceeds the compressive failure criteria, the stiffness of the material in all directions is reduced and all stress is released.

#### 3.3.1.2 Description of the Endochronic Model

The endochronic model for concrete is an extension of the inelastic endochronic model first introduced by Valanis.[5] In this model, the

inelastic strain accumulation is characterized by a scalar parameter $z$, called intrinsic time, whose increment is a positive definite function of the strain increment. The principal features introduced by Bazant were to include: (1) the sensitivity of the intrinsic time increments caused by hydrostatic pressure; (2) the inelastic dilatancy resulting from shear straining, and (3) a description of the strain-softening that occurs after the peak stress has been achieved. The inclusion of strain-softening in the constitutive relations eliminates the necessity for defining separate compressive failure surfaces.

To satisfy the condition of isotropy, the incremental stress-strain relations are expressed independently in terms of the volumetric and deviatoric components of stress and strain; the resulting relations are:

$$de_{ij} = (ds_{ij}/2G) + (s_{ij}/2G)dz$$

and (3)

$$d\varepsilon = d\sigma/3K + d\lambda \ ,$$

where $d\varepsilon$ and $d\sigma$ are increments of the volumetric strain and hydrostatic stress, and $de_{ij}$ and $ds_{ij}$ are increments of the deviatoric strain and stress; the variable $d\lambda$ is the increment in inelastic volumetric strain, and $dz$ is the increment in intrinsic time. The shear and bulk moduli $G$ and $K$ are taken to be decreasing functions of the inelastic dilatancy given by

$$G = G_0[1 - 0.25(\lambda/\lambda_0)]$$

and (4)

$$K = K_0[1 - 0.25(\lambda/\lambda_0)] \ ,$$

where $G_0$ and $K_0$ are the initial moduli, and $\lambda_0$ is a constant. The increment in the inelastic dilatancy is related to the increment in the deviatoric strains by

$$d\lambda = \ell(\lambda)\ L[J_2(\varepsilon),\ I_1(\sigma),\ \lambda]\sqrt{J_2(d\varepsilon)}\ , \tag{5}$$

where $\ell(\lambda)$ and $L[J_2(\varepsilon),\ I_1(\sigma),\ \lambda]$ are functions, $I_1(\sigma)$ is the first invariant of the stress tensor, and $J_2(\varepsilon)$ is the second invariant of the strain tensor. The increment in the intrinsic time is related to an increment in the deviatoric strains by

$$dz = |d\eta/f(\eta)|$$

and (6)

$$d\eta = F(\varepsilon,\ \sigma)\sqrt{J_2(\varepsilon)}\ ,$$

where $f(\eta)$ and $F(\varepsilon,\ \sigma)$ are functions of stress and strain invariants. The explicit forms of the functions $\ell$, $L$, $f$, and $F$ developed by Bazant are complicated and will not be included.[3] The functional form developed by Bazant requires the specification of 19 constants. Using previously published experimental data, all 19 constants were related to a single material property — the compressive strength of the particular concrete.

### 3.3.1.3 Comparisons with Experimental Data

A subcontract was negotiated with The University of Tennessee to assist in verification of the endochronic constitutive model. The University of Tennessee study consisted of comparisons of (1) predicted and measured response of homogeneous concrete test specimens subjected to uniaxial, biaxial, and triaxial states of stress and (2) the results of finite-element analyses of concrete structures with available test data.

The major findings of the first segment of the study included the discovery of a dip in the predicted stress-versus-strain curve of

triaxial specimens and the realization that the modulus of elasticity should be a variable parameter in the endochronic model. A dip at approximately 6% strain, which is believed to be caused by a spike in the equations controlling shear compaction, is shown in Fig. 3.1. Typical results, using the endochronic model to predict behavior of a uniaxially loaded specimen of relatively low strength, are given in Fig. 3.2. Figure 3.3 is a plot of the uniaxial response of a high-strength concrete. The endochronic model generally underestimates the modulus of elasticity of low-strength concretes much more severely than of high-strength concretes.

Structures analyzed during the second segment of the study included beams tested as part of an ORNL study of grouted versus nongrouted tendons. Figures 3.4 and 3.5 show the load versus centerline deflection for two of the beams. In both cases the predictions were reasonable; however, the actual ultimate load was larger than predicted.

To partially verify the suitability of the endochronic concrete model to represent complex states of stress in PCRVs and related structures, an analysis was made of the ORNL half-depth 1/15-scale Gas-Cooled

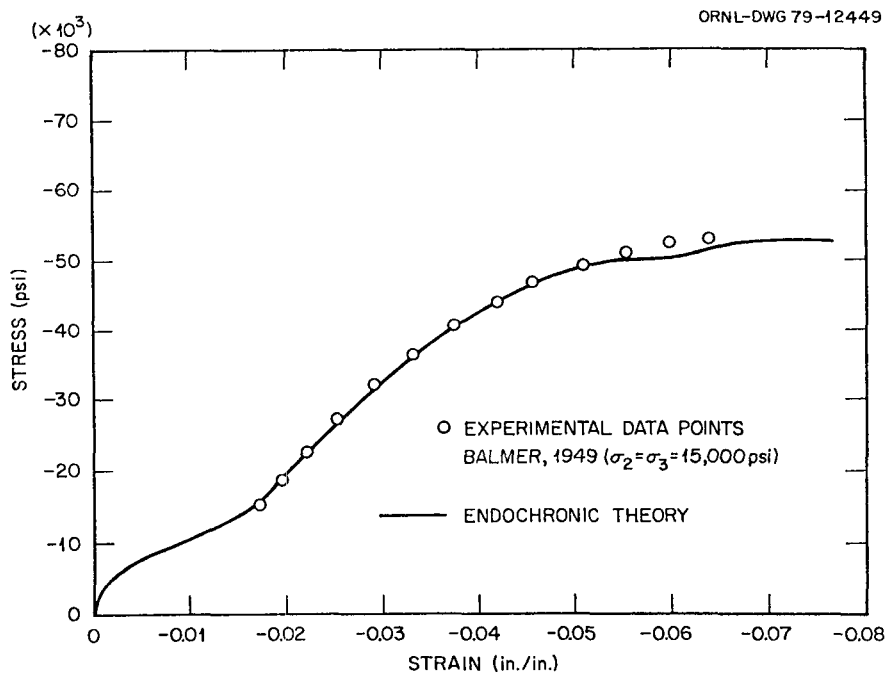


Fig. 3.1. Stress-Strain Response of a Triaxially Loaded Specimen.

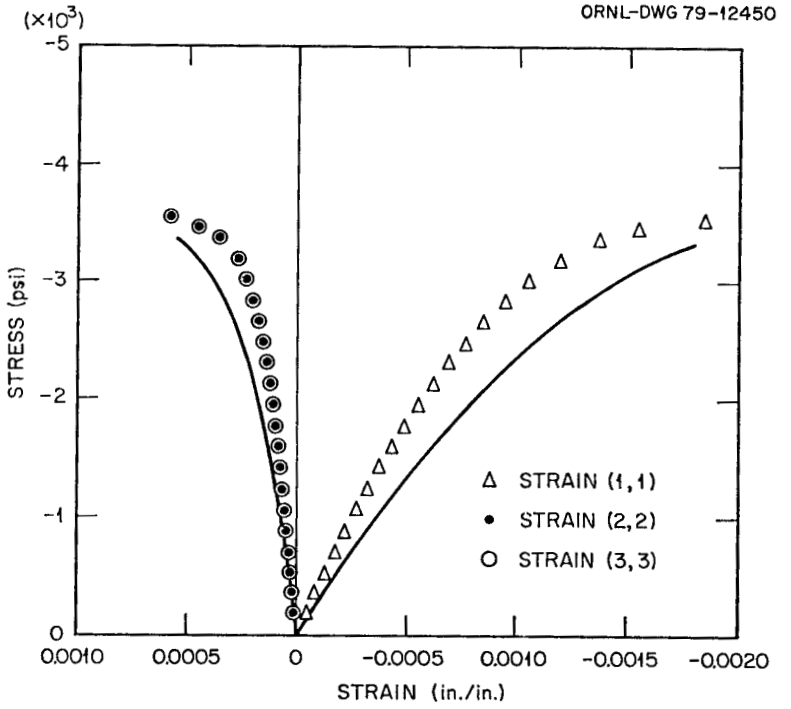


Fig. 3.2. Stress-Strain Response of a Low-Strength Concrete.

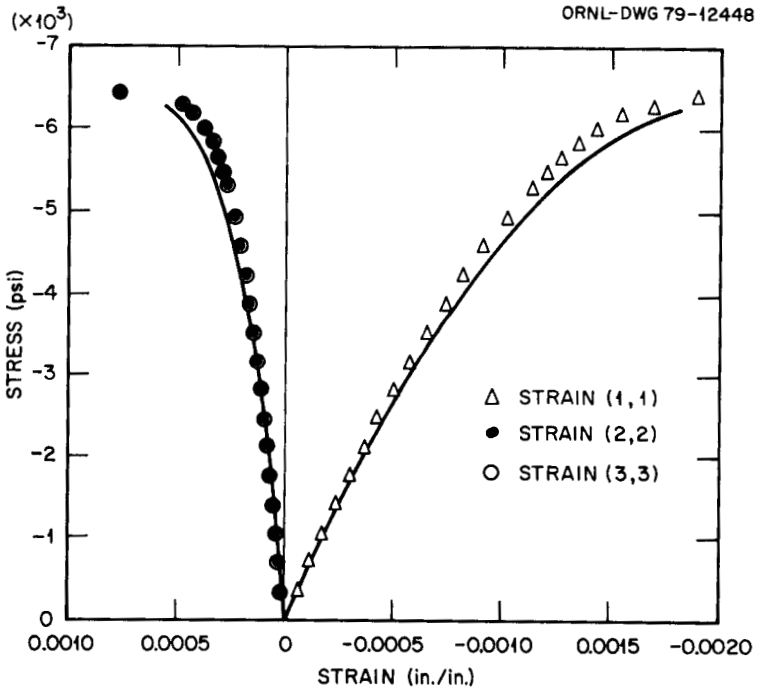


Fig. 3.3. Stress-Strain Response of a High-Strength Concrete.

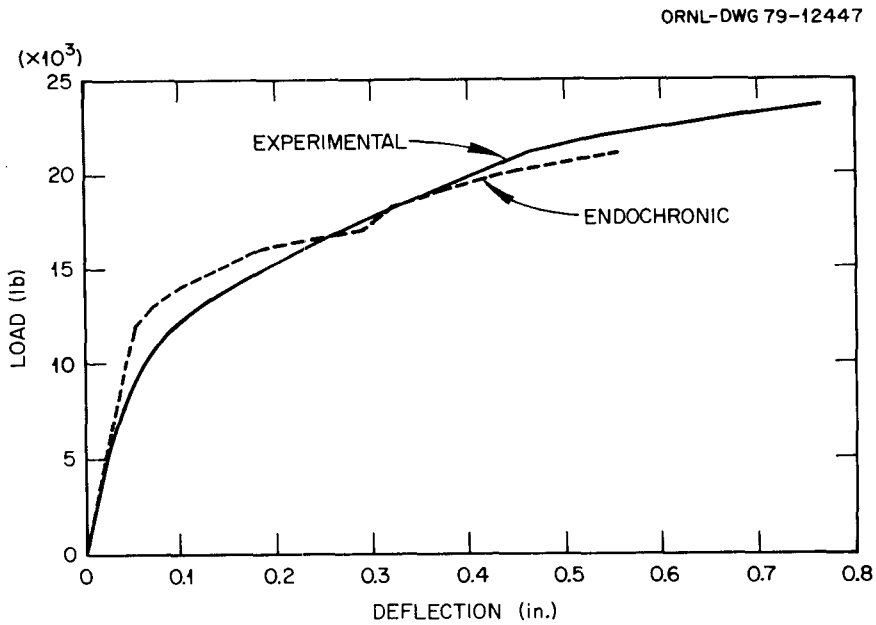


Fig. 3.4. Beam G3 Versus Endochronic Prediction.

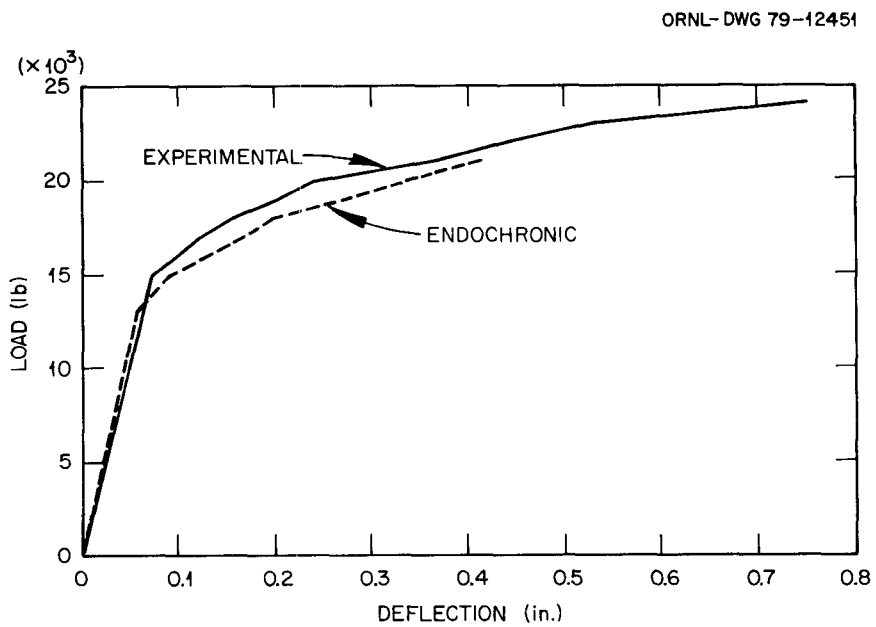


Fig. 3.5. Beam G4 Versus Endochronic Prediction.

Fast Reactor (GCFR) steam-generator cavity closure model. This closure model had previously been analyzed by use of the ADINA concrete model. The results of both analyses are shown with the corresponding experimental data at two gage locations in Figs. 3.6 and 3.7. According to the results obtained by use of the ADINA concrete model, nonlinear behavior

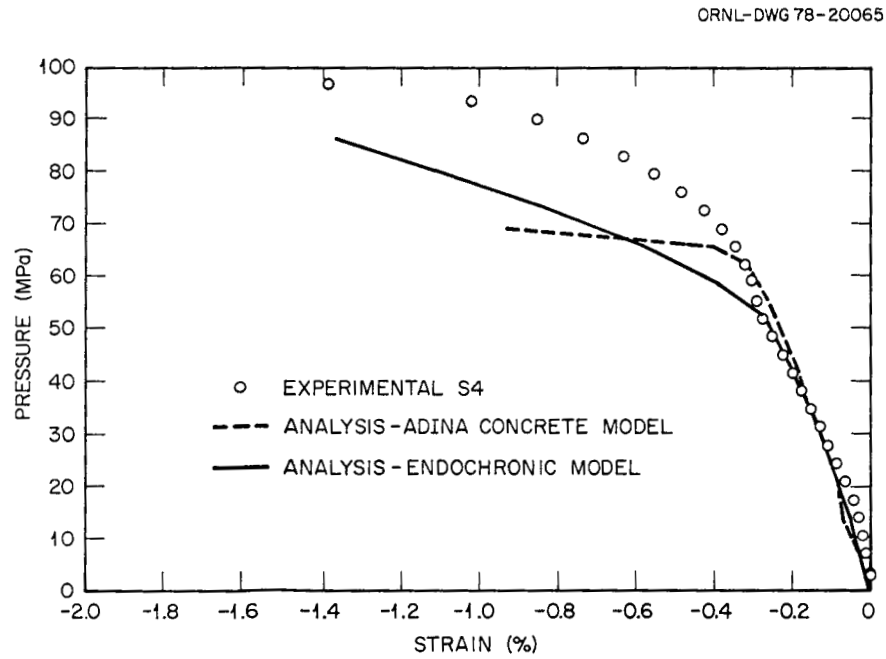


Fig. 3.6. Axial Strain on the Outside Surface of the Outer Liner for the Half-Depth GCFR Steam-Generator Cavity Closure Model.

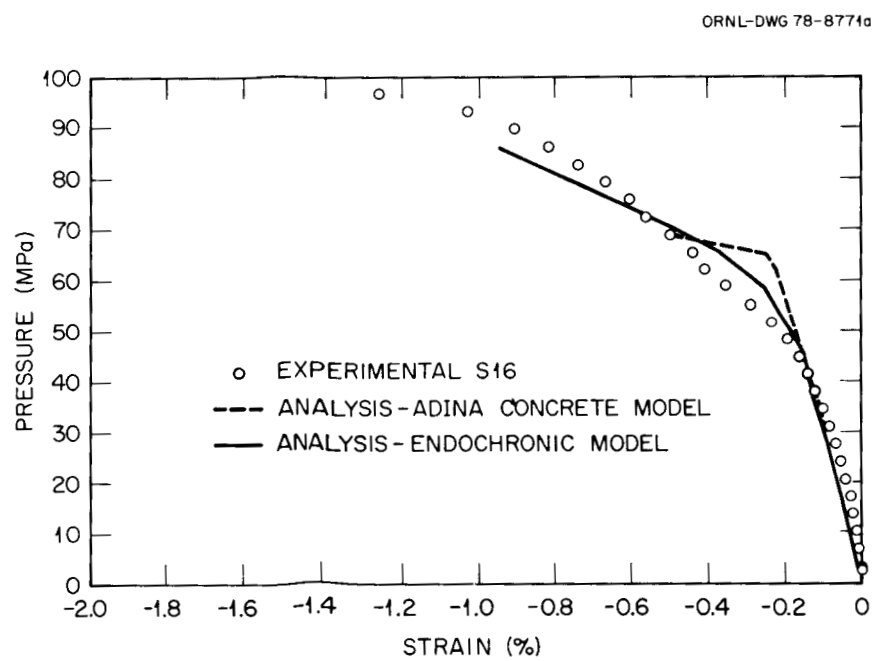


Fig. 3.7. Axial Strain on the Inside Surface of the Outer Liner for the Half-Depth GCFR Steam-Generator Cavity Closure Model.

begins at a pressure of about 65 MPa, and failure occurs shortly thereafter at about 68 MPa. The endochronic model analysis predicts that nonlinear behavior will begin near 50 MPa and failure at 86 MPa. The actual closure model failed at 97 MPa. These results indicate that the endochronic model predicts nonlinear behavior and ultimate load much more accurately than did the ADINA concrete model.

### 3.3.2 Embedded Bar Modeling Technique

When conducting a finite-element analysis of a multicavity PCRV, it is essentially impossible to represent each individual rebar by use of the truss element, which is included for that purpose in most finite-element codes.

The current practice is to model the vessel by use of relatively large isoparametric elements, each of which may contain portions of several rebars. The truss element incorporated in the majority of finite-element codes permits the rebar to lie along only the edges of the continuum elements. Consequently, most rebars must be omitted from the analysis or combined to form single large bars. A procedure developed at ORNL that arbitrarily permits embedment of oriented rebars in isoparametric continuum elements is currently being incorporated into the ORNL version of ADINA. This procedure requires the introduction of positional nodes to define the location of the rebar as well as an additional basis coordinate $\lambda$. The mapping from the dual-basis system, Fig. 3.8, is defined by

$$\vec{P}(\xi,\eta) = \sum N_i(\xi,\eta)\vec{P}_i \tag{7}$$

and

$$\vec{\overline{P}}(\lambda) = \sum \overline{N}_i(\lambda)\vec{\overline{P}}_i \ , \tag{8}$$

where $\vec{P}_i$ is the position vector of the $i$th node of the element, $\vec{P}$ is the position vector of the point in the global space corresponding to

ORNL-DWG 79-12985

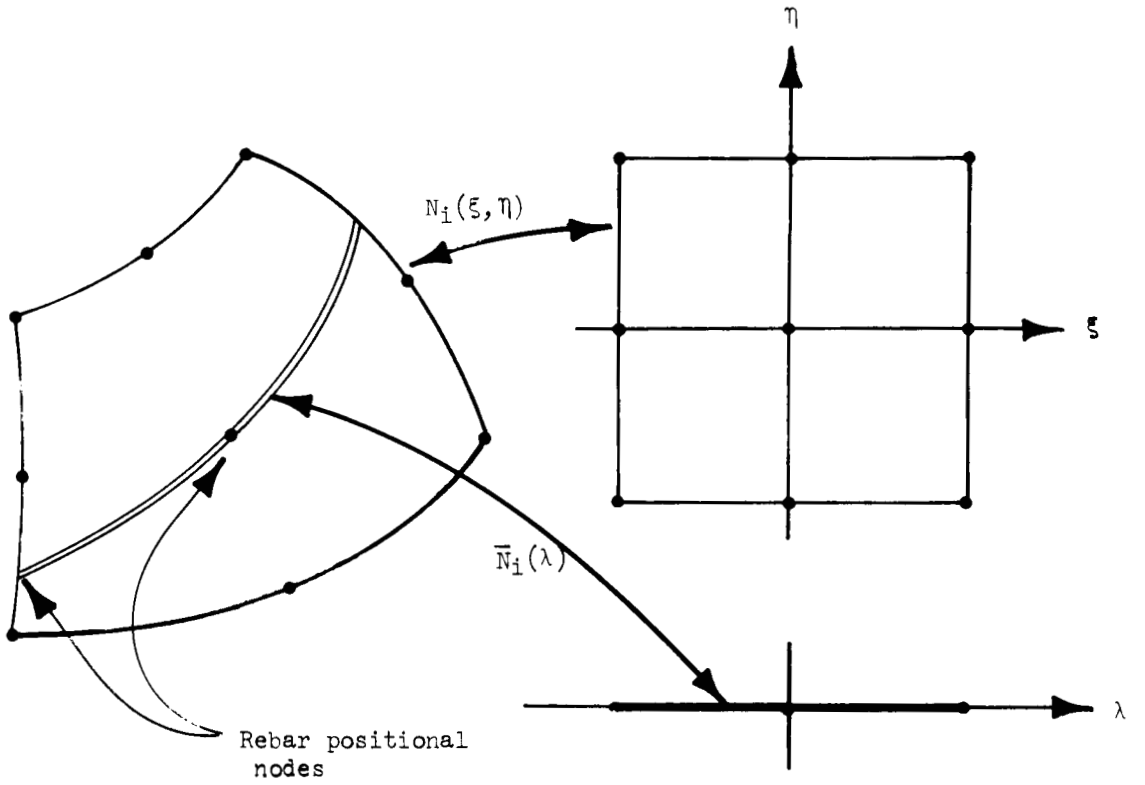


Fig. 3.8. Dual Mapping of Solid Element Containing Embedded Rebar.

the basis coordinates $(\xi,\eta)$, and $N_i(\xi,\eta)$ is the shape function that defines the mapping. The quantities $\vec{\overline{P}}(\lambda)$, $\overline{N}_i(\lambda)$, and $\vec{\overline{P}}_i$ are corresponding quantities defining the mapping of the rebar.

The total stiffness for the element is given by

$$[k_{ij}] = [k_{ij}]_C + [k_{ij}]_B \ , \tag{9}$$

where

$$[k_{ij}]_C = \int_{\text{element}} [B]^T [D][B] dV \ , \tag{10}$$

and

$$[k_{ij}]_B = \int_{\text{bar}} [\overline{B}]^T \, \overline{D} \, [\overline{B}] d\ell \ . \tag{11}$$

The matrix $[B]$ is defined in the usual manner as the matrix that relates element strains $\{\varepsilon\}$ to nodal displacements $\{\delta_i\}$; that is,

$$\{\varepsilon\} = [B]\{\delta_i\} \ , \tag{12}$$

and is obtained by assuming that the displacement field is defined by

$$\vec{\delta}(\xi,\eta) = \sum N_i(\xi,\eta)\vec{\delta}_i \ . \tag{13}$$

The $[D]$ matrix relates stress to strain; that is,

$$\{\sigma\} = [D]\{\varepsilon\} \ . \tag{14}$$

The row matrix $[\overline{B}]$ relates the axial strain in the bar $\varepsilon_d$ to the nodal displacements and is determined by assuming compatibility of deformation between the concrete and the rebar. The quantity $\overline{D}$ defines the relation between axial strain and axial force in the rebar.

The matrix $[k_{ij}]_C$ is calculated in the usual manner, using numerical integration by summing the corresponding weights and function values at the integration points of the $(\xi,\eta)$ coordinate system; that is,

$$[k_{ij}]_C = \int_{\text{element}} [B]^T[D][B]dV \doteq \sum w_i f(\xi_i, \ \eta_i) \ . \tag{15}$$

Similarly, the matrix $[k_{ij}]_B$ is calculated using numerical integration by summing the corresponding weights and function values in the $\lambda$ coordinate system; that is,

$$[k_{ij}]_B = \int_{\text{bar}} [\overline{B}]^T \, \overline{D} \, [\overline{B}] d\ell \doteq \sum h_i g(\lambda_i) \ . \tag{16}$$

The difficulty that arises is that the $[\overline{B}]$ matrix is defined in terms of the basis coordinates $(\xi,\eta)$ and that the value of the variables corresponding to the integration points $\lambda_i$ cannot be determined directly. The problem was overcome by mapping the integration points into the global system by use of Eq. (8) and iteratively solving Eq. (7) for the corresponding values of $\xi$ and $\eta$.

This procedure has been implemented and validated for certain test cases. Although the algorithm is somewhat complex, the execution times are reasonable, and it offers the advantage that the user can develop the discrete finite-element matrix without restrictions on element orientations or on boundary positions relative to rebar positions, which is particularly desirable and almost necessary in modeling the haunch and steam-generator cavity regions of a multicavity PCRV.

## 3.4 CONCRETE PROPERTIES IN A NUCLEAR ENVIRONMENT

Analysis methods developed for PCRVs generally have used either a plasticity or a hyperelasticity model for simulating the concrete nonlinear response under multiaxial loadings. A review of methods of analysis for PCRVs[6] has identified the following problem areas associated with each of these models: (1) the plasticity model does not adequately represent the yield function and hardening law, (2) the model implies isotropic material damage that is not generally true for concrete, (3) the hyperelasticity model cannot account for irreversibility under loading, and (4) a difficulty in achieving functional relations for the coefficients that account for the stress-induced anisotropy accompanying nonlinear stress-strain response. An associated review of concrete properties in a nuclear environment[7] indicated that the data available, for use in the refinement of these models or in the development of new constitutive models to represent better the concrete stress-strain nonlinear behavior under multiaxial loadings, are quite limited. This limitation is especially true for elevated temperature cases such as would be encountered under hot-spot or postulated accident conditions.

To provide data required for development of more representative concrete constitutive models, experimental studies will be conducted. These studies are to be designed so that concrete stress-strain data provided will be representative of the loadings (multiaxial and thermal) likely to be encountered in a PCRV under both normal and postulated accident conditions. Activities during this reporting period were related to three topics: (1) a literature survey of previously conducted concrete multiaxial tests, (2) an overview of facilities in which the multiaxial tests have been conducted, and (3) design of an enclosure for housing the multiaxial test facility to be developed at ORNL. Results of the literature survey and the associated collection and logging of multiaxial test data are presented in Sect. 3.3.

Although there is an obvious need for data on the multiaxial behavior of concrete, only a few organizations are involved in this activity. In an effort to reduce design time and to develop an optimum facility at ORNL, each of these organizations was visited for discussions with the principal investigators. Included in these visits were the University of Colorado at Boulder, New Mexico State University at Las Cruces, the University of California at Davis, Virginia Polytechnic University at Blacksburg, Bundesanstalt für Materialprufung in Berlin, Institut für Massivbau in Munich, Imperial College in London, and Taylor Woodrow Construction Ltd, in Southall, Middlesex. Two major areas of controversy that were apparent during the visits were the type of interface that should be provided between the test fixture and the specimen (boundary conditions) and the technique that should be used for measurement of surface deformations (strains). Interfaces used by these organizations have ranged from perfectly flexible fluid cushions to rigid steel plates with brush platens providing intermediate restraint. Methods that have been used for measurement of displacements have included strain gages, proximity devices, strain-gauge-based deformeters, linear variable differential transformers, and direct-current differential transformers. Each organization provided reasons for its selection of interface and measurement techniques. In an effort to resolve the controversies about the methods of load application and strain measurements, most of the above institutions are participating in a cooperative

testing program. The program, undertaken by seven institutions in the United States, Germany, United Kingdom, and Italy, is designed so that any differences in results obtained from testing mortar and concrete specimens under a variety of biaxial and triaxial loadings are attributed entirely to the test methods employed. To date, two papers have been presented on the test results.[8,9] A third paper presenting a critique on the various test methods is being drafted and will provide valuable information for design of the ORNL concrete multiaxial testing machine.

Activities related to the development of the concrete multiaxial testing facility at ORNL during this reporting period have been related to the design of an enclosure for the multiaxial testing machine that is to be developed. The enclosure is required both to provide standard laboratory conditions so that data obtained will be meaningful and to protect the complex servohydraulic loading system and peripheral equipment from thermal fluctuations and contaminents that would impair their operation. To date, the facility design, including electrical and heating, ventilating, and air conditioning, has been completed, and the plans have been circulated for comment. Construction of the equipment enclosure will be initiated during the next reporting period.

## 3.5 INSTRUMENTATION EVALUATION AND DEVELOPMENT

Numerous concrete embedment instrumentation systems are commercially available for use in PCRVs. Because these systems are so vital to providing continuing assurance of the safe operation of PCRVs, it is imperative that the systems provide highly reliable information over the entire life of a PCRV, which may be as long as 40 years. To provide information on performance of these systems, investigations are being conducted under conditions representative of those that would be encountered in service. Results obtained will be used (1) to evaluate current commercially available systems and (2) to provide data for modification of existing designs and/or development of new systems. The initial instrumentation selected for evaluation was strain measuring devices. Parallel studies are also being conducted to evaluate the applicability of acoustic emission for monitoring the structural integrity of pressurized systems, especially PCRVs.

### 3.5.1 Concrete Embedment Strain-Gauge Evaluation

An evaluation of 13 commercially available concrete embedment strain meters was completed during this reporting period. Included in the evaluation were (1) an overview of meter performance criteria for PCRV applications and techniques for strain measurements in concrete, (2) an assessment of the reliability of manufacturer-supplied calibration factors, and (3) an evaluation of the performance of the strain meters under a variety of conditions, which included unloaded, thermally loaded, simulated-PCRV loading (pressure and thermal), and extreme environmental conditions. Although only a limited number of each of the 13 types of meters selected for evaluation were investigated, the following general conclusions were derived: (1) calibration factors should be determined (verified) for the meters prior to their use by embedding samples of the meters from each fabrication batch in test specimens fabricated from a representative concrete mix; (2) improved corrosion-resistant materials and sealing techniques should be developed for meters that are to be used in PCRV environments; (3) a need exists for the development of meters that are capable of surviving in concretes at temperatures in excess of 66°C for extended periods of time; and (4) research should be conducted on other measurement techniques such as inductance, capacitance, and fluidic. Documents published in this reporting period provide more details of results obtained during evaluation of concrete embedment strain meters.[10,11]

### 3.5.2 Acoustic Emission

The state of the art of acoustic emission (AE) has advanced quite rapidly in the last few years through numerous applications. The applicability of AE for monitoring metallic materials and components as well as the corrosion of metallic materials has been well established.[12,13] In fact, at least one company has developed an AE system that is being used to inspect nuclear power plant coolant systems and metallic containment vessels. However, only limited applications of AE have been made to concrete material systems.

The limited results obtained from AE applications to concrete material systems indicate that (1) onset and failure progression can be detected, (2) stress wave emission characteristics may be correlated with the material modulus of elasticity, (3) loading levels can be evaluated nondestructively, (4) flaws may be located, and (5) the sensitivity of AEs for detection of failure processes and deformation in materials is superior to conventional techniques.[14,15] These results are sufficiently encouraging to conclude that AE may be feasible for in-service monitoring of the structural integrity of PCRVs; however, fundamental laboratory characterization studies on concrete material behavior are required before implementating AE techniques for the monitoring of structures as complex as a PCRV.

#### 3.5.2.1 Acoustic-Emission Laboratory Investigation

The ability of AE to monitor structural test members, specifically PCRVs, is being evaluated through laboratory studies. To develop a reservoir of data on AE, steel structures as well as concrete are being monitored. During this reporting period, the multichannel AE source-location system (Fig. 3.9) has been used to monitor three test series: (1) plain concrete members, (2) prestressed concrete-beam members, and (3) a flawed, thick-walled pressure vessel tested under the Heavy Section Steel Technology (HSST) Program.

#### 3.5.2.2 Monitoring of Plain Concrete Specimens

Three sets of 0.15-m-diam, 0.54-m-long concrete cylinders and 0.15 × 0.15 × 0.91 m flexure prisms, fabricated according to ASTM C 192-76, were cast to obtain AE data on concrete under compressive and tensile loadings. Four compression cylinders and three flexure specimens were contained in each specimen set. The basic mix design used for specimen fabrication is presented in Table 3.1. The variable between mixes was the water content, which was adjusted so that AE data could be obtained from low-, medium-, and high-strength concretes.

After having undergone curing for five months, the compression specimens were prepared for testing by instrumenting with two 0.10-m

ORNL-PHOTO 6387-78

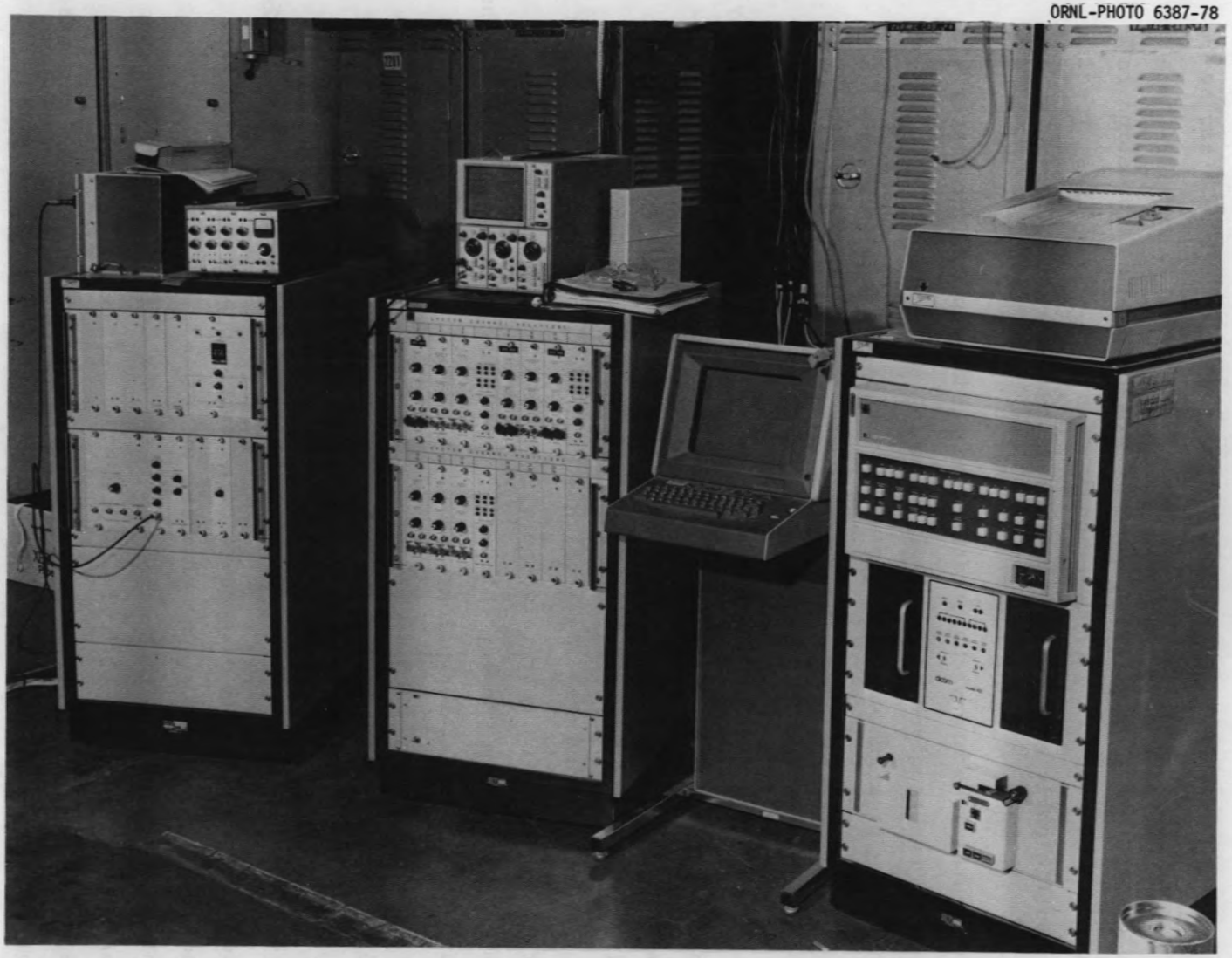

Fig. 3.9. Multichannel Acoustic-Emission Source Location System.

Table 3.1. Concrete Mix Design

| Material | Size range | Mix proportion (wt %) |
|---|---|---|
| Type II cement | | 16.37 |
| Sand | <No. 4 | 33.55 |
| Gravel | No. 4 to 20 mm | 43.12 |
| Water | | 6.96 |

gauge-length strain gauges placed at 180° intervals on the circumference of each cylinder in the direction of loading.* Two 50-kHz resonant-frequency transducers were attached to the specimens to be tested at a longitudinal spacing of 0.30 m, and two additional 50-kHz transducers were attached to the upper and lower loading platens to minimize noise from the platen-cylinder interface (Fig. 3.10). The testing procedure followed for three of the cylinders in each set included: (1) adjusting the amplifier gain of the active AE transducers for an equal level of background noise of about 0.8 V (gains of active transducers labeled *T* and *B* in Fig. 3.10 were 91 dB and 92 dB, respectively), (2) setting the threshold voltage for detecting an AE event of about 0.4 V above the background noise, (3) zeroing and calibrating strain and load transducer responses, (4) programming the multisensor source-location AE system for one-dimensional source location, and (5) loading the cylinder to failure, with load-strain and AE data obtained throughout. Preparation for testing the fourth cylinder of each set was the same as for the three previous cylinders of each set. Specimen testing, however, was different. Specimens were loaded to failure in cycles in which each succeeding load cycle (after an initial cycle to 20% of failure load) was incremented by 10% of the average failure stress of that obtained for the first three cylinders tested of each set. After completion of a load cycle, the load was reduced to 22.2 kN prior to initiation of a new cycle. Results obtained for the three low- (19.5-GPa), medium- (36.8-GPa),

*The strain gauges on each cylinder were wired in series to minimize the possible effects of bending.

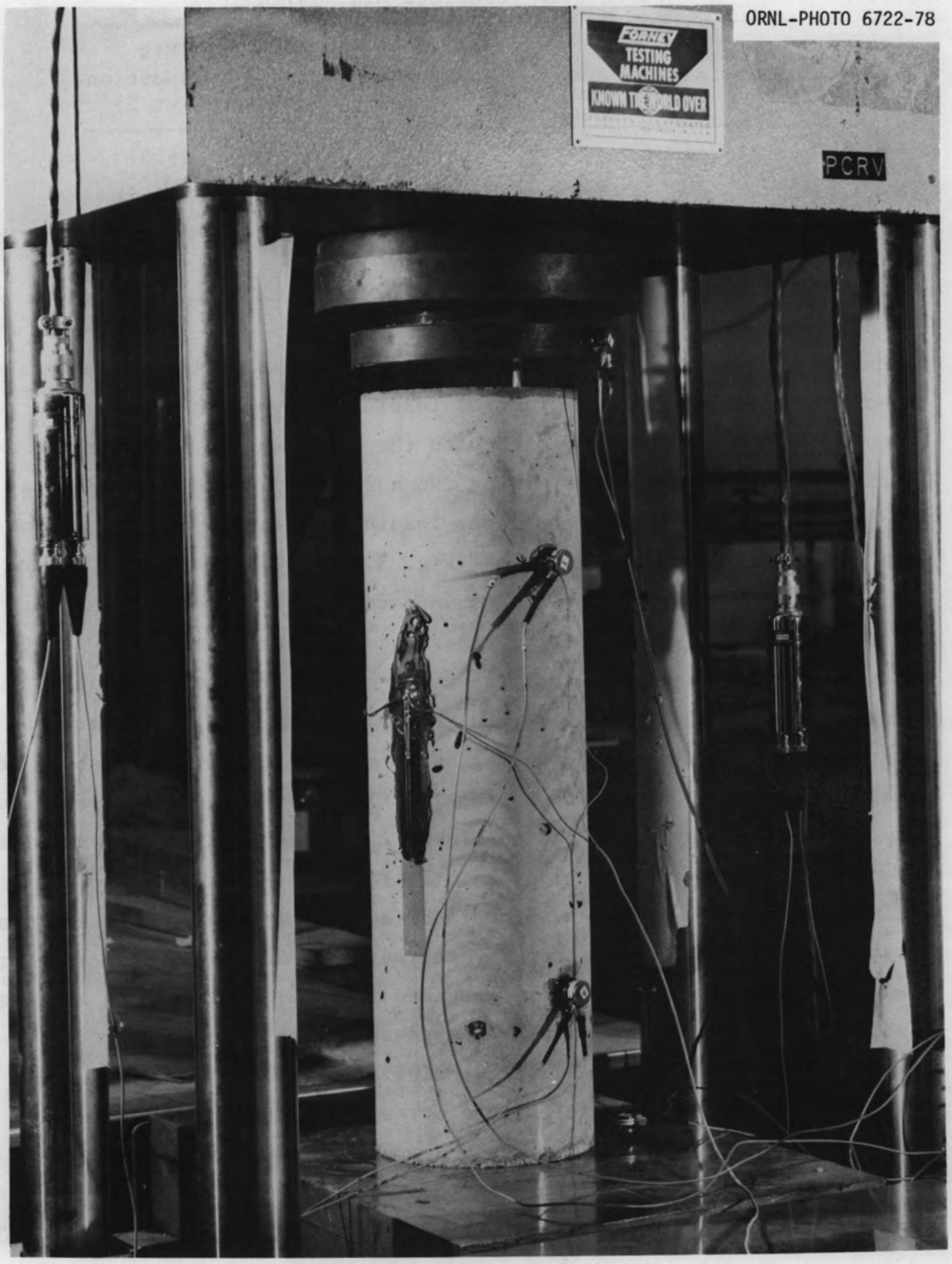


Fig. 3.10. Acoustic-Emission Compression Test Setup.

and high-strength (50.8-GPa) cylinders loaded to failure in one cycle are presented in Figs. 3.11, 3.12, and 3.13, respectively. The figures present AE-event histograms, cumulative AE-event counts,* and normalized strain as a function of the percentage-of-failure stress. The effects of load cycling on AE activity for the low-, medium-, and high-strength concrete are summarized in Tables 3.2, 3.3, and 3.4, respectively. Results indicate that, for the specimens loaded to failure in one cycle, there was good correlation between low- and medium-strength concrete's AEs and their stress-strain curves; that is, from 0 to 30% ultimate strength, the stress-strain curve was essentially linear and AE activity was small; from 30 to 70% ultimate strength, the stress-strain curve began deviating from linearity because of an increase in bond cracks between the aggregate and matrix, and the AE activity increased; and above about 70% ultimate failure strength, a rapid deviation of the

*Dashed line for cumulative event count is a smoothed curve that has eliminated initial noise resulting from platen-cylinder interaction.

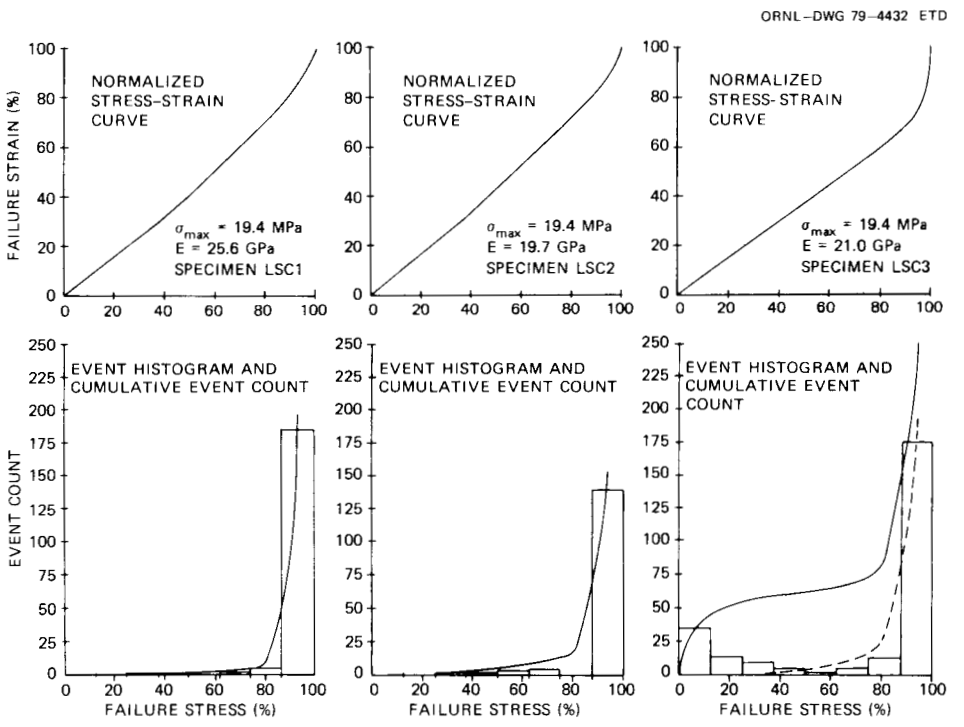


Fig. 3.11. Acoustic-Emission Compression Test Results: Low-Strength Concrete.

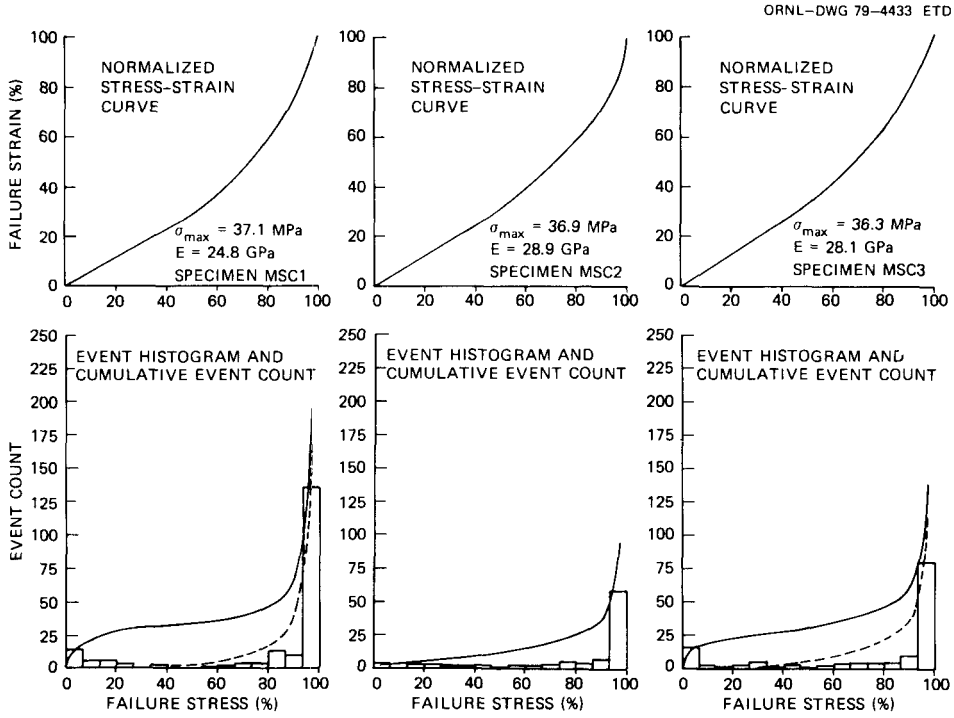


Fig. 3.12. Acoustic-Emission Compression Test Results: Medium-Strength Concrete.

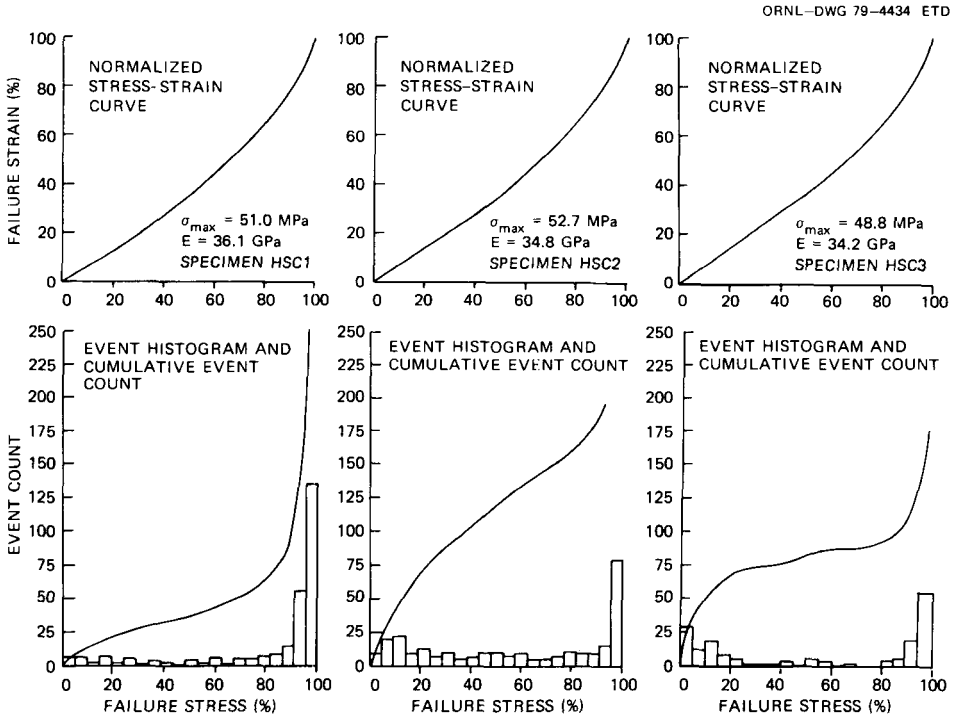


Fig. 3.13. Acoustic-Emission Compression Tests Results: High-Strength Concrete.

Table 3.2. Number of Events by Load Interval for Increasing Load Cycling of Low-Strength Concrete

| Load range (kN) | Number of valid events per load range interval for cycle — | | | | | | | | | |
|---|---|---|---|---|---|---|---|---|---|---|
| | 1 | 2 | 3 | 4 | 5 | 6 | 7 | 8 | 9 | 10 |
| 0.0–71.2 | 10 | 0 | 0 | 0 | 0 | 0 | 0 | 0 | 0 | 0 |
| 22.2–106.8 | | 2 | 2 | 0 | 0 | 0 | 0 | 1 | 0 | 0 |
| 22.2–142.3 | | | 0 | 2 | 0 | 0 | 0 | 0 | 0 | 0 |
| 22.2–177.9 | | | | 4 | 1 | 0 | 0 | 0 | 0 | 0 |
| 22.2–213.5 | | | | | 3 | 0 | 0 | 0 | 0 | 0 |
| 22.2–249.1 | | | | | | 4 | 0 | 0 | 1 | 0 |
| 22.2–284.7 | | | | | | | 6 | 0 | 0 | 0 |
| 22.2–320.3 | | | | | | | | 5 | 0 | 0 |
| 22.2–355.9 | | | | | | | | | 8 | 1 |
| 22.2–438.2 | | | | | | | | | | 81 |

Table 3.3. Number of Events by Load Interval for Increasing Load Cycling of Medium-Strength Concrete

| Load range (kN) | Number of valid events per load range interval for cycle — | | | | | | | |
|---|---|---|---|---|---|---|---|---|
| | 1 | 2 | 3 | 4 | 5 | 6 | 7 | 8 |
| 0.0–133.4 | 18 | 1 | 0 | 0 | 0 | 0 | 0 | 0 |
| 22.2–200.2 | | 4 | 0 | 0 | 0 | 0 | 0 | 0 |
| 22.2–266.9 | | | 7 | 0 | 0 | 0 | 0 | 0 |
| 22.2–333.6 | | | | 2 | 0 | 0 | 0 | 0 |
| 22.2–402.6 | | | | | 6 | 0 | 0 | 0 |
| 22.2–469.7 | | | | | | 5 | 3 | 1 |
| 22.2–536.9 | | | | | | | 10 | 2 |
| 22.2–604.1 | | | | | | | | 26[a] |

[a]Floppy-disc error after this number of events.

stress-strain curve from linearity occurred because of a rapid increase in matrix cracking, and an associated sharp increase in AE activity also occurred. The high-strength concrete specimens exhibited relatively uniform activity from initiation of loading until about 85 to 90% ultimate strength, at which time the activity increased sharply. Results obtained for the specimens cyclically loaded to failure, wherein each

Table 3.4. Number of Events by Load Interval for Increasing Load Cycling of High-Strength Concrete

| Load range (kN) | Number of valid events per load range interval for cycle — | | | | | | | | |
|---|---|---|---|---|---|---|---|---|---|
| | 1 | 2 | 3 | 4 | 5 | 6 | 7 | 8 | 9 |
| 0.0–186.8 | 37 | 0 | 0 | 0 | 0 | 0 | 0 | 0 | 0 |
| 22.2–302.5 | | 7 | 5 | 0 | 0 | 0 | 0 | 0 | 0 |
| 22.2–373.7 | | | 6 | 0 | 0 | 0 | 0 | 0 | 0 |
| 22.2–467.1 | | | | 3 | 3 | 2 | 0 | 0 | 1 |
| 22.2–560.5 | | | | | 14 | 5 | 2 | 0 | 3 |
| 22.2–653.9 | | | | | | 11 | 3 | 1 | 3 |
| 22.2–742.9 | | | | | | | 22 | 17 | 18 |
| 22.2–836.3 | | | | | | | | 113 | 82 |
| 22.2–851.8 | | | | | | | | | 85 |

succeeding load cycle was at a higher load level, indicate that the Kaiser effect* applies to concrete material systems.

The 0.15 × 0.15 × 0.91 m flexure specimens, after undergoing curing for five months, were prepared for testing by applying a 0.10-m gauge-length strain gauge to one face of each of the three specimens cast for the low-, medium-, and high-strength concretes. Immediately prior to testing, two AE transducers (50-kHz resonant frequency) were attached to the specimens at a spacing of 0.50 m on the same surface as was the strain gauge. Each specimen was then placed in the flexure test setup (ASTM C 78-75) shown in Fig. 3.14; the surface containing the AE transducers and strain gauge was placed so that the transducers and gauge were located on the tensile surface of the specimen. Major and minor spans for the flexure tests were 0.25 and 0.75 m, respectively. After placing the specimen in the fixture, amplifier gains for the AE transducers were adjusted as described previously (transducer gains, 91 and 92 dB), load and strain outputs were zeroed and calibrated, and the AE system was programmed for one-dimensional source location. The specimens were then loaded in flexure to failure with stress-strain and AE data

*The theory that, once a load has been applied to a member and the associated AE activity resulting from its application ceases, no more emission will occur until the load level is exceeded, even if the load is completely removed.[16]

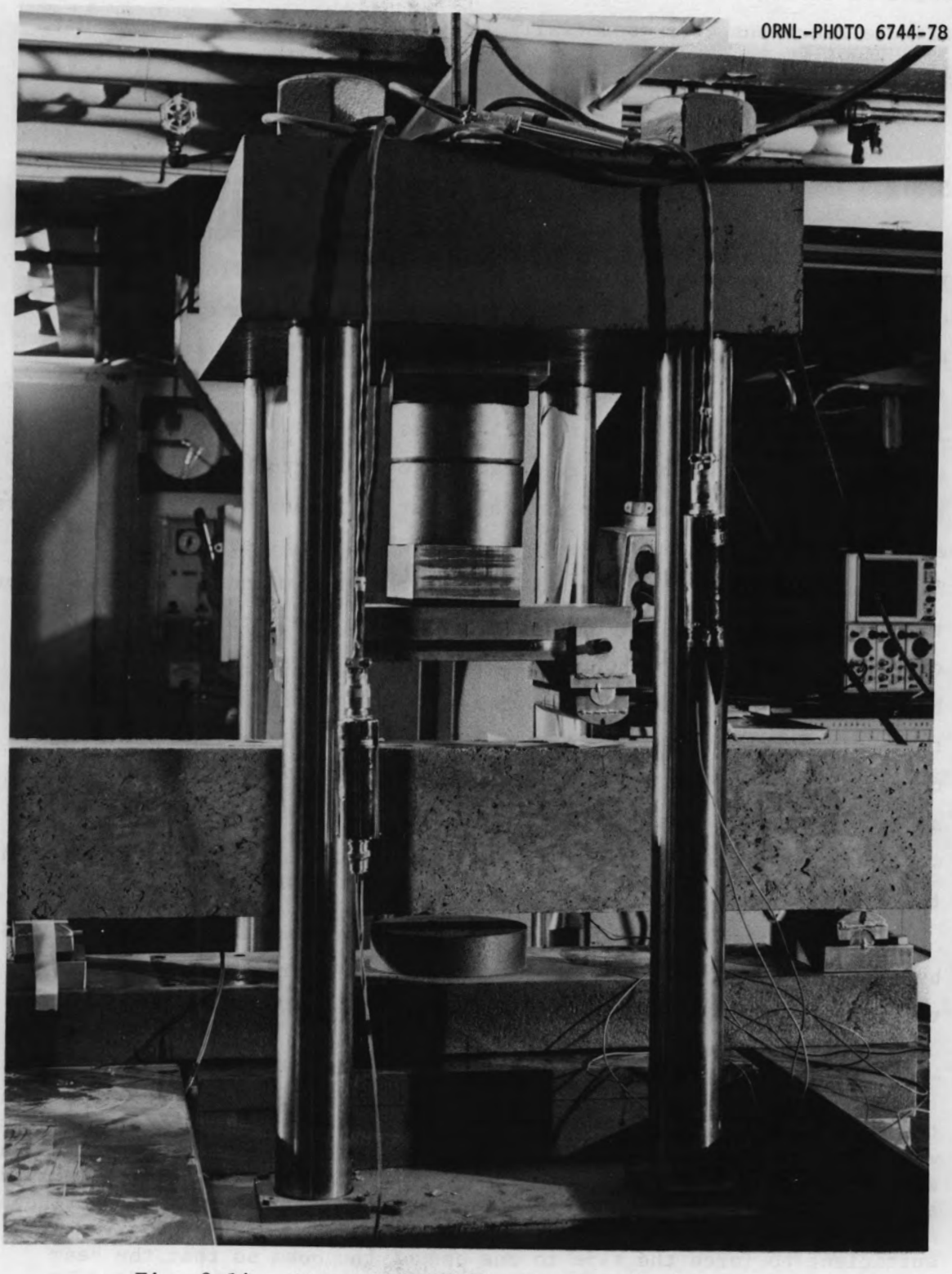


Fig. 3.14. Acoustic-Emission Flexure Test Setup.

obtained throughout loading. Stress-strain curves obtained for all the flexure specimens were essentially linear up to failure. As a result, AE activity was absent until immediately prior to failure when a few (<10) events occurred.

3.5.2.3 Monitoring of Prestressed Concrete Beam Members

The ability of AE to locate regions of distress (cracks) in relatively simple concrete structures was evaluated by monitoring several of the posttensioned grouted and nongrouted tendon-beam structural models tested under the structural model task (Sect. 3.6). Specimen fabrication and testing procedures, except for the inclusion of AE monitoring, are described in earlier progress reports. Prior to testing, six 50-kHz AE transducers were attached to the bottom surface of the beam to be tested. Two were attached near the major span reaction points and used as slave transducers to lock out localized reaction noises. The remaining four transducers were spaced at 0.6-m increments to monitor the central 1.80 m of the beam and thus to provide data on flexural crack locations. Transducer amplifier gains were adjusted for equal background-noise output as described previously, and the detection threshold voltage was adjusted to about 0.4 V above ambient background noise. The AE system was programmed for one-dimensional source location, and the beam was loaded in flexure to failure; AE source-location data was obtained throughout the test. The AE grouted-nongrouted tendon-beam test setup is presented in Fig. 3.15.

Seventeen of the grouted and nongrouted tendon beams were monitored by AE while they were being tested to failure.* The results are too voluminous to include in this report; results from only one grouted

---

*One of these beams containing a grouted tendon was fabricated such that a 0.15-m length of tendon in the constant-moment region of the beam was deliberately unbonded by coating it with grease and wrapping it with electrician's tape prior to grouting. It was hoped that AE might provide a technique for locating voids or regions of unbonding in grouted tendon elements; however, during grouting, the grout pressure was apparently sufficient to force the tape to one end of the beam so that the beam acted as a continuously grouted beam. Tape location was verified by sawing the beam after testing.

Fig. 3.15. Acoustic-Emission Grouted-Nongrouted Tendon Beam Test Setup.

tendon and one nongrouted tendon beam, which are typical of the other results obtained, are therefore presented. Typical AE data in the form of event activity as a function of location along the length of the beam for a nongrouted and a grouted tendon beam are presented in Figs. 3.16 and 3.17, respectively. Superimposed above the AE activity plots are photographs of the beams after testing, which show agreement between crack locations and active AE areas. Results indicate that, for nongrouted tendon beams in which only one or two major cracks occurred during testing to failure, AE-determined crack locations and actual crack locations correlated quite well. In grouted tendon beams tested to failure, four or more major cracks generally formed, and the correlations between AE-identified crack locations and actual crack locations was not as definite. (Locational accuracy of the first crack in the

ORNL DWG 78-8434

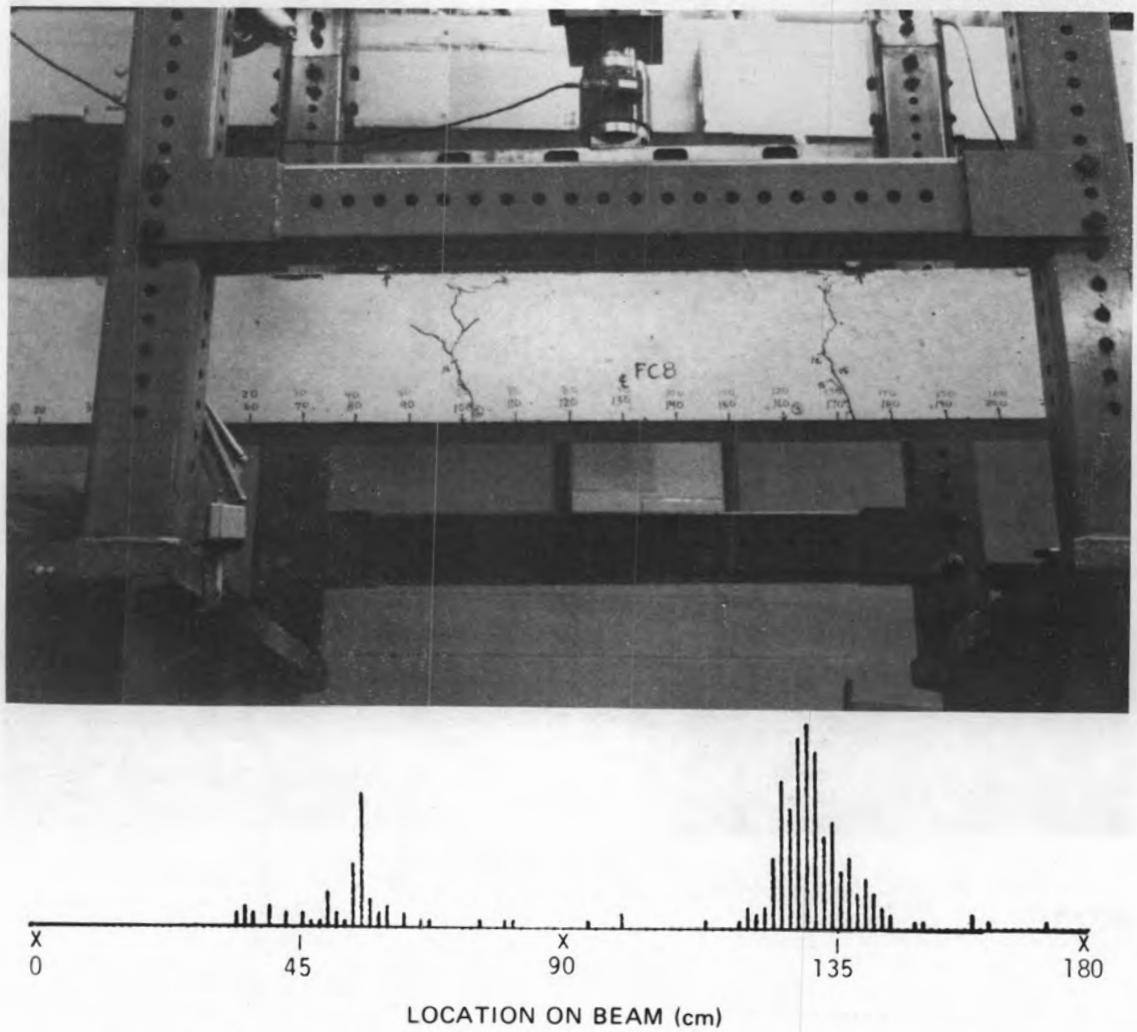


Fig. 3.16. Acoustic-Emission Flexure Test Results: Nongrouted Tendon Beam.

beam was good, but the accuracy decreased as more cracks formed.) This "smearing" of AE-active regions was related to development of several cracks so that it was necessary for a source-initiated stress wave to travel around cracks from transducer to transducer for source location. As the cracking matured, the initial main cracks branched and propagated horizontally (Fig. 3.17).

ORNL DWG 78-8435

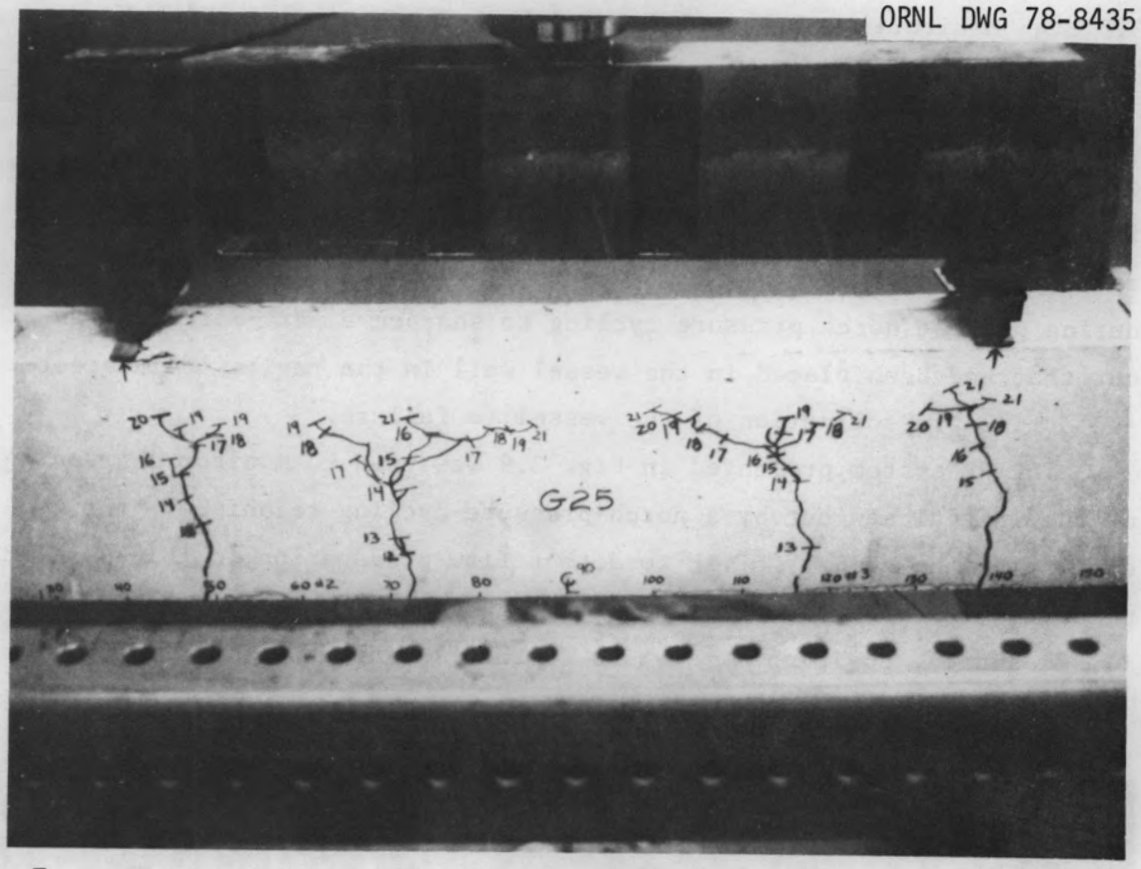


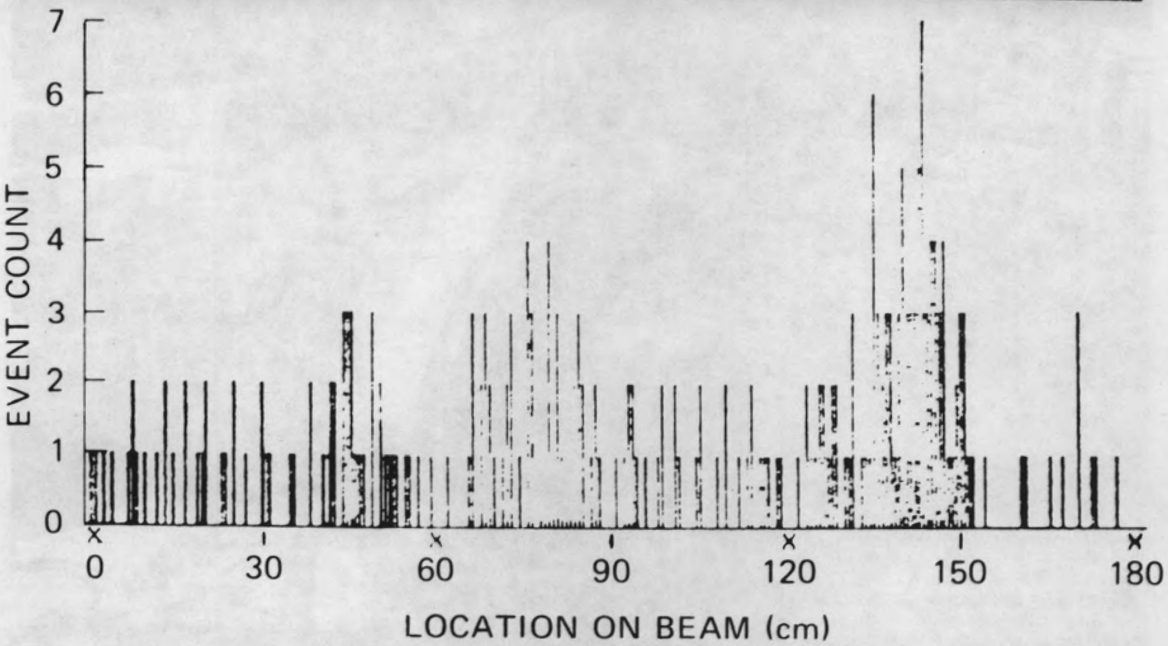


Fig. 3.17. Acoustic-Emission Flexure Test Results: Grouted Tendon Beam.

3.5.2.4 Monitoring of Flawed Thick-Walled Steel Pressure Vessel

Intermediate test vessel V-8 of the HSST program was fabricated from ASTM A533, grade B, class 1 steel plate. The test vessel had an outside diameter of 0.99 m and an inside diameter of 0.69 m. Contained in the vessel was a flaw in a half-bead weld repair region in which residual stresses were high. Acoustic-emission data was obtained both during pretest notch pressure cycling to sharpen a part-circular saw cut that had been placed in the vessel wall in the region of interest and during pressurization of the vessel to failure.

The AE system presented in Fig. 3.9 was used to monitor sharpening of the initial saw cut by a notch-pressure-cycling technique[17] for evaluating the ability of AE to detect flaw propagation in thick-walled members. The test setup is shown in Fig. 3.18. Three active sensors (1, 7, and 8), positioned relative to the flaw as shown in Fig. 3.19,

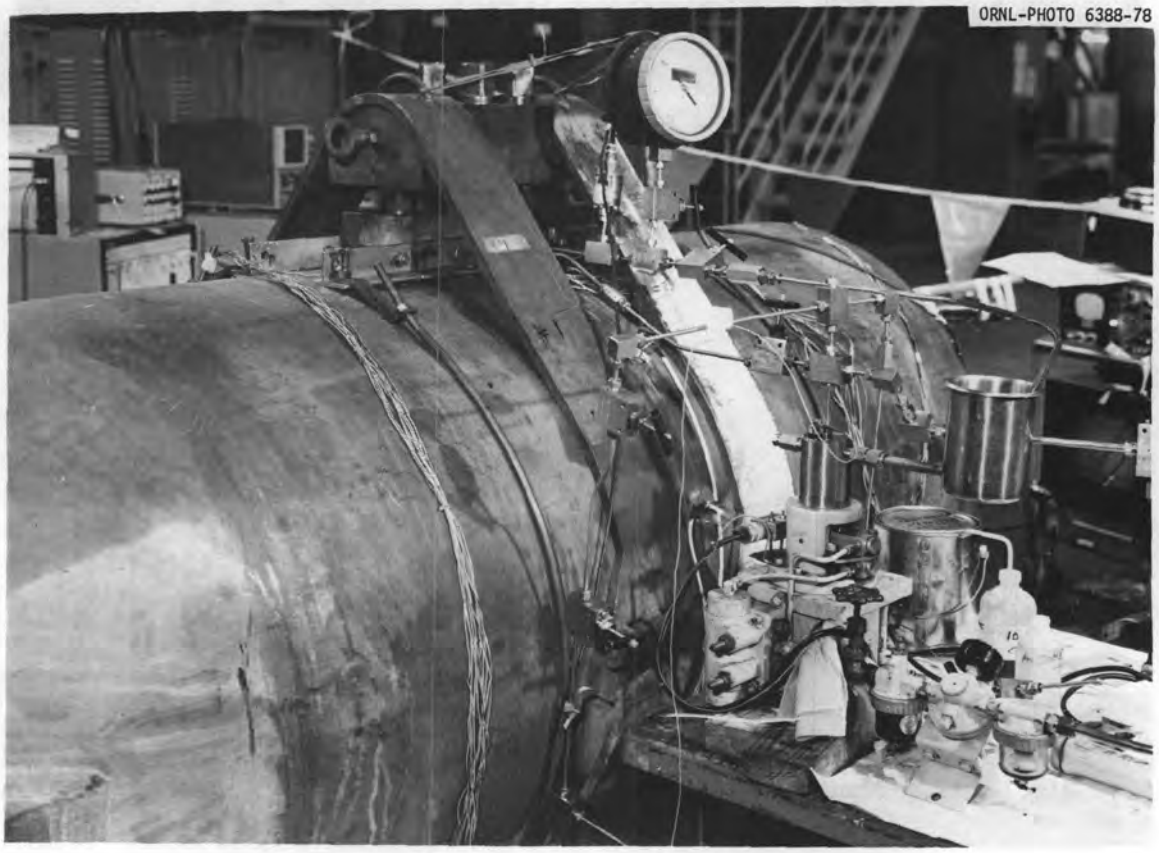


Fig. 3.18. Intermediate Test Vessel V-8 Test Setup.

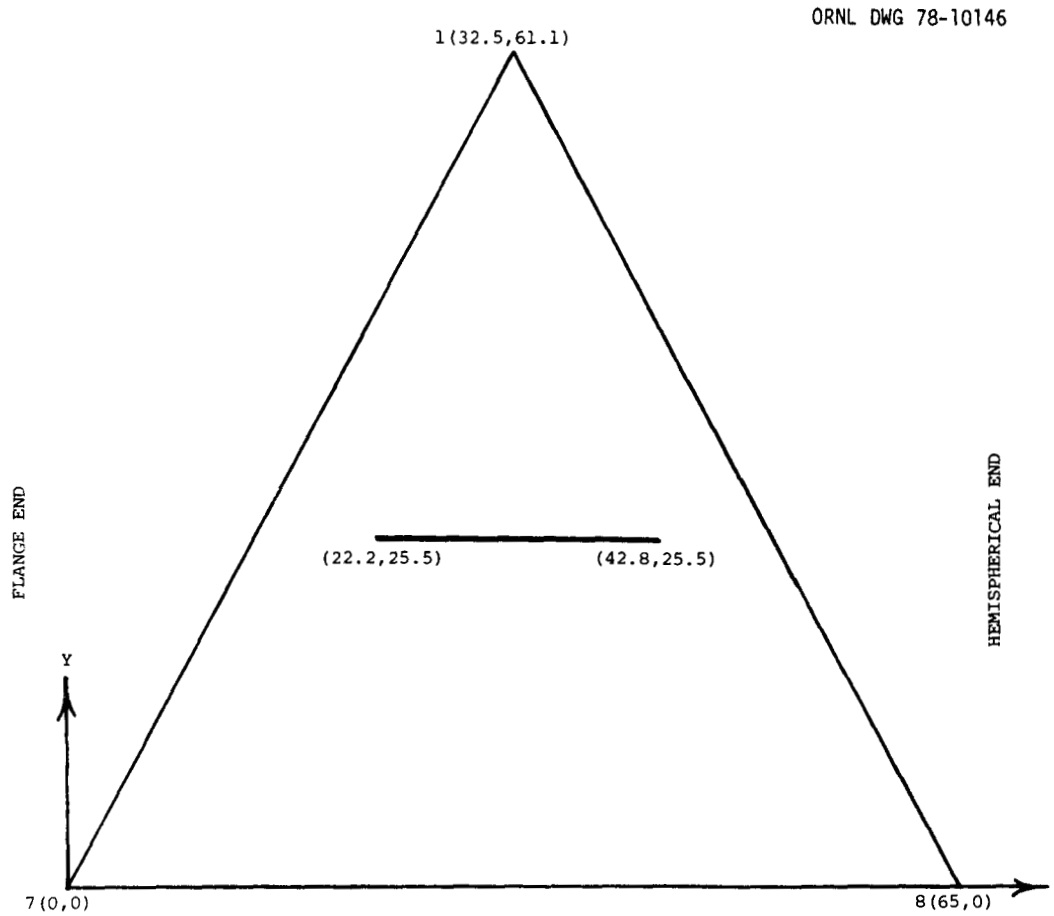


Fig. 3.19. Sensor-Positioning ITV-8 Flaw Growth Test.

were used during the test. Coupling between the sensors and epoxy shoes that had been attached to the vessel by a 5-min epoxy was provided by a thin layer of PYROGEL. Acoustic-emission-system specifications during the test were as follows:

Transducers: 500-kHz resonant frequency, single-ended
Filters: 200 to 800 kHz
Preamplifier gain: channel 1 — 51 dB (91 dB total), channel 7 — 49 dB (89 dB total), and channel 8 — 48 dB (88 dB total)
Arrival time resolution: 1 μs
Threshold: 1 V
$\Delta T$ range selector: 500 μs

Cycle count was monitored throughout the test by use of a parametric input to the AE system. Acoustic-emission monitoring was continuous during the 58,637 flaw-pressurization cycles required to grow the flaw to the desired 12.7 mm, except for two 15-min intervals that occurred at about 44,000 and 52,000 cycles, during which equipment problems arose. A summary of AE results obtained during the test is given in Fig. 3.20.

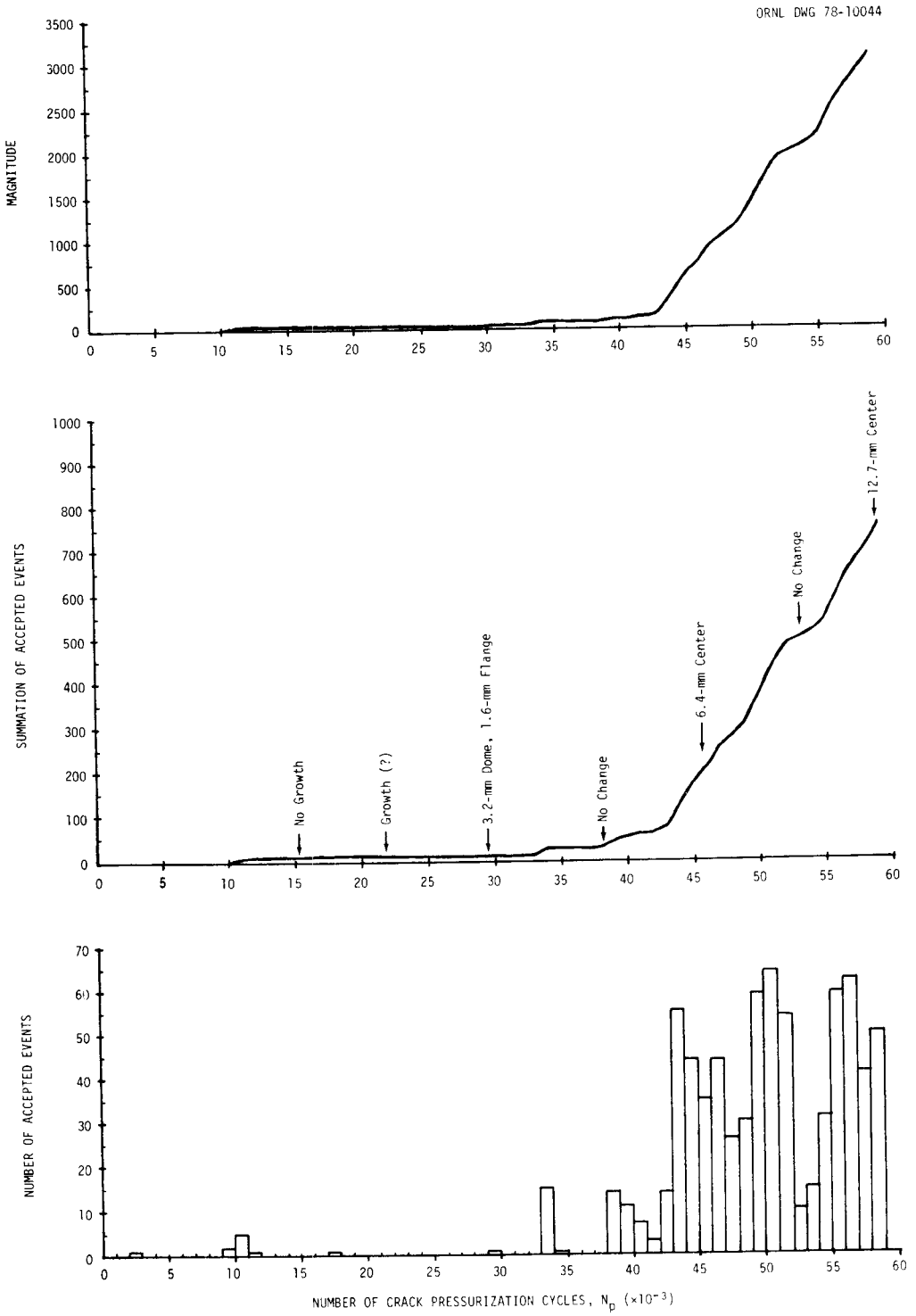


Fig. 3.20. Acoustic-Emission Test Results: ITV-8.

Presented in the figure as a function of crack pressurization cycles are (1) a histogram of even occurrence (per 1000 cycles), (2) a cumulative total of valid events, and (3) a cumulative total of event voltage magnitudes. Superimposed on the summation of accepted events graph are ultrasonic data results (estimated flaw growth) that were also obtained during the test. Results indicate that (1) there is an incubation period of about 33,000 cycles prior to initiation of flaw growth; (2) flaw growth was erratic, as evidenced by periods of lower-event activity occurring after high-activity periods; and (3) the rate of flaw growth increased as the number of cycles (flaw length) increased.

Three AE sensors were also used to monitor the region of the flaw during pressure testing of the vessel to failure. Positioning of the sensors relative to the flaw is shown in Fig. 3.21. Monitoring of the entire cylindrical section of the vessel could not be accomplished during the test because the cooling elements required to obtain the vessel test temperature of −23°C covered most of the surface. Transducers were attached directly to the vessel by use of a structural acrylic adhesive. Sensor locations (S1-S3) relative to the flaw and cooling elements are shown in Fig. 3.22. Acoustic-emission specifications during the test were as follows:

Transducers: 500-kHz resonant frequency, differential
Filters: 200 to 800 kHz
Preamplifier gain: channel 1 — 49 dB (89 dB total), channel 7 — 47 dB (87 dB total), and channel 8 — 51 dB (91 dB total)
Arrival time resolution: 1 μs
Sensor activity constant: 1 ms
Threshold: 0.90 V

ORNL-DWG 78-21801

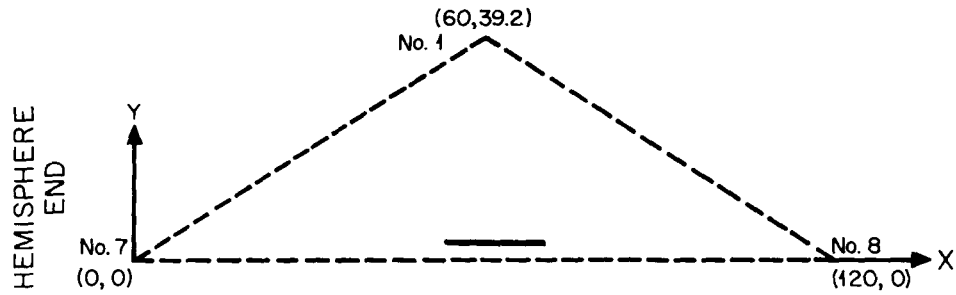


Fig. 3.21. ITV-8 Pressure Test to Failure Sensor-Positioning Relative to 20-cm-Long Flaw Parallel to X-Axis and Centered at X = 60 cm and Y = 5 cm.

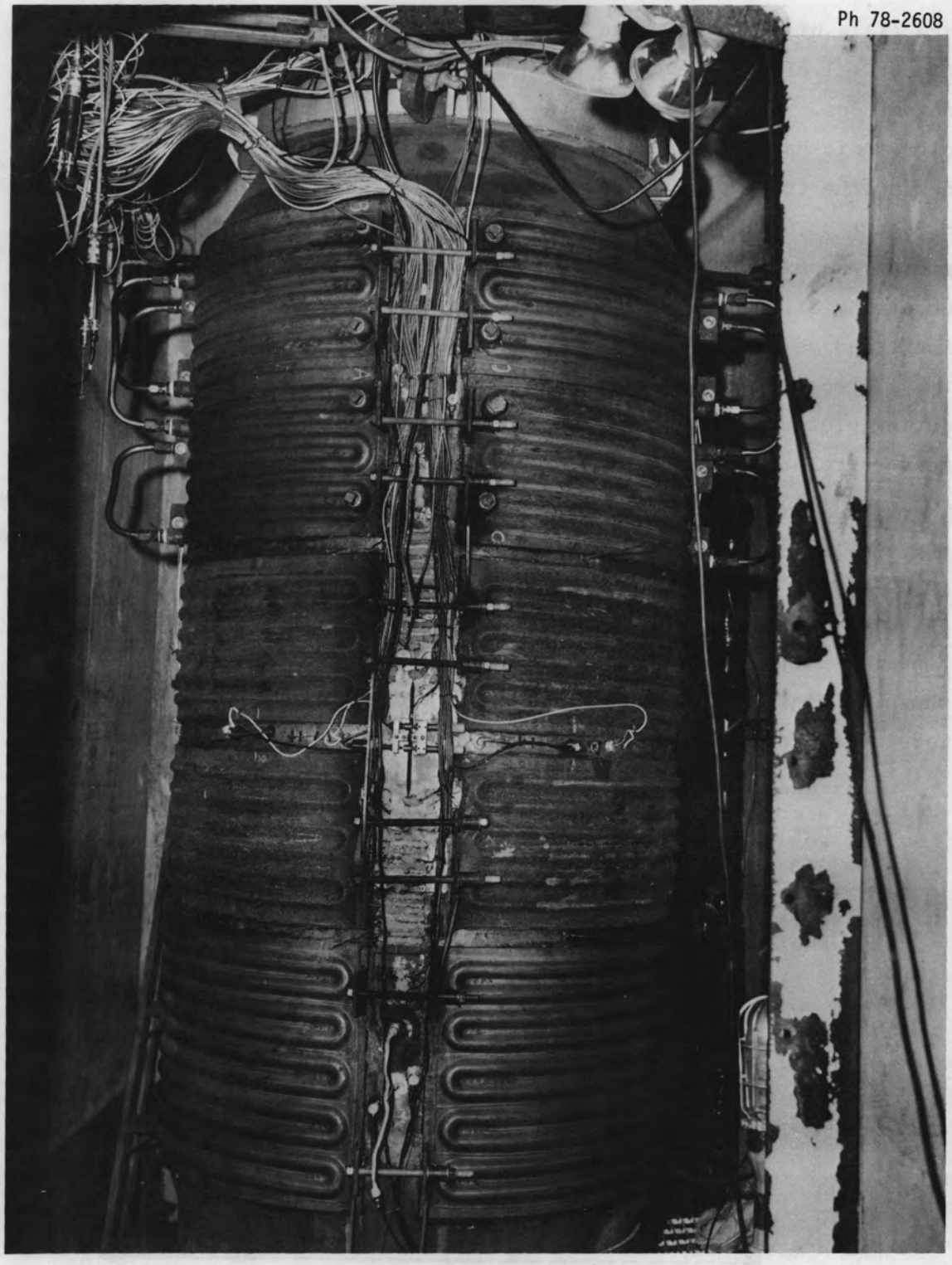


Fig. 3.22. Sensor Locations on Test Vessel.

Pressurization of the vessel was done hydraulically according to the pressure-versus-time curve in Fig. 3.23. Acoustic-emission data were obtained throughout the test except for the pressure interval from 54.1 to 62.1 MPa, where a problem with the computer occurred that required the system to be reinitiated. Acoustic-emission results obtained during the test are summarized in Figs. 3.24 and 3.25. Figure 3.24 presents an event histogram showing the number of accepted events for each loading interval and a summation of events versus pressure level. The number above each loading interval is the frequency of event occurrence (event per second). Correspondingly, Fig. 3.25 presents an event histogram showing the peak voltage (magnitude) totals for the events occurring in each of the loading intervals and a summation of peak volts versus pressure level. The number above each loading interval is the average voltage magnitude of the events in that particular interval. Results indicate that prior to flaw pop-in, an increase in both event activity and the magnitude of events occurs. After pop-in, a period of low-level activity followed by a period of increasing activity occurs. Unfortunately, results are not available for the period immediately prior to the second pop-in, which penetrated the vessel wall so that the

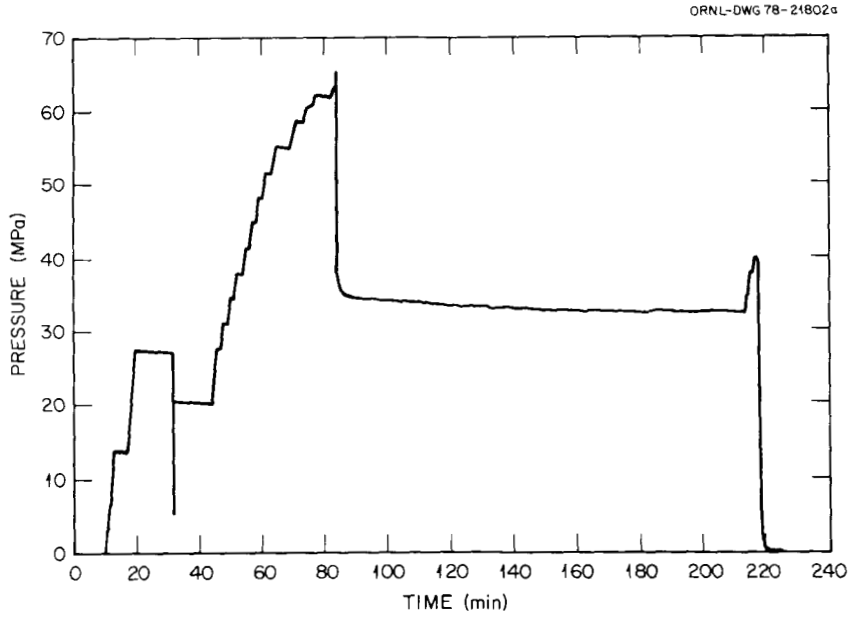


Fig. 3.23. Pressure Versus Time History: ITV-8.

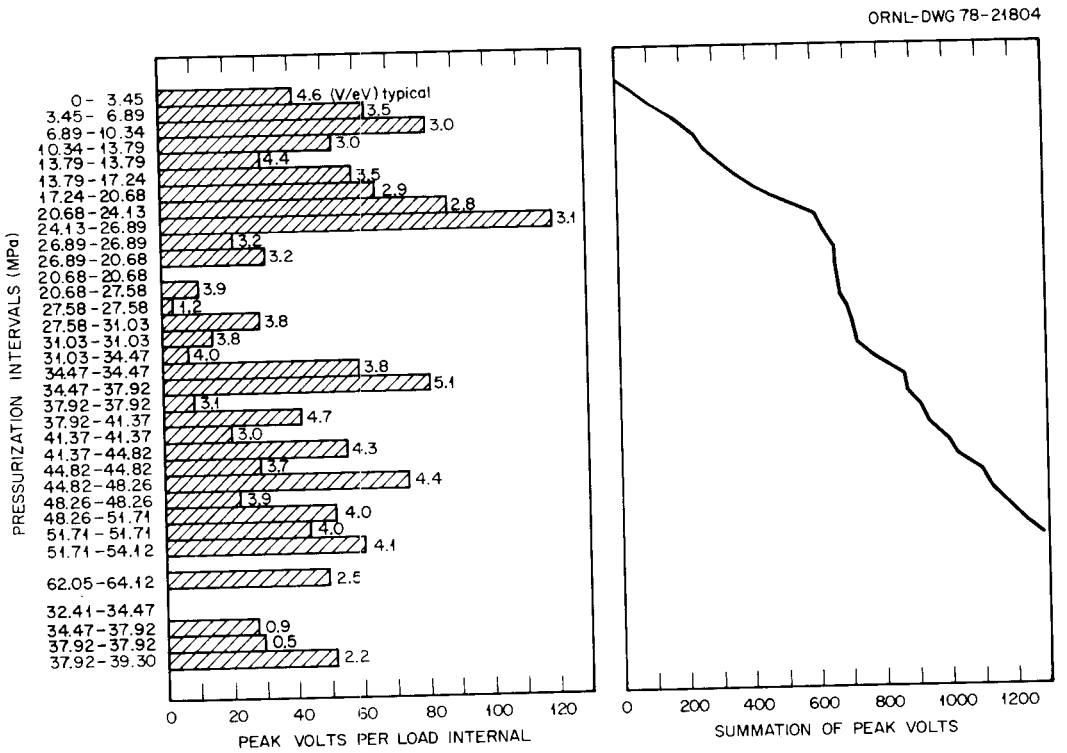


Fig. 3.24. Event Histogram and Summation of Events Versus Load Interval.

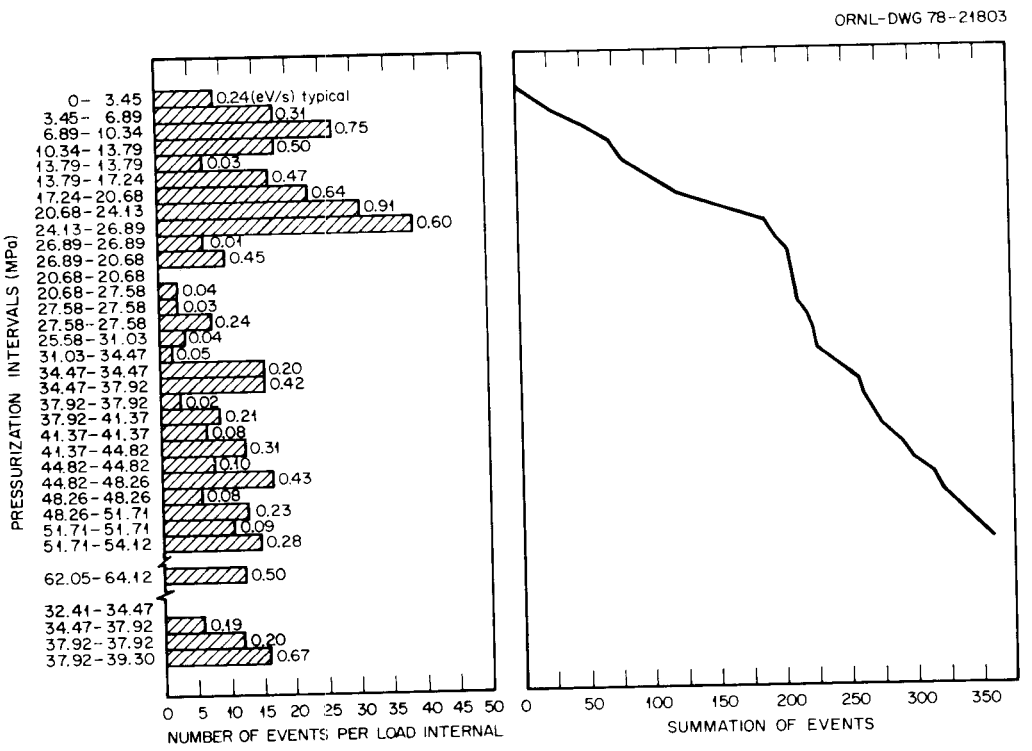


Fig. 3.25. Peak Voltage Histogram and Summation of Peak Volts Versus Load Interval.

rapid increase in AE activity just prior to leak could be shown; however, the system indicated clearly the presence of the leak (system saturation caused by continuous emission).

The following conclusions are derived from the results of AE monitoring of the fatigue crack sharpening of the flaw for test vessel V-8 and pressure testing of the vessel to failure:

1. acoustic emission was capable of monitoring flaw growth by the fatigue crack sharpening process in thick-walled (152.4-min) pressure vessels,
2. acoustic-emission data may be used to provide an indication of the rate of crack extension (event frequency),
3. acoustic-emission activity (event frequency) during the flaw sharpening test phase correlates with fatigue crack growth data observed in weldments (incubation period followed by erratic crack growth),[18]
4. correlation between ultrasonic data obtained during the test and AE results was generally good, and
5. acoustic emission indicates both the presence of leaks and the onset of crack growth in hydraulically pressurized thick-walled steel vessels.

## 3.6 STRUCTURAL MODEL TESTS

### 3.6.1 Grouted-Nongrouted Tendon Study

Requirements for increased generating capacity of nuclear reactors in conjunction with increased operating pressures have pushed the limits of steel primary containment vessel design to the point that postweld heat treatment is not permitted. This fact has led to the development of designs that use concrete for fabrication of the primary containment structure. Inasmuch as the structures are required to remain relatively crack-free and behave elastically at work stress levels, large quantities of reinforcement must be incorporated, which has necessitated the use of large-capacity posttensioning tendons that may be either grouted or nongrouted.

Prestressed concrete pressure vessels (PCPV) for HTGRs are massive concrete structures. They are constructed of relatively high-strength concrete that is reinforced by both conventional steel and a steel posttensioning system, which consists of vertical tendons and circumferential wire-strand windings. Anchorage of the PCRV to the support structure and foundation mat is either by reinforcing bars or vertical tendons or by a combination of the two. Although only one PCRV has been built in the United States, European experience has demonstrated that these structures are safe and economical.

Currently in this country, nongrouted tendons are primarily used as the prestressing system for PCRVs because prestressing losses and corrosion are discernable through periodic inspections; however, grouted tendon prestressing systems offer advantages that make them potentially cost effective for application to PCRVs. To appraise the applicability of grouted tendon systems for PCRVs, a model study was conducted under this task. Included in the study were a literature review and an experimental investigation. Literature was reviewed to: (1) provide insight on the behavior of grouted tendon systems, (2) establish performance histories for structures using grouted tendons, (3) identify arguments for and against using grouted tendons, and (4) aid in the development of the experimental investigation. The experimental investigation was conducted in four phases: (1) grouted-nongrouted tendon behavior, (2) potential "new" materials for PCRV applications, (3) effectiveness of organic petrolatum base and portland cement corrosion inhibitors, and (4) AE as a technique for PCRV structural integrity monitoring. A summary of experimental results only is presented; details may be obtained elsewhere.[19,20]

The relative behavior of members containing either grouted or nongrouted tendons was investigated by testing in flexure beam structural members 0.15 m wide by 0.31 m deep by 3.05 m long that contained one 12.7-mm-diam seven-wire prestressing strand. Variables were prestressing level (0.5 to 0.7 ultimate) and loading rate (0.074 to 74 kN/s). Results show that grouted tendon beams have increased cracking and ultimate loads for the same level of prestressing, exhibit improved crack control (increased number but of smaller width), and can sustain significant loadings if an anchorage is removed (simulated failure). For the load-

ing rates investigated, no significant effect on ultimate load was noted for either tendon system, but centerline deflection at maximum load increased as the loading rate increased.

Fibrous concrete and polymer silica cement systems were investigated as candidate PCPV materials. Flexure tests of grouted and nongrouted tendon beam elements fabricated from fibrous concrete (1.5 vol % steel fibers) showed that the addition of fibers did not significantly affect beam flexure strength but that the presence of fibers did greatly increase their ductility (energy absorption capacity). Polymer silica cements were evaluated as both candidate grout and elevated-temperature materials. Results obtained from bond pull-out and prestressing transfer (transmission) length tests show that the polymer silica cements have significantly improved bond strengths of prestressing materials. Limited data from elevated-temperature tests, in which 25.4-mm cubes of polymer silica cement were subjected to temperatures up to 816°C for periods ranging from 3 to 56 d, indicate that exposure of the material to temperatures up to 538°C produced significant (>100%) increases in compressive strength and moduli compared with values obtained for specimens maintained at room temperature; however, exposures to 816°C for greater than 7 d produced decreases. These results indicate that the fibrous concrete has potential for reducing reinforcement in areas where there are stress concentrations such as at penetrations and that the polymer silica system has application where short bond development lengths (anchorages) or strength retention at elevated temperature is required.

Specimens obtained from the center (straight wire of a seven-wire prestressing strand and coated by either petrolatum-base materials containing corrosion inhibitors or portland cement grout) were subjected to corrosive environments ($H_2S$-saturated water, 0.2 *M* $NH_4NO_3$, and 0.1 *M* NaCl) to determine the effectiveness of the coatings for preventing corrosion. Specimens were either stressed or unstressed during exposure (up to 164 d). Results demonstrate the importance of protecting prestressing materials and the fact that both the petrolatum-base and cement-grout materials provide positive exclusion of corrosive environments when properly applied.

A preliminary assessment of AE as a technique for monitoring structural integrity of PCPVs was conducted by monitoring grouted and non-grouted tendon beams tested in flexure. Results show that the technique can identify, locate, and indicate the severity of flaw propagation in prestressed concrete structures as well as detect the onset of failure.

### 3.6.2 PCRV Model Program Definition

The PCRV Model Program Definition (document 903777, dated Oct. 17, 1978) reproduced on subsequent pages was prepared by GA to serve as guidance for the development of the PCRV model test for the reference 900 MW(e) HTGR steam cycle plant. Although the document refers to the test of a specific configuration, the basic elements are equally applicable to PCRVs for the advanced HTGRs as well.

Notations in this column indicate where changes have been made

## 1. INTRODUCTION

The prestressed concrete reactor vessel (PCRV) functions as the primary containment for the reactor core, the primary coolant system, and portions of the secondary coolant system for the High Temperature Gas-Cooled Reactor (HTGR) plant. The use of multi-cavity PCRVs to house reactors with symmetrical component arrangement is well established. Recent HTGR designs incorporate an asymmetric arrangement of major cavities in the PCRV. Where the number of main loops permits, the center of the core cavity is offset from the geometric center of the vessel. The asymmetric layout allows a more effective utilization of space in grouping all the steam generators and their associated piping over a portion of the PCRV, and facilitates separation of safety-related piping from main steam piping.

The PCRV configuration adopted for the reference 900 MW(e) HTGR-Steam Cycle (SC) plant is shown in Fig. 1. There are four cylindrical cavities for steam generators and three smaller cavities for auxiliary circulators in the wall. The cavities are linked by radial ducts to the top and bottom plenums of the core cavity. The upper end of each steam generator cavity is closed by a concrete plug held down by a prestressed concrete retaining ring. The PCRV top head contains the refueling penetrations and a number of pits, access shafts and pipe chases that extend the full height of the vessel wall. All cavities and penetrations have continuous welded steel liners which act as primary coolant flow boundary and sealing membrane. The PCRV is reinforced both vertically and cirumferentially with deformed reinforcing bars. Prestressing of the vessel is accomplished by two independent systems. Vertical prestress is achieved by unbonded longitudinal tendons. The circumferential prestressing system consists of multi-layered bands of seven-wire strand, wound under tension into channels in the surface of the vessel wall. The PCRV is cast integrally with a central pedestal and peripheral ring support structure.

The purpose of a scaled model test for the 900 MW(e) PCRV is to confirm the preliminary assessments of the asymmetric PCRV layout employing an offset core cavity. The model test results together with correlations with analytical predictions will provide convincing demonstration of the adequacy of the PCRV design.

## 2. OBJECTIVE AND SCOPE

The objective of the model test program is to demonstrate the overall structural response of the asymmetric PCRV to overpressure as meeting the ultimate structural capacity criterion of twice the maximum cavity pressure (MCP), and to identify the most probable ultimate failure mode

Notations in this column indicate where changes have been made

The test program should be designed to yield the following summary information:

a) Deflection profiles of top head and barrel of the model.

b) Strain distribution in concrete at critical sections and strain profiles.

c) Representative variations of force in prestressing steel during prestressing and pressurization.

d) Elastic limit and the onset of non-linear response including crack propagation in concrete.

e) Yielding of reinforcing and prestressing steels.

f) Lift-off of closures to steam generator cavities.

g) Ultimate pressure and mode of failure.

Instrumentation together with the logging system should be designed to obtain adequate test data which can be used in subsequent correlation with analytical results. The means of obtaining and the type of test information should be defined in detail in the test specification to be prepared jointly by ORNL and GA.

## 3. MODELING PHILOSOPHY AND REQUIREMENTS

3.1 Model Scale and Similitude: The geometric scale factor of the PCRV model should allow sufficient instrumentation and realistic modeling of significant features of a multi-cavity PCRV. The model scale should be consistent with that recommended in ASME Code, Section III Div. 2, for the purpose of pressure tests. The stress-strain characteristics of the model concrete should be similar to those of the prototype concrete. Typical stress-strain curve of the concrete proposed for use in the prototype PCRV is given in Fig. 2. In addition to 6" x 12" concrete strength cylinders, 2" x 4" cylindrical specimens should be prepared and tested to investigate the effect of size on properties. Compressive strength of model concrete at time of model testing should preferably not exceed the design strength of prototype concrete at the age of 60 days. Geometric scaling of bonded rebars and unbonded tendons on a 'one for one' basis is not considered necessary. Model reinforcement and prestressing steels should have mechanical properties similar to those used in the prototype vessel. For model reinforcement, commercially available deformed wire/ bar may be used. The area and distribution of reinforcing steel should be modeled. The distribution of prestressing forces and prestress levels equivalent to the end of design life condition of prototype vessel should be closely reproduced at the time of model testing. Modeling of vertical tendon tubes and wire winding channel liner is not required. Exact scaling of cavity thickness may not be necessary.

Notations in this column indicate where changes have been made

Steel plate of minimum workable thickness may be used. Penetration liners may be modeled by representative steel pipes in the model. The number and pitch of refueling penetration and effective stiffness of the top head should be simulated. The stress-strain characteristics of the model cavity and penetration liners should be determined so that their contribution to the load carrying capacity can be established.

The concrete plugs over the steam generator cavities need not be modeled. Closure devices directly held down by model vertical prestressing steel are considered acceptable provided that load transfer mechanisms are represented in such a manner that the overall behavior of the prototype under overpressure condition is accurately reproduced. This can be acheived by introducing a restraining structure over the closures secured by steel rods passing through the model, once lift-off of the closure occurs. Reproducing the structural details of penetration liner shear anchors is not necessary. The load paths in the shear transfer to the concrete should be simulated.

3.2 Loading Requirements: The PCRV model should be hydraulically pressurized at normal ambient temperature. Loading should include pressurization of the core cavity, steam generator and auxiliary circulator cavities, cross ducts, top head penetrations and the lower penetrations of steam generator cavities. To minimize the possibility of premature leakage of the pressurizing medium, non-scale cavity liners in a more flexible material than steel may be used. Alternatively, the cavities may be pressurized by means of rubber bags as sealing membranes. Pressure tests of the model can be accomplished in two primary phases.

(a) Phase I. The model should be subjected to three cycles of pressurization up to a pressure corresponding to MCP of the prototype vessel and on the third cycle the pressure is further increased beyond MCP until non-linear behavior is indicated. Small increments of pressure should be applied in order that the elastic limit of model response can be established and that the onset of non-linear response due to concrete cracking can be detected.

(b) Phase II. The response of the model under pressure incrementally increased to a pressure of 2 times MCP will be examined. The overpressure performance of the model will be studied with particular attention to crack propagation, yielding of reinforcing and prestressing steel, and failure mode. Pressure increments include MCP, 2 MCP and then pressure should be increased incrementally from depressurization up to failure. Failure is considered to occur when further increment of pressure is not possible due to excessive leakage of pressurizing medium and structural damage. Action should be taken to preclude termination of the test resulting from premature leakage at pressure level below 2 MCP.

Notations in this column indicate where changes have been made

3.3 Boundary Conditions: The effect of the foundation mat on the PCRV response to pressure loading should be considered. The central pedestal and peripheral ring support with the base slab should be included as part of the PCRV model in order to examine their contribution to pressure resisting capacity of the bottom head. The boundary conditions at the lower ends of the peripheral vertical tendons can be satisfied by anchoring at the side of the ring support or at the bottom of the base slab.

## 4. REVIEW RESPONSIBILITY

To ensure that the model accurately represents a prototype with characteristics similar to those of the current PCRV design for the reference 900 MW(e) HTGR plant, close interfacing between ORNL and GA should be maintained during the model design phases of the test program. Budgets and funding for the model program should include provisions for continued review by GA through design and testing phases to assure consistency between the model and prototype.

## 5. SCHEDULE

The recommended schedule for the PCRV model test program is given in Table 1. The schedule is based on milestones of PSAR submittal in FY-80 and completion of final PCRV design report in FY-84 for the reference 900 MW(e) SC plant. Major milestones for model test program are established to ensure that maximum benefits are derived from model test results to support GA design effort.

GENERAL ATOMIC COMPANY

GA-1484

TITLE: PCRV MODEL PROGRAM DEFINITION DOCUMENT

Document No. 903777 | Issue A

Notations in this column indicate where changes have been made

ORNL-DWG 79-12445

TABLE 1. RECOMMENDED SCHEDULE FOR PCRV MODEL TEST PROGRAM

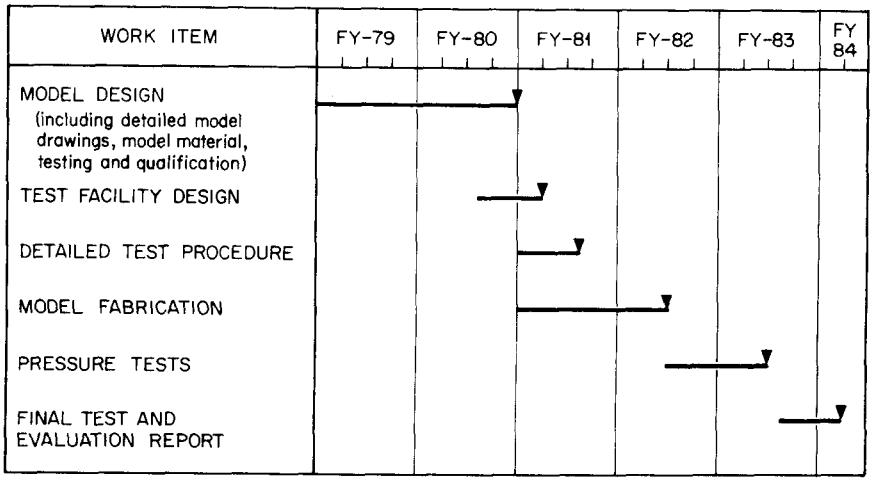

GENERAL ATOMIC COMPANY

GA-1484

TITLE: PCRV MODEL PROGRAM DEFINITION DOCUMENT

Document No. 903777 | Issue A

Notations in this column indicate where changes have been made

ORNL-DWG 79-12444

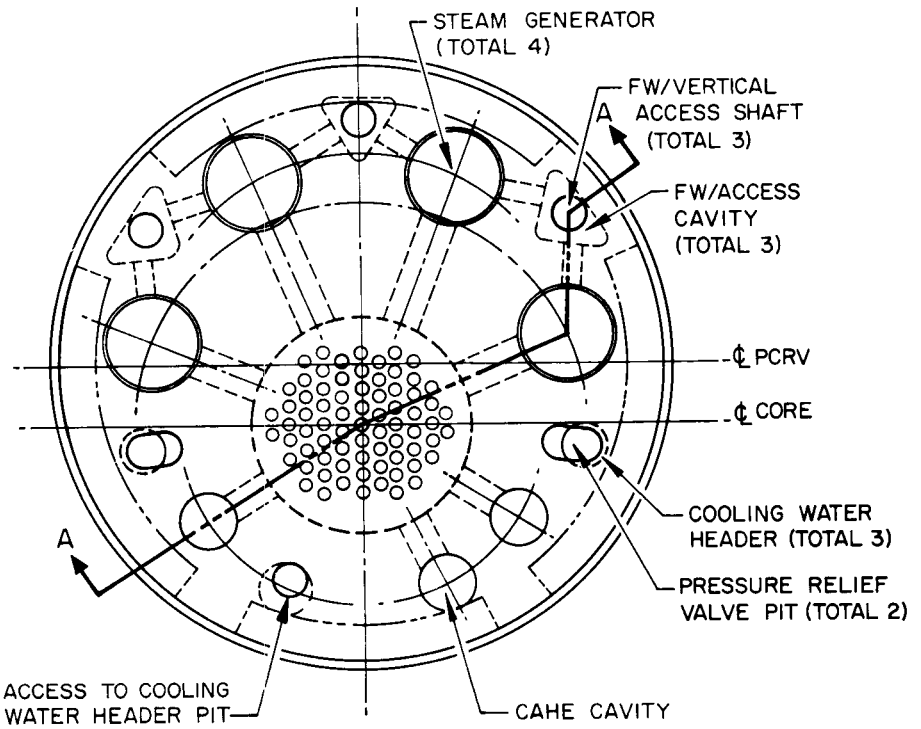


PLAN-PCRV TOP HEAD

Fig. 1(a) PCRV CONFIGURATION

GA-1484

# GENERAL ATOMIC COMPANY

TITLE: PCRV MODEL PROGRAM DEFINITION DOCUMENT

Document No. 903777 | Issue A

Notations in this column indicate where changes have been made

ORNL-DWG 79-12443

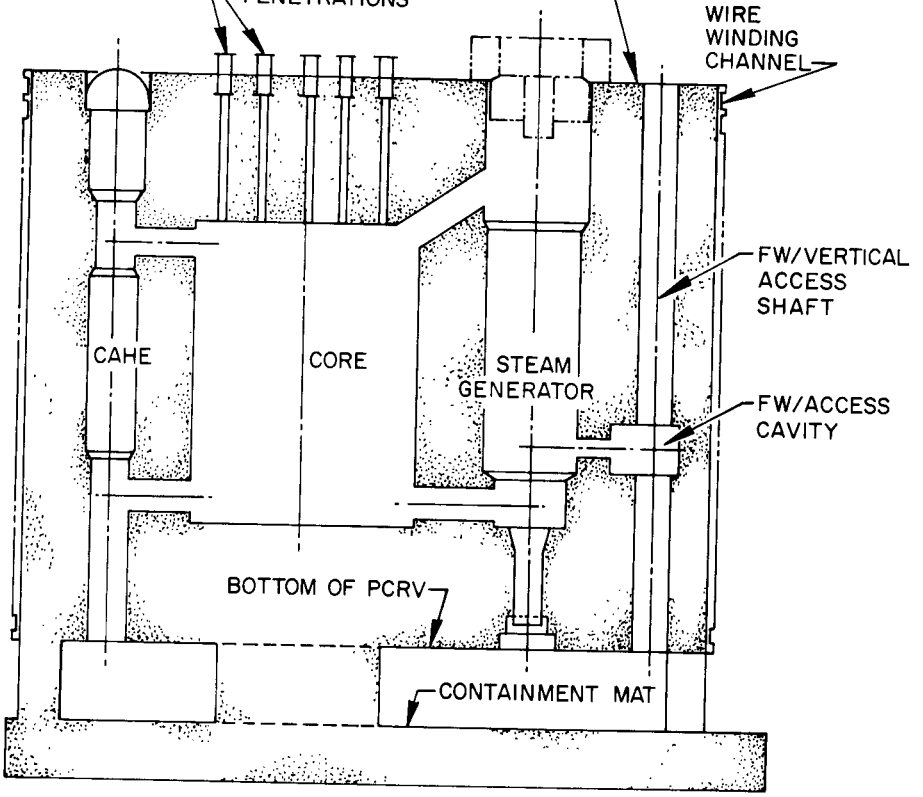


VERTICAL SECTION A-A

Fig. 1(b) PCRV CONFIGURATION

GENERAL ATOMIC COMPANY

GA-1484

TITLE: PCRV MODEL PROGRAM DEFINITION DOCUMENT

Document No. 903777 | Issue A

Notations in this column indicate where changes have been made

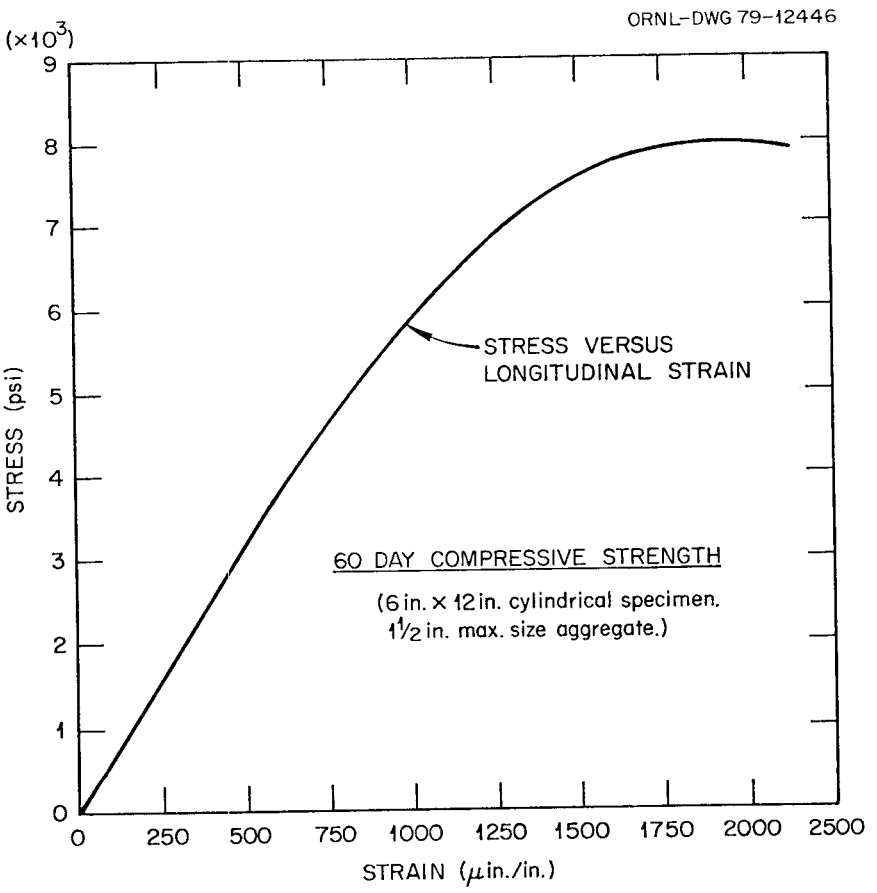


Fig. 2 Typical Stress-Strain Curve for Prototype Concrete

## 3.7 LINER AND PENETRATION STUDIES — R. K. Nanstad and D. A. Canonico

The PCRV for the HTGR contains several steel penetrations and closures, which are part of the liner system. In previous annual reports the requirements of Appendix G to Div. I, Sect. III of the *ASME Boiler and Pressure Vessel Code,* were discussed in detail, especially regarding the $K_{IR}$ (reference fracture toughness) curve and $RT_{NDT}$ (reference nil-ductility temperature) requirement. The materials of interest to the liner testing program as well as specimens and test procedures are also discussed in previous reports.

Further results of Charpy impact and fracture toughness tests for the A 508, class 1, and A 537, classes 1 and 2, base materials are presented in this report along with the initial results of tests on weldment W-3 (A 508, class 1, to A 537, class 2).

The $K_{IR}$ curve has been discussed in previous reports and is presented again in this report in Fig. 3.26. The curve is normalized and plotted relative to the $RT_{NDT}$, which depends on the material being

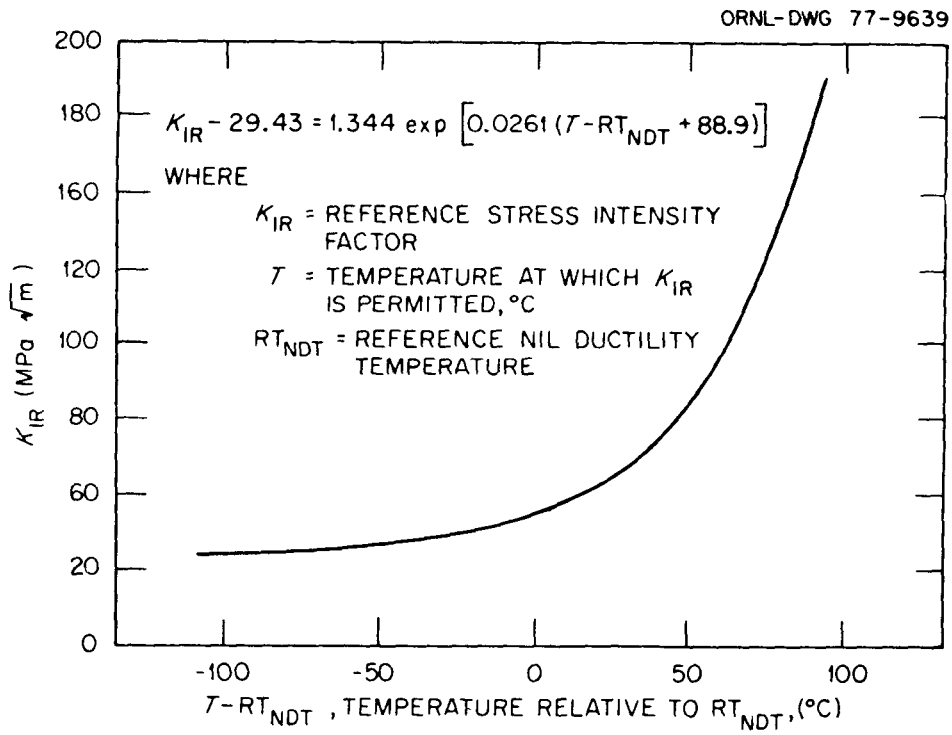


Fig. 3.26. Reference Fracture Toughness Curve from ASME Code.

tested. Thus the curve can be overlaid on a graph of fracture toughness versus actual test temperature, provided that it is plotted with respect to the $RT_{NDT}$ of the particular heat of the material being evaluated.

In the case of base materials, specimens were removed from the $(1/4)t \times t$ location. The longitudinal axis of the specimen is oriented transversely to the major working direction, and the notch is perpendicular to the surface. For weldment W-3, specimens are oriented transversely to the direction of welding. The direction of welding is parallel to the major working direction of the base materials. A macroscopic view of the weldment cross section is shown in Fig. 3.27. The direction of welding is perpendicular to the photograph. The heat-affected zones (HAZ) are evident on both sides of the weld metal, and the weld root is quite pronounced. Because of the relatively narrow weld root, the possibility of carbon dilution (from the base metal) of the weld metal motivated the study of both root and bulk weld metal properties. Weldment W-3 was fabricated from A 508, class 1 (forging F1), and A 537, class 2, plate material. The weld root was made with the shielded-metal-arc process (10%), and the weld was completed with the flux-core-arc process (90%). The weldment was given a postweld heat treatment at 566 to 621°C for 5 h.

Further results from Charpy impact tests with various base materials have resulted in extending the curves to higher temperatures, as shown in Fig. 3.28. The two quenched and tempered materials, A 508, class 1, and A 537, class 2, show similar impact toughness properties. The two heats of A 537, class 1, steel are somewhat different in their behavior, especially at the higher temperatures, where P2 exhibits an unexplained increase in energy absorption. Both P2 and P4 exhibit the "intermediate shelf" phenomenon, at which point the materials experience 100% shear fracture. Thus the further increase in absorbed energy at higher temperatures represents a significantly increased energy-absorbing capability after attainment of full shear fracture. The force-time traces shown in Fig. 3.29 for two different P2 specimens show that the significant change in energy absorption (integrated area under the curve) occurs after maximum load when ductile tearing is the fracture mode.

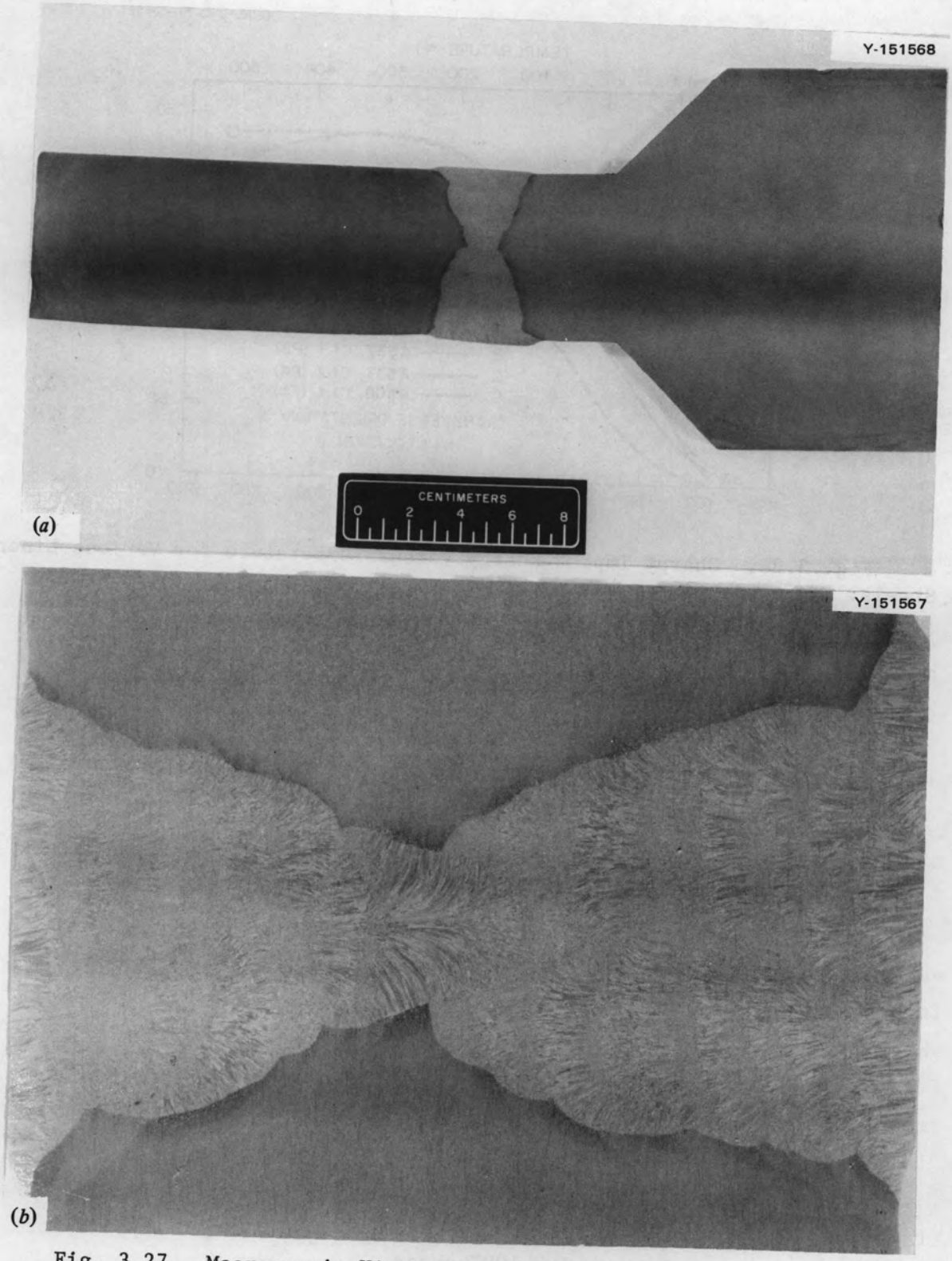


Fig. 3.27. Macroscopic View of Weldment W-3. Top photo, the A 508, Cl.1, forging is on the right, the A 537, Cl.2, plate on the left. Bottom photo, forging is above weld; plate is below weld.

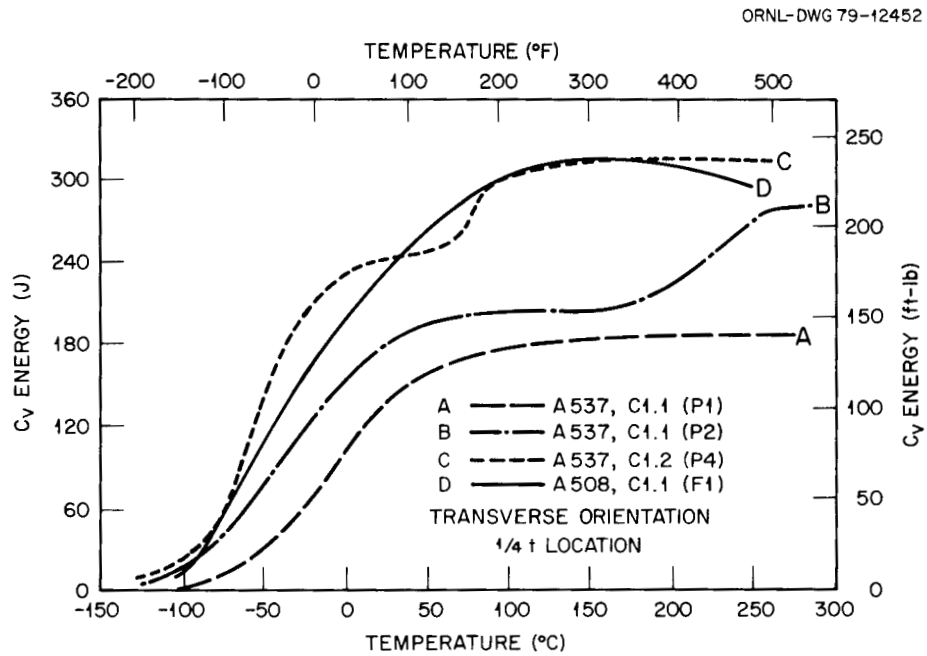


Fig. 3.28. Charpy Impact Energy Versus Temperature for Various Liner Steels.

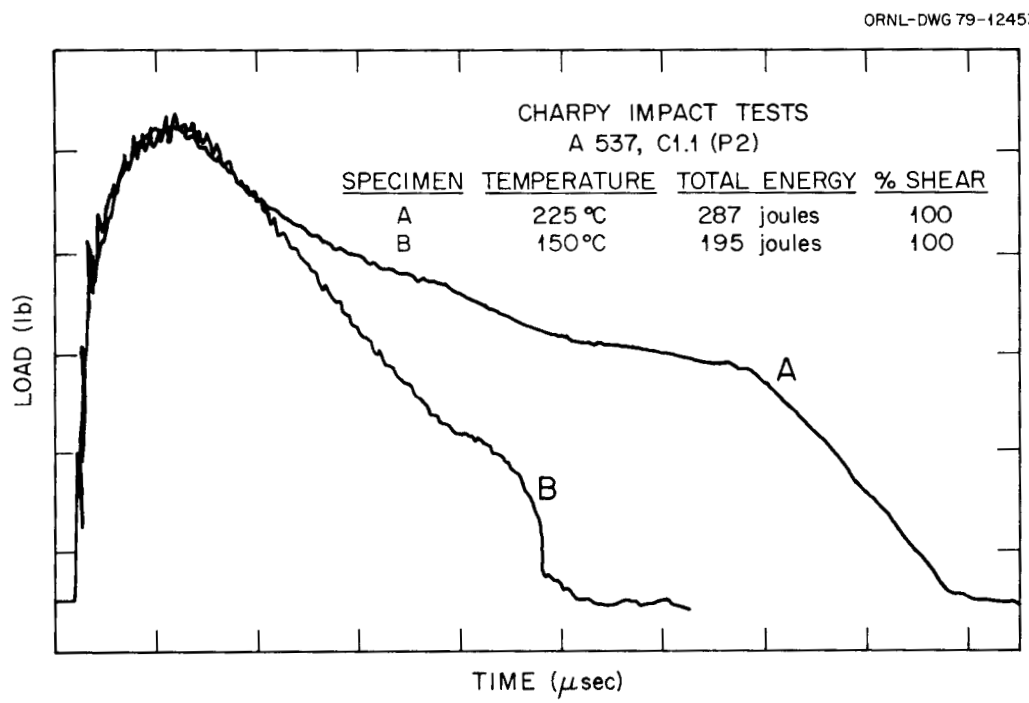


Fig. 3.29. Load-Time Traces for Two A 537, C1.1, Charpy Impact Specimens. Both failed with 100% shear.

Initial results from Charpy impact tests of weldment W-3 are shown in Fig. 3.30. The impact toughness for the plate and the forging HAZ are very similar over the entire temperature range. The weld metal shows lower toughness than the HAZ with respect to the upper shelf levels as well as the transition temperature. A noteworthy observation is the difference between the toughness of the bulk weld metal and the root weld metal. As mentioned previously, the root weld location is being examined because of its probable increased carbon content. The impact toughness results support this suggestion, and further toughness testing as well as chemical analyses will be conducted.

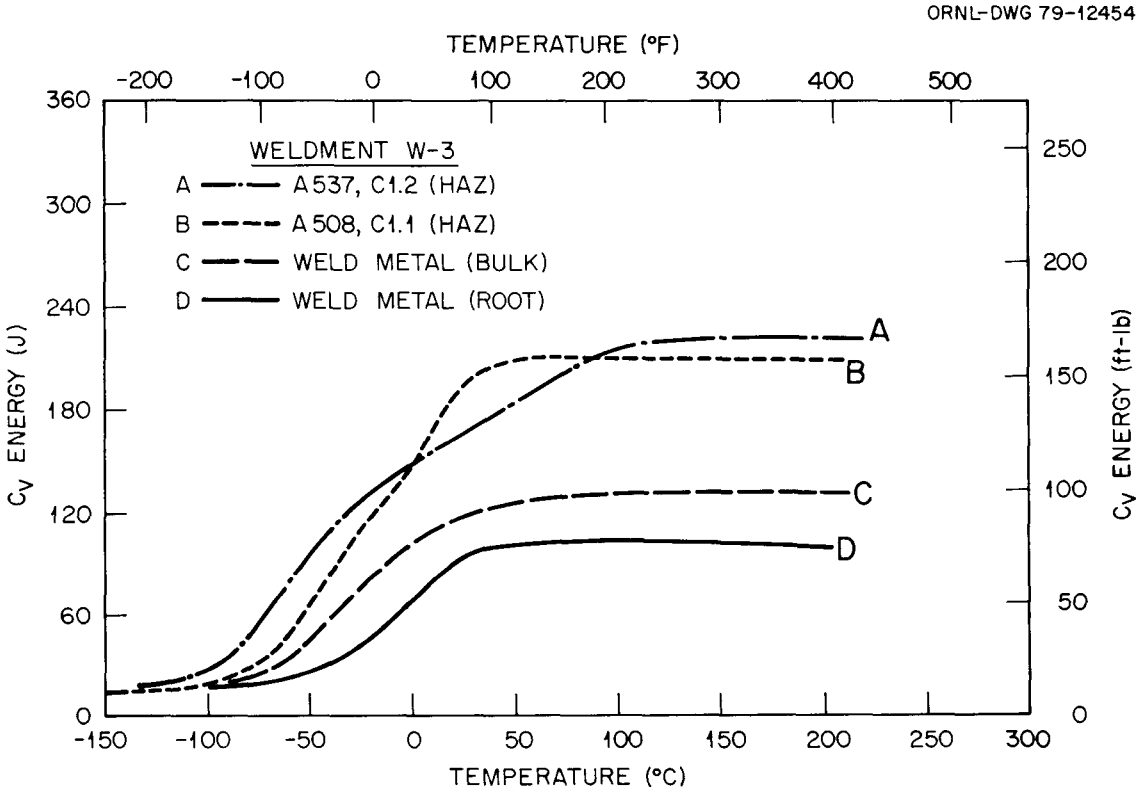


Fig. 3.30. Charpy Impact Energy versus Temperature for Weldment W-3.

Regarding fracture toughness testing, results for the forging and plate materials were presented and discussed in the previous report. Additional testing has been performed (primarily at higher temperatures) to extend the curves of fracture toughness versus temperature for these materials, and the results are shown in Figs. 3.31 through 3.33. In no case did the recent results affect the relationship of fracture toughness to the $K_{IR}$ curve.

Initial results of slow-bend precracked Charpy ($PCC_V$) fracture toughness tests for weldment W-3 are shown in Fig. 3.34. Tests of the HAZ from the forging (A 508, class 1) and plate (A 537, class 2) give results very similar to those of the base metals (Figs. 3.31 and 3.33, respectively). The weld metal fracture toughness is substantially lower than that of HAZ. The curves are preliminary, however, and additional testing is required before conclusions can be drawn. The weld root has not yet been tested for fracture toughness properties.

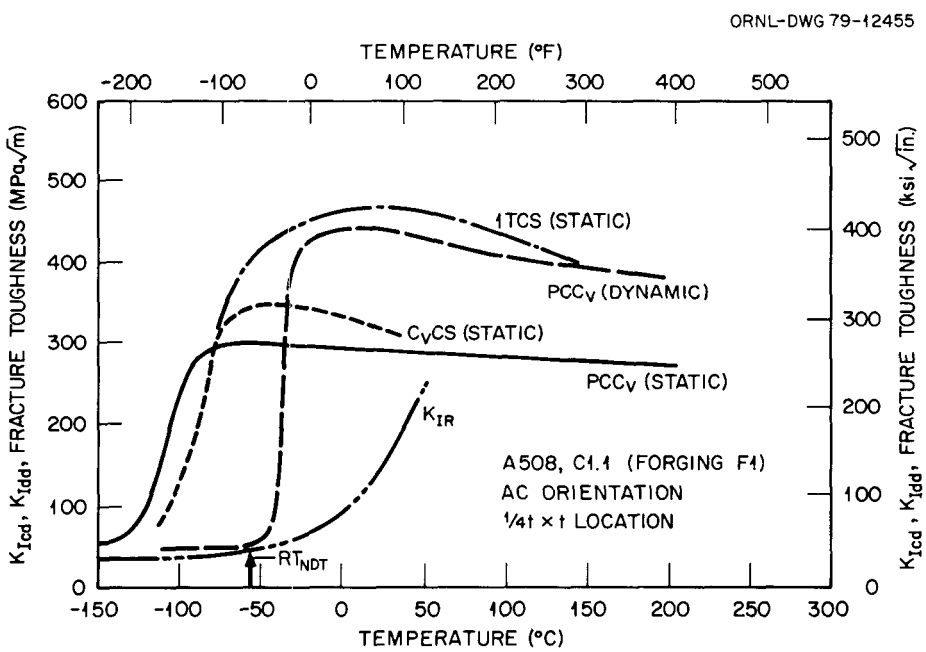


Fig. 3.31. Static and Dynamic Fracture Toughness of A 508, Cl.1. Steel (forging F1) measured with precracked Charpy ($PCC_V$) and compact specimens (CS).

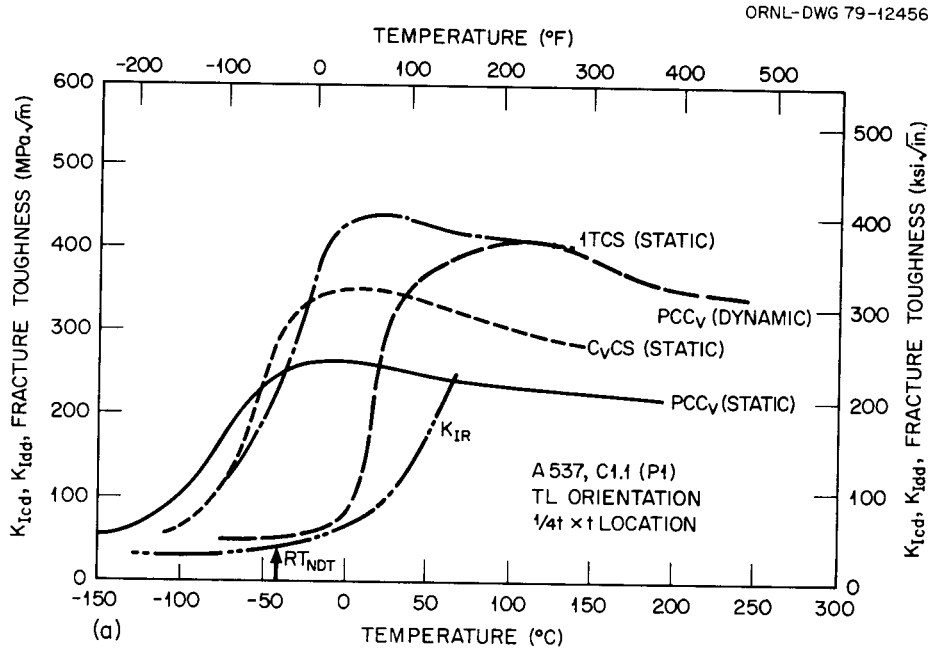


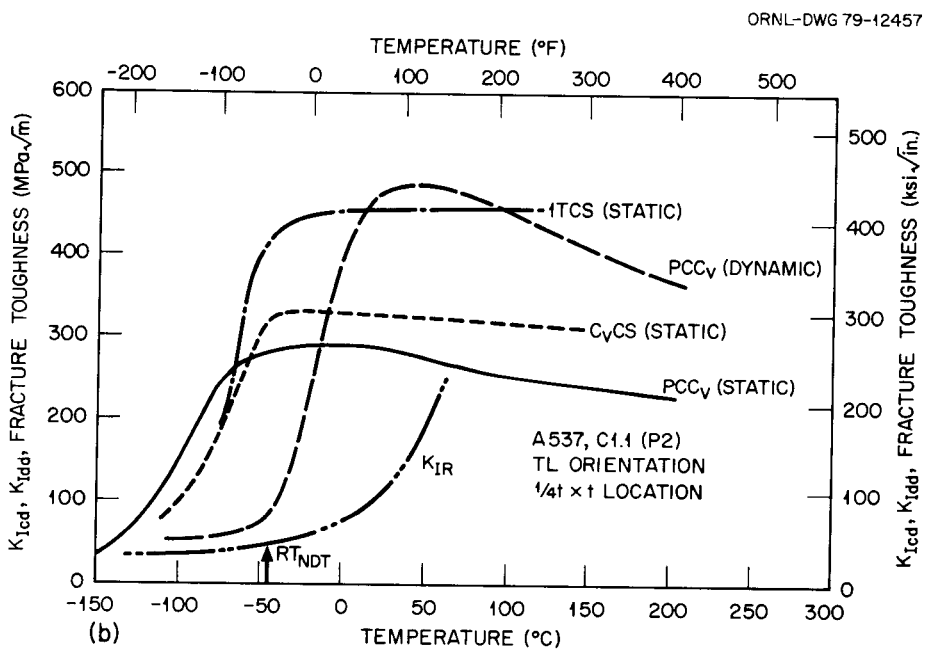


Fig. 3.32. Static and Dynamic Fracture Toughness of A 537, Cl. 1, Steel Measured with Precracked Charpy (PCC$_V$) and Compact Specimens (CS). (*a*) Plate 1; (*b*) plate 2.

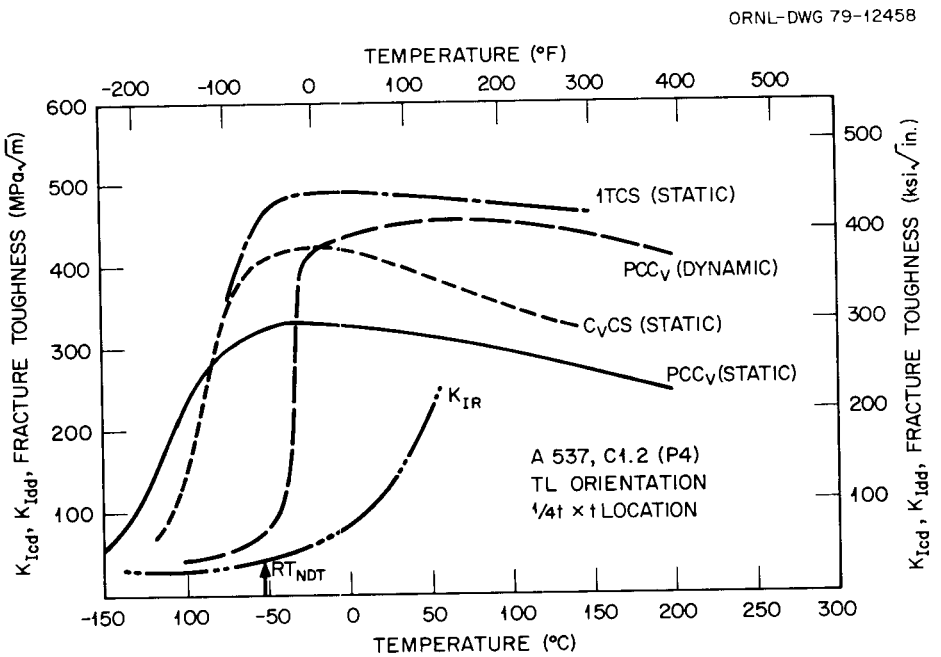


Fig. 3.33. Static and Dynamic Fracture Toughness of A 537, Cl. 2, Steel (Plate P4) Measured and Precracked Charpy ($PCC_V$) and Compact Specimens (CS).

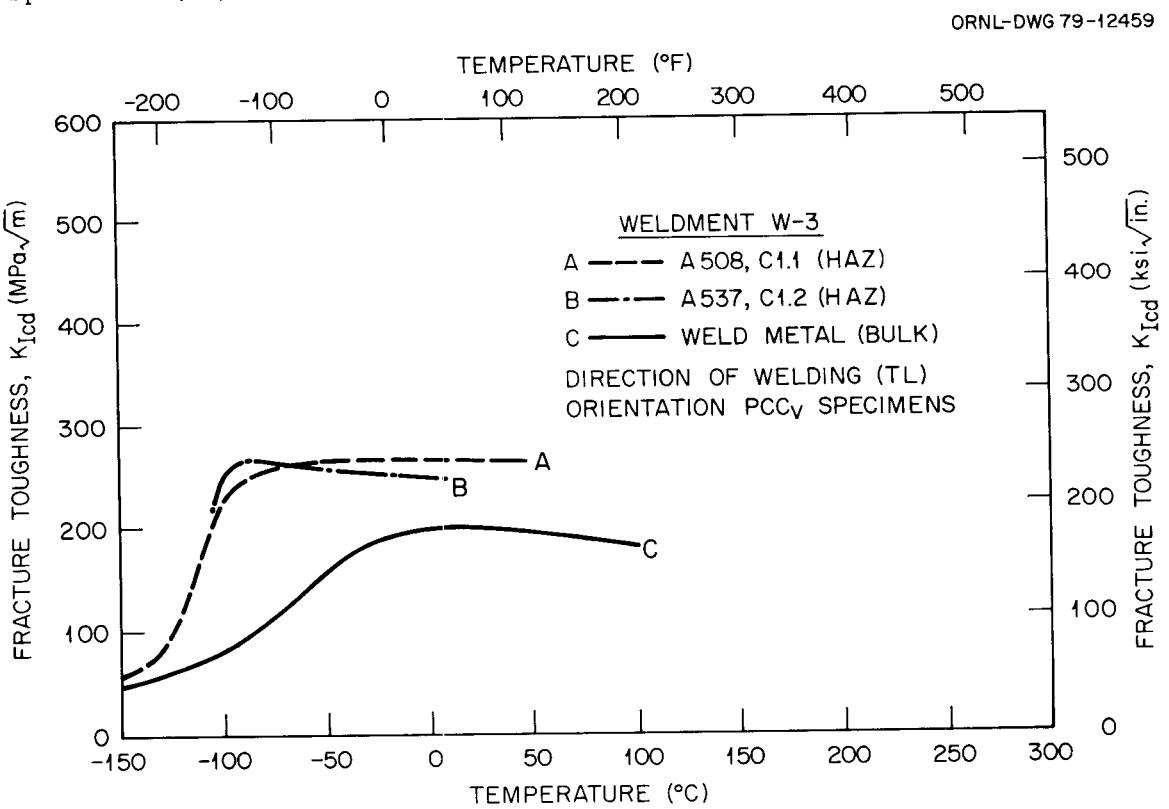


Fig. 3.34. Static Fracture Toughness of Weldment W-3 Measured with Precracked Charpy ($PCC_V$) Specimens.

## 3.8 REFERENCES


1. H. L. Gotschall (Gas Cooled Reactor Associates), J. R. Roberts (Stone and Webster, Boston), and J. P. Callahan, *Optimized PCRV for HTGR Power Plant,* ORNL/TM-6606, to be published.
2. K. J. Bathe, *ADINA, A Finite Element Program for Automatic Dynamic Incremental Nonlinear Analysis,* Report. 82448-1, Massachusetts Institute of Technology, Cambridge, Mass. (September 1975).
3. Z. P. Bazant, P. D. Bhat, and C. L. Shieh, *Endochronic Theory for Inelasticity and Failure Analysis of Concrete Structures,* Structural Engineering Report 1976-12/259, Northwestern University, Evanston, Ill. (December 1976).
4. M. H. Khan and B. Saugy, "Evaluation of the Influence of Some Concrete Characteristics on Nonlinear Behavior of a Prestressed Concrete Reactor Vessel," *Concrete for Nuclear Reactors,* Publ. SP-34 American Concrete Institute (1972).
5. K. C. Valanis, "A Theory of Viscoplasticity Without a Yield Surface," *Arch. Mech. Stosow.* 23: 517-51 (1971).
6. W. G. Dodge, Z. P. Bazant, and R. H. Gallagher, *A Review of Analysis Methods for Prestressed Concrete Reactor Vessels,* ORNL-5173 (February 1977).
7. R. K. Nanstad, *A Review of Concrete Properties for Prestressed Concrete Pressure Vessels,* ORNL/TM-5497 (October 1976).
8. K. Gerstle et al., "Strength of Concrete Under Multiaxial Stress States," pp. 103-32 in *Douglas McHenry International Symposium on Concrete and Concrete Structures,* ACI SP55, American Concrete Institute (1978).
9. K. Gerstle et al., "Behavior of Concrete Under Multiaxial Stress States," paper 7 presented at session 38 of the American Society for Civil Engineers Annual Convention, Inelastic Response of Normal, Lightweight and High-Strength Concrete, October 1978.
10. D. J. Naus and C. C. Hurtt, *Monitoring of Prestressed Concrete Pressure Vessels. 1. An Overview of Concrete Embedment Strain Instrumentation and Calibration Test Results for Selected Concrete Embedment Strain Meters,* ORNL/TM-6191/V1 (June 1978).

11. D. J. Naus and C. C. Hurtt, *Monitoring of Prestressed Concrete Pressure Vessels. 2. Performance of Selected Concrete Embedment Strain Meters Under Normal and Extreme Environmental Conditions,* ORNL/TM-6191/V2 (October 1978).

12. American Society for Testing and Materials, *Acoustic Emission,* Spec. Tech. Publ. 505, 1972, p. 337.

13. American Society for Testing and Materials, *Monitoring Structural Integrity by Acoustic Emission,* Spec. Tech. Publ. 571, 1975, p. 289.

14. W. McCabe et al., "Acoustic Emission Behavior of Concrete Laboratory Specimens," *J. Am. Concr. Inst.* 73(7): 367–71 (July 1976).

15. A. T. Green, *Stress Wave Emission and Fracture of Prestressed Concrete Reactor Vessel Materials,* Rep. 4190, Aerojet-General Corporation, June 1969, p. 105.

16. J. C. Spanner, *Acoustic Emission — Techniques and Applications,* Intex Publishing Company, Evanston, Ill. 1974, p. 3.

17. J. G. Merkle et al., *Test of 6-in.-Thick Pressure Vessels. Series 4: Intermediate Test Vessels V-5 and V-9 with Inside Nozzle Corner Cracks,* ORNL/NUREG-7 (August 1977).

18. G. D. Whitman, *Heavy-Section Steel Technology Quart. Prog. Rep. January–March 1977,* ORNL/NUREG/TM-120, pp. 19-23.

19. D. J. Naus, *Structural Model Testing for Prestressed Concrete Pressure Vessels: A Study of Grouted vs Nongrouted Posttensioned Prestressing Tendon Systems,* ORNL/TM-6478, to be published.

20. D. J. Naus, *An Evaluation of the Effectiveness of Selected Corrosion Inhibitors for Protection of Prestressing Steels in PCPVs,* ORNL/TM-6479, to be published.

# 4. STRUCTURAL MATERIALS

J. R. DiStefano

## 4.1 INTRODUCTION

The overall objective of the ORNL structural-materials program is to assist in developing the data required to optimize and validate the design of safe, reliable components for current and advanced Gas-Cooled Reactor (GCR) systems. The ORNL program, together with the generic-materials program at the General Atomic Company (GA) and the advanced materials program at General Electric (GE), forms the national structural-materials program in support of gas-cooled reactors.

Three main task areas are included in the ORNL program: (1) helium effects, (2) welding development, and (3) steam corrosion. Mechanical-properties, corrosion, and thermal-stability studies are included in the helium-effects task area. The types of mechanical-properties tests being conducted on both base metal and weldments are tensile, creep, low-cycle fatigue, creep/fatigue, creep/crack growth, and fatigue/crack growth. In the ORNL program, particular attention is focused on the determination of time-dependent mechanical properties. Corrosion testing was recently initiated and includes special-effects studies, such as determining the influence of thermal instability as a result of carburization on creep rate.

The welding development program is aimed at providing information on the influence of process variables and filler metals on weldability. The program also includes the assessment of component-design reliability. During the past year our studies were focused on the effect of weld dilution on transition joints made of 2-1/4 Cr-1 Mo steel.

Steam-corrosion studies are primarily aimed at evaluating long-term compatibility of potential steam-generator materials with superheated steam. During the past year we have also investigated the effect of small caustic concentrations in steam on the stress-corrosion resistances of alloy 800H.

Recent indications are that emphasis on developing gas-cooled reactors may be shifted to advanced systems. With this change in emphasis, we expect to de-emphasize some of the detailed, design-inspired experiments and to broaden the variety of materials tested. We have recently initiated a program to evaluate structural ceramics for GCR applications. So far, work has been concentrated on preparation of an experimental plan. Studies will include stress relaxation, static fatigue, fracture mechanics, and material characterizations.

## 4.2 MECHANICAL PROPERTIES — C. R. Brinkman

### 4.2.1 Creep Testing of Base Metals and Weldments — H. E. McCoy and B. McNabb

Creep tests are being carried out in air and High-Temperature Gas-Cooled Reactor (HTGR) helium environments. Additional equipment was installed during the past year to bring the total testing capacity up to 34 controlled-environment and 22 air-environment creep frames. This test equipment was described previously.[1] Tests are being conducted primarily on Hastelloy X and 2-1/4 Cr-1 Mo steel base metals, with lesser efforts on Hastelloy S, Inconel 617, Incoloy 800H, and 9 Cr-1 Mo steel. Transverse weld specimens of Hastelloy X and Hastelloy X joined to Incoloy 800H are being tested. These test materials were described previously.[1]

The status of the base-metal creep program was summarized in a topical report.[2] Creep tests on Hastelloy X showed that the creep behavior of the alloy to test times of 20,000 h is not detectably different in air and helium, although carburization occurs in the helium environment. The fracture strain values in helium at elevated temperatures were slightly lower than those in air, but the main concern is the reduction in room-temperature ductility in the helium environment. The kinetics of carburization become rapid above about 850°C. Creep tests of 2-1/4 Cr-1 Mo steel showed that the creep strength was less in helium than in air because of decarburization. The kinetics of decarburization become quite rapid above about 600°C. This loss of creep strength as a result of decarburization is the property change of most concern. Limited creep

tests are in progress on 9 Cr-1 Mo steel, Incoloy 800H, Hastelloy S, and Inconel 617; the testing has not progressed sufficiently to show significant differences in creep strengths of the materials in air and in helium environments. The tests, however, have affirmed that Inconel 617 is considerably stronger than Hastelloy X. Helium compatibility tests on unstressed wires of an Ni-7% Cr-12% Mo-4% Fe-2% Ti alloy (modified Hastelloy N) have been encouraging in that the alloy has completely resisted carburization during exposure to helium for 1028 h at 871°C.

Creep tests on weldments are only partially completed, but sufficient test results are available to show several important trends. We joined Hastelloy X to itself with Hastelloy X and Hastelloy S filler metals by using the gas-tungsten arc (GTA) and the shielded-metal arc (SMAW) processes. Samples were creep tested in the as-welded condition after aging for 2,000 and 10,000 h. The creep tests were conducted in HTGR helium, but aging was carried out in argon. The rupture lives of the transverse specimens were generally equivalent to those of Hastelloy X base metal and never fell short of these values by more than a factor of 2. Specimens made by the SMAW process consistently had rupture lives shorter than those made by the GTA process, and in both, the fractures almost always occurred in the weld metal. Minimum fracture strains of 3% were noted for the SMAW deposits tested at 649°C, whereas minimum values for Hastelloy X filler metal deposited by the GTA process were 6.5% and those for Hastelloy S deposited by the GTA process were 10%.

Creep tests were also run on transverse specimens of Hastelloy X-Incoloy 800H weldments. These two materials were joined by (1) Inco 82 filler metal by the GTA process and (2) Inco weld A filler metal by the SMAW process. Failures consistently occurred in the Incoloy 800H base metal or in the heat-affected zone (HAZ) of the Incoloy 800H end of the weld. Thus, failure times correlated well with those for the Incoloy 800H end of the weld. Fracture strain values were as low as 2% but were artificially low because about two-thirds of the gauge length consisted of relatively stronger material that deformed very little during the creep test. At the point of fracture the reduction in area was at least 15%. Tests of all-weld metal specimens are needed to determine the creep properties of the weld deposit.

### 4.2.2 Low-Cycle Fatigue and Creep Fatigue — J. P. Strizak

Fatigue tests on 2-1/4 Cr-1 Mo steel were conducted in helium at the impurity levels shown in Table 4.1. Test specimens came from a heat (3P5601) of commercial ASME SA-387 grade D plate, which was given an isothermal anneal heat treatment prior to specimen fabrication. Chemical composition, heat-treatment, tensile, fatigue, and creep-fatigue (hold time) data that were obtained in air have been published.[3,4] Fully reversed, push-pull, strain-controlled fatigue testing of the hourglass-shaped test specimens was performed in accordance with ASTM guidelines.[5] Additional details concerning experimental techniques can be found elsewhere.[3] Results of tests conducted in the above environment and data generated in air are compared in Table 4.2.

Table 4.1. Compositional Limits of Test Gases[a]

| Impurity | Level noted (ppm) |
|---|---|
| $H_2$ | 150-184 |
| $O_2$ | $10^{-22}$ atm[b] |
| $N_2$ | ∿1 |
| $CH_4$ | 12-16 |
| $H_2O$ | ∿5 |

[a]Test chambers operate at 184 kPa. Multiply ppm × 1.82 to obtain μatm; by 0.184 to obtain Pa.

[b]Gas passed through furnace at 500°C to react $O_2$ with $H_2$. Estimate based on equilibrium.

Results of environmental continuous-cycle, zero-hold-time tests conducted at 538°C are compared in Fig. 4.1. Most of the data from continuous-cycle tests generated in air were deleted, and a "best fit" of the air-data line covering the range of $10^3$ to $10^6$ cycles to failure is shown in the figure. When the cyclic lives of specimens tested in impure helium are compared with those tested in air (Table 4.2, Fig. 4.1), it is apparent that the cyclic lives of specimens tested in impure helium either exceed or are equivalent to those tested in air. The slight

Table 4.2. Comparison of Results of Continuous Cycling and Creep-Fatigue tests[a] for 2-1/4 Cr-1 Mo Steel[b] Conducted in Air and a Simulated HTGR Helium Environment

| Environment | Specimen number[c] | Total strain range, $\Delta\varepsilon_t$ (%) | Hold period[d] (h) | Stress range, $\Delta\sigma$ (MPa) | Values at $N_f/2$: Stress amplitudes (MPa) | | | | Strain ranges (%) | | Cycles to failure, $N_f$ | Time to failure, $t_f$ (h) |
|---|---|---|---|---|---|---|---|---|---|---|---|---|
| | | | | | Peak | | Relaxed | | | | | |
| | | | | | Tensile, $\sigma_t$ | Compressive, $\sigma_c$ | Tensile, $\sigma_{tr}$ | Compressive, $\sigma_{cr}$ | Elastic, $\Delta\varepsilon_e$ | Plastic, $\Delta\varepsilon_p$ | | |
| | | | | | Tests conducted at 538°C | | | | | | | |
| Air | MIL-21 | 2.0 | 0.0 | 518 | 246 | 272 | | | 0.334 | 1.666 | 881 | 2.4 |
| Impure He | ITL-132 | 2.0 | 0.0 | 621 | 300 | 321 | | | 0.400 | 0.600 | 1,059 | 3.1 |
| Air | MIL-15 | 2.0 | 0.5T | 494 | 233 | 261 | 107 | | 0.237 | 1.763 | 640 | 322.2 |
| Impure He | ITL-131 | 2.0 | 0.5T | 638 | 308 | 330 | 143 | | 0.305 | 1.695 | 546 | 273.3 |
| Air | MIL-14 | 2.0 | 0.5C | 529 | 268 | 261 | | 130 | 0.256 | 1.744 | 714 | 359.0 |
| Impure He | ITL-130 | 2.0 | 0.5C | 615 | 297 | 318 | | 148 | 0.287 | 1.713 | 715 | 358.0 |
| Air | MIL-17 | 2.0 | 0.5TC | 480 | 234 | 245 | 110 | 114 | 0.144 | 1.856 | 583 | 534.5 |
| Air | ITL-134 | 1.0 | 0.0 | 510 | 259 | 252 | | | 0.329 | 0.671 | 2,377 | 3.5 |
| Impure He | ITL-136 | 1.0 | 0.0 | 545 | 259 | 286 | | | 0.351 | 0.649 | 5,913 | 8.8 |
| Air | MIL-10 | 0.5 | 0.0 | 391 | 192 | 199 | | | 0.252 | 0.248 | 16,036 | 11.0 |
| Impure He | ITL-111 | 0.5 | 0.0 | 510 | 248 | 261 | | | 0.329 | 0.177 | 21,643 | 15.0 |
| Air | ITL-106 | 0.5 | 0.1T | 436 | 200 | 236 | 157 | | 0.254 | 0.246 | 15,450 | 1,555.6 |
| Impure He | ITL-101 | 0.5 | 0.1T | 436 | 195 | 241 | 136 | | 0.243 | 0.257 | 5,860 | 589.9 |
| Air | MIL-12 | 0.5 | 0.1C | 368 | 191 | 171 | | 122 | 0.202 | 0.298 | 4,496 | 453.0 |
| Impure He | ITL-109 | 0.5 | 0.1C | 417 | 211 | 206 | | 137 | 0.202 | 0.298 | 11,220 | 1,129.3 |
| Air | ITL-127 | 0.5 | 0.1TC | 406 | 208 | 198 | 165 | 121 | 0.184 | 0.316 | 1,954 | 392.0 |
| Impure He | ITT-27 | 0.5 | 0.1TC | 412 | 195 | 217 | 149 | 174 | 0.208 | 0.292 | 2,950 | 592.4 |
| Impure He | ITL-202 | 0.5 | *e,f* | 399 | 184 | 215 | | | 0.218 | 0.282 | 7,192 | 254.9 |
| Impure He | ITL-138 | 0.5 | *d,e,f,g* | 428 | 219 | 209 | | | 0.212 | 0.288 | 10,466 | 365.5 |
| Impure He | ITL-102 | 0.4 | 0.0 | 428 | 205 | 223 | | | 0.276 | 0.124 | 89,137 | 49.5 |
| Impure He | ITL-104 | 0.35 | 0.0 | 425 | 206 | 219 | | | 0.274 | 0.076 | 180,925 | 88.0 |
| Impure He | ITL-108 | 0.3 | 0.0 | 411 | 196 | 215 | | | 0.265 | 0.035 | 243,851 | 101.6 |
| | | | | | Test conducted at 482°C | | | | | | | |
| Air | MIL-44 | 0.5 | 0.0 | 444 | 220 | 224 | | | 0.263 | 0.237 | 51,656 | 36.0 |
| Impure He | ITL-123 | 0.5 | 0.0 | 483 | 235 | 248 | | | 0.286 | 0.214 | 69,742 | 48.6 |
| Air | MIL-36 | 0.5 | 0.1T | 417 | 202 | 215 | 158 | | 0.221 | 0.279 | 20,147 | 2,029.0 |
| Impure He | MIL-125 | 0.5 | 0.1T | 450 | 204 | 246 | 153 | | 0.236 | 0.264 | 18,154 | 1,826.5 |
| Air | MIL-27 | 0.5 | 0.1C | 424 | 211 | 213 | | 175 | 0.228 | 0.274 | 6,111 | 615.0 |
| Impure He | ITL-126 | 0.5 | 0.1C | 458 | 229 | 229 | | 198 | 0.253 | 0.247 | 14,740 | 1,484.0 |
| Air | MIL-65 | 0.5 | 0.1TC | 418 | 204 | 214 | 165 | 179 | 0.204 | 0.296 | 3,420 | 686.0 |
| Impure He | ITL-124 | 0.5 | 0.1T6 | 474 | 225 | 245 | 181 | 196 | 0.223 | 0.277 | 5,481 | 1,009.0 |

[a]Fully reversed, axial, push-pull strain-controlled fatigue tests employing a triangular waveform with a strain rate $\dot{\varepsilon}$ of $4 \times 10^{-3}$/s except as noted.

[b]Heat 3P5601, isothermally annealed.

[c]Hourglass-shaped gauge area with a radius-to-diameter ratio of 6 and a minimum diameter of 5.08 mm for ITL specimens and 6.35 mm for MIL specimens.

[d]T ≡ hold period at peak tensile strain amplitude; C ≡ compression; TC ≡ both T and C.

[e]Variable strain rate tests, i.e., tensile going strain rate $\dot{\varepsilon}_T \neq$ compressive going strain rate $\dot{\varepsilon}_C$.

[f]Slow/fast test, i.e., $\dot{\varepsilon}_T = 4 \times 10^{-5}$/s and $\dot{\varepsilon}_C = 4 \times 10^{-3}$/s.

[g]Fast/slow test, i.e., $\dot{\varepsilon}_T = 4 \times 10^{-3}$/s and $\dot{\varepsilon}_C = 4 \times 10^{-5}$/s.

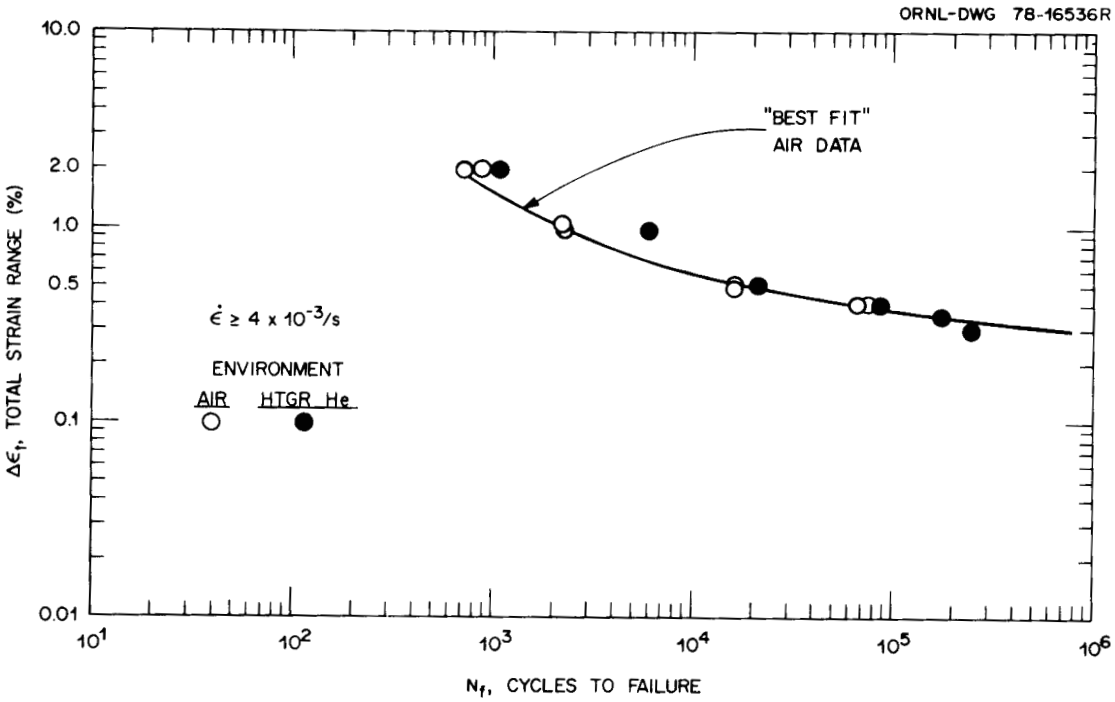


Fig. 4.1. Comparison of Continuous-Cycle Strain-Controlled Fatigue Data from Tests Conducted on 2-1/4 Cr-1 Mo at 538°C. Little or no influence of impure helium in comparison with an air environment is apparent.

increase in fatigue life in the helium environment may be caused by low oxygen rather than by the decarburization that occurs after prolonged exposure at high temperatures in this environment (Fig. 4.2).

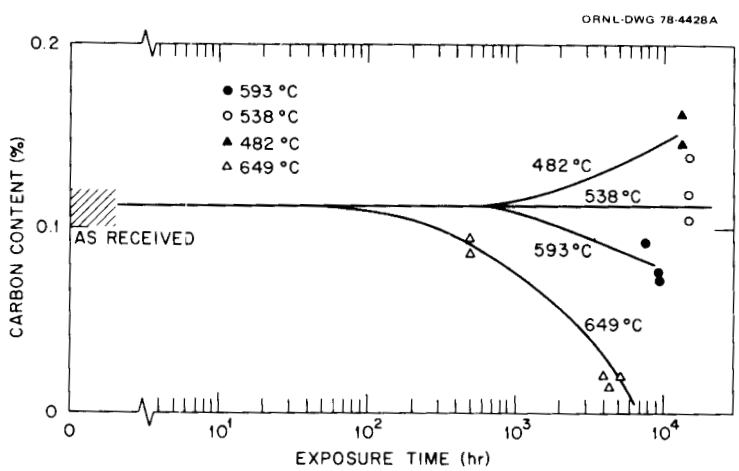


Fig. 4.2. Carbon Contents of 2-1/4 Cr-1 Mo Steel Exposed to HTGR Helium.

Cyclic lives of strain-controlled tests conducted in both impure helium (Table 4.2) and air are compared in Fig. 4.3 for several strain-time waveforms. All tests were conducted at a single strain range of 0.5% and at temperatures of either 482 or 538°C. From a comparison of the cyclic lives of the specimens tested in air, it is apparent that (1) hold periods, that is, 0.1 h, reduce the cyclic life below that of the continuous-cycle or no-hold-time test results, (2) compressive holds are more damaging than tensile holds, and (3) combined tensile and compressive holds of equal duration are more damaging than either tensile or compressive holds. A comparison of the representative results of 2%-strain-range tests conducted in air (Table 4.2) makes it apparent that these trends are also true at the higher strain ranges, except for the indication that tensile holds are equally or slightly more damaging than compressive holds. Similarly, tests conducted in impure helium showed reductions in life when hold periods were introduced into each cycle (Fig. 4.2). However, in contrast to the air data, tensile holds were slightly more damaging than compressive holds (Fig. 4.2 and Table 4.2). Accordingly, we concluded that environment plays a role in determining the mode of the more damaging hold period.

Data indicate that the mechanical strain-cycle interaction, or the mean stress development resulting from hold periods, may also help

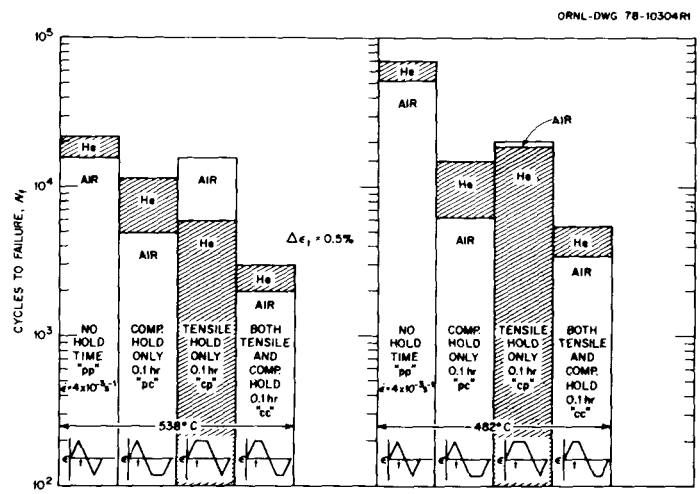


Fig. 4.3. Tests Conducted in Helium with Controlled Impurities Show Improved Cyclic Lifetimes for Several Waveforms in Comparison with Air. Tensile hold times only, however, appear to be an exception.

to explain why one mode of hold is more damaging than another. Lord and Coffin[6] characterized the low-cycle fatigue and hold-time behavior of cast Rene 80 and found that compressive hold times were more damaging than tensile hold times. This behavior was qualitatively explained in terms of the capacity of the material to sustain a mean stress at cycle lives beyond the transition fatigue life; that is, the elastic strain range was greater than the plastic strain range. These workers postulated that, in this material, compressive hold times were particularly deleterious at low-strain ranges because tensile mean stresses that would enhance crack growth rates could be maintained. The cyclic transition life of 2-1/4 Cr-1 Mo steel tested at 482°C was about 10,000 cycles so that specimens tested at a strain range of 0.5% or less clearly had elastic strain ranges in excess of the plastic strain ranges. In the case of 2-1/4 Cr-1 Mo steel tested at 538°C, the transition point occurred at about 10,000 cycles with a total strain range of about 0.39%. If the mean stress postulate were entirely correct, one would expect to see the hysteresis loop shifts shown in Fig. 4.4. An examination of the large data base[4,7] generated for this material revealed that, indeed, in nearly all cases when a tensile-only hold period was imposed, a small mean compressive stress developed. However, when a compressive-only hold cycle was imposed, it did not necessarily result in a mean tensile stress; that is, no consistency was apparent. Additional long-term tests in both air and helium, as well as metallographic observations of fatigued specimens, are currently under way. We hope that these tests will provide additional information about why compressive holds are more damaging than tensile holds at low-strain ranges.

### 4.2.3 Fatigue Crack Growth — T. Weerasooriya

Subcritical crack growth studies were conducted on Hastelloy X, Hastelloy X weld metal, 2-1/4 Cr-1 Mo steel, and HAZ of 2-1/4 Cr-1 Mo steel/ERNiCr-2 weldments. Details of results, chemical compositions, and mechanical properties of tests conducted on 2-1/4 Cr-1 Mo steel have been reported;[8] results are summarized here.

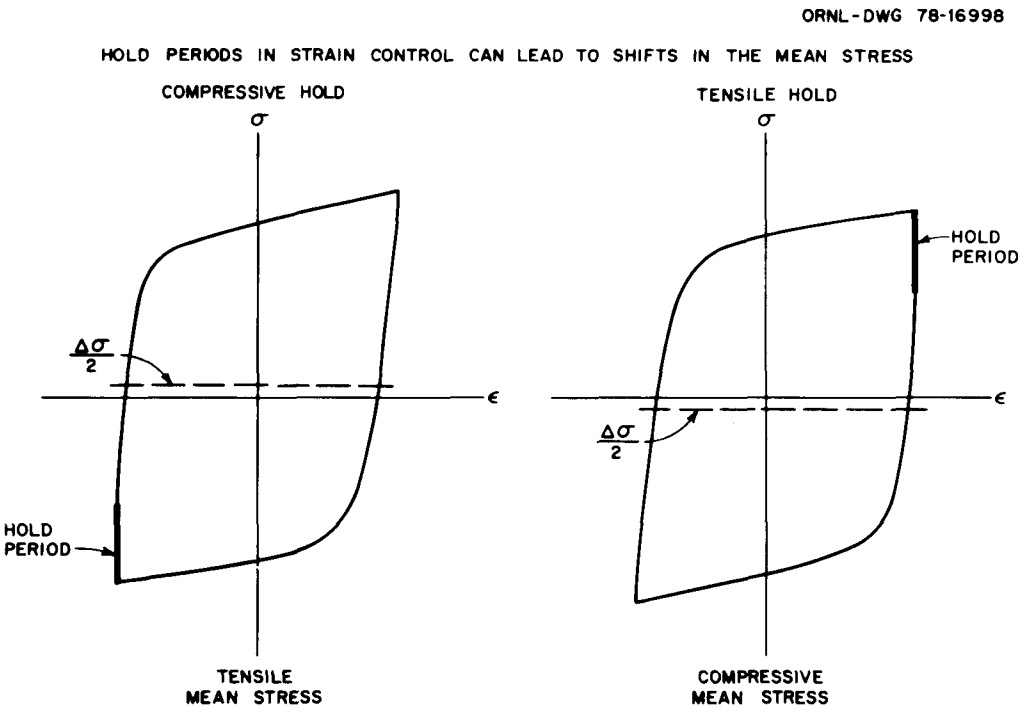


Fig. 4.4. Representative Hysteresis Loops Occurring During Elevated-Temperature, Strain-Controlled Fatigue Tests.

4.2.3.1 Hastelloy X and Hastelloy X Weld Metal

The objective of this program is to study the fatigue crack growth behavior of Hastelloy X and Hastelloy X weld metal in the temperature range of 25 to 871°C. Some tests were performed to determine the effect of frequency on fatigue crack-growth properties of Hastelloy X weld metal. The Hastelloy X used for testing was solution annealed. All tests were conducted by use of an $R$ value (ratio of minimum to maximum load) of 0.05.

Results of the tests performed to evaluate the effect of temperature on the fatigue crack-growth rates (FCGRs) of Hastelloy X weld metal are presented in Fig. 4.5. These tests were conducted in air on 1T compact tension (CT) specimens at a constant $R$ value of 0.05 and a constant frequency of 1 Hz. The FCGR increased with increasing temperature for Hastelloy X weld metal. The FCGRs of weld metal are compared with those of base metal in Figs. 4.6 and 4.7; at both 538 and 649°C, the rate in the base metal was higher than the rate in the weld metal.

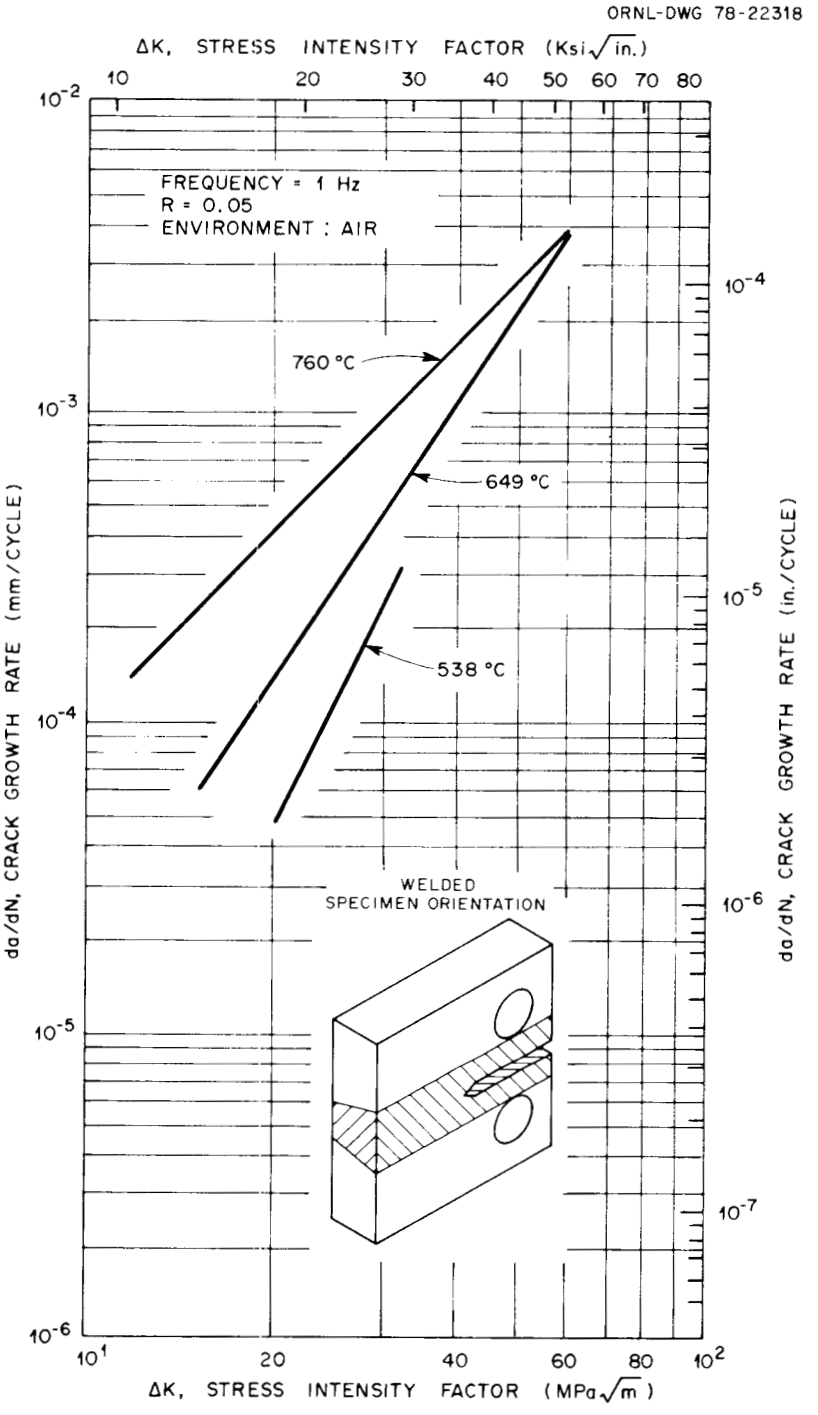


Fig. 4.5. The Effect of Temperature on the Fatigue Crack-Growth Rates of Hastelloy X Weld Metal.

ORNL-DWG 78-18701

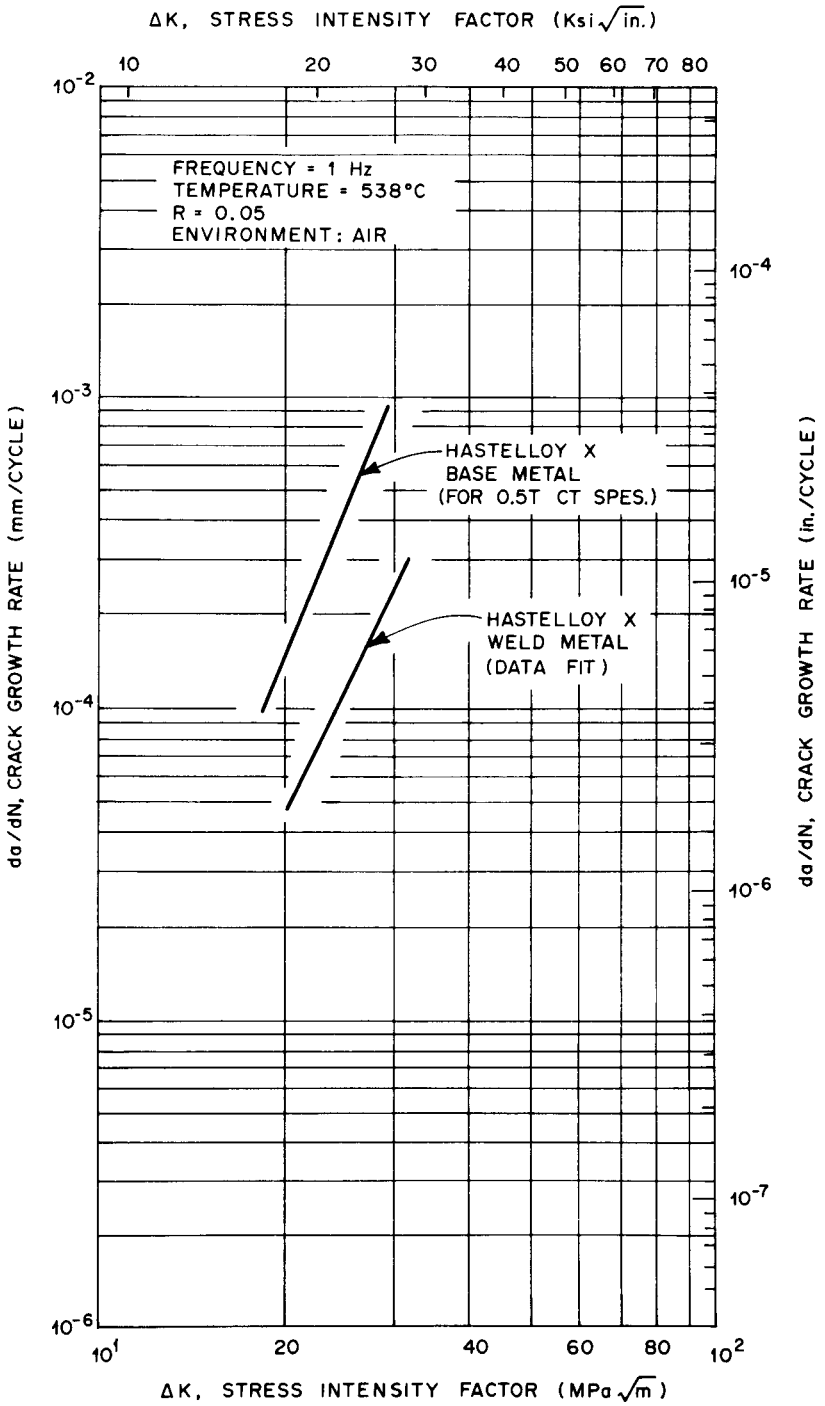


Fig. 4.6. Comparison of Fatigue Crack-Growth Rates of Hastelloy X and Hastelloy X Weld Metal at 538°C. SPES, specimens.

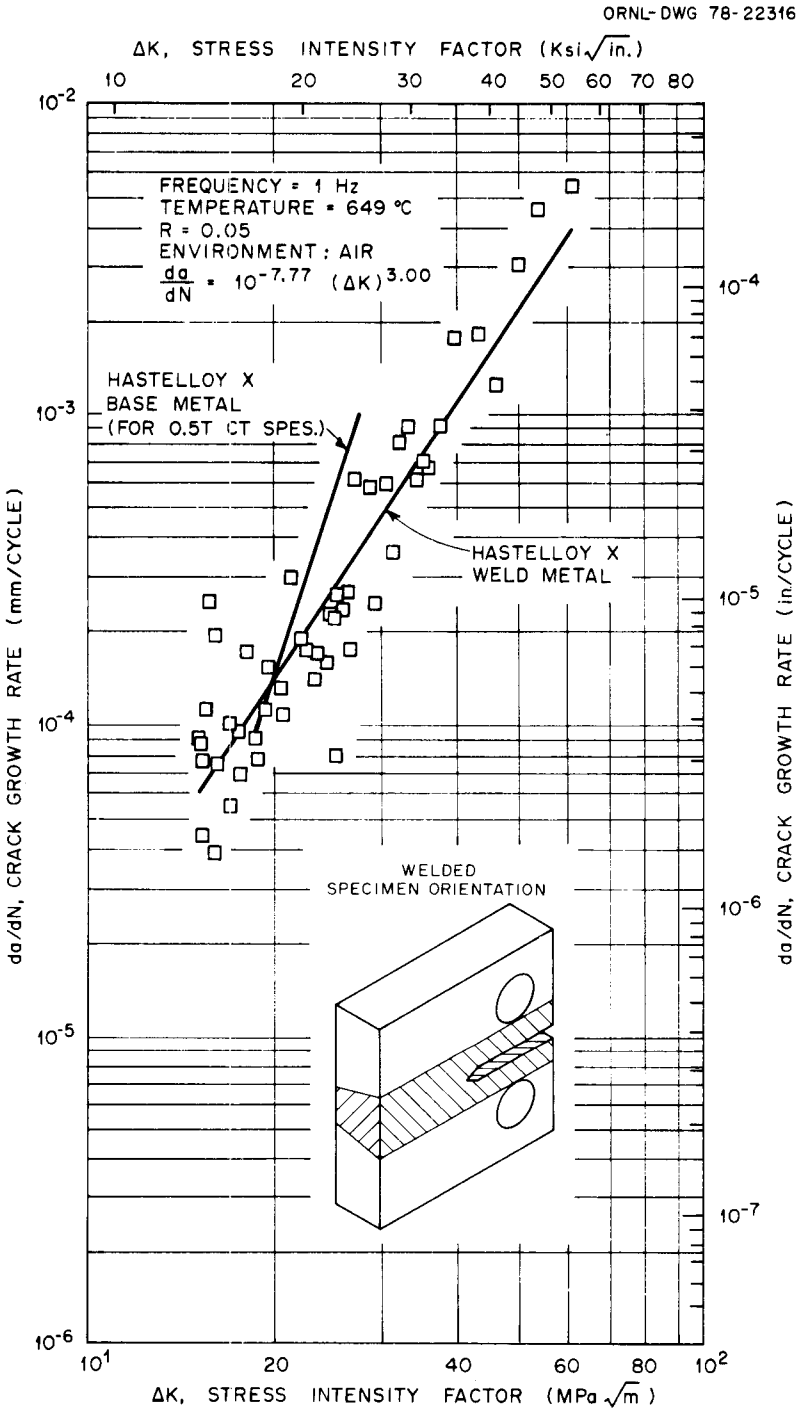


Fig. 4.7. Comparison of Fatigue Crack-Growth Rates of Hastelloy X and Hastelloy X Weld Metal at 649°C. SPES, specimens.

Figure 4.8 shows the effect of specimen geometry on the FCGR of base metal. For this comparison, a 0.5T CT specimen was used. This CT specimen is small compared with the remaining ligament width, crack length, and the plastic zone size. In this case, therefore, the calculated $\Delta K$ values may be inaccurate.

4.2.3.2 2-1/4 Cr-1 Mo Steel

Fatigue crack-growth tests performed on 2-1/4 Cr-1 Mo steel are reported elsewhere.[8] Figure 4.9 shows the effect of environment. The FCGRs are higher in air and steam than in HTGR helium and vaccum environments. This effect can be attributed to the exclusion of oxygen from the crack tip in the vacuum and helium environments.

The simulated HTGR helium used in this study is not completely inert, as reflected by the FCGRs observed in HTGR helium, which are higher than the FCGRs observed in vacuum. The results in steam also show that HTGR helium is even less inert than impure helium. Only a small reduction in the FCGR in steam was observed over that in air, whereas rates in vacuum or HTGR helium were much lower than in air. Similar corrosion products were produced in both steam and air environments; however, less corrosion occurred in steam because of a lower effective oxygen potential.[8,9] This lower oxygen potential in steam is believed to be responsible for the lower observed crack-growth rates in steam compared with those in an air environment.

The crack-growth model,[8]

$$da/dN = A_0(DK)^{3.5} , \tag{1}$$

is proposed for 2-1/4 Cr-1 Mo steel, where $da/dN$ = crack growth rate (mm/cycle),

$$DK(\mathrm{MPa}\sqrt{\mathrm{m}}) = \Delta K/\sqrt{1 - R} , \tag{2}$$

ORNL-DWG 78-18699

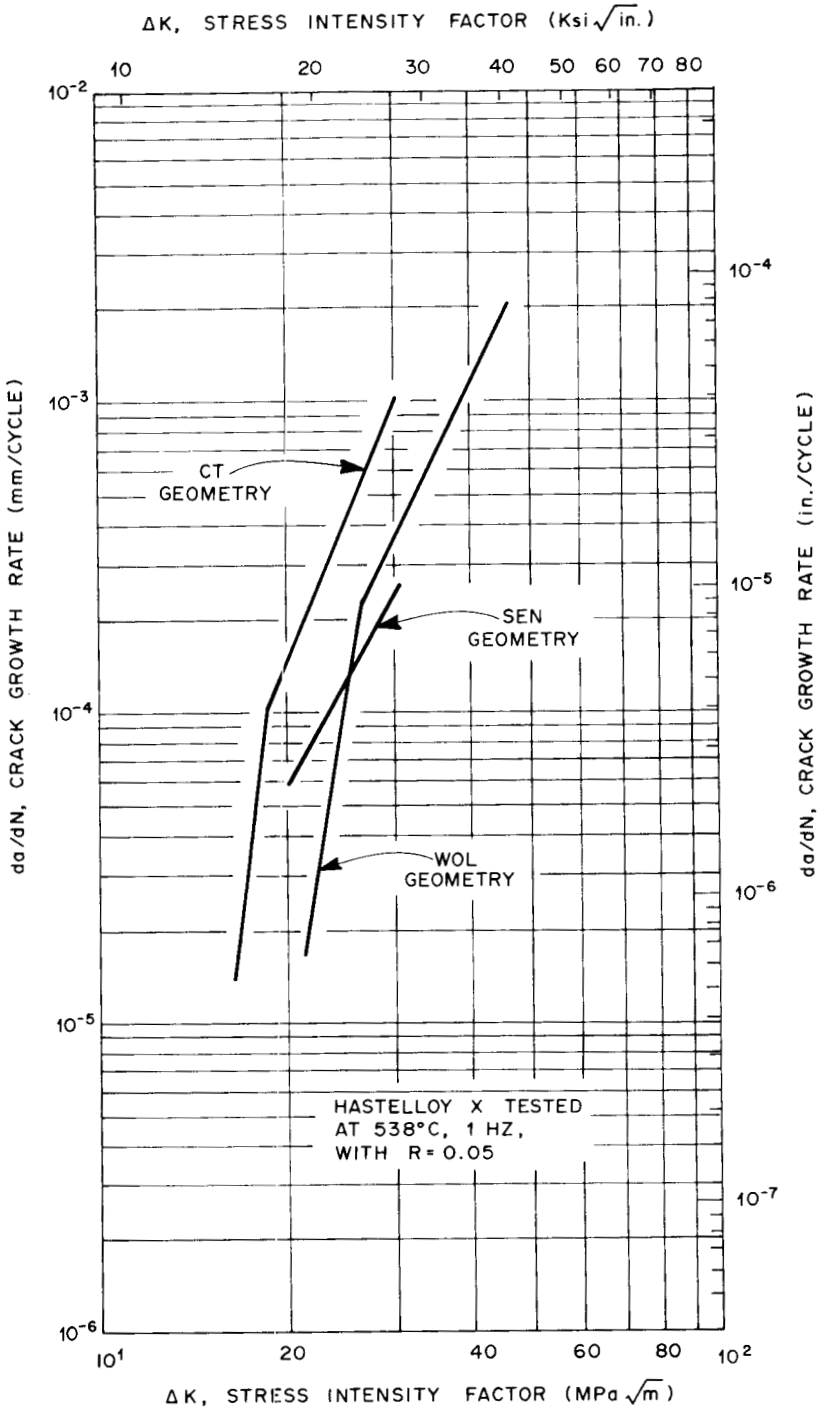


Fig. 4.8. Specimen Geometry Effect on the Fatigue Crack-Growth Rates of Hastelloy X at 538°C.

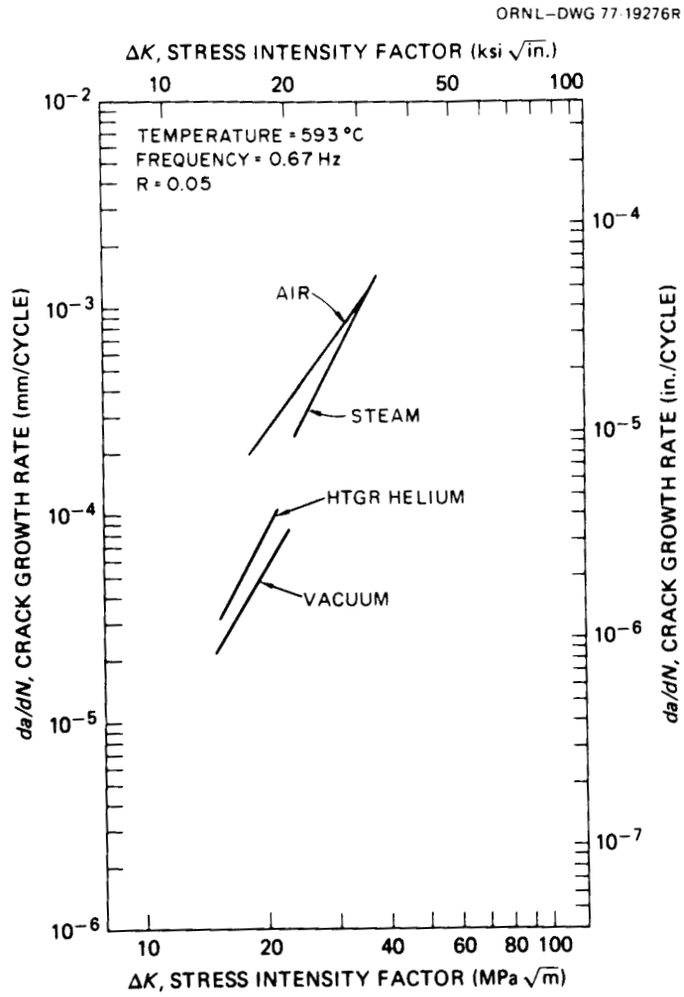


Fig. 4.9. Effect of Environment on Fatigue Crack-Growth Rate of 2-1/4 Cr-1 Mo Steel at 593°C.

$$\Delta K = K_{max} - K_{min} \ , \tag{3}$$

and

$$\log A_0 = -10.106 + 1.359 \times 10^{-5} T^2 - 1.432 \times 10^{-8} T^3 - 1.7 \times 10^{-9} T^3 \log v \ , \tag{4}$$

where $T$ = temperature, °C; and $v$ = frequency, Hz. This model predicts the $\log(da/dN)$ values with a standard deviation of 0.253.

#### 4.2.3.3 Heat-Affected Zone of 2-1/4 Cr-1 Mo Steel-ERNiCr-3 Weld Metal

Tests were conducted to evaluate the FCGR in the HAZ of 2-1/4 Cr-1 Mo steel-ERNiCr-3 weldments in air. In this program the effect of frequency on the FCGR in HAZ was studied. The temperature was kept constant at 510°C, and the $R$ value was kept constant at 0.05.

Figure 4.10 shows the effect of frequency on FCGR in the HAZ of 2-1/4 Cr-1 Mo steel. The FCGR increases with decreasing frequency because of an increase in environmental attack at the crack tip. This effect is also evident in the FCGRs for 2-1/4 Cr-1 Mo steel base metal.[8] Figure 4.11 compares the FCGRs in base metal (2-1/4 Cr-1 Mo steel) and in weld metal (ERNiCr-3). The FCGR of the HAZ lies between the scatter bands of the FCGRs of 2-1/4 Cr-1 Mo steel base metal and ERNiCr-3 weld metal.

### 4.2.4 Thermal Stability — H. E. McCoy

The property changes of Hastelloy X and Inconel 617 during exposure to inert gas at elevated temperatures are significant. The results of tensile tests on material aged 2500 and 10,000 h at 538, 704, and 871°C have been reported.[1] To further characterize the behavior of these materials, samples will be aged for 20,000 h at 538, 704, and 871°C; thus far, the samples have been aged for 17,000 h. After aging, tensile and impact tests will be run at ambient temperature, and tensile tests will be run at the temperature used for aging.

Because of the carburization of materials in impure helium, the combined effects of aging and carburization need to be evaluated. Test samples of Hastelloy X and Inconel 617 base metal and welds are being exposed to HTGR helium. The three chambers in this program operate at 538, 704, and 871°C and contain 144 creep and tensile, 48 fatigue, and 18 crack-growth specimens. Currently, the samples have been aged for 7000 h of the target times of 10,000, 20,000, and 50,000 h. After aging, the samples will be removed and tested to evaluate the mechanical property changes.

ORNL DWG 78-16914R

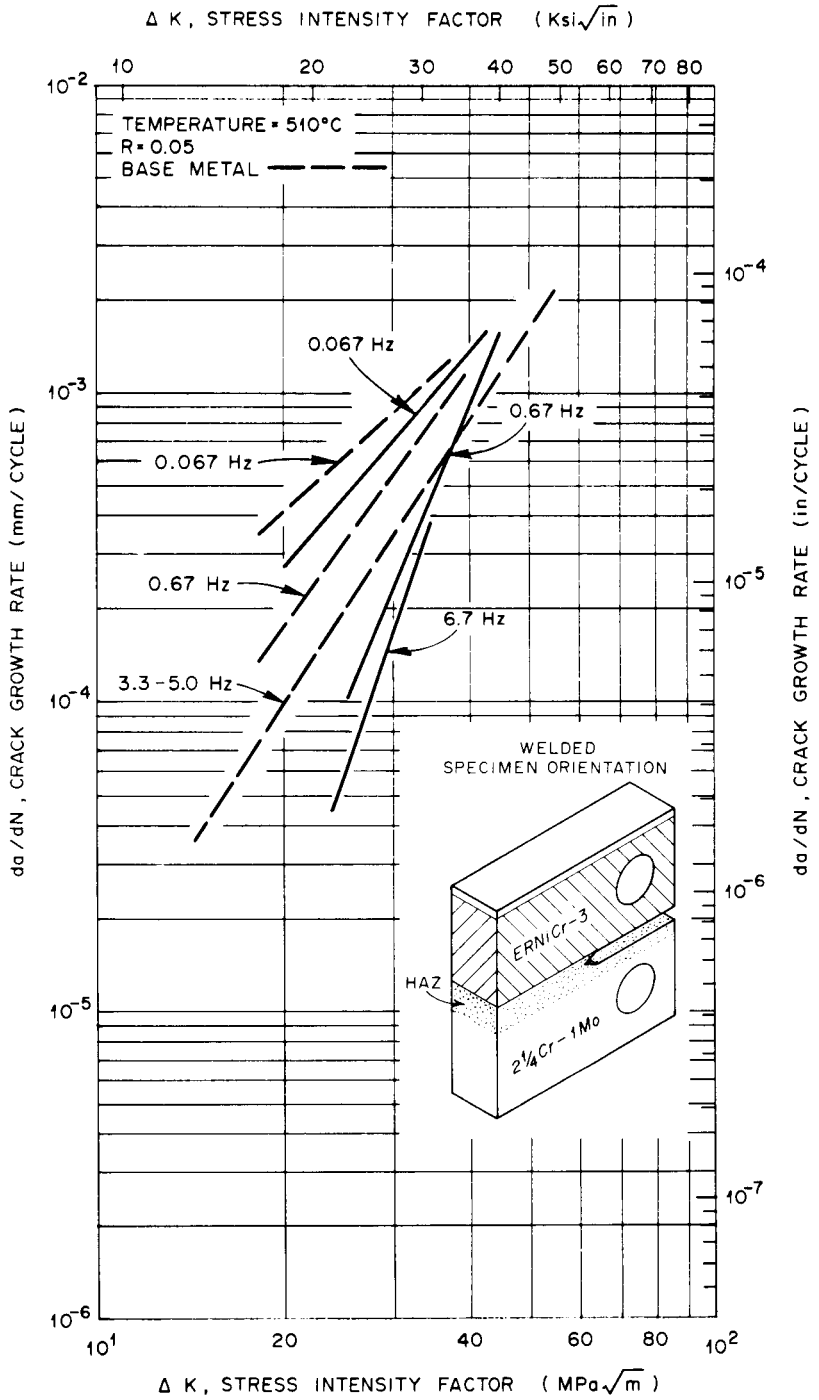


Fig. 4.10. The Effect of Frequency on the Fatigue Crack-Growth Rates of Heat-Affected Zones of 2-1/4 Cr-1 Mo Steel ERNiCr-3 Weld Metal.

ORNL-DWG 78-16917R

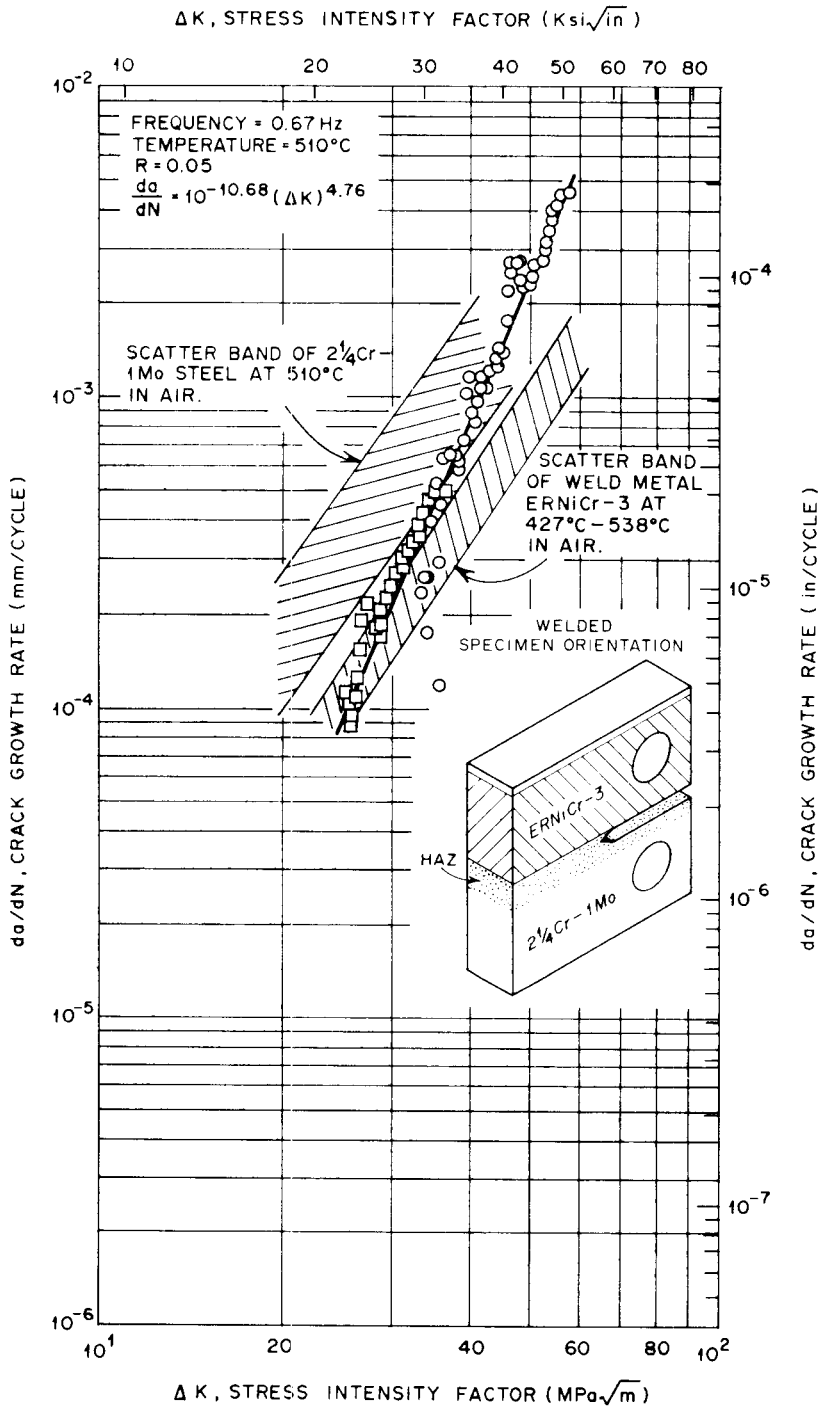


Fig. 4.11. Comparison of the Elevated-Temperature Crack Propagation Rates of 2-1/4 Cr-1 Mo Steel, ERNiCr-3 Weld Metal, and the Heat-Affected Zone of the Weldments of 2-1/4 Cr-1 Mo Steel and ERNiCr-3 Weld Metal.

### 4.2.5 Corrosion — H. Inouye

The objective of this subtask is to provide a basic understanding of the corrosion behavior of structural alloys in GCR helium. Our approach is to analyze and interpret existing data, to identify study areas requiring more information, and then to conduct tests designed to provide the required data. For example, previous investigators have determined that carburization is one of the major problems associated with the corrosion of candidate alloys. These investigators generally agree that the extent of the carburization must be predictable and controllable over the projected life of the structure. Reliable extrapolations are not currently possible, however, because the kinetics are not well established, and confidence in the identification of the controlling variables is insufficient. The progress achieved toward our objective is summarized.

An understanding of corrosion behavior and, specifically, kinetic processes requires accurate analysis and control of impurities in the helium. To determine the test gas composition, absolute standards (Table 4.3) were initially used to calibrate a Bendix model 2300 gas

Table 4.3. Calibration Standards for Impurity Gases in Helium

| Gas species | Standard | Procedure |
|---|---|---|
| $H_2O$ | Vapor pressure of $H_2O(s)$ | Hygrometer reading versus $P_{H_2O}(s)$ between −15 and −110°C |
| $H_2$ | $Fe + H_2O \rightleftharpoons FeO + H_2$ | Equilibrate at various $P_{H_2O}$ levels and temperatures |
| $CO_2$ | $CaCO_3 \rightleftharpoons CaO + CO_2$ | Equilibrate at various temperatures |
| CO | $Fe + CO_2 \rightleftharpoons FeO + CO$ | Equilibrate at various $CO_2$ levels and temperatures |
| $CH_4$ | $H_2/CH_4/CO/CO_2$[a] | Dilute gas mixture with pure helium to give constant $P_{CO_2}$, $P_{CO}$, or $P_{H_2}$ |

[a] 50.48/30.20/17.20/2.12 (vol %).

chromatograph and a Panametrics 2000 hygrometer. These calibrated instruments were then used to analyze and establish a reference gas composition. A comparison of the test gas with the reference gas now fixes the composition of the test gas and eliminates the tedious calibration procedure. Figure 4.12 is a schematic of the apparatus used to obtain the data that follow.

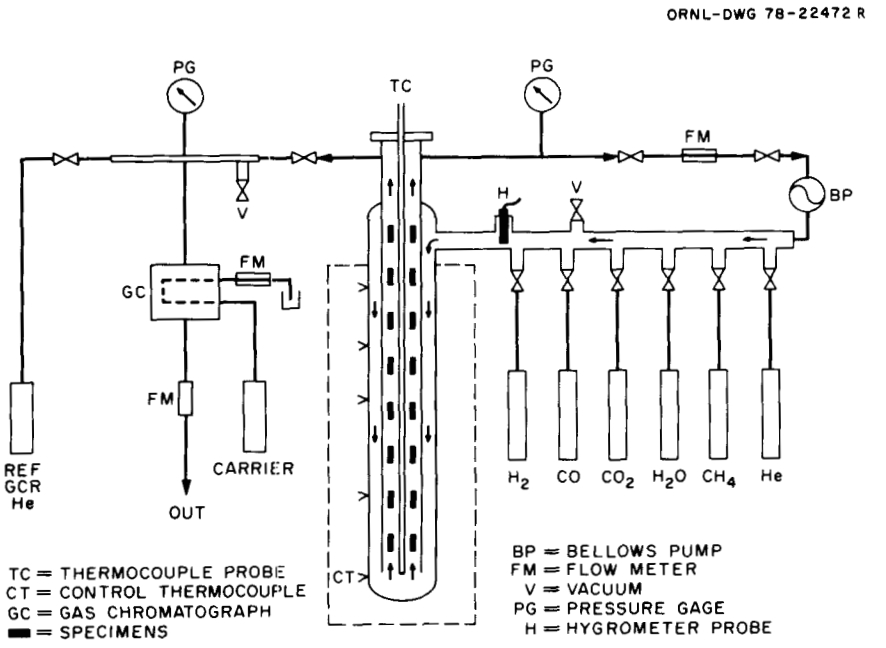


Fig. 4.12. Schematic Diagram for Testing Corrosion Specimens in GCR Helium.

Where possible, all components external to the furnace were constructed of high-vacuum stainless steel fittings and metal gaskets, whereas the heated components such as the double-walled retort and the thermocouple probe were constructed of porcelain. The temperatures of specimens suspended on two 0.32-cm-diam nickel rods are measured with a traveling Pt/Pt-10% Rh thermocouple. The test gas is recirculated at a rate of 1 liter per minute with the metal-bellows pump in a closed system. Its composition is determined by bleeding the required impurity into high-purity helium and/or by venting at a rate of about 100 $cm^3$/min to the gas chromatograph. Based on the dimensions of the retort, the gas velocity is calculated as 105 cm/min and the residence time as less

than 1 min. This procedure minimizes errors in the gas composition resulting from impurity depletion or generation and avoids the lack of composition control in premixed gases.

The carburization behavior of at least 13 heats of Hastelloy X in six different environments up to 7000 h has been summarized.[10,11] Despite the large number of data points, the carburization kinetics remain poorly defined by a maximum of two exposure times for any particular heat or by only one exposure time at three temperatures. To obtain the required data, a series of corrosion tests for exposures of 700, 1200, 2000, and 3000 h to phase IV helium ($500H_2/50CH_4/33CO$) has been scheduled. The tests will be conducted at five exposure temperatures between 750 and 950°C.

Table 4.4 lists the carbon contents of Hastelloy X specimens exposed to $504H_2/49CH_4/38CO/0.036CO_2 \cdot 0.3H_2O/3N_2$ (in microatmospheres)* for 1200 h. Each 0.635-cm-diam by 2.22-cm-long specimen was machined to six successively smaller diameter specimens about 0.32 cm long. These were then sectioned and analyzed for carbon. The specimen ends were not analyzed but were reserved for other tests. Values for specimens listed in line A of Table 4.4 represent the final carbon contents of the unmachined specimens, and the values for specimens in line F are assumed to represent the starting carbon content. The carbon increases for the line A specimens were converted to a carburization rate assuming that $\Delta C/A \sim \sqrt{t}$ ($\Delta C$ is the change in carbon content of the specimen, $A$ is the cross-sectional area, and $t$ is the time). When the log of this rate is plotted versus $1/T$, an activation energy of 10.5 kcal/mol is suggested for temperatures above 854°C and 43.7 kcal/mol for temperatures below 854°C.

The carbon content in each of the six layers was calculated as the difference between the carbon contents of specimens of a given diameter and the next smaller diameter (e.g., carbon in $L_1$ = (carbon A − carbon B)/(wt A − wt B). Figure 4.13 shows data typically obtained by this procedure, and the presence of a steep carbon gradient near the surface is confirmed.

---

*Time-compensated average of 39 analyses.

Table 4.4 Carbon Content[a] of Hastelloy X Specimens[b] Exposed for 1200 h to Phase IV Helium then Machined to Various Diameters

| Specimen No. | Diameter (cm) | Carbon (wt ppm) at exposure temperatures — | | | |
|---|---|---|---|---|---|
| | | 828°C | 854°C | 902°C | 946°C |
| A | 0.635 | 950 | 1056 | 1100 | 1178 |
| B | 0.627 | 944 | 979 | 1058 | 1140 |
| C | 0.610 | 894 | 864 | 988 | 1089 |
| D | 0.574 | 827 | 853 | 912 | 1024 |
| E | 0.533 | 815 | 817 | 880 | 912 |
| F | 0.381 | 798 | 802 | 802 | 810 |

[a]Determined by the combustion-gas chromatograph method.

[b]The original dimensions of the specimens were 0.635 cm diameter by 2.223 cm long. The Hastelloy X was from the Cabot Corp., Heat No. 2600-4-4284, 1.2-cm-thick plate. Its composition was 21.79 Cr, 19.06 Fe, 8.82 Mo, 2.40 Co, 0.63 W, 0.35 Si, 0.59 Mn, and 0.06 C. Preparation specifications were 1177°C, 15 min in helium, water quench, machine and polish to 0.635 cm diameter.

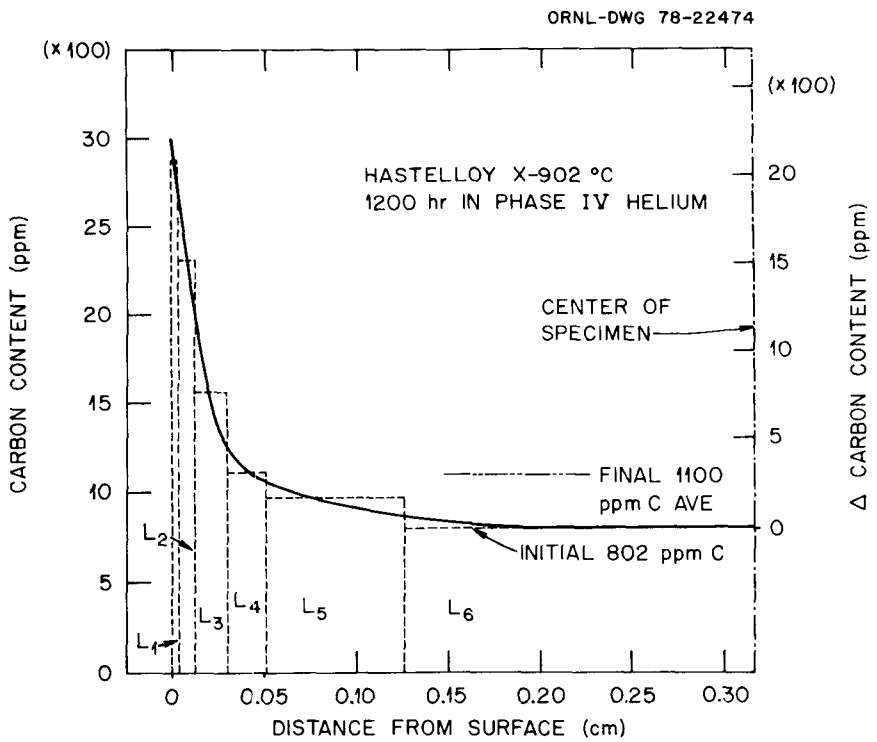


Fig. 4.13. Carbon Gradient in Hastelloy X.

A comparison of the carbon profiles for exposures at 828 and 946°C is presented in Fig. 4.14. The surface carbon is at a maximum at 854°C, and as expected, the penetration depth increases with the exposure temperature.

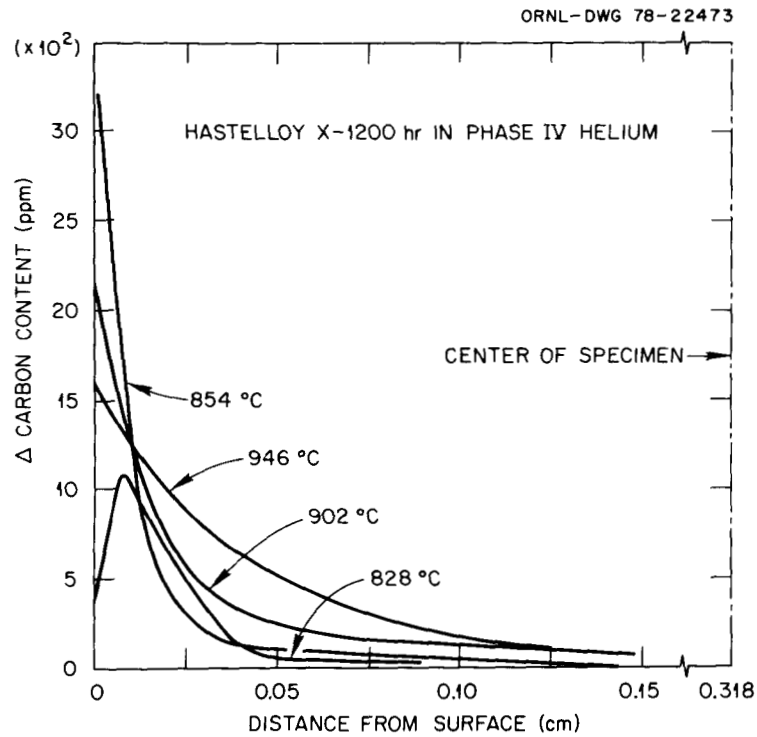


Fig. 4.14. Carbon Gradient in Hastelloy X at Various Temperatures.

Tests in progress include the determination of the 1200-h carburization behavior of Incoloy 800H and LRO-1 and the extension of the phase IV helium exposures to 300 h.

## 4.3 WELDING DEVELOPMENT — J. F. King

The use of dissimilar metal welds is important in certain components of a GCR. In joints that contain a ferritic steel, it is important to select a filler metal that prevents or minimizes carbon migration from the steel to the weld. It has been shown[12] that nickel-based filler metals are preferred in these joints for elevated temperature service. Considerable work has been and is being conducted to characterize the

mechanical properties of essentially undiluted nickel-based weld metals. An investigation of the effect of weld dilution on nickel-based weld metals for dissimilar metal joints looked at the effect of dilution on aging characteristics of the weldments and the short-term creep properties.

### 4.3.1 Dilution Effects on Weld Creep Properties

Comparative creep tests were made to indicate trends in the effect of weld dilution on three nickel-based weld metals. These alloys were ENiCrFe-3 and ENiCrFe-2 shielded metal-arc electrodes and ERNiCr-3 filler metal, for which the nominal chemical compositions are presented in Table 4.5. Two sets of weld deposits were produced by using these materials. The first set was made from undiluted base material: the second set was diluted with the 2-1/4 Cr-1 Mo steel base material. Weld dilution in these deposits was about 20 to 30%. We produced creep specimens from the two types of weld deposits for each of the three weld metals.

Table 4.5. Chemical Composition of Filler Metals Used in This Investigation

| Filler metal | Chemical composition (wt %) | | | | | | |
|---|---|---|---|---|---|---|---|
| | Ni | Cr | Mn | Fe | Cb | Ti | Mo |
| ERNiCr-3 | 67 | 20 | 3 | 3 | 2.5 | 0.75 | |
| ENiCrFe-3 | 67 | 15 | 8 | 8 | 2.5 | 1 | |
| ENiCrFe-2 | 68 | 15 | 1.5 | 9 | 2.5 | | 2 |

Results showed that, for ERNiCr-3 and ENiCrFe-3 tested at 649°C in air, weld dilution reduces the creep-rupture life compared with a pure undiluted sample (Figs. 4.15 and 4.16). Because of small sample size, only the differences observed among specimens are important. No definite trend was established for ENiCrFe-2 weld metal.

Reduction in creep-rupture life of the weld metal as demonstrated in these tests shows the importance of weld dilution in dissimilar metal

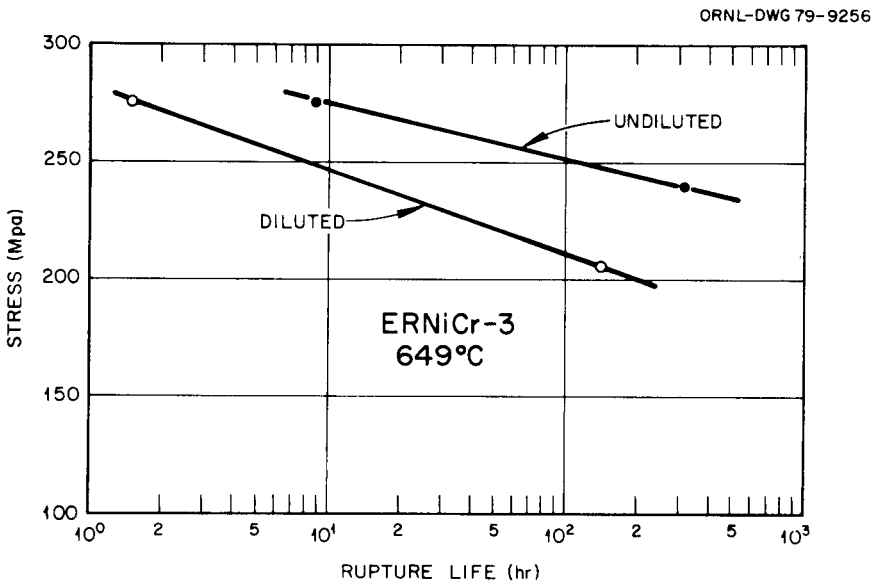


Fig. 4.15. Stress-Rupture Lives of Diluted and Undiluted ERNiCr-3 Weld Metal.

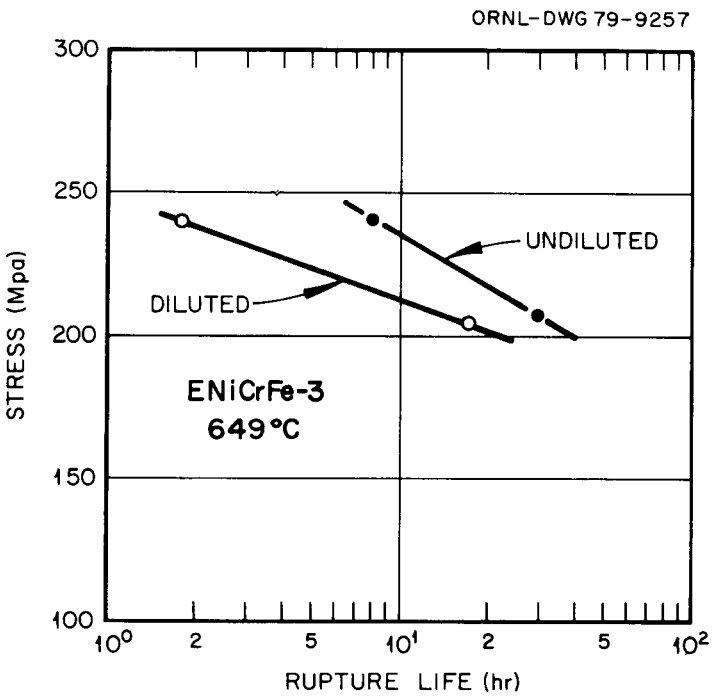


Fig. 4.16. Stress-Rupture Lives of Diluted and Undiluted ENiCrFe-3 Weld Metal.

welds containing a ferritic steel. Weld dilution should be controlled to low levels if available mechanical property data on nickel-based weld metal are used to determine the performance of joints by design analysis techniques.

### 4.3.2 Fusion Line Aging

Fusion line aging characteristics of three nickel-based weld metals were examined for dissimilar metal joining applications that involve ferritic steel as one of the members. Of specific interest was determining if carbon migration from the ferritic steel to the weld varied for the three weld metals. We made weld deposits on 2-1/4 Cr-1 Mo steel by using ENiCrFe-3, ERNiCr-3, and ENiCrFe-2 electrodes and filler metals. Welding conditions were controlled to produce high and low weld dilution with each alloy. Specimens of each sample type were aged at 566 and 621°C for various periods of time up to 5000 h. Metallographic examinations were made at 500, 1000, and 5000 h.

Aging characteristics of all samples were found to be similar. Neither weld dilution nor weld metal composition appeared to have a significant effect on fusion line aging characteristics. Precipitates, assumed to be carbides, were observed along grain boundaries in the weld metal near the fusion line. The precipitates were more prevalent in samples aged at 621 than at 566°C, as expected. However, carbon diffusion from the ferritic steel was not sufficient to show any apparent carbon depletion in the HAZ.

The low dilution specimens of ERNiCr-3 weld metal aged at 621°C produced the semicontinuous globular phase in the ferritic steel adjacent to the weld fusion line. This phase was reported previously[13] in an investigation of a failed transition joint taken from a coal-fired utility boiler. The fracture of this joint progressed through the region of this phase after a service life of 17 years. In the current study, this phase was observed to form after 1000 h of aging and to be more prevalent after 5000 h. No evidence of this phase was observed prior to 1000 h of aging. Figure 4.17 is a photomicrograph of the semicontinuous globular phase.

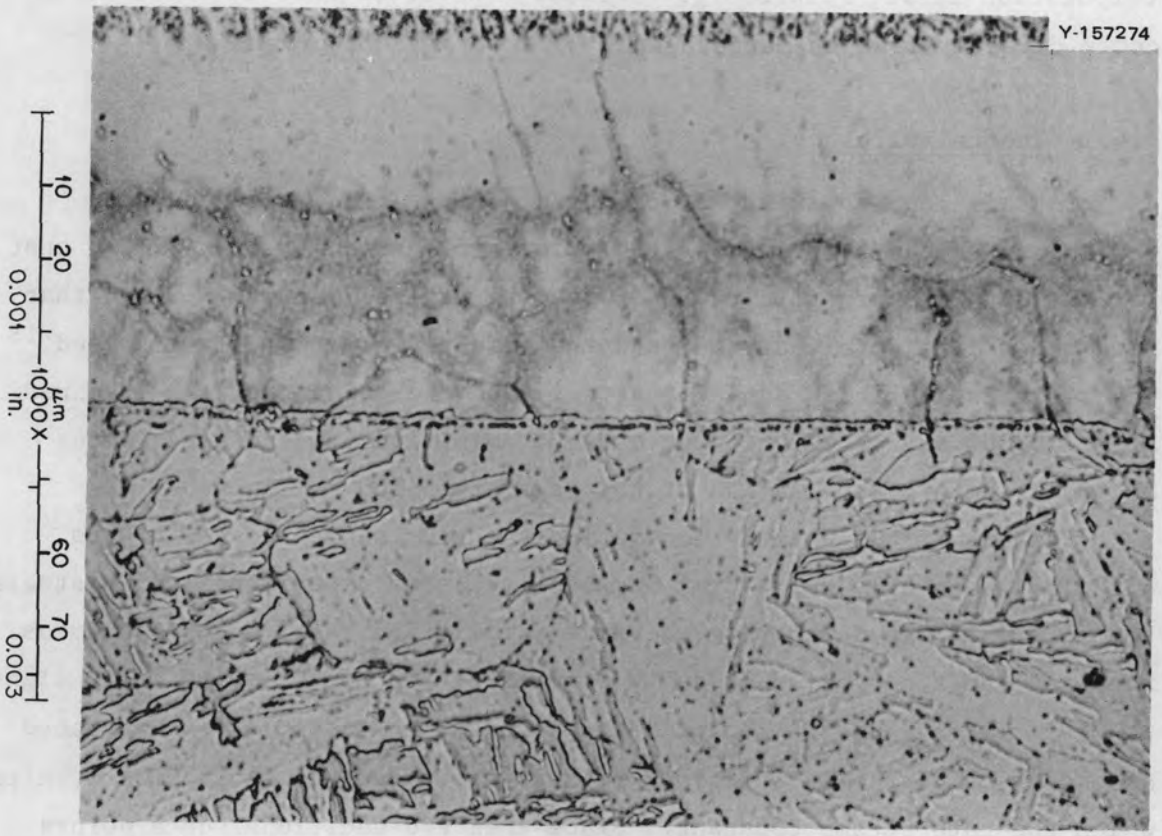


Fig. 4.17. Fusion Line Between ERNiCr-3 Weld Metal and 2-1/4 Cr-1 Mo Steel After 500 h Aging at 621°C.

Our study has shown that, for the three filler metals most commonly used for transition weld joints made of ferritic steel, no significant differences in the fusion line aging characteristics are apparent after 5000 h of aging. One possible exception is the presence of the globular phase that is observed in welds made of ERNiCr-3 weld metal; the actual importance of this phase to the service life of a transition joint is not known.

## 4.4 STEAM CORROSION — J. C. Griess, J. H. DeVan, and W. A. Maxwell

The purpose of this task is to determine the corrosion behavior of selected materials in superheated steam under both normal and faulted conditions and to evaluate the effect of high heat fluxes across corroding surfaces. All testing is performed by the NUS Corporation, under subcontract to ORNL, at the Bartow Plant of the Florida Power

Corporation in St. Petersburg, Florida. The steam used in these tests comes directly from the superheater circuit of that plant.

### 4.4.1 Inconel 617 Loop

In this loop a variety of different alloys are exposed to pure superheated steam at 482 and 538°C. In last year's annual report[14] test results obtained after 12,000 h of testing were summarized. Since that time these data were analyzed, and the results were formally reported.[15] The test was continued during the year, and the specimens were examined after 15,000 and 18,000 h. One other examination is scheduled (after 21,000 h) before termination of the test at 25,000 h.

Results of the examination during the year showed no new trends. After 18,000 h only 2-1/4 Cr-1 Mo steel and some experimental 9 Cr steels tested at 538°C had experienced oxide exfoliation. All other specimens retained their corrosion products completely and continued to gain weight slowly. In last year's report[14] it was noted that most alloys corroded according to parabolic reaction kinetics for about the first 5000 h, after which the rate became constant. Since then two additional data points have been obtained for each specimen, and except for those specimens that obviously lost oxide, the weight-gain data still indicate low constant corrosion rates — in all cases less than 10 μm/year.

During FY 1979 this test will be completed and a final report will be issued.

### 4.4.2 Inconel 625 Loop

In cooperation with personnel at GA, a test was run in the Inconel 625 loop to determine the effect of a very low concentration of sodium hydroxide dissolved in superheated steam on the corrosion of Incoloy 800H. In this test unstressed specimens and specimens stressed to 90% of the ASME design yield stress were exposed to 538°C steam containing 20 to 30 ppb sodium (as NaOH) for 3991 h. The steam pressure was 10.5 MPa.

The complete results of this experiment have been published.[16] In summary, there were no signs of stress corrosion cracking or other forms

of localized attack, but the presence of caustic in the steam produced a slightly more corrosive environment than did pure steam under the same conditions; however, the highest average corrosion rate observed during the 3991-h test was only 6.1 μm/year. Because caustic concentrations as high as those in this test are expected to exist in the steam of an operating power reactor only occasionally and for brief periods, we concluded that such excursions will have no significant effect on the integrity of Incoloy 800H superheater tubes.

### 4.4.3 Heat-Transfer Corrosion Test Loop

During FY 1978 testing in this loop was suspended and the loop was removed from the power plant. During the current fiscal year, this program was reestablished, and the loop has been reinstalled at the Bartow Power Plant. Preliminary calibration of the loop and instrumentation and fabrication of specimens have begun, and tests should start during February 1979. Initial tests will evaluate the behavior of 2-1/4 Cr-1 Mo steel at heat fluxes 50% greater than in previous tests (189 vs 126 $kW/m^2$). Subsequent tests will compare the behavior of 9 Cr steel with 2-1/4 Cr-1 Mo steel.

## 4.5 REFERENCES


1. J. R. DiStefano et al., *HTGR Base-Technology Program Annu. Prog. Rep. Dec. 31, 1977*, ORNL 5412, pp. 255-278.
2. H. E. McCoy, *Creep Behavior of Hastelloy X, 2 1/4 Cr-1 Mo Steel, and Other Alloys in Simulated HTGR Helium*, ORNL/TM report, to be published.
3. C. R. Brinkman et al., *Interium Report on the Continuous Cycling Elevated-Temperature Fatigue and Subcritical Crack Growth Behavior of 2 1/4 Cr-1 Mo Steel*, ORNL/TM-4992 (December 1975).
4. C. R. Brinkman, J. P. Strizak, M. K. Booker, and C. E. Jaske, "Time-Dependent Strain-Controlled Fatigue Behavior of Annealed 2 1/4 Cr-1 Mo Steel for Use in Nuclear Steam Generator Design," *J. Nucl. Mater.* 62(2,3): 181-204 (1976).

5. American Society for Testing and Materials, "Tentative Recommended Practice for Constant Amplitude Low Cycle Fatigue Testing," pp. 626-35 in *1978 Annual Book of ASTM Standards, ASTM-E606-77T*, Philadelphia, February 1977.

6. D. C. Lord and L. D. Coffin, Jr., "Low Cycle Fatigue Hold Time Behavior of Cast Rene 80," *Metall. Trans.* 4: 1647-69 (1973).

7. C. R. Brinkman, J. P. Strizak, and M. K. Booker, *Experiences in the Use of Strain-Range Partitioning for Predicting Time-Dependent, Strain-Controlled Cyclic Lifetimes of Uniaxial Specimens of 2 1/4 Cr-1 Mo Steel and Hastelloy X*, ORNL-5396 (June 1978).

8. W. R. Corwin, M. K. Booker, B. L. P. Booker, and C. R. Brinkman, *Fatigue Crack Propagation in 2 1/4 Cr-1 Mo Steel*, ORNL-5355 (February 1978).

9. H. E. McCoy and B. McNabb, *Corrosion of Several Iron and Nickel-Base Alloys in Supercritical Steam at 1100°F*, ORNL/TM-4552 (August 1974).

10. D. Lupton, KFA, Jülich, Germany, personal communication, July 24, 1978.

11. A. V. Dean, KFA, Jülich, Germany, personal communication, July 24, 1978.

12. J. F. King, *Behavior and Properties of Welded Transition Joints Between Austenitic Stainless Steels and Ferritic Steels — A Literature Review*, ORNL/TM-5163 (November 1975).

13. R. J. Gray, J. F. King, J. M. Leitnaker, and G. M. Slaughter, *Examination of a Failed Transition Weld Joint and the Associated Base Metals*, ORNL-5223 (January 1977).

14. J. C. Griess, J. H. DeVan, and W. A. Maxwell, *HTGR Base-Technology Program Annu. Prog. Rep. Dec. 31, 1977*, ORNL-5412 (July 1978), pp. 309-19.

15. J. C. Griess and W. A. Maxwell, *The Corrosion of Several Alloys in Superheated Steam at 482 and 538°C*, ORNL/TM-6465 (November 1978).

16. J. C. Griess and W. A. Maxwell, *The Corrosion of Incoloy Alloy 800H in Caustic-Contaminated Steam*, ORNL/TM-6797 (May 1979).

# 5. HTGR GRAPHITE STUDIES

W. P. Eatherly and J. A. Conlin

## 5.1 GRAPHITE CREEP EXPERIMENT

### 5.1.1 Graphite Creep Capsules — R. L. Senn

Capsule OC-2 was fabricated and inserted in the Oak Ridge Reactor (ORR) position E-5 on June 28, 1978, for a two-cycle (110-d) irradiation. This capsule contained a number of changes to circumvent the problems encountered with capsule OC-1. The two principal changes were (1) improved alignment of the pressure links that apply the compression load to the samples and (2) substitution of a pneumatic load-measuring device for the linear differential transformers that failed in OC-1. The programming and display capabilities of the Data Acquisition and Control System (ORRDACS) were also improved and extended.

The experiment was operated at a nominal 600°C, with the reactor power at 28 MW rather than the normal 30 MW because of the summer heat. The movable thermocouples that scan the centerline of the unloaded samples operated almost perfectly throughout the irradiation and thus permitted set points for the control thermocouples to be updated as necessary. The sample temperatures were consequently controlled to 600°C, with a total range of ±18°. A temporary loss of the south movable thermocouple motion was traced to the jamming of the motor drive train, which was replaced during reactor shutdown. Other untoward events during the irradiation were several reactor setbacks, which were traced to noise on the ORRDACS electrical lines. The setbacks occur automatically if the computer senses an over-temperature and are meant to protect the experimental samples from thermal annealing of the radiation damage.

The capsule was removed on October 16, 1978, with a peak accumulated fluence of $2 \times 10^{21}$ neutrons/cm$^2$ ($E$ >0.18 MeV). The irradiation is considered to be wholly successful.

The capsule OC-3 assembly was completed; insertion is planned for January 1979. This capsule will be operated at 900°C for a scheduled

two-cycle irradiation. The samples are being recycled from experiment OC-1 to accumulate a planned total peak fluence of $3 \times 10^{21}$ neutrons/cm$^2$.

### 5.1.2 Neutronics Analysis for OC-2 Experiment — W. E. Thomas

Analysis of the OC-2 experiment in ORR facility E5 was quite limited during the report period. Flux results from a 3-D VENTURE[1] calculation for a rearranged core configuration were compared with previous fluxes for a "normal" ORR core. The purpose of the comparison was to provide information on fast neutron flux ($E$ > 183 KeV) distribution in the somewhat "nonconventional" loaded core that existed prior to OC-2 operation. Within the E-5 facility, axial distribution of fast neutron flux was similar for the two cores, about 10% higher for the nonconventional core [i.e., $\sim 3.5 \times 10^{18}$ neutrons m$^{-2}$ s$^{-1}$ versus $\sim 3.2 \times 10^{18}$ neutrons m$^{-2}$ s$^{-1}$ for the peak at $\sim$76 mm below the horizontal midplane of the reactor (HMP)]. Our calculation also showed a similar trend for nuclear heating in graphite ($\sim$9 W/g maximum in the nonconventional core versus $\sim$8 W/g maximum in a normal ORR core). Fuel elements were arranged to provide a more normal fuel distribution prior to OC-2 operation. The irradiation period ended October 16, 1978; 18 of the 20 neutron dosimeter packages were recovered during disassembly of the experiment in the hot cell. Flux monitors within each package are yet to be counted.

### 5.1.3 Graphite Creep Data — C. R. Kennedy

The graphite samples from experiment OC-2 were transferred to the laboratory and measurements initiated in late October. The samples looked identical to their preirradiation appearance. Determinations of dimensions, weights, eddy-current conductivities, sonic velocities, and sonic attenuations were completed, and data reduction is in progress. As expected, the preliminary indication is that the creep at 600°C is less than at 900°C but that the changes in elastic constants and conductivities are much greater. Thermal expansion and electrical conductivities by voltage drop are in progress.

### 5.1.4 Creep Bench Test (1250°C) — H. C. Roland

The bench test for the 1250°C creep capsule design was finally completed, and measurements were initiated in November. The delays were caused by difficulties in obtaining and machining the hollow tungsten cylinder that acts as both a radiation reflector and a gamma-ray susceptor. The situation was further complicated by the inability of the heater manufacturer to fabricate 5/6-in.-diam heater rods and the consequent redesigning of the experiment to accommodate 3/8-in.-diam rods.

## 5.2 KERNFORSCHUNGSANLAGE GRAPHITE IRRADIATIONS IN HFIR

### 5.2.1 Capsule Construction — R. L. Senn

Capsule HTK-1, the first of the German graphite capsules, was inserted in the High Flux Isotope Reactor (HFIR) target position G-5 on March 28, 1978, for a five-cycle irradiation. The capsule was removed on July 24, 1978, with a peak accumulated fluence of $10.7 \times 10^{21}$ neutrons/cm$^2$ ($E > 0.18$ MeV), equivalent to $6.4 \times 10^{21}$ neutrons/cm$^2$ EDN. The samples showed significant activity up to 2 R/h per sample at contact. Despite this activity, the samples could be handled successfully and were reinserted into capsule HTK-2, which was placed into target position B-1 on September 14, 1978. The planned six-cycle irradiation should be completed about February 1, 1979.

### 5.2.2 Preirradiation Characterization — C. R. Kennedy

Each of the blocks of German graphites was mapped to determine areas of uniformity and representativeness. These mappings included eddy-current conductivities, x-radiography, x-ray densitometry, and both longitudinal and shear sonic moduli. The blocks were quite uniform with the exception of the two extruded grades, ATR-2E and UKAEA-11. The German grade ATR-2E showed strong flow lines in the direction of extrusion, and the UKAEA graphite had a low mean density and exhibited a low-density, high-resistivity region.

Samples were selected to represent mean and extreme properties of the blocks, with representative material generally from the center of the billet and nonrepresentative material from the edges. The exception was the UKAEA block, from which all samples were selected to avoid the low-density region.

Values for the elastic constants from sonic measurements are given in Table 5.1, and the Young's moduli as compared with the Kernforschungsanlage (KFA) data are shown in Fig. 5.1. With the exception of the questionable UKAEA block, which is different from the block used by KFA, the data are in excellent agreement.

Table 5.1. Elastic Constants from Sonic Measurements

| Elastic constants | Grade | | | | | | |
|---|---|---|---|---|---|---|---|
| | V483 | V356 | ATR-2R | ATR-2E | ASR-1R | ASR-2R | UKAEA-11 |
| $C_{11}$, GPa | 10.49 | 10.69 | 10.90 | 9.08 | 11.01 | 9.36 | 8.69 |
| $C_{33}$, GPa | 10.24 | 9.61 | 9.33 | 10.66 | 9.41 | 7.70 | 9.42 |
| $C_{44}$, GPa | 4.33 | 4.56 | 3.87 | 3.98 | 4.13 | 3.48 | 3.64 |
| $C_{66}$, GPa | 4.21 | 4.78 | 4.07 | 3.73 | 4.39 | 3.82 | 3.54 |
| $C_{12}$, GPa | 2.07 | 1.13 | 2.76 | 1.62 | 2.23 | 1.71 | 1.61 |
| $C_{13}$, GPa | 1.70 | 1.01 | 2.33 | 1.82 | 1.90 | 1.50 | 1.76 |
| $-S_{12}/S_{11}$ | 0.18 | 0.10 | 0.21 | 0.15 | 0.17 | 0.16 | 0.15 |
| $-S_{13}/S_{11}$ | 0.14 | 0.11 | 0.20 | 0.14 | 0.17 | 0.16 | 0.09 |
| $-S_{13}/S_{33}$ | 0.14 | 0.09 | 0.17 | 0.17 | 0.14 | 0.14 | 0.17 |
| $1/S_{11}$, GPA | 9.90 | 10.47 | 9.86 | 8.59 | 10.31 | 8.85 | 8.29 |
| $1/S_{33}$, GPa | 9.68 | 9.44 | 8.54 | 10.04 | 8.88 | 7.30 | 8.82 |

Data on flexural strength, brittle-ring strength, electrical resistivity, and thermal expansion have been determined on the seven grades. The brittle-ring data have been extended from our normal 17.8-mm-diam ring to a 10-mm-diam ring, which is comparable to the rings to be irradiated. Data on a number of archival samples in the two geometries as well as that on the German graphites are given in Table 5.2 along with

Table 5.2. Fracture Strength Testing of Graphite

| Grade | Density | Orientation | Fracture strengths (MPa) | | | |
|---|---|---|---|---|---|---|
| | | | KFA bend | ORNL bend | 17.8 mm brittle ring | HFIR brittle ring |
| | | KFA grades | | | | |
| V483 | 1.75 | W/G[a] | 31.4 | 33.8 | 40.1 | 46.5 |
| | | A/G[b] | 30.5 | 32.4 | | |
| V356 | 1.76 | W/G | 32.2 | 37.4 | 39.7 | 48.3 |
| | | A/G | 29.4 | 31.8 | | |
| ATR-ZR | 1.74 | W/G | 24.4 | 25.1 | 32.5 | 43.7 |
| | | A/G | 22.4 | | | |
| ATR-2E | 1.82 | W/G | 23.5 | 22.6 | | |
| | | A/G | 18.5 | 19.9 | 31.8 | 41.4 |
| ASR-1R | 1.82 | W/G | 26.0 | 26.6 | 35.4 | 45.4 |
| | | A/G | 23.0 | | | |
| ASR-2R | 1.72 | W/G | 19.4 | 20.2 | 26.4 | 39.1 |
| | | A/G | 15.8 | | | |
| UKAEA-11 | 1.75 | W/G | | 20.3 | | |
| | | A/G | | 19.9 | 27.4 | |
| | | HTGR grades | | | | |
| H451 | 1.74 | W/G | | 30.7 | | |
| | | A/G | | | 32.8 | 41.1 |
| H451 | 1.70 | W/G | | 24.9 | | |
| | | A/G | | 18.2 | 27.7 | 36.8 |
| | | Miscellaneous grades | | | | |
| A681 | 1.64 | Iso[c] | | 37.2 | | 48.3 |
| AXM-5Q | 1.68 | Iso | | 60.7 | | 77.1 |
| AXF-5Q | 1.80 | Iso | | 79.2 | | 102.5 |
| ATJ-S | 1.85 | W/G | | 47.0 | | 56.1 |
| H337 | 1.99 | Iso | | 42.7 | | 56.5 |
| AGOT | 1.74 | A/G | | 9.6 | | 20.8 |
| SA45 | 1.55 | Iso | | 11.6 | | 13.6 |

[a]W/G, with grain.

[b]A/G, against grain.

[c]Iso, isotropic.

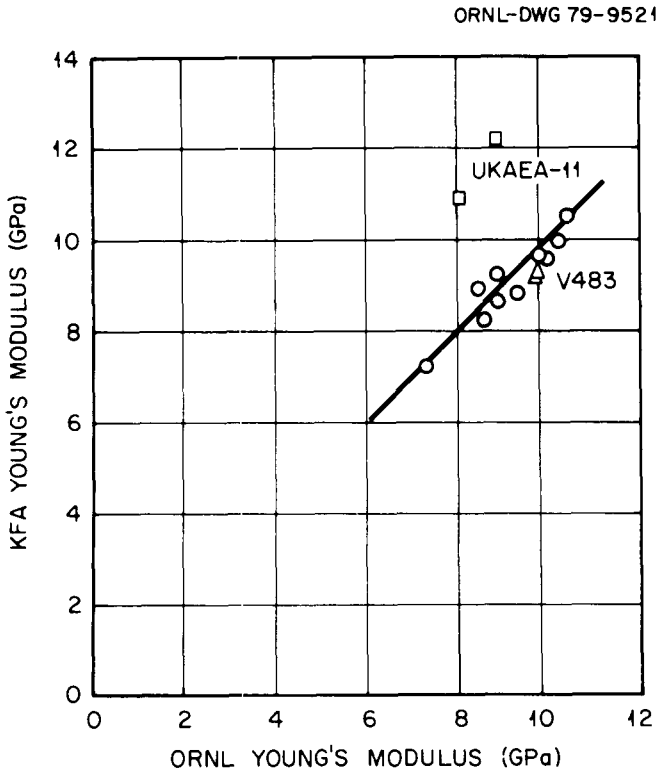


Fig. 5.1. ORNL and Kernforschungsanlage Dynamic Moduli Are in Good Agreement.

KFA and our flexural strengths. The flexural strengths from the two laboratories are plotted in Fig. 5.2. Agreement is excellent, with the slightly higher ORNL values attributable to a slightly smaller stress volume (Weibull effect). This stress-volume effect is more marked in the rings, for which there is a significant difference in geometry. Clearly, however, the small rings give a good measure of strength.

Metallographic examination of polished surfaces has also been performed; V483 and V356 are the finest grained and most crystalline. Grades ATR-2R (molded) and ATR-2E are structurally similar and have a large grain size that appears to be agglomerates. Grades ASR-1R and -2R are even coarser grained and again have an appearance of agglomerates and an intermediate degree of crystallinity. The UKAEA-11 material is quite different; it has extremely low crystallinity and includes much that is structureless.

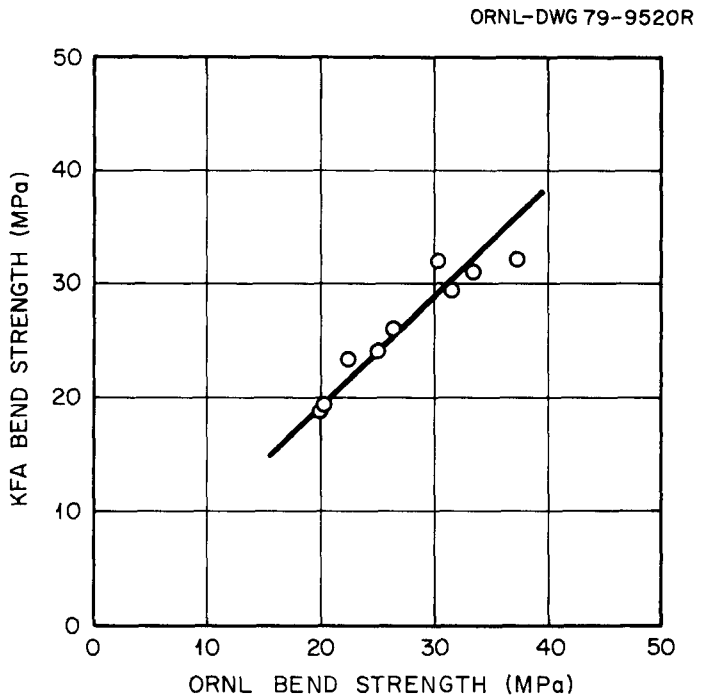


Fig. 5.2. KFA Bend Strengths Correlate Well with ORNL Bend Strengths.

### 5.2.3 Irradiation Results from HTK-1 — C. R. Kennedy

The data package on the HTK-1 irradiation has been completed, and typical results are given in Figs. 5.3 through 5.9. Of note is the correlation of the initial densification rate as related to porosity and thermal-expansion deficiency. This correlation implies that these graphites will behave in a "normal" pattern, although one cannot extrapolate this initial rate to predict necessarily the graphite lifetime.

We have normally measured sonic velocities at frequencies of 0.5 and 1 MHz because graphite is much more transparent to lower frequencies. However, the small size of the HFIR samples precludes these frequencies because of the "near-field" effect generated by the piezo-electric crystal. Measurements could be made successfully at 2-1/4 MHz; sonic attenuation could also be determined. Typical sonic Young's moduli are given in Fig. 5.5, assuming isotropy.

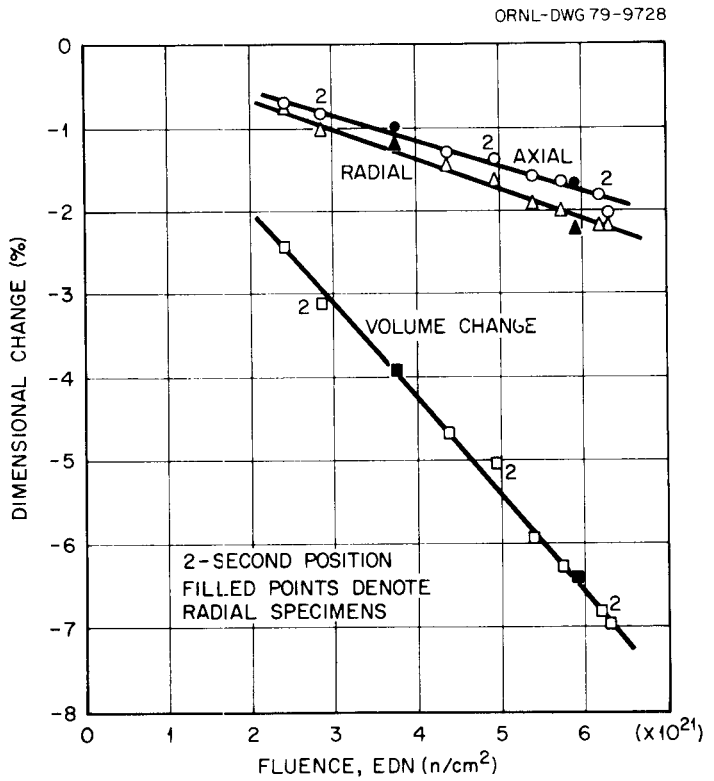


Fig. 5.3. Dimensional Changes of Graphite Grade V-483 on Irradiation at About 550°C.

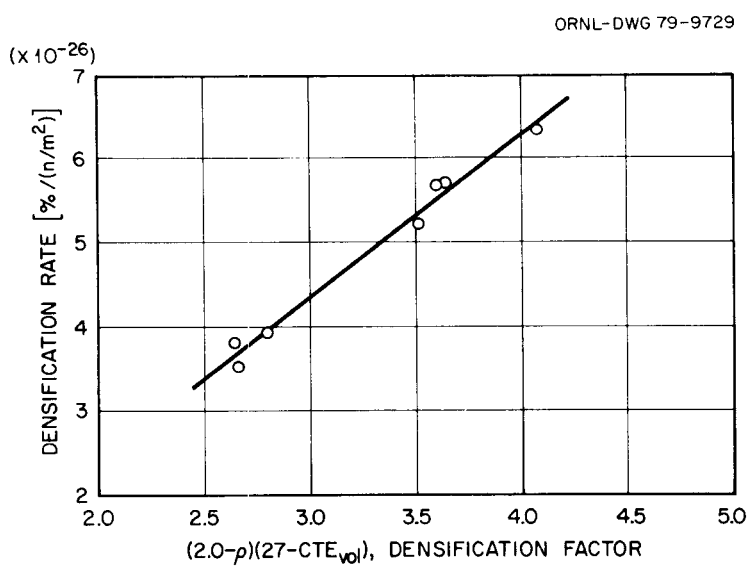


Fig. 5.4. Initial Densification Rate as Related to the "Densification Factor." The symbol ρ represents bulk porosity and $CTE_{vol}$ the volumetric thermal expansion × $10^6$.

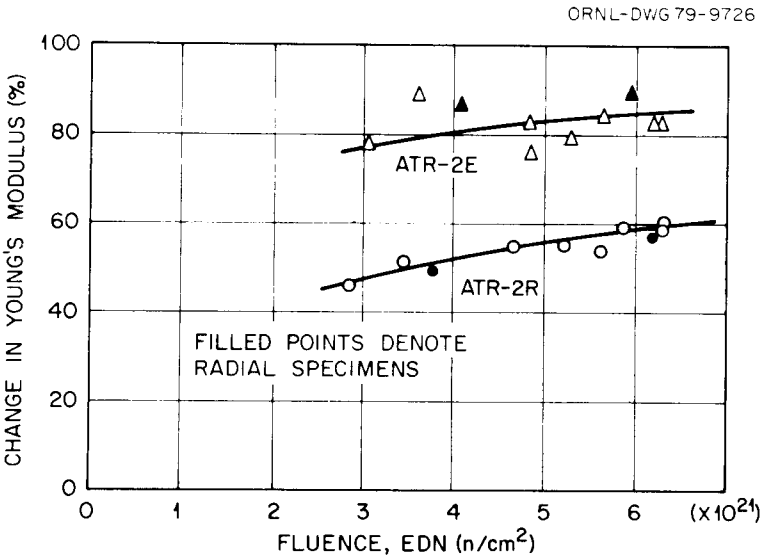


Fig. 5.5. Changes in Sonic Young's Modulus of Graphite Grades ATR-2E and ATR-2R on Irradiation at About 550°C.

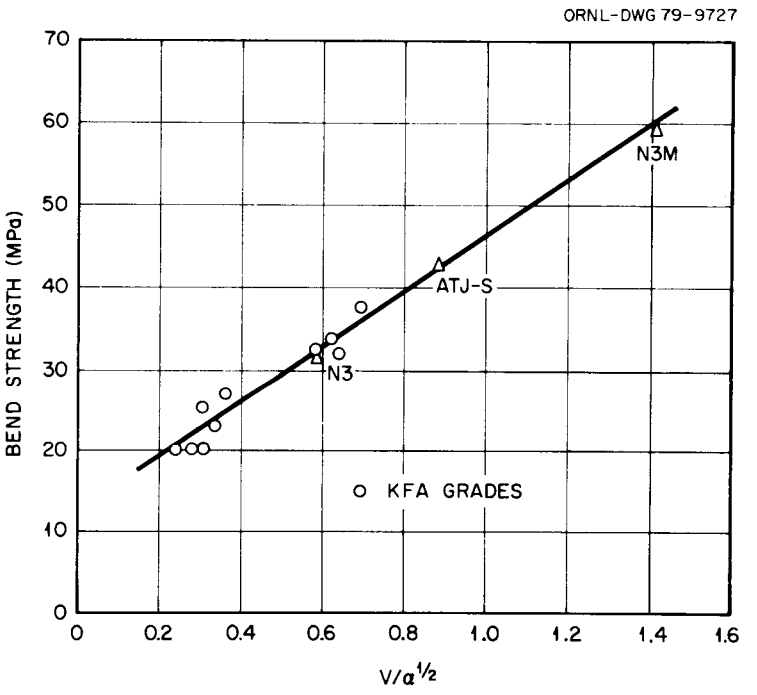


Fig. 5.6. Fracture Stress as Related to the Factor Sonic Velocity $V$ Divided by Square Root of Attenuation Coefficient $\alpha$.

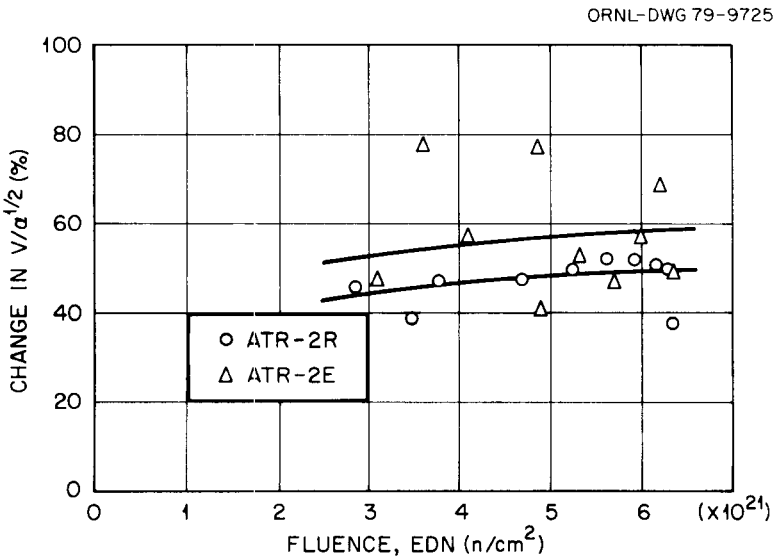


Fig. 5.7. Change in Sonic Velocity Divided by Square Root of Attenuation Coefficient as a Function of Irradiation. This quality should be proportional to fracture strength.

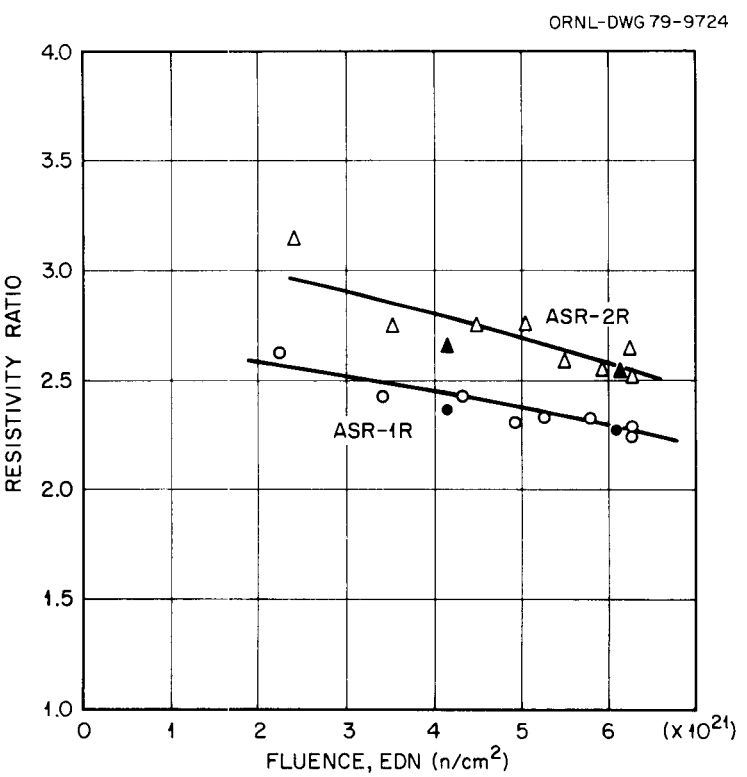


Fig. 5.8. Change in Eddy-Current Resistivity Ratio as a Function of Fluence.

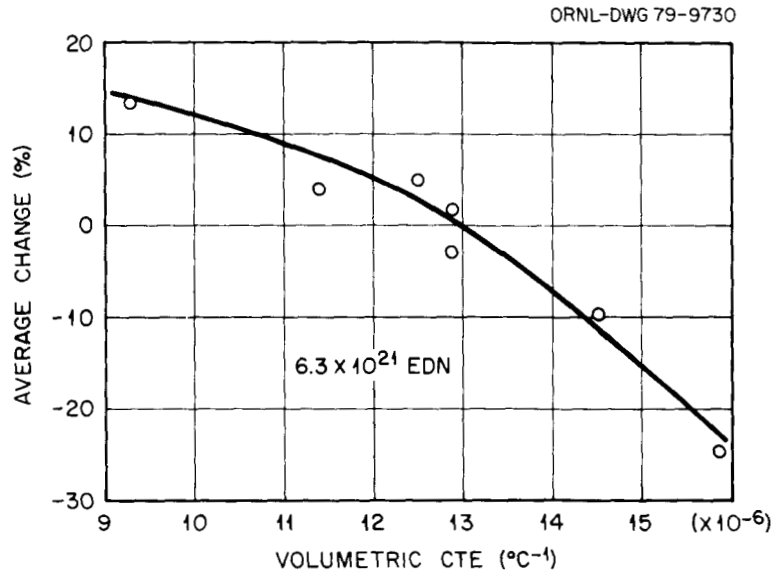


Fig. 5.9. Change in Thermal Expansion Coefficient as Related to Initial (Unirradiated) Coefficient.

From fracture mechanics there should be a monotonic relationship between the fracture strength and the sonic velocity divided by the square root of the attenuation coefficient. That is to say, the velocity is related to Young's modulus, and attenuation is a measure of the background "flaw" field. These graphites show this relationship (Fig. 5.6). The effect of irradiation on this quantity is shown in Fig. 5.7; the data are too scattered to be conclusive, but no major change in strength occurs at this point.

## 5.3 REFERENCE

1. D. R. Vondy et al., *VENTURE A Code Block for Solving Multigroup Neutronics Problems Applying the Finite-Difference Diffusion-Theory Approximation to Neutron Transport*, ORNL-5062 (October 1975).

# 6. EVALUATION OF PEBBLE-BED-TYPE HTR

D. E. Bartine, D. R. Vondy, and B. A. Worley

## 6.1 INTRODUCTION

Both the design and the mode of operation of the high-temperature, gas-cooled, graphite-moderated pebble-bed reactor concept are under study to project reactor performance. Ore use and fuel cost are of primary interest, with design constraints being satisfied. The concept could be used for electrical energy and process-heat production or for a combination of the two. The concept could make an unusually high energy-conversion efficiency possible, which is of special interest. With continuous fueling, the concept can have the advantage of a higher fuel-conversion ratio and availability than do concepts that require the use of control rods to offset the reactivity swing accompanying periodic refueling. An interim report was issued on the early assessment of breeding capability,[1] and a report documenting recent effort is in preparation.[2] This work is under a technical information exchange umbrella agreement with the Federal Republic of Germany.

Reactor performance calculations have been made which emphasize designs for the breeder or near-breeder that uses $^{233}U$ fuel, the pre-breeder that uses $^{235}U$ fuel to produce $^{233}U$ fuel, the nonproliferation operation (throwaway) that uses medium- or low-enriched-uranium feed, and the burner (throwaway) or converter (recycle) that uses fully enriched uranium feed.

The local capability for solving problems by computer has been enhanced for specific application to the continuously fueled core, and development of methods continues. Emphasis in the continuing effort of analysis is on: comparison of the pebble-bed and fixed-fuel prismatic concepts; resonance-shielding, control-rod, and thermal hydraulics calculations; benchmarking methods; and assessment of designs and modes of operation.

## 6.2 ANALYSIS METHODS — M. A. Bjerke, D. R. Vondy, R. M. Westfall, and B. A. Worley

The pebble-bed reactor presents an analysis challenge, especially because, with once-through continuous fueling, the neutron flux distribution is skewed toward the top, where the fresh fuel is located. We discuss here our specific effort to enhance local analysis capability. An effort has also been directed to multiple plant symbiosis calculations.

### 6.2.1 Neutronics and Exposure

Modifications were made to the VENTURE, BURNER, and related codes to permit direct solution of the steady-state, continuous-fueling problem for the critical reactor. One- and two-dimensional problems are solved routinely by the application of the finite-difference, diffusion-theory representation of neutron transport. Special techniques were found to be necessary for stabilizing the tendency of the global two-dimensional neutronics and exposure iterate solutions to oscillate. Capability to follow long plant histories with recycle was also implemented by applying a simple multibatch-point reactor model.

### 6.2.2 Cross Sections

A method for treating multiheterogeneous systems was developed for resonance self-shielding calculations. As applied to the Pebble-Bed Reactor fuel elements, the method determines the double-space shielding effects that result from the presence of coated kernels in a graphite matrix surrounded by a dense outer graphite shell. More than a single pebble type and/or a single kernel type can be treated in an iterative process, which rebalances the surface neutron current sources. Microscopic, cell-averaged cross sections are calculated for the resonance nuclides, dependent on pebble type if desired. The method is being implemented in the local cross-section processing system.

### 6.2.3 Thermal Hydraulics

The primary work is being done under contract by the Technology for Energy Corporation. A one-dimensional calculational procedure has been used for testing and is being coupled to the local core physics codes. A two-dimensional code developed at the Los Alamos Scientific Laboratory is being modified and enhanced to satisfy the basic needs and will be coupled to the core physics codes. The analysis effort is directed at assessment of the coolant flow characteristics and prediction of temperatures in the pebbles and includes consideration of the effect of exposure and temperature history.

## 6.3 PERFORMANCE CHARACTERISTICS OF SPECIFIC FUEL CYCLES — D. R. Vondy and B. A. Worley

### 6.3.1 Burner Operation

The Pebble-Bed Reactor concept can be used as a burner that is fueled with fully enriched $^{235}U$, with subsequent "throwaway" of spent fuel. Calculations have been made over a wide range of values of the key parameters to assess performance. One recycle of fertile pebbles without reprocessing appears to be feasible, although the reductions in ore consumption and fuel cost were found to be small. Diffusion theory is used in the primary analysis effort, but calculations have been made with the discrete ordinates and Monte Carlo methods to study the effects from reflection around the gas space over the coolant inlet region and control-rod insertion.

### 6.3.2 Converter Operation with Recycle

The reprocessing of discharged pebbles and the recyling of fuel would minimize ore requirements. Ore consumption can be reduced from the minimum fuel-cost value by increasing the conversion ratio, but there is a cost penalty. The conversion ratio is increased by reducing the exposure (burnup) and decreasing the carbon-to-heavy-metal ratio. Table 6.1 is a summary of the results obtained.

Table 6.1. Summary of Ore Requirements and Fuel Cycle Costs For Cases Studied

| Exposure [MW(t)d/kg] | Conversion ratio | Ore requirement [kg $U_3O_8$/MW(e) installed] | | Fuel cost [mill/kW(e)h] | |
|---|---|---|---|---|---|
| | | Consumption | Commitment | Low (indirect) | Reference |
| 128 | 0.60 | 2,450 | 2,700 | 4.3 | 5.4 |
| 113 | 0.63 | 2,290 | 2,600 | 4.2 | 5.3 |
| 97 | 0.66 | 2,120 | 2,500 | 4.2 | 5.3 |
| 82 | 0.69 | 1,950 | 2,410 | 4.3 | 5.4 |
| 66 | 0.72 | 1,780 | 2,320 | 4.4 | 5.5 |
| 51 | 0.75 | 1,610 | 2,230 | 4.7 | 5.9 |
| 36 | 0.78 | 1,450 | 2,150 | 5.3 | 6.5 |
| 20 | 0.81 | 1,280 | 2,080 | 7.0 | 8.3 |

The ore commitment to operate the reactor through its life is reduced much less than is the consumption by decreasing the exposure. The cost penalty to reduce the ore consumption 34% is estimated at 24%, but to reduce it 26%, the cost would be increased only 12%.

### 6.3.3 Denatured Fuel

An incentive exists to use a $^{235}U$-$^{238}U$ feed mixture with low to medium enrichments for proliferation-resistant purposes. The feed fuel cannot be used directly for weapons production, and the discharged fuel can be stored without reprocessing. For throwaway cycles, the optimum cost and ore use occur at high burnups and at high carbon-to-heavy-metal ratios. The use of medium-enriched fissile feed ($\sim$0.20 $^{235}U$) with a fertile thorium pebble feed stream for radial blanketing is much more cost effective than is use of lower-enriched feed without thorium.

Parameter studies have been performed over a range of carbon-to-heavy-metal ratios, burnups, and enrichments for use in assessing reactor performance. Axial and radial blankets that use a flowing stream of pebbles containing thorium were examined. Recycle of the fertile (thorium) pebbles without reprocessing reduces the $^{235}U$ feed requirements by as much as 6%.

### 6.3.4 Breeder Operation

With a short residence time and a low carbon-to-heavy-metal ratio, it seems possible to achieve a break-even fuel balance; production would equal consumption, with consideration of processing losses. A significant cost penalty is associated with net breeding, and the amount of net fuel production would be small. The conditions required for breeding lead to a high system fissile inventory. These conditions significantly increase both processing and indirect costs.

### 6.3.5 Prebreeder Operation

The concept can use $^{235}U$ fuel to produce $^{233}U$ fuel. Thus the system for one breeder reactor could be supplied with a fuel inventory annually

from the operation of about 15 prebreeder plants. Energy supply scenarios that contemplate depletion of our ore supply indicate that the prebreeder may play a role in competition with breeders that have higher costs.

The flexibility of the Pebble-Bed Reactor concept can be exploited. A short residence time of fueled pebbles is necessary to effect a high production of $^{233}U$, whereas a long residence time of the fueled pebbles is needed to reduce the fuel cost. One recycle of the fueled pebbles without reprocessing shows advantage, but an associated increase in the peak pebble power density and temperatures may limit feasibility to only partial recycle.

## 6.4 ORE UTILIZATION AND FUEL COSTS — D. R. Vondy and B. A. Worley

A summary of the results of the recent analysis effort covering the range of primary modes of operation is given in Table 6.2.

## 6.5 REFERENCES

1. D. R. Vondy, *Interim Report on Core Physics and Fuel Cycle Analysis of the Pebble Bed Reactor Power Plant Concept*, ORNL/TM-6142 (1977).
2. D. R. Vondy and B. A. Worley, *Pebble Bed Reactor Core Physics and Fuel Cycle Analysis*, ORNL-5484, to be published.

Table 6.2. Performance Summary for the Pebble-Bed Reactor Concept at a Net Plant Efficiency of 0.4[a]

| Service and technology level | Nominal carbon to heavy metal (atomic) | Nominal fueled pebble residence (full power years) | Average conversion ratio | Peak pebble power (kW) | Fueled pebble exposure [MW(t)d/kg HM] | Fissile inventory [kg/installed MW(e)] | | External fissile feed [kg/MW(e) yr] | Fissile commitment [kg/installed MW(e)] | Ore requirement [kg $U_3O_8$/installed MW(e)] | | Fuel cost [mill/kW(e)h] | |
|---|---|---|---|---|---|---|---|---|---|---|---|---|---|
| | | | | | | Plant | System | | | Consumption | Commitment | Low indirect | Reference |
| **Burner, low-enriched uranium** | | | | | | | | | | | | | |
| Low technology | 600 | 2.0 | 0.52 | 1.8 | 130. | 1.2 | 1.4 | 0.97 | 23.2 | 4,900 | 5,250 | 6.3 | 7.0 |
| **Burner, medium-enriched (denatured) uranium fuel** | | | | | | | | | | | | | |
| Low technology | 450 | 2.5 | 0.53 | 2.5 | 110. | 1.3 | 1.5 | 0.81 | 20.0 | 4,200 | 4,500 | 5.4 | 6.1 |
| Reference 450 | 450 | 2.5 | 0.56 | 5.1 | 180. | 1.1 | 1.3 | 0.75 | 18.0 | 3,900 | 4,200 | 5.1 | 5.8 |
| High technology | 450 | 2.5 | 0.54 | 5.5 | 200. | 1.1 | 1.3 | 0.65 | 15.7 | 3,300 | 3,600 | 4.8 | 5.5 |
| **Burner, fully enriched uranium** | | | | | | | | | | | | | |
| Low technology | 250 | 3.8 | 0.55 | 2.6 | 90. | 1.3 | 1.5 | 0.73 | 17.9 | 3,800 | 4,100 | 5.2 | 5.9 |
| Reference | 250 | 3.8 | 0.58 | 4.0 | 225. | 1.3 | 1.5 | 0.68 | 16.8 | 3,500 | 3,900 | 4.6 | 5.5 |
| High technology | 250 | 4.2 | 0.57 | 4.4 | 250. | 1.4 | 1.6 | 0.60 | 15.1 | 3,100 | 3,500 | 4.6 | 5.3 |
| **Converter, fully enriched uranium, recycle** | | | | | | | | | | | | | |
| Low cost | | | | | | | | | | | | | |
| Low technology | 250 | 3.8 | 0.64 | 2.1 | 95. | 1.3 | 2.0 | 0.45 | 11.4 | 2,220 | 2,620 | 4.5 | 5.6 |
| Reference | 250 | 3.8 | 0.66 | 3.0 | 225. | 1.3 | 2.0 | 0.42 | 10.8 | 2,100 | 2,500 | 4.2 | 5.3 |
| High technology | 250 | 4.2 | 0.68 | 3.4 | 250. | 1.4 | 2.1 | 0.40 | 10.4 | 1,980 | 2,380 | 4.0 | 5.1 |
| Low ore | | | | | | | | | | | | | |
| Low technology | 175 | 2.0 | 0.75 | 3.5 | 36. | 1.6 | 2.7 | 0.41 | 10.8 | 1,750 | 2,450 | 5.7 | 6.9 |
| Reference | 175 | 2.0 | 0.78 | 5.0 | 90. | 1.6 | 2.7 | 0.36 | 9.7 | 1,540 | 2,240 | 5.3 | 6.5 |
| High technology | 175 | 2.0 | 0.81 | 5.3 | 100. | 1.7 | 2.8 | 0.32 | 8.7 | 1,330 | 2,030 | 5.1 | 6.4 |
| **Prebreeder, fully enriched uranium[b]** | | | | | | | | | | | | | |
| Low cost | 175 | 2.5 | 0.70 | 2.9 | 45. | 2.0 | 2.8 | 0.60 | 16.3 | 3,110 | 3,760 | 4.6 | 5.8 |
| Reference | 175 | 1.5 | 0.73 | 3.5 | 79. | 1.9 | 3.0 | 0.70 | 18.8 | 3,630 | 4,330 | 5.1 | 6.3 |
| High performance | 175 | 3.0 | 0.71 | 4.5 | 135. | 2.2 | 2.8 | 0.70 | 18.6 | 3,630 | 4,280 | 4.8 | 5.9 |
| **Near breeder, breeder, $U^{233}$ fuel** | | | | | | | | | | | | | |
| Low cost | 250 | 4.2 | 0.710 | 3.7 | 250. | 1.1 | 1.6 | 0.28 | 7.6 | | | 4.0 | 5.1 |
| Intermediate | 175 | 1.5 | 0.890 | 2.5 | 50. | 1.1 | 2.3 | 0.11 | 4.7 | | | 5.5 | 6.8 |
| High conversion | 110 | 2.0 | 0.990 | 2.5 | 40. | 3.0 | 5.6 | 0.030 | 6.3 | | | 5.6 | 8.0 |
| Break-even | 90 | 1.5 | 1.023 | 2.8 | 26. | 3.8 | 8.1 | | 8.1 | | | 7.9 | 11.3 |
| Breeder | 80 | 1.5 | 1.036 | 2.7 | 24. | 4.6 | 9.8 | | 9.8 | | | 9.0 | 13.0 |

[a]Burner and converter load factor 0.75; prebreeder, near breeder, and breeder are high technology; load factor, 0.85; ore enrichment tails, 0.002, 30-year plant life.
[b]Breeder fuel generation for these cases in kg/MW(e) yr (net); 0.28, 0.36, and 0.38.

# GAS-COOLED REACTOR PROGRAMS

JANUARY 1, 1979

PAUL R. KASTEN,* DIRECTOR CMO
JUNE L. ZACHARY, SECRETARY CMO

**AFCEP FUEL CYCLE CHARACTERIZATION AND ECONOMIC STUDIES**
P. R. KASTEN,* MANAGER CMO
A. R. OLSEN,* TASK LEADER MC
W. L. CARTER* CT
R. R. JUDKINS* MC
R. H. RAINEY* ORAU
W. E. UNGER,* TASK LEADER CT

**DIVISION MANAGERS AND COORDINATORS**
J. P. CALLAHAN* ET
D. A. COSTANZO* AC
F. J. HOMAN* MC
R. E. MacPHERSON* ET
A. P. MALINAUSKAS CT

**HTGR BASE TECHNOLOGY PROGRAM**
F. J. HOMAN,* MANAGER MC
DARLENE KECK,* SECRETARY MC

**PCRV DEVELOPMENT**
J. P. CALLAHAN* ET
D. A. CANONICO* MC
W. G. DODGE* ET
D. N. FANNING ET
R. K. NANSTAD* MC
D. J. NAUS* ET
J. E. SMITH* ET
C. C. HURTT* ET

**HTGR STRUCTURAL MATERIALS STUDIES**
J. R. DiSTEFANO* MC
J. C. GRIESS* MC
H. INOUYE* MC
J. F. KING* MC
H. E. McCOY* MC
J. P. STRIZAK* MC
G. W. WEBER* MC
T. WEERASOORIYA* MC
E. BOLLING* MC
L. K. EGNER MC
J. C. FELTNER* MC
W. C. HAWKINS* MC
V. T. HOUCHIN* PE
E. J. LAWRENCE* MC
B. McNABB* MC
E. B. PATTON* MC

**HTGR CHEMISTRY PROGRAM**
R. P. WICHNER CT
R. B. BRIGGS*
F. F. DYER* AC
W. P. EATHERLY* MC
L. L. FAIRCHILD* CT
J. D. KINTIGH* AC
M. F. OSBORNE* CT
S. K. WHATLEY CT

**ANALYTICAL CHEMISTRY STUDIES**
D. A. COSTANZO* AC
J. D. KINTIGH* AC
F. L. LAYTON* AC
W. F. ROGERS* AC

**SPECIAL ASSIGNMENT**
H. CORDS** MC
M. J. KANIA† MC
P. L. RITTENHOUSE† MC

**CHARACTERIZATION AND STANDARDIZATION OF GRAPHITE**
W. P. EATHERLY* MC
J. A. CONLIN* ET
C. R. KENNEDY* MC
R. L. SENN* ET
F. P. JEFFERS* MC

**PEBBLE-BED REACTOR DESIGN STUDY**
D. E. BARTINE* EP
T. J. BURNS* EP
J. P. RENIER CS
D. R. VONDY EP
B. A. WORLEY EP

**FUELED GRAPHITE DEVELOPMENT**
F. J. HOMAN* MC

**FABRICATION AND CHARACTERIZATION**
W. J. LACKEY* MC
V. J. TENNERY* MC
C. S. MORGAN* MC
J. M. ROBBINS* MC
D. P. STINTON* MC
B. R. CHILCOAT* MC
W. H. ELLIOTT, JR.* MC
C. HAMBY, JR.* MC

**IRRADIATION TESTING**
J. A. CONLIN* ET
E. L. LONG, JR.* MC
R. L. SHEPARD* IC
K. R. THOMS* ET
C. A. WALLACE* ET

**NUCLEAR ANALYSIS**
W. E. THOMAS* ET

**POSTIRRADIATION EXAMINATION AND EVALUATION**
F. J. HOMAN* MC
E. L. LONG, JR.* MC
J. M. ROBBINS* MC
T. N. TIEGS* MC
T. J. HENSON* MC
E. L. RYAN* MC
L. G. SHRADER* MC

**IRRADIATION FUEL CHEMISTRY**
T. B. LINDEMER CT
R. L. PEARSON CT

**GAS-COOLED FAST REACTOR PROGRAM**
URI GAT,* PROGRAM MANAGER ET
PEGGY McNUTT,* SECRETARY ET

**PRESSURE VESSELS AND CLOSURES**
J. P. CALLAHAN,* MANAGER ET
W. G. DODGE* ET
D. N. FANNING ET
G. C. ROBINSON* ET

**SHIELDING AND REACTOR PHYSICS STUDIES**
D. E. BARTINE,* MANAGER EP
D. T. INGERSOLL, TASK LEADER EP
T. J. BURNS* EP
N. S. CRAMER* EP
M. B. EMMETT* EP
F. J. MUCKENTHALER* EP
C. O. SLATER EP
J. R. WHITE* EP
L. R. WILLIAMS* EP

**CORE FLOW TEST LOOP PROJECT**
URI GAT,* MANAGER ET
A. G. GRINDELL,* DEPUTY MANAGER* ET

**CFTL LOOP DESIGN DEVELOPMENT SUPPORT**
A. G. GRINDELL,* TASK LEADER ET

**I & C SUPPORT**
S. P. BAKER,* TASK LEADER IC
J. E. BATEY* QAI
D. W. McDONALD* IC

**CIRCULATOR DEVELOPMENT**
H. C. YOUNG,* TASK LEADER ET
T. B. CONLEY* ET

**ELECTRICAL ENGINEERING**
T. L. HUDSON,* TASK LEADER E

**CFTL BUNDLE DESIGN AND CONSTRUCTION**
H. C. YOUNG,* BUNDLE ENGINEER ET

**BUNDLE DESIGN**
C. W. COLLINS,* PRINCIPAL DESIGN ENGINEER E
J. A. SENEKER* E

**FUEL ROD SIMULATOR DEVELOPMENT**
R. W. McCULLOCH,* TASK LEADER ET

**DESIGN DEVELOPMENT FOR BUNDLE**
H. C. YOUNG,* BUNDLE ENGINEER ET
T. B. CONLEY* ET

**I & C DEVELOPMENT FOR BUNDLE DESIGN**
S. P. BAKER,* TASK LEADER IC
R. L. ANDERSON* IC

**BUNDLE PROCUREMENT**
H. C. YOUNG,* BUNDLE ENGINEER ET
T. B. CONLEY* ET

**CFTL ANALYSIS**
J. P. SANDERS, TASK LEADER ET
J. C. CONKLIN* ET
W. G. DODGE* ET

**CFTL LOOP DESIGN**
W. R. HUNTLEY,* LEAD ENGINEER ET
C. W. COLLINS, PRINCIPAL DESIGN ENGINEER E

**MECHANICAL DESIGN**
W. R. CLARK* E
W. A. HARTMAN E
J. A. SENEKER* E

**ELECTRICAL DESIGN**
R. B. BIGGS, LEAD ENGINEER E
C. F. HOLLOWAY E
T. L. HUDSON* E
M. D. TRUNDLE E

**I & C DESIGN**
P. G. HERNDON, PRINCIPAL ENGINEER IC
S. J. BALL,* DYNAMIC ANALYSIS AND CONTROLS IC
K. J. CROSS,* DATA ACQUISITION IC
A. D. McNUTT E
C. I. ROSE E
D. W. McDONALD* IC

**PROJECT ENGINEERING**
H. L. MITCHELL, TASK LEADER E
K. D. COOK,* ESTIMATING E
F. K. BOOTH,* RUST INTERFACE E
P. A. TABOR,* SCHEDULING E

**CFTL PROCUREMENT**
W. R. HUNTLEY,* LOOP ENGINEER ET
T. B. CONLEY* ET
E. M. LEES* ET
J. R. McGUFFEY QAI
H. C. YOUNG,* CIRCULATORS ET

**CFTL CONSTRUCTION**
W. R. HUNTLEY,* LOOP ENGINEER ET
T. B. CONLEY* ET
P. P. HAYDON, CPAF COORDINATOR ET
D. B. AuBUCHON* QAI

**CFTL QUALITY ASSURANCE**
C. A. MILLS,* CFTL QAC ET

**HTGR SAFETY STUDIES FOR NRC RSR**
S. J. BALL,* MANAGER IC
RENEE WRIGHT,* SECRETARY IC

J. C. CLEVELAND* ET
J. C. CONKLIN* ET
H. GHEZELAYAGH*** ET
J. P. SANDERS* ET

*CONSULTANT
*PART TIME/DUAL CAPACITY
**ASSIGNEE FROM KFA, JULICH
***ASSIGNEE FROM IRAN
†ASSIGNED TO KFA, JULICH

AC ANALYTICAL CHEMISTRY DIVISION
CMO CENTRAL MANAGEMENT OFFICES
CS COMPUTER SCIENCES
CT CHEMICAL TECHNOLOGY DIVISION
EP ENGINEERING PHYSICS DIVISION
ET ENGINEERING TECHNOLOGY DIVISION
IC INSTRUMENTATION AND CONSTROLS DIVISION
MC METALS AND CERAMICS DIVISION
QAI QUALITY ASSURANCE AND INSPECTION

ORNL-5536
Distribution
Category UC-77

## INTERNAL DISTRIBUTION

1-2. Central Research Library
3. Document Reference Section
4-6. Laboratory Records Department
7. Laboratory Records, ORNL RC
8. Patent Office
9. D. E. Bartine
10. I. H. Brogden
11. J. P. Callahan
12. D. A. Canonico
13. J. A. Conlin
14. D. A. Costanzo
15. W. G. Dodge
16. R. G. Donnelly
17. F. F. Dyer
18. W. P. Eatherly
19. L. L. Fairchild
20. D. N. Fanning
21. D. E. Ferguson
22. Uri Gat
23. J. C. Griess
24. R. F. Hibbs
25. M. R. Hill
26-49. F. J. Homan
50. H. Inouye
51. J. D. Jenkins
52. M. J. Kania
53-68. P. R. Kasten
69. C. R. Kennedy
70. J. F. King
71. J. D. Kintigh
72. W. J. Lackey
73. F. L. Layton
74. T. B. Lindemer
75. E. L. Long, Jr.
76. A. P. Malinauskas
77. H. E. McCoy, Jr.
78. C. S. Morgan
79. R. K. Nanstad
80. D. J. Naus
81. M. F. Osborne
82. R. L. Pearson
83. H. Postma
84. J. P. Renier
85. P. L. Rittenhouse
86. J M Robbins
87. W. F. Rogers
88. R. L. Senn
89. J. E. Smith
90. D. P. Stinton
91. J. P. Strizak
92. V. J. Tennery
93. W. E. Thomas
94. K. R. Thoms
95. E. T. Thomlinson
96. T. N. Tiegs
97. D. B. Trauger
98. D. R. Vondy
99. J. R. Weir
100. S. K. Whatley
101. R. P. Wichner
102. B. A. Worley

## EXTERNAL DISTRIBUTION

103-104. DOE Division of Nuclear Power Development, Washington, DC 20545, Director
105. DOE Idaho Operations Office, P.O. Box 2108, Idaho Falls, ID 83401, Barry Smith
106. DOE Office of Program Management, Research and Space Programs, P.O. Box 81325, San Diego, CA 92138, J. B. Radcliffe
107. DOE San Francisco Operations Office, 1333 Broadway, Wells Fargo Building, Oakland, CA 94612, Manager

108-110. DOE Oak Ridge Operations Office, P.O. Box E, Oak Ridge, TN 37830; Assistant Director, Energy Research and Development; Director, Reactor Division; F. E. Dearing, Reactor Division

111-286. DOE Technical Information Center, Office of Information Services, P.O. Box 62, Oak Ridge, TN 37830, for distribution as shown in TID-4500 Distribution Category, UC-77 (Gas-Cooled Reactor Technology)

☆U.S. GOVERNMENT PRINTING OFFICE: 1979-640-079-81